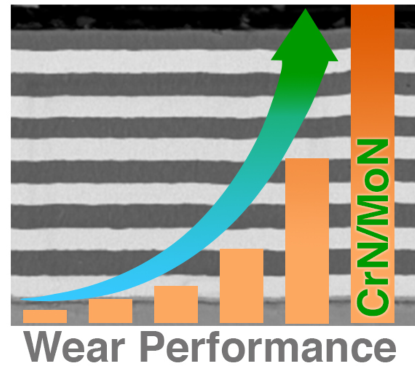

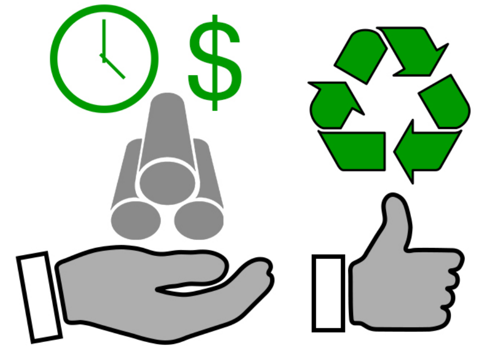

Superhard Protective Coatings with Enhanced Toughness: Multi-Layered Nanocomposite Metal Nitrides

Bogdan Postolnyi
Doutoramento em Física (MAP-fis)
Departamento de Física e Astronomia
2020

Orientador
Professor João Pedro Esteves de Araújo,
Faculdade de Ciências da Universidade do Porto

Coorientador
Professor Alexander Pogrebnjak,
Sumy State University

Coorientador
Professor Luís Manuel Fernandes Rebouta,
Centro de Física, Universidade do Minho

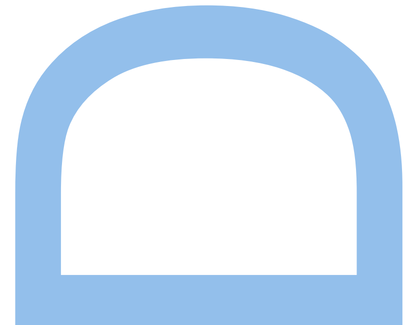
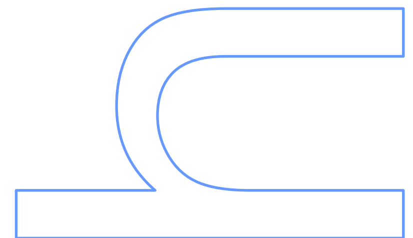
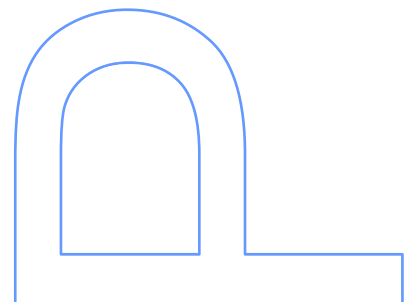

Institutions involved in this Thesis work

IFIMUP
Institute of Physics for
Advanced Materials,
Nanotechnology and Photonics
The University of Porto

**Sumy
State
University**

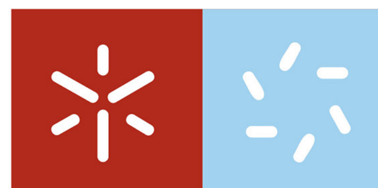

Universidade do Minho
Escola de Ciências

This PhD work was supported by the Portuguese Foundation for Science and Technology (FCT - Fundação para a Ciência e a Tecnologia), grant number SFRH/BD/129614/2017.

FCT
Fundação
para a Ciência
e a Tecnologia

"If you want to go fast, go alone. If you want to go far, go together."

— African proverb

Acknowledgements

Acknowledgement section is a great reason to write PhD Thesis! And the most pleasant part of the writing process! This is an opportunity to hold on for a second, look back for all performed work, remember everyone who met on the way and thank them. I am happy and proud to say that I met many beautiful, intelligent and open-minded people with big heart, rich life experience and wisdom. Without their trust, help and professionalism, I would not be who I am now. I am glad to thank you all!

I would like to express my gratitude to my first scientific supervisor, Professor Alexander Pogrebnjak, Head of the Department of Nanoelectronics at Sumy State University, Ukraine, for selecting me and for the introduction to scientific work. Many thanks for organising and sharing his worldwide scientific network to allow our research group to perform study and do a science of high quality in very limited circumstances of Ukrainian science. I also grateful to him that despite any difficulties encountered during our work he never gave up! Besides this, Professor Alexander Pogrebnjak is a great example to follow in such high productivity, energy and dedication to work.

I am deeply thankful to Daryna Leus (Boronos), who suddenly passed away in the prime of life, for her timely advice and support when I almost gave up with my application for the Erasmus Mundus project. If she had not called, the series of further events would have been significantly different, and I would not have open Portugal and the University of Porto for myself in 2014.

I want to thank my supervisor Professor João Pedro Esteves de Araújo, President of the Institute of Physics for Advanced Materials, Nanotechnology and Photonics (IFIMUP) at the University of Porto, Portugal, for everything he did for me! For his decision, among hundreds of his duties, to consider and approve my application for a 10-month internship at the Faculty of Sciences of the University of Porto, which opened Portugal for me for many years! I thank him for the first warm and friendly meeting and for the introduction to colleagues at IFIMUP. I am immensely grateful to Professor João Pedro Araújo for believing in me, for the invitation for PhD study, for all help with research and finding funds, for my autonomy, for support in my development and professional growth. He is a professional and excellent leader and a Great Man, who is a role model for me that I want to follow!

Many thanks to my co-supervisor Professor Luís Manuel Fernandes Rebouta from the Centre of Physics of the University of Minho, Portugal, for his openness and welcoming, for his competence and professionalism, for accepting to help with my PhD Thesis and research. I am grateful for all experimental work of thin films deposition performed at his labs, for help with interpretation results, for reviewing the papers and for valuable suggestions, for his fast and responsible comments, for friendly and warm communication!

I am very thankful to Professor Gregory Abadias from Pprime Institute, CNRS - University of Poitiers - ISAE-ENSMA, France, for the warm welcome and care in Futuroscope and Poitiers.

I appreciate all time he spent during one month of intensive work with me. Thanks so much for the training in SEM/EDS/WDS operation, for all efforts in thin films deposition and study, for teaching, sharing knowledge and experience with me. I am grateful for his support of my PhD research, his expertise and assistance in the paper preparation, for his contribution and careful editing of the manuscript. It was always a pleasure to meet him somewhere at international conferences or attend his lectures or tutorials!

Many thanks to Professor Vyacheslav Beresnev from V.N. Karazin Kharkiv National University in Kharkiv and Dr. Viacheslav Stolbovyi from the National Science Center "Kharkiv Institute of Physics and Technology", Ukraine, for their help with deposition of the coatings studied in this PhD Thesis, Professor Fadei Komarov and Dr. Stanislav Konstantinov from Belarusian State University in Minsk, Republic of Belarus, for help with performing Rutherford backscattering spectrometry analysis, Professor Piotr Konarski from the Tele and Radio Research Institute in Warsaw, Poland, for help with performing secondary-ion mass spectrometry analysis, Professor Stefan Jurga, Dr. Emerson Coy and Dr. Karol Zaleski from NanoBioMedical Centre, Adam Mickiewicz University in Poznan, Poland, for help with performing transmission electron microscopy experiments.

I would like to thank to the members of the Jury, Professor Albano Augusto Cavaleiro Rodrigues de Carvalho, Professor Orlando M. N. D. Teodoro, Professor Rui Ramos Ferreira e Silva, Professor Bernardo Gonçalves Almeida, Professor André Miguel Trindade Pereira and Professor José Luís Campos de Oliveira Santos, for their availability and time to read this Thesis, for their work, reasonable and valuable comments.

I thank to *Fundação para a Ciência e a Tecnologia* (FCT) and the Ukrainian State Budget for the very important partial funding of this research both through the PhD personal fellowship and group projects. I also thank to Erasmus Mundus Action 2 Programme of the EU for the Doctorate Mobility within the framework of the EMINENCE II project.

One more key-element that recently influenced my PhD research, my scientific interests and ideology, is the COST Action "Solutions for Critical Raw Materials Under Extreme Conditions" (CRM-EXTREME) focused on the substitution of CRMs or minimisation of their use in high value alloys and metal-matrix composites used in the industry. The Action helped me to understand the place and relevance of my research in modern material science, machinery manufacturing industry and circular economy. Many thanks to Dr. Maria Letizia Ruello, the Chair of the Action, for accepting me to become a member of CRM-EXTREME and to benefit from the networking tools and activities. Warmly thank also for all members of the network for fruitful discussions, work and collaboration, especially to Antonella, Maria Luisa, Saurav, Pavel, Vjaceslavs, Lucyna, Dragan, Zara, Andrei, Roberto, Andreas.

I am very grateful to all IFIMUP members for their work and support as a big family. Especially I would like to express my appreciation to João Horta Bello and Arlete Apolinário for

their selfless help from the first days of my staying at IFIMUP even though they didn't know for how long I am going to stay there. Isabel Alves for all paperwork help and assistance. Gonçalo Oliveira for help in XRD laboratory. Catarina Dias, Rui Vilarinho, Bernardo Bordalo, Paula Quitério for their help and company during MAP-courses and all along the way at IFIMUP.

Administrative and teaching staff of Sumy State University for all given classes and experience, especially Faculty of Electronics and Information Technologies, Department of Electronics and Computer Technologies. Many thanks to active students participating and supporting all social life we performed at the University! Kind regards to our young research group headed by Professor Alexander Pogrebnjak, with whom I spend first years of my scientific activity, namely Ivan Yakushchenko, Vladyslav Rogoz, Andrii Shypylenko, Aleksandr Pshyk, Artem Demianenko, Margarita Lisovenko, Kateryna Smyrnova.

My heartfelt thanks go to Olena Kostylenko for being with me all these unforgettable years, for all your love, care and support! Thank you for following me to "the edge of the World" and for all moments shared together, for young years, for all trips, presents, warmth, raspberry tea, borsch, cakes, laugh, bike rides, Shambhala, croissants, pizzas and litres of coffee!

It is not enough to say thank you to my parents carrying and loving throughout life their only son, living nowadays thousands of kilometres away and visiting them just once per several years. Thank you for all the sacrifices you have made for me! Thank you for my childhood, Santa's gifts, our cat Anfisa, comfort and warmth at home, homemade food, tomatoes from the own garden, all opportunities for education and growth! Thank you for allowing me to be independent and have freedom of choice! I appreciate all that you did for me and will remember and follow it all my life!

Resumo

As exigências para materiais e ferramentas estão em constante crescimento. As necessidades recentes da engenharia, indústria de defesa, e do sector das empresas e tecnologias exigem novos materiais com propriedades superiores capazes de trabalhar sob condições extremas. Torna-se assim indispensável o uso de materiais únicos com propriedades únicas. Frequentemente, esses materiais estão disponíveis em locais recônditos da Terra, o seu volume disponível é muito limitado e é controlado por apenas alguns países. Para além disso, o processo de extração de matérias-primas pode ser muito caro, arriscado e poluente. A Comissão Europeia nomeou essas substâncias como matérias-primas críticas (MPC), cujo fornecimento está associado a um alto risco, sendo de alta importância para a economia da União Europeia.

A maior parte dos materiais utilizados em engenharia mecânica e civil, ferramentas, peças de máquinas, etc., são de aço e carbonetos cimentados. Ambos contêm elementos que formam carbonetos, como W, Mo, V, Cr entre outros. Pelo menos sete deles pertencem à lista dos MPC de 2017.

Todos os tipos de mecanismos de falha, como adesão, abrasão, oxidação, difusão, etc., ocorrem na superfície. Portanto, são resultado de interações nas interfaces entre ferramenta e peça de trabalho ou ferramenta e meio ambiente, respetivamente. É possível proteger uma ferramenta por tratamento de superfície, criando alguma interface ou revestimento adicional especialmente desenhada para o efeito. Revestimentos de proteção superduros com resistência reforçada resultam numa menor taxa de desgaste para as ferramentas e, consequentemente, numa vida útil prolongada de cada unidade, sem perda de velocidade operacional, ou possibilitando manter a mesma vida útil com aumento da velocidade de trabalho. Quando o revestimento é destruído, é fácil reciclar o produto através da limpeza e remoção do filme protetor seguida da deposição de um novo revestimento.

Para produzir um novo revestimento com maior dureza, tenacidade e resistência ao desgaste, propõe-se empregar principalmente duas abordagens e obter benefícios dessa combinação: fortalecimento *Hall-Petch* com base no efeito do controle de tamanho de grão e desenho de filmes em multicamadas. O primeiro assume um aumento dos valores de dureza quando o tamanho do grão se reduz até cerca de 10 nm. A segunda abordagem, i.e. uma arquitetura em multicamada dos revestimentos, melhora as propriedades protetoras dos filmes multicamadas, reduzindo a propagação de falhas em direção ao substrato pela deflexão de falhas nas interfaces entre camadas. Além disso, pelo controle da espessura das camadas individuais nos revestimentos, é possível predeterminar o tamanho dos grãos nos revestimentos: camadas mais finas – grãos menores.

O desenho de revestimentos em multicamadas permite também tomar partido da combinação das excelentes propriedades dos diferentes materiais usados como camadas individuais nos filmes. O CrN foi selecionado para revestimento devido à sua alta estabilidade

térmica, alta resistência à corrosão e ao desgaste, forte adesão à superfície. Além disso, o óxido produzido na superfície do revestimento serve como um bom lubrificante para reduzir o desgaste. O nitreto de molibdénio é um nitreto metálico duro ainda relativamente pouco estudado. A diversidade de fases possíveis com uma ampla gama de estequiometria e estruturas cristalinas torna-o interessante para o estudo aqui apresentado.

Os revestimentos multicamadas CrN/MoN considerados nesta tese de doutoramento foram fabricados por evaporação, em atmosfera de nitrogénio, por arco catódico de crómio e molibdénio em vácuo (deposição física de vapor por arco catódico, Arc-PVD). Para além das técnicas convencionais de caracterização avançada de filmes finos utilizadas, nomeadamente microscopia eletrónica de varrimento (SEM), espetroscopia de raios X por dispersão em energia (EDS), espetroscopia de raios X por dispersão em comprimento de onda (WDS), difração de eletrões retrodispersos (EBSD), espetrometria de retrodispersão de Rutherford (RBS), difração de raios X (XRD), espetrometria de massa por iões secundários (SIMS), microscopia eletrónica de transmissão de elevada resolução (HRTEM), nanoindentação e testes tribológicos, foram realizados abordagens específicas no estudo das estruturas multicamadas. Em particular, as técnicas de difração de raios X de baixos ângulos, como "in-plane" XRD e de varrimento assimétrico, incluindo XRD com incidência rasante (GIXRD), foram usadas para estudar duas fases principais de CrN e γ-Mo_2N cúbicas com estruturas cristalinas e constantes de redes muito semelhantes resultando em picos de difração sobrepostos e mais largos quando o revestimento multicamada é estudado com XRD convencional θ/2θ, complicando a análise. O *in-plane* XRD permite estudar planos de difração orientados na direção normal à superfície. Varrimento assimétrico e θ/2θ com offset em ω permitiram calcular os parâmetros de rede através de planos cristalográficos orientados em qualquer direção. Desta forma, foi possível realizar a medição das tensões/deformações residuais.

Os revestimentos superduros baseados em multicamadas de CrN/MoN foram estudados e demonstraram ser apropriados para aplicações industriais em revestimentos protetores. Foi observado que o aumento do valor absoluto da tensão de polarização negativa aplicada à superfície do substrato durante a deposição leva a alterações na orientação cristalográfica preferencial das duas principais fases cúbicas CrN e γ-Mo_2N apresentadas nos filmes, indo de uma orientação (311) quando $U_b = -20$ V para (111) quando $U_b = -150$ V, mais estável, e depois para (200) em $U_b = -300$ V. Quando a pressão de nitrogênio na câmara diminui para 0.09 Pa, ocorre a formação da fase β-Cr_2N, o que causa a deterioração das propriedades tribológicas das multicamadas. A diminuição da espessura da camada individual dos revestimentos leva à diminuição do tamanho das cristalites (até 5.8 nm quando a espessura da bicamada é de 44 nm). A série depositada com $U_b = -20$ V demonstrou ser a mais promissora. Os revestimentos apresentaram alta dureza (38-42 GPa), relação H/E = 0.107 e alta resistência ao desgaste de acordo com o teste tribológico. Para as melhores condições de deposição testadas: $U_b = -20$ V,

p_N = 0.4 Pa sendo a espessura da camada individual 22 nm. Os resultados apresentados demonstram a elevada qualidade dos materiais produzidos.

Palavras-chave: multicamadas, revestimentos superduros, nitretos, deposição física de vapor, difração, microestrutura, composição de fases, propriedades mecânicas, dureza, desgaste, relação H/E, matérias-primas críticas.

Abstract

Requirements for materials and tools are constantly growing every day. Modern needs of engineering, defence industry, business and technologies call for new materials with superior properties to provide sustainable work under extreme conditions. This forces to use unique materials with unique properties. Often these materials are hidden somewhere deep in the bowels of the Earth, and their available volume is very limited and controlled by certain countries. Also, the extraction process of raw materials may be very costly and risky. The European Commission names such raw materials of a high importance to the economy of the European Union and whose supply is associated with a high risk as Critical Raw Materials (CRMs).

Major part of materials used in mechanical and civil engineering, tools, parts of machines etc. are steel and cemented carbides. Both of them contain carbide-forming elements, such as W, Mo, V, Cr and others. At least seven of them belongs to the 2017 CRMs list.

All types of failure mechanisms, such as adhesion, abrasion, oxidation, diffusion, etc., occur on the surface. Therefore, they are results of interactions at the interfaces between tool and workpiece or tool and ambient medium, respectively. It is possible to protect a tool by surface treatment, creating some additional interface or coating with individually designed features. Superhard protective coatings with enhanced toughness provide lower wear rate for the tools and, hence, extended lifetime of each unit with no loss in operational velocities and increased working speeds at the same level of time in service. When the coating is destroyed, it is easy to recycle a product by cleaning the bulk base and deposition of a new coating.

To produce a new coating with superior hardness, toughness and wear resistance it is proposed to employ mainly two approaches and get the benefit of this combination: Hall-Petch strengthening based on the effect of grain size control and multilayer design of the films. The first assumes the increase of hardness values when the grain size reduces up to around 10 nm. The second approach, multilayer architecture of coatings, improves the protective properties of the multilayer films by reduction of cracks propagation towards the substrate by the deflection of cracks on the interlayer interfaces. Additionally, by control of individual layers thickness in coatings, it’s possible to predetermine the grain size in coatings: thinner layers - smaller grains.

Multilayer design of the coatings also allows benefitting from the combination of outstanding properties of different materials used in the deposition of individual layers in the films. CrN was selected for coating due to its high thermal stability, high corrosion and wear resistance, strong adhesion to the surface. Also, its oxide produced on the surface of the coating serves as a good lubricant to reduce the wear. Molybdenum nitride is the hardest superconductive metal nitride but still has been less studied. The diversity of possible phases with a wide range of stoichiometry and lattice structures makes it interesting for the presented research.

CrN/MoN multi-layered coatings considered in this PhD Thesis were fabricated by vacuum-arc evaporation of chromium and molybdenum cathodes (cathodic arc physical vapour

deposition, Arc-PVD) and deposition in a nitrogen atmosphere. Among conventional but high-end techniques of thin films characterisation such as scanning electron microscopy (SEM), energy-dispersive X-ray spectroscopy (EDS), wavelength-dispersive X-ray spectroscopy (WDS), electron backscatter diffraction (EBSD), Rutherford backscattering spectrometry (RBS), X-ray diffraction (XRD), secondary-ion mass spectrometry (SIMS), high-resolution transmission electron microscopy (HRTEM), nanoindentation and tribological tests performed during research, some specific approaches very important for the study of multilayer structures were employed. Low-angle XRD techniques, such as in-plane XRD and asymmetric scans, including grazing incidence XRD (GIXRD), were employed to study two main cubic CrN and γ-Mo_2N phases with the similar crystal structure and lattice constants resulting in overlapped and broadened diffraction peaks in patterns obtained by conventional θ/2θ XRD on multi-layered coatings, which is difficult to analyse. GIXRD allows to perform a depth-sensitive analysis and evaluate individual layers. In-plane XRD allows studying diffraction planes oriented in a direction normal to the surface. Asymmetric scans and θ/2θ scans with ω-offset were used to calculate lattice parameters from diffraction planes oriented in any direction. Thus, the measurement of residual strain and stresses have been performed.

Superhard CrN/MoN coatings have been studied and approved as appropriate for industrial applications as protective ones. The increase of the absolute value of negative bias voltage applied to the surface leads to the changes in the preferential crystallographic orientation of two main cubic phases CrN and γ-Mo_2N presented in films from (311) when $U_b = -20$ V to more stable (111) when $U_b = -150$ V and then to (200) at $U_b = -300$ V. When the nitrogen pressure in the chamber decreases to 0.09 Pa the formation of β-Cr_2N phase occurs, which causes the deterioration of tribological properties of the multilayer system. The decrease of the individual layer thickness of the coatings leads to the decrease of crystallite size (up to 5.8 nm when bilayer thickness is 44 nm). The most promising is the series deposited at $U_b = -20$ V. Coatings showed high hardness up to 38-42 GPa, ratio H/E = 0.107 and high wear resistance according to tribological test. The best tested deposition conditions: $U_b = -20$ V, $p_N = 0.4$ Pa and individual layer thickness is 22 nm.

Keywords: multilayers, hard coatings, nitrides, physical vapour deposition, diffraction, microstructure, phase composition, mechanical properties, hardness, wear, H/E ratio, critical raw materials.

Contents

Abstract ..... *xv*

List of Figures *5*

List of Tables *9*

List of Abbreviations *11*

Thesis Outline *13*

Chapter 1. Protective Coatings for Needs of Modern Material Science *15*

1.1. Introduction **15**

1.2. Critical Raw Materials Problem and Role of Protective Coatings **16**

1.2.1. Critical Raw Materials in the European Union Region 16

1.2.2. Protective Coatings as a Solution for Critical Raw Materials Problem 16

1.3. Important Aspects of Protective Coatings **18**

1.3.1. Hardness 19

1.3.2. Young's Modulus and H to E ratios 20

1.3.3. Adhesion 22

1.4. Types of Modern Protective Coatings **28**

1.4.1. Diamond 28

1.4.2. Diamond-Like Carbon 29

1.4.3. Transition Metal Nitrides, Carbides and Borides 30

1.4.4. Ternary and Quaternary Compounds 31

1.4.5. High Entropy Alloy Coatings 33

1.4.6. Thermal Barrier Coatings 33

1.5. Concepts for the Enhancement of Protective Properties **34**

1.5.1. Nanostructural Approach 34

1.5.2. Nanocomposites 35

1.5.3. Multilayer Architecture 36

1.6. Multi-Layered CrN/MoN TMNs Protective Coatings **37**

Objectives of the Thesis *41*

Chapter 2. Experimental and Characterisation Techniques *43*

2.1. Scanning Electron Microscopy **44**

2.1.1. Electron Beam Interaction with Matter 44

2.1.2. Basic Parts of Scanning Electron Microscope 44

2.1.3. Electron Sources for Scanning Electron Microscopes 46

2.1.4. Image Formation in Scanning electron Microscopes 47

2.1.5. Energy Distribution and Detection of Electrons in SEM 48

2.1.6. Samples Preparation for SEM 55

2.1.7. Experimental Details 57

2.2. X-Ray Spectroscopy Techniques for Microanalysis in SEM **57**

2.2.1. Energy-Dispersive X-ray Spectroscopy 57

2.2.2. Wavelength-Dispersive X-Ray Spectroscopy (WDS) 61

2.2.3. Practical Applications of EDS/WDS Techniques for Thin Films and Coatings Characterisation............. 66
2.2.4. Experimental Details........ 70

2.3. X-ray Diffraction 71
2.3.1. Introduction 71
2.3.2. Basics of X-ray Diffraction 71
2.3.3. X-ray Diffraction Modes........ 77
2.3.4. Experimental Details - Equipment........ 80
2.3.5. X-ray Diffraction Data Analysis Methods and Software........ 84
2.3.6. Residual Stresses Measurements........ 85

2.4. Electron Backscatter Diffraction 87
2.4.1. Introduction to the Electron Backscatter Diffraction Technique........ 87
2.4.2. Experimental Details........ 91

2.5. Transmission Electron Microscopy 92
2.5.1. Basic Parts of Transmission Electron Microscope 92
2.5.2. TEM Imaging Concepts 95
2.5.3. X-ray Analysis in TEM........ 99
2.5.4. Thin Films or Coatings Specimen Preparation for TEM........ 99
2.5.5. Experimental Details........ 100

2.6. Secondary Ion Mass Spectroscopy........ 100
2.6.1. Basic Principles of Secondary Ion Mass Spectroscopy........ 100
2.6.2. SIMS Operation Modes........ 102
2.6.3. Secondary Ions Transfer 102
2.6.4. Secondary Ions Energy and Mass Analysis........ 103
2.6.5. Secondary Ions Detectors 106
2.6.6. Experimental Details........ 106

2.7. Rutherford Backscattering Spectrometry 106
2.7.1. Basic Principles of Method........ 106
2.7.2. Instrumentation: Ion Beam and Detectors 109
2.7.3. Experimental Details........ 112

2.8. Hardness Measurements........ 112
2.8.1. Brinell Hardness 113
2.8.2. Meyer Hardness 114
2.8.3. Rockwell Hardness 115
2.8.4. Vickers Hardness 115
2.8.5. Indentation Depth and Load Aspects of Hardness Measurement for Coatings 117
2.8.6. Knoop Hardness (Microhardness) 118
2.8.7. Nanohardness or Nanoindentation........ 119
2.8.8. Experimental Details........ 124

2.9. Tribological Tests and Measurements 126
2.9.1. Basic Principles of Tribological Tests for Protective Coatings 126
2.9.2. Experimental Details........ 127

Chapter 3. Methods of CrN/MoN Films Fabrication 129

3.1. Thin Films and Coatings Deposition Techniques........ 129

3.2. Physical Vapour Deposition: Sputtering 130
3.2.1. Direct Current and Radio-Frequency Sputtering........ 130

3.2.2. Magnetron Sputtering 132
3.2.3. Ion Beam Sputter Deposition 133

3.3. Physical Vapour Deposition: Evaporation 134
3.3.1. Resistive and Induction Heating 134
3.3.2. Electron Beam Heating and Flash Evaporation 135
3.3.3. Molecular Beam Epitaxy 136
3.3.4. Laser Ablation 137
3.3.5. Arc Evaporation 138

3.4. Experimental Details on Fabrication of Arc-PVD Multi-Layered CrN/MoN Coatings 142

Chapter 4. Micro- and Nanostructural Characterisation 147

4.1. Multilayer Structures 147

4.2. Elemental Composition 149
4.2.1. WDS Elemental Analysis 149
4.2.2. EDS Elemental Analysis 151
4.2.3. RBS Analysis of Coatings 153
4.2.4. SIMS Analysis 155

4.3. Morphology of the Surface 155

4.4. Micro- and Nanostructure 156
4.4.1. X-ray Diffraction Analysis 156
4.4.2. Low-Angle X-Ray Diffraction Methods 160
4.4.3. Crystallite Size Calculation Using XRD Data 163
4.4.4. EBSD Analysis and Grain Size Evaluation 164
4.4.5. TEM and SAED Analysis 168
4.4.6. TEM-EDS Elemental Analysis 169

4.5. Evaluation of Residual Stresses 170

Chapter 5. Mechanical and Tribological Properties of CrN/MoN Coatings 175

5.1. Hardness and Elastic Modulus 175

5.2. H/E and H^3/E^2 Ratios 182

5.3. Wear Resistance and Tribological Properties 184

Chapter 6. Final Discussion and Further Perspectives 189

6.1. Conclusions: "The Strongest" Layers and Correlation Between Deposition Conditions, Structure and Mechanical Properties 189

6.2. CrN/MoN Hard Coatings as a Solution for Critical Raw Materials Problem in Machining Tools and Other Industrial Applications 190

6.3. Future Work and Perspectives 193

List of Publications 195

References 199

List of Figures

Fig. 1.1 - World market of cemented carbide cutting tools....15
Fig. 1.2 - Supply risk and economic importance evaluation of 61 candidates to Critical Raw Materials List. 17
Fig. 1.3 - Comparison of enhancement factors of coated tools over the uncoated 18
Fig. 1.4 - Criteria necessary for cutting tools' protective coatings success 19
Fig. 1.5 - Classification of hardness....19
Fig. 1.6 - Adhesive and cohesive failure events occurring in deposited protective coatings....23
Fig. 1.7 - Thin film failure under high residual tensile or compressive stress....24
Fig. 1.8 - Adhesion Tests....27
Fig. 1.9 - SEM micrographs of rake and flank face after the dry milling test for $AlCu_{2.5}Si_{18}$ alloy 29
Fig. 1.10 - Properties of transition metal nitrides, carbides and borides 30
Fig. 1.11 - 3D profiles of the wear tracks of $Ti_{0.47}Al_{0.46}N$ and $Ti_{0.28}Al_{0.31}Cr_{0.51}N$ films 32
Fig. 1.12 - Schematic illustration of Hall-Petch strengthening effect: hardness as a function of grain size....35
Fig. 1.13 - Toughening and strengthening mechanisms in multilayer coatings....36
Fig. 2.1 - Electron beam interaction with matter, interaction volume scheme....43
Fig. 2.2 - Schematic model of secondary electrons and backscattered electrons emission 44
Fig. 2.3 - Schematic diagram of the core components of a scanning electron microscope....45
Fig. 2.4 - Illustrative comparison of thermionic and field emission types of electron emitting sources. 46
Fig. 2.5 - Principles of image formation in SEM 48
Fig. 2.6 - Energy spectrum N(E) of electron emission, showing secondary (SE), backscatter (BSE), Auger electrons regions 49
Fig. 2.7 - Generation of secondary electrons and the position of SE detectors. 49
Fig. 2.8 - Scheme of Everhart-Thornley detector for secondary and backscattered electrons....50
Fig. 2.9 - Scheme of solid-state backscattered electrons detector and its location in SEM....53
Fig. 2.10 - Design of multi-channel plate detector 54
Fig. 2.11 - Scheme of typical lithium-drifted silicon detector for EDS....58
Fig. 2.12 - Working principles of Si(Li) detector 60
Fig. 2.13 - Charge-to-voltage conversion process 60
Fig. 2.14 - Schematic operation of a silicon drift detector with integrated FET preamplifier 61
Fig. 2.15 - Comparison of EDS and WDS resolution: overlapped X-ray peaks in EDS are well separated in WDS scan 62
Fig. 2.16 - Diagrams of various WDS diffraction geometries 63
Fig. 2.17 - Principal scheme of a gas proportional counter used in WDS....65
Fig. 2.18 - EDS spectrum obtained from intermetallic layer between welding seam and SUS304 stainless steel showing the presence of various elements....67
Fig. 2.19 - Examples of EDS scan lines and elemental depth profiles 69
Fig. 2.20 - X-ray map showing elemental distribution within the thermal barrier coating (TBC) sample....69
Fig. 2.21 - Electromagnetic spectrum. 71
Fig. 2.22 - Generation of continuous white X-ray spectrum....72
Fig. 2.23 - Characteristic X-rays generation process. Schematic model for a copper atom with electronic energy levels 73
Fig. 2.24 - Spectrum of White and Characteristic (Kα, Kβ) X-rays....74
Fig. 2.25 - Interaction of X-rays with matter. 75

Fig. 2.26 - Simplified illustration of Bragg's condition for the family of crystallographic planes spaced by the distance *d*......75
Fig. 2.27 - Illustration of Bragg X-ray diffraction geometry in general case where scattering takes place at the position of atoms in consecutive planes. 77
Fig. 2.28 - Geometry of symmetric θ/2θ X-ray diffraction scan......77
Fig. 2.29 - Geometry of asymmetric X-ray diffraction scans with ω-offset (a) or sample tilting for angle ω-offset (b)......78
Fig. 2.30 - Geometry of X-ray diffraction in grazing incidence mode (GIXRD)......78
Fig. 2.31 - In-plane geometry of X-ray diffraction measurements......79
Fig. 2.32 - X-ray sources used in modern X-ray diffractometers......80
Fig. 2.33 - Schematic geometry of Bragg–Brentano para-focusing and parallel beam optics......81
Fig. 2.34 - Multilayer mirrors in optics for X-ray diffractometers 82
Fig. 2.35 - Umbrella effect......82
Fig. 2.36 - Window of sample alignment configuration. 83
Fig. 2.37 - Sample alignment sequence for thin films and coatings for Rigaku SmartLab 84
Fig. 2.38 - Strain and stress effects on the diffraction peaks......85
Fig. 2.39 - Examples of d-spacing vs $\sin^2\psi$ plots for residual stresses evaluation 86
Fig. 2.40 - X-ray diffraction analyses: (a) conventional symmetric θ/2θ scan, (b) asymmetric 2θ scan with fixed position of X-ray source 86
Fig. 2.41 - Monte Carlo simulation of backscattered electrons emission and escape from aluminium at various tilt angles of the incident electron beam......87
Fig. 2.42 - Emission and escape of backscattered electrons from in SEM depending on tilting angle of the specimen......88
Fig. 2.43 - Examples of Kikuchi patterns. EBSD patterns were obtained from cubic (a) and hexagonal (b, c) crystal systems......89
Fig. 2.44 - Scheme of EBSD pattern (backscatter Kikuchi pattern) formation......89
Fig. 2.45 - Origin of Kikuchi lines from EBSD 90
Fig. 2.46 - Comparison of square and hexagonal scanning grids for EBSD analysis......92
Fig. 2.47 - Basic Components of Transmission Electron Microscope (TEM)......93
Fig. 2.48 - Schemes of electron optics and electron beam trajectories for diffraction pattern and imaging TEM-modes 96
Fig. 2.49 - Formation of a virtual aperture in the plane of the specimen by an aperture in the image plane 97
Fig. 2.50 - HRTEM images and SAED patterns (insets) of AgCuSeTe and CuSeTe/PbSeTe nanowires......97
Fig. 2.51 - Ray diagrams showing how the objective lens and objective aperture are used in combination to produce BF (a), displaced-aperture DF (b) and centered DF (c) TEM-images 98
Fig. 2.52 - High-energy ion beam interaction with the matter in SIMS......101
Fig. 2.53 - Principal blocks of secondary ion mass spectroscopy analysis......101
Fig. 2.54 - Secondary ions transfer from the specimen to the spectrometer 103
Fig. 2.55 - Energy and mass analysers typical used in SIMS systems 104
Fig. 2.56 - Kinematic scheme of elastic collisions......107
Fig. 2.57 - Pathway of 18 keV e^- and He^+ striking a Si_3N_4 layer with a SiO_2 substrate 108
Fig. 2.58 - Schematic backscattering spectra for MeV $^4He^+$ ions incident on 100 nm Ni film on Si and after reaction to form Ni_2Si 108
Fig. 2.59 - Ions Generation for Rutherford Backscattering Spectrometry......110
Fig. 2.60 - Two-stage tandem particle accelerator......111
Fig. 2.61 - Main types of indenter tips......113

Fig. 2.62 - Scheme for derivation of Brinell hardness number (BHN) 114
Fig. 2.63 - Illustration of the divergence of Brinell from Vickers hardness number at high hardness values 116
Fig. 2.64 - Scheme of indentation hardness of a polycrystalline material at macro-, micro- and nanoscale 118
Fig. 2.65 - Example of load-displacement curve obtained from nanoindentation experiment .121
Fig. 2.66 - Schematic representation of deformation pattern of an elastic–plastic sample during and after indentation showing parameters characterizing the contact geometry 122
Fig. 2.67 - Principal scheme of NanoTest™ instrument for micro- and nanoindentation 124
Fig. 2.68 - Scanning electron microscopy (SEM) images of Berkovich indenters by HITACHI S-4800 (Tokyo, Japan) 125
Fig. 2.69 - Examples of test geometries used for tribological tests involving sliding motion 126
Fig. 2.70 - Schematic drawing of ball-on-disk wear test 127
Fig. 3.1 - Classification of physical vapour deposition techniques and their place among thin films and coatings deposition methods. 129
Fig. 3.2 - Physical Sputtering Processes 130
Fig. 3.3 - DC and RF sputtering systems. 131
Fig. 3.4 - Magnetron Sputtering 133
Fig. 3.5 - Ion beam and dual ion beam sputter deposition techniques...................................134
Fig. 3.6 - Schematic illustration of: resistive heating thermal evaporation, crucible containing source materials, inductive heating, and electron beam heating 135
Fig. 3.7 - Schematic diagram of flash evaporation reactor 136
Fig. 3.8 - Scheme of a typical molecular beam epitaxy growth chamber.................................137
Fig. 3.9 - Schematic view of a PLD system 137
Fig. 3.10 - The evolution of the cathodic-arc process 139
Fig. 3.11 - Different types of filter systems..141
Fig. 3.12 - Basic setup of DC cathodic-arc plasma system and simple pulsed CA device...........142
Fig. 3.13 - Principal scheme of vacuum-arc deposition system for multilayer films.................143
Fig. 3.14 - Timeline diagram for automatic control system used in modified deposition unit "Bulat-6" 144
Fig. 3.15 - Illustrative comparison of the individual layer thickness (qualitatively) within the series of coatings according to the deposition time per layer...146
Fig. 4.1 - SEM-images of polished cross-section samples 1.1 (a), 1.3 (b) and 1.6 (c) of multilayer CrN/MoN coatings. 147
Fig. 4.2 - Dependence of deposition rate on layer deposition time..149
Fig. 4.3 - Estimated penetration depth of electron beam (accelerated voltage U_{ac} = 10 kV) into multilayer CrN/MoN coatings with various bilayer thickness (series 1) 151
Fig. 4.4 - EDS spectrum and elemental analysis of CrN/MoN multilayer film, sample 2.1 152
Fig. 4.5 - EDS elemental mapping image for Cr, Mo, N and Fe of Sample 1.1 cross-section......152
Fig. 4.6 - EDS elemental depth profile for Sample 1.1. 153
Fig. 4.7 - RBS spectra and depth profiles of elements for samples 3.1, 3.4 and 3.6.................154
Fig. 4.8 - Results of SIMS analysis of CrN/MoN coatings (sample 3.6) 155
Fig. 4.9 - SEM-images of multilayer CrN/MoN coatings surface for samples 1, 3 and 6............156
Fig. 4.10 - X-ray diffraction patterns (theta/2theta) of CrN/MoN multi-layered coatings.........157
Fig. 4.11 - X-ray diffraction pattern of CrN/MoN multi-layered coatings deposited at different pressures of nitrogen 159
Fig. 4.12 - X-ray diffraction patterns taken in several low-angle modes 162

Fig. 4.13 - Dependence of X-ray beam penetration depth on incident angle in low range of values for most expected structures of studied multilayer coating: cubic CrN and Mo_2N........163
Fig. 4.14 - Crystallites size of CrN/MoN films calculated from XRD data (Series 1). 164
Fig. 4.15 - Kikuchu diffraction patterns obtained on cross-sections of the deposited CrN/MoN coatings. 165
Fig. 4.16 - EBSD results for CrN layer of sample 1.1 165
Fig. 4.17 - EBSD mapping for CrN layer of sample 1.1...166
Fig. 4.18 - One of the pole figures and texture calculations for sample 1.1.............................166
Fig. 4.19 - EBSD unique grain colour map for CrN layers of Sample 1.1 near to the surface and near to the substrate. 167
Fig. 4.20 - Grain size distribution and average grain size values in CrN/MoN multilayer coatings with different bilayer thickness (series1)..168
Fig. 4.21 - Results of TEM study for sample 3.6 169
Fig. 4.22 - Results of TEM-EDS analysis for sample 3.6 170
Fig. 4.23 - Series of XRD patterns at selected incident angles for Samples 1.1 and 1.2............171
Fig. 4.24 - $Sin^2\psi$ plots recorded for the reflections from (111), (200), (220) and (311) planes of CrN and γ-Mo_2N layers..172
Fig. 5.1 - Load-displacement curves of indentation hardness test for Sample 1.1 175
Fig. 5.2 - Schematic cross-section view of indentation process under the maximum load at the maximum penetration depth, comparison for the multilayer coatings with different bilayer thickness...176
Fig. 5.3 - Load-displacement curves of indentation hardness test for Sample 1.3. 177
Fig. 5.4 - Load-displacement microindentation curve of hardness test for Sample 1.6 178
Fig. 5.5 - Timeline of applied load during microindentation of Sample 1.6 179
Fig. 5.6 - Displacement timeline during hardness test for Sample 1.6.....................................179
Fig. 5.7 - Load-displacement curves of indentation hardness test for uncoated steel.............180
Fig. 5.8 - Results of hardness measurements for three series of CrN/MoN coatings. 181
Fig. 5.9 - Results of hardness and Young's modulus measurements vs bilayer thickness for multi-layered CrN/MoN coatings of Series 1...182
Fig. 5.10 - Hardness vs Young's modulus divided by H/E = 0.1 for Series 1 of CrN/MoN multi-layered coatings..183
Fig. 5.11 - H/E and H^3/E^2 ratios vs bilayer thickness of CrN/MoN coatings of Series 1.............184
Fig. 5.12 - Results of tribological tests for Sample 2.4..185
Fig. 5.13 - Results of tribological tests: resulting profilograms of dynamical test of the coatings for samples 1.3, 1.4 and 1.6 with bilayer thickness 0.6 µm, 0.25 µm and 44 nm respectively..186
Fig. 5.14 - Results of tribological tests: averaged friction coefficients versus corresponding values of negative bias voltage applied to the substrate during the deposition......................186
Fig. 5.15 - Results of tribological tests: data recorded during tribological test with spherical Al_2O_3 counterbody for Sample 2.4 187
Fig. 6.1 - Cutting tools global market distribution forecast for 2018 by Dedalus Consulting.....191
Fig. 6.2 - Critical raw materials list 2011-2017 overlaid on the periodic table of elements.......192
Fig. 6.3 - Lifetime comparison of uncoated steel tool, tools coated with ZrN, TiN, TiCN, TiAlN, AlCrN, AlTiCrN, Ti-B-N, Ti-Cr-B-N-T and CrN/MoN (estimated). 193

List of Tables

Table 1.1 - Parameters based on the hardness and elastic moduli, used as indicators of abrasion resistance and their physical meanings 21
Table 1.2. Properties and behaviours (schematically) of materials depending on the prevailing chemical bonding character 22
Table 2.1. Comparison of thermionic emission, cold field emission and Schottky field emission sources 47
Table 2.2. Characteristics of the Principal Electron Sources for TEM (data is for 100 kV acceleration voltage) 94
Table 2.3. Classification of hardness tests 112
Table 2.4. Hardness Testing Scales Based on ISO 14577-1 and Corresponded Measurement Methods 118
Table 3.1. Deposition parameters of the MoN/CrN coatings 145
Table 4.1. Total thickness and thickness of layer period measured by SEM on cross-sections . 148
Table 4.2. Elemental concentration in CrN/MoN multilayer films taken by WDS 150
Table 4.3 - Crystallite and grain size for multilayer CrN/MoN coatings 164
Table 4.4 - Results of residual stresses calculation for multilayer CrN/MoN thin films 173
Table 5.1. Tribological properties of CrN/ MoN coatings obtained at Ub = −150 V and different nitrogen pressures 184

List of Abbreviations

Arc-PVD	Cathodic Arc Physical Vapour Deposition
ATM	Automated Teller Machine or Cash Machine
BB	Bragg-Brentano
BF	Bright-Field
BSE	Backscattered Electrons
BSED	Backscattered Electron Detector
CA	Cathodic-Arc
CRMs	Critical Raw Materials
CVD	Chemical Vapour Deposition
DC	Direct Current
DF	Dark-Field
DLC	Diamond-Like Carbon
EBSD	Electron Backscatter Diffraction
EDS	Energy Dispersive X-ray Spectroscopy
FCC	Face-Centred Cubic
FWHM	Full Width at Half Maximum
GIXRD	Grazing Incidence X-ray Diffraction
HEA	High-Entropy Alloy
HRTEM	High-Resolution Transmission Electron Microscopy
IBD	Ion Beam (Sputter) Deposition
PB	Parallel Beam
PLD	Pulsed Laser Deposition
PVD	Physical Vapour Deposition
RBS	Rutherford Backscattering Spectrometry
RF	Radio Frequency
SAED	Selected Area Electron Diffraction
SE	Secondary Electrons
SEI	Secondary Electron Imaging
SEM	Scanning Electron Microscopy
SIMS	Secondary-Ion Mass Spectrometry
TBC	Thermal Barrier Coating
TEM	Transmission Electron Microscopy
TM	Transition Metal
TMB	Transition Metal Borides
TMC	Transition Metal Carbides
TMN	Transition Metal Nitride
WDS	Wavelength-Dispersive X-ray Spectroscopy
XRD	X-Ray Diffraction

Thesis Outline

People design and produce many various tools and goods every day to make their life more comfortable, safe, effective, longer and easier. New challenges require superior properties of used natural or artificial materials. For that, people extract more and more raw materials from the bowels of our planet. Later, when the tool or product is broken, used or outdated, very often it goes to the garbage for many years. Some of them may be stored in landfills for decades and even hundreds of years, taking up valuable space and polluting the planet. In turn, new raw materials are needed. More often, the extraction process, or mining, becomes dangerous and expensive for people, harmful to the Earth, and developed sources of elements are exhausted and new places are more difficult to reach. Moreover, they are not distributed proportionally but located in the "hands" of certain countries, and the trading process is under the influence of political situation in countries, decisions of the governments and international relations.

Just very recently, companies have started to care about environmental issues, which is also, for sure, driven by the industrial goals to optimise their expenses. Recycling, sustainability and circular economy are new world trends. Several European Union countries, as well as Japan and China, are leading the process by adopting circular economy legislation and implementing corresponding policies, while other countries are much far away from that.

Hard protective coatings are one of the key elements to extend the lifetime of many tools, working parts and machines. More than 90% of cemented carbide cutting tools nowadays are protected by coatings. Moreover, 70% of the cutting tools' world market in 2018 were represented by cemented carbides and high-speed steel as a workpiece material, which contain critical raw materials. With a proper coating, such tools or other products may have lifetime extended by 200-500% and even more maintaining the same operational velocities, or higher service speeds with no loss in a lifetime. Therefore, coatings reduce wastes of workpiece materials, including critical raw elements, and also may improve the recycling process by depositing new protective films when the coating is broken or erased. Furthermore, PVD processes mainly used for deposition of protective coatings in industrial scales are environmentally friendly, don't produce hazardous side products or wastes and don't require costly (in energy, money and time-consuming meanings) filtration or cleaning systems.

The PhD research project was performed under the collaboration between the Institute of Physics for Advanced Materials, Nanotechnology and Photonics (IFIMUP) at Faculty of Sciences of the University of Porto (FCUP) led by Professor João Pedro Esteves de Araújo, Department of Nanoelectronics and Surface Modification at Sumy State University led by Professor Alexander Pogrebnjak and Laboratory of Functional Coatings II, Centre of Physics at the University of Minho led by Professor Luís Manuel Fernandes Rebouta.

The thesis is structured in six chapters, comprising an introduction, deposition techniques, experimental details, results of elemental and structural characterisation, achieved mechanical

and tribological properties, final discussion, conclusions and further perspectives. The brief summary is as follows:

- Chapter 1 gives to the reader a brief introduction to the field of protective coatings, main types of modern protective coatings, their important aspects and parameters are discussed. The look on the protective coatings from the critical raw materials problem point of view is given. The main concepts and approaches for the enhancement of protective properties of the coatings are considered. Finally, hard protective coatings are proposed as an advanced solution in the field of protective coatings for industrial needs;
- Objectives of the Thesis are given at the end of Chapter 1;
- In Chapter 2, the summary of the experimental techniques used in this study is presented. This comprises both methods of elemental and structural characterisation (scanning electron microscopy, energy-dispersive X-ray spectroscopy, wavelength-dispersive X-ray spectroscopy, X-ray diffraction analysis, electron backscatter diffraction analysis, secondary-ion mass spectrometry, Rutherford backscattering spectrometry) and methods of evaluation of mechanical and tribological properties (microindentation, wear tests);
- Chapter 3 gives an overview of the most adequate modern deposition methods for protective coatings and more detailed description of vacuum-arc evaporation of cathodes (Arc-PVD) deposition technique as used in this PhD research. The description and principal scheme of the deposition unit is shown, used modes and regimes, as well as the main deposition parameters, are given. The principles of samples design and the full list of the samples considered in the report are introduced;
- Chapter 4 describes the results of elemental and phase composition analysis, micro- and nanostructural characterisation of deposited CrN/MoN coatings. Multilayer design of the films is considered as well as the morphology of the surface. Additionally, the evaluation of residual stresses was performed;
- Chapter 5 is devoted to the mechanical and tribological properties of the coatings and deals with microhardness, Young's modulus, their ratios, wear rates and profiles, friction coefficients and their comparison;
- Chapter 6 contains the final discussion of the results, the correlation between deposition conditions, structure and mechanical properties. Multi-layered CrN/MoN transition metal nitride coatings are considered as a solution for critical raw materials problem in machining tools and compared with other competitors present in the market or recently published research papers. Conclusions and further perspectives and steps are summarised at the end of the Chapter.

Chapter 1.

Protective Coatings for Needs of Modern Material Science

1.1. Introduction

Since first modern humans appeared on the Earth, around 20000 to 50000 years ago, they always try to create and enhance their tools to survive, to hunt, to fight, to protect, to transport, to conquer, to explore, to improve, to make their life safe, long and comfortable. From the Stone Age to the nuclear power, space shuttles, artificial intelligence or renewable energy a huge work has been done and a huge progress has been achieved. At all steps of this evolution and revolutions the new materials were needed, while created and used tools, goods and machines were facing many new difficult problems.

Nowadays, the art of materials creation, study and characterisation has grown into the independent interdisciplinary field of study - Material Science, a hub between Chemistry, Physics, Engineering and Computational Science. As new needs of modern industry and human activity arise, new materials or their enhancements are needed to overcome the present challenges, such as mechanical loads and wear, corrosion, oxidation, high or low temperatures, dimensional requirements, increased velocities of operations, extended exploitation period and other extreme conditions.

All types of failure mechanisms, such as adhesion, abrasion, oxidation, diffusion, etc., occur on the surface of the cutting tool. Therefore, they are results of interactions at the interfaces between tool and workpiece or tool and ambient medium respectively. This leads to the conclusion that it is possible to protect a tool by surface treatment, creating some additional interface or coating with individually designed features. Fig. 1.1 shows the distribution of uncoated and coated cemented carbide cutting tools, where the growth of the latter is clearly visible in a timeline perspective.

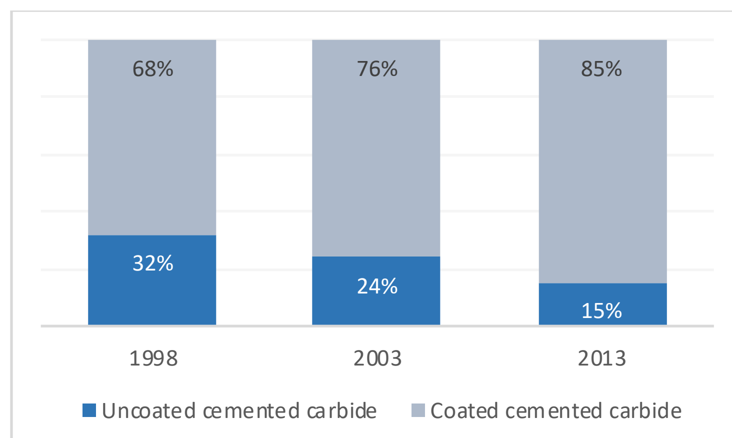

Fig. 1.1 - World market of cemented carbide cutting tools [1]. Published in [2].

Protective coatings may significantly prolong the life time of tools at the same operational speeds or (and) may increase the operational velocities while the lifetime is maintained at the same level.

1.2. Critical Raw Materials Problem and Role of Protective Coatings

1.2.1. Critical Raw Materials in the European Union Region

Modern needs of engineering, defence industry, business and technologies require new materials with superior properties to provide sustainable work under extreme conditions. More often it becomes necessary to develop a compilation of several individual features in one single material. It forces to use unique materials with unique properties. Often these materials are hidden somewhere deep in the bowels of the Earth and their available volume is very limited. Some of them are characterised by high supply risk (level of danger and difficulty of extraction, supplier countries' governance performance, import reliance, trade restrictions and agreements, availability and criticality of substitutes) and by high economic importance. European Commission names such raw materials of a high importance to the economy of the Europe Union and whose supply is associated with a high risk as Critical Raw Materials (CRMs) [3].

The first significant initiative of European Union regarding materials was implemented in 2008 by the European Parliament and the Council [4]. In 2011 the first list of 14 CRMs was published in the communication on raw materials [5] which then was updated in 2014 [6] and the most recent edition with list of 27 CRMs was published in September 2017 [3,7]. In January 2018 the European Commission released a detailed report highlighting the potential for a more circular usage of CRMs in EU economy, which names important sectors for CRMs and describes EU policies regarding their regulation, includes key initiatives, gives sources of data, good practices and possible further actions [8]. Summarised data about supply risk and economic importance evaluation of 61 candidates to be included in the 2017 CRMs list (58 individual and 3 grouped materials) is shown in Fig. 1.2. As seen from the diagram by parameters of 2.8 and 1.0 threshold for economic importance and supply risk, 26 raw materials and groups of raw materials were identified as critical.

1.2.2. Protective Coatings as a Solution for Critical Raw Materials Problem

Because of its strength and relatively low cost, the major material used in mechanical and civil engineering, tools, parts of machines etc. is steel. With very long history of its developing nowadays steel has high number of types for broad range of applications. More often they are related to the service of goods under extreme conditions: high temperatures, loads, corrosion, dirt, harsh chemical environment. For machine parts and tools with high intensity of service it is extremely necessary. Regardless of the type of application (cold work steel, hot work steel, high speed steel), methods of steelmaking and heat treatment procedures, steel always includes

carbide-forming elements (W, Mo, V, Cr and others). As shown in Fig. 1.2, at least seven of possible carbide-forming elements belongs to the 2017 CRMs list. That is why it is necessary to reconsider the application of steel in CRMs strategy point of view.

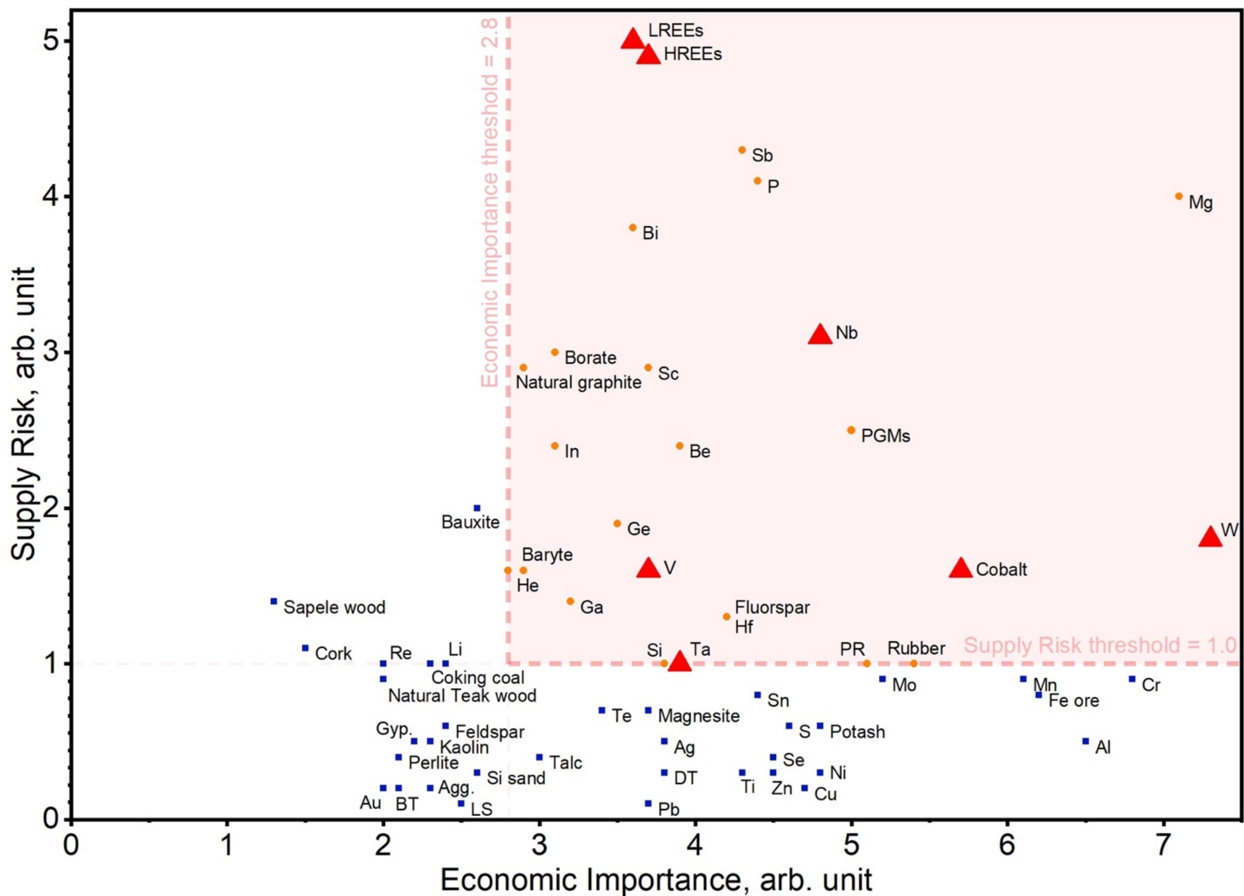

Fig. 1.2 - Supply risk and economic importance evaluation of 61 candidates to Critical Raw Materials List. Based on European Commission's report in 2017 [3]. Triangle-shaped marks indicate carbide-forming CRMs-elements.

The author considers in this Thesis two approaches to CRMs problem by reducing needs in steel and tungsten carbide for new tools and machine parts producing: extension of lifetime for produced goods and improving of recycling efficiency. For both approaches the one solution is proposed. Superhard protective coatings with enhanced toughness provide lower wear rate for the tools and, hence, extended lifetime of each unit [9–17]. When the coating is destroyed, in many cases it is easy to recycle a product by cleaning of steel base and deposition of new coating. Properties and quality exhibited by coatings will result in the efficiency of solving task of CRMs reduction.

Protective coatings may significantly increase the life time of tools and, thus, reduce consumption of CRM content in bulk materials. Furthermore, most of the modern coatings are CRM-free. The evolution of protective effect of coatings by extension of tools' lifetime and comparison of coatings with data available in selected published works [18–22] are shown in Fig. 1.3. It is seen that coated cutting tools may have an extra lifetime of 200-500% and more at the

same cutting velocities. This also can lead to the increase of operational velocities (by 50 to 150%) for the same lifetime of cutting tools [23].

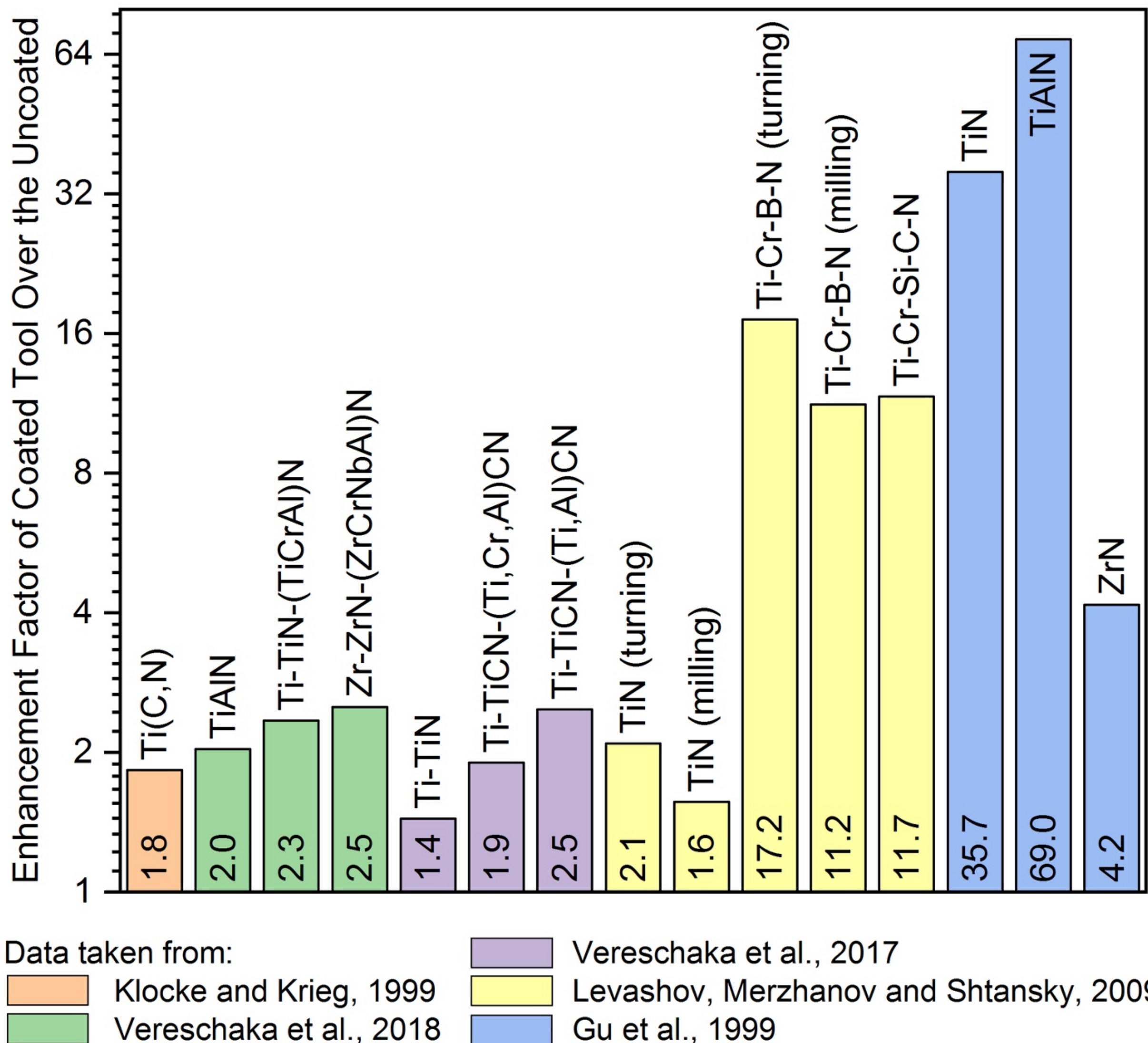

Fig. 1.3 - Comparison of enhancement factors of coated tools over the uncoated. Analysed data is taken from selected published works [18–22]. Results strongly depend on operational conditions, such as cutting method and speed, workpiece material, thickness of protective coating and, thus, should not be used for the direct selection of the "best" coating among existed. Published in [2].

1.3. Important Aspects of Protective Coatings

Each application area requires specific properties of protective coatings to reach maximum performance. Extreme conditions of cutting tools service mean that working parts face with high wear, high pressure, elevated temperatures caused by high machining speed, oxidation, corrosion from lubricants or cooling agents. Main criteria of protective coatings evaluation are summarised in Fig. 1.4. It is quite hard to have the best score in all positions. Usually, the winner in one of the criteria may lose in many of others. The enhancement of all necessary properties together is still a great challenge for modern material science.

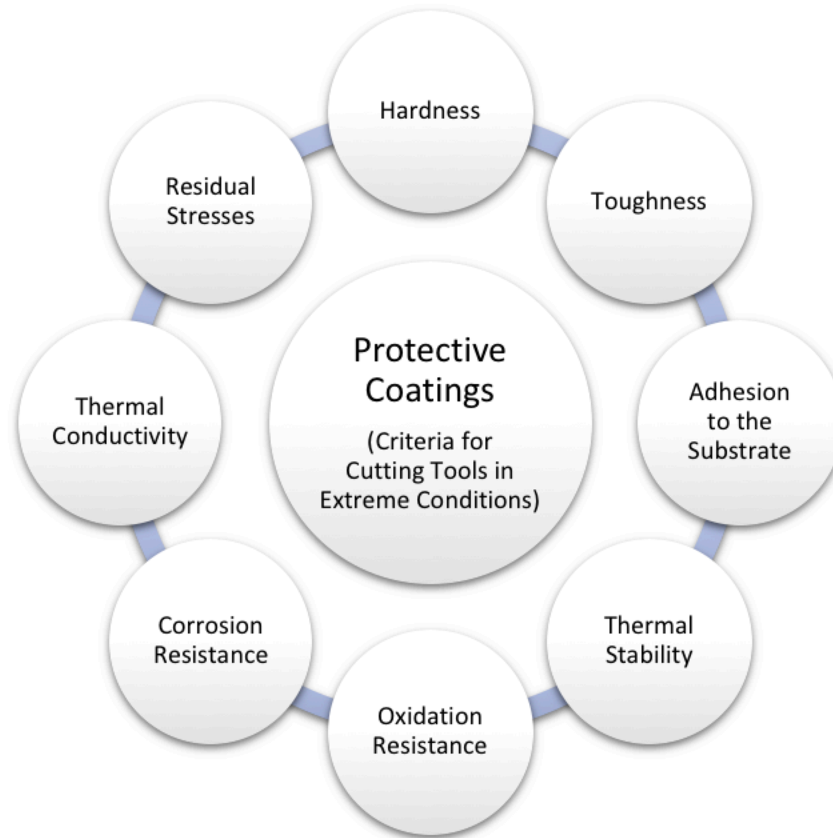

Fig. 1.4 - Criteria necessary for cutting tools' protective coatings success. Published in [2].

1.3.1. Hardness

Hardness may be broadly defined as the resistance of a body to the deformation upon an applied load [24]. This is one of the most important mechanical characteristics of a material. Also it may give ideas about other characteristics of the material if hardness is known. Hardness is an indicator of the material's resistance against scratching, cutting, abrasion, an puncture [25]. Based on this, hardness usually falls into three main categories shown in Fig. 1.5.

	Hardness / Material		
By nature of load	Scratch hardness	Indentation hardness	Dynamic/impact hardness
By origin of hardness	Intrinsically hard		Extrinsically hard
By values range	Hard (up to 40 GPa)	Superhard (40 GPa or more)	Ultrahard (70 GPa or more)

Fig. 1.5 - Classification of hardness.

Scratch hardness is the oldest form of hardness measurement and describes the ability of one solid to scratch another or to be scratched by another solid. This type of hardness is not very suitable for material scientists and engineers because it is strongly nonlinear. The most widely used methods of hardness measuring in metals determine the static indentation hardness. It is an average pressure under the indenter upon fully developed plastic deformation, i.e., the applied load divided by the area of contact between the indenter and the tested material after unloading should be load-invariant. Another type of hardness is that measured from the involved dynamic deformation or indentation of the metal specimen. The dynamic impact hardness, or rebound hardness, is important, e.g., in interrupted cutting, such as milling, for the lacquer on the front part of a vehicle exposed to impact of particles etc. [24,26]. It is the resistance offered by a material to strike and absorb energy for plastic deformation under impact loads, causing the hammer to rebound. Some authors state separately about wear or abrasion hardness, the resistance of a material to abrasion and wear, when subjected to rotational or sliding motion, and cutting hardness, the resistance of a material to various cutting or drilling operations. The latter is a measure of machinability of a material [27].

By definition, materials whose hardness exceeds 40 GPa are usually called superhard [28]. In last decades a new group of ultrahard materials has been separated, whose hardness is more than 70 GPa [26]. Recently researchers who work in this field start to move this edge from 70 to 80 GPa [29]. Therefore, hard, superhard and ultrahard materials may be encountered among protective thin films and coatings, as seen in Fig. 1.5 bottom line.

Materials with elevated hardness may be distinguished by the origin of their hardness into intrinsically hard (super-, ultrahard), such as diamond with Vickers hardness, HV in range of 70-100 GPa, cubic boron nitride c-BN with HV = 48 GPa etc., and extrinsic. The intrinsic hardening depends on the response of well-localised atomic bonds to shear [30,31], whereas the extrinsic hardness and other mechanical properties of materials are determined and driven by their microstructure and may include solid solution hardening, precipitation hardening, grain boundary hardening, compressive stresses hardening and others [32]. However, often high hardness by itself doesn't mean high protective properties of the coatings.

1.3.2. Young's Modulus and H to E ratios

For a long time, high hardness was considered as the prime factor and parameter for conclusions about high wear resistance of a surface. However, later it was observed that many materials with relatively lower hardness may exhibit excellent wear resistance, as well as very hard materials may be quite brittle and prone for cracking. Thus, other parameters should be taken into account together with hardness. Nowadays, a special place is given to the elasticity of materials and ratios of hardness to elasticity modulus.

In general, elasticity describes the ability of a material body to resist a deformation under the load and to recover its original shape and size when that force is removed. The main

characteristic of this property for coatings is the elasticity modulus also called Young's modulus (E). It is a measure of the tensile stiffness or resistance of the coating to the elastic deformation (reversible deformation) under the load, which is described numerically as a ratio of a uniaxial stress to the caused increase in the elastic deformation. The higher Young's modulus, the higher load is needed to create the same amount of strain. Other common elastic properties, such as shear modulus or Poisson's ratio, are determined for coatings more rarely [33].

A. Leyland and A. Matthews [34] concluded that coating elasticity and toughness can be equally or even more important factors than hardness, especially in abrasion, impact and erosive wear. They showed that fracture toughness (indicates resistance to crack propagation) may be improved by both high hardness (a high critical stress for fast fracture) and a relatively low elastic modulus:

$$G_c = {\sigma_c}^2 \frac{\pi a}{E}, \tag{1.1}$$

where G_c is the critical strain energy release rate, a measure of fracture toughness, σ_c is the critical stress for fast fracture, *a* is the critical crack size.

Indeed, it was recognised by many authors that the ranking of materials according to their H/E ratio gives extremely close agreement to their ranking in terms of wear [35–42]. This parameter may be considered as a measure of the resistance of the material to elastic deformation. J. Musil [38] suggested that for the coating to exhibit a high wear resistance and resistance to cracking the H/E ratio should be in high elasticity zone, which means $H/E^* \geq 0.1$, where $E^* = E/(1-v^2)$.

Another important parameter for wear resistant coatings is H^3/E^2 ratio, which follows from the equation proposed by T. Tsui et al. [43] for load P_y needed to induce plastic deformation by a rigid sphere of radius *r* pressed into contact with an elastic/plastic half-space:

$$P_y = 0.78 r^2 \frac{H^3}{E^2} \tag{1.2}$$

Thus, H^3/E^2 ratio may be considered as a measure of the material to dissipate energy at plastic deformation during loading, and evaluate resistance to the plastic deformation.

G. Pintaude [44] summarised five parameters based on the H to E ratio used as indicators for evaluation of the abrasion resistance as shown in Table 1.1.

Table 1.1 - Parameters based on the hardness and elastic moduli, used as indicators of abrasion resistance and their physical meanings [44].

Parameter	Physical meaning (taking into account a rigid-plastic material)
H/E	Deformation relative to yielding [45]
$(H/E)^2$	Transition on mechanical contact – elastic to plastic [45]
$H^2/2E$	Modulus of resilience [45]
H/Er^2	Resistance to the plastic indentation [46]
H^3/E^2	Resistance to the plastic indentation [43]

These rather simple considerations suggest that the fracture toughness of the advanced coatings would be improved by both a low Young's modulus and high hardness. In particular, above-mentioned H/E and H^3/E^2 ratios may be employed as a reliable indicator for evaluation and ranking of the protective coatings in terms of their wear resistance and potential lifetime of coated tools. However, recently X. Chen et al. published the critical commentary on using H/E and H^3/E^2 as proxies for fracture toughness of hard coatings suggesting some restrictions on application of this approach [47].

1.3.3. Adhesion

While cohesion describes the mutual attraction between the same type of material on the level of interatomic or intermolecular forces, adhesion is the mechanical strength joining two different materials. In the context of thin films and coatings it means that adhesion is responsible for the contact and sticking between substrate and deposited coatings and between individual layers in case of multi-layered architecture. Good adhesion between substrate and layers of the coating is an indispensable requirement for any system of protective coatings. The origin of films adhesion to a surface of the substrate or another film is the chemical bonding between two types of materials at the interface and mechanical bonding between two surfaces.

1.3.3.1. Nature of Adhesion and Adhesion Failure

Ionic bonding occurs when the electron is transferred from one atom to another one, which causes to assume their net charge as positive and negative respectively, and, thus gives strong electrostatic attraction. Covalent bonding occurs when two atoms share one or more electrons (often a pair of electrons). In ionic compounds, electrons are tightly hold by the ions, and the ions cannot move translationally relative to each other. That is why they are hard and brittle materials. Covalent compounds tend to be softer and more flexible (see Table 1.2). Both mentioned types of bonding also result in low electrical conductivity, as not many "free electrons" are available.

Metallic bonding occurs when a lattice of positively charged ions is immersed in a mobile "sea" of valence electrons. The valence orbitals are delocalised over the entire metal lattice, electrons are not linked with individual cations and are free to move.

Table 1.2. Properties and behaviours (schematically) of materials depending on the prevailing chemical bonding character [48].

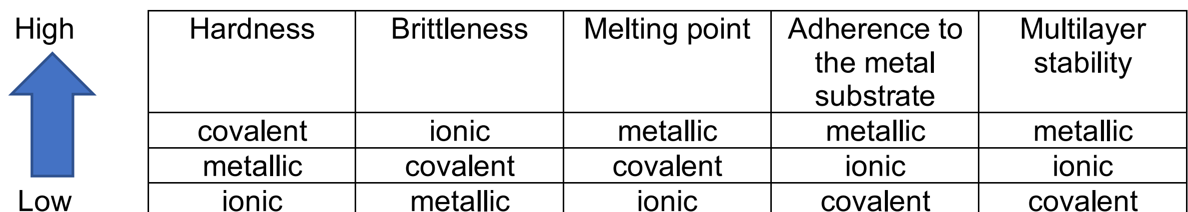

	Hardness	Brittleness	Melting point	Adherence to the metal substrate	Multilayer stability
High	covalent	ionic	metallic	metallic	metallic
	metallic	covalent	covalent	ionic	ionic
Low	ionic	metallic	ionic	covalent	covalent

This explains good electrical conductivity of metals and that they are malleable and ductile, or less brittle. The comparison of some key properties necessary for protective coatings is shown in Table 1.2. As seen from there, metallic compounds usually exhibit the best adherence to the metal substrate and stability in multi-layered structures. In some materials there is a mixture of

bond types, which may extend a range of the exhibited properties and enhance them (superior hardness, toughness, thermal stability and adhesion).

Adhesion by mechanical bonds happens when the two surfaces are mechanically coupled in such way that at least one of them must deform or rupture to separate materials. This requires a good conformity of the deposited film to a rough surface of substrate and an absence of poorly or not contacting zones at the interface [49,50].

The loss of adhesion is called deadhesion or adhesion failure and can occur over a large area causing film delamination from the substrate or over a small area causing pinholes. Deadhesion can happen at a sharp interface between materials (Fig. 1.6 (a - d)), in the near - interface region of the coating (Fig. 1.6 (e,h)) or substrate (Fig. 1.6 (f)), between films in a layered structure (Fig. 1.6 (d)), or in an interfacial region containing both materials (Fig. 1.6 (g)). As seen, in Fig. 1.6, the deadhesion can occur both by adhesive and cohesive failure.

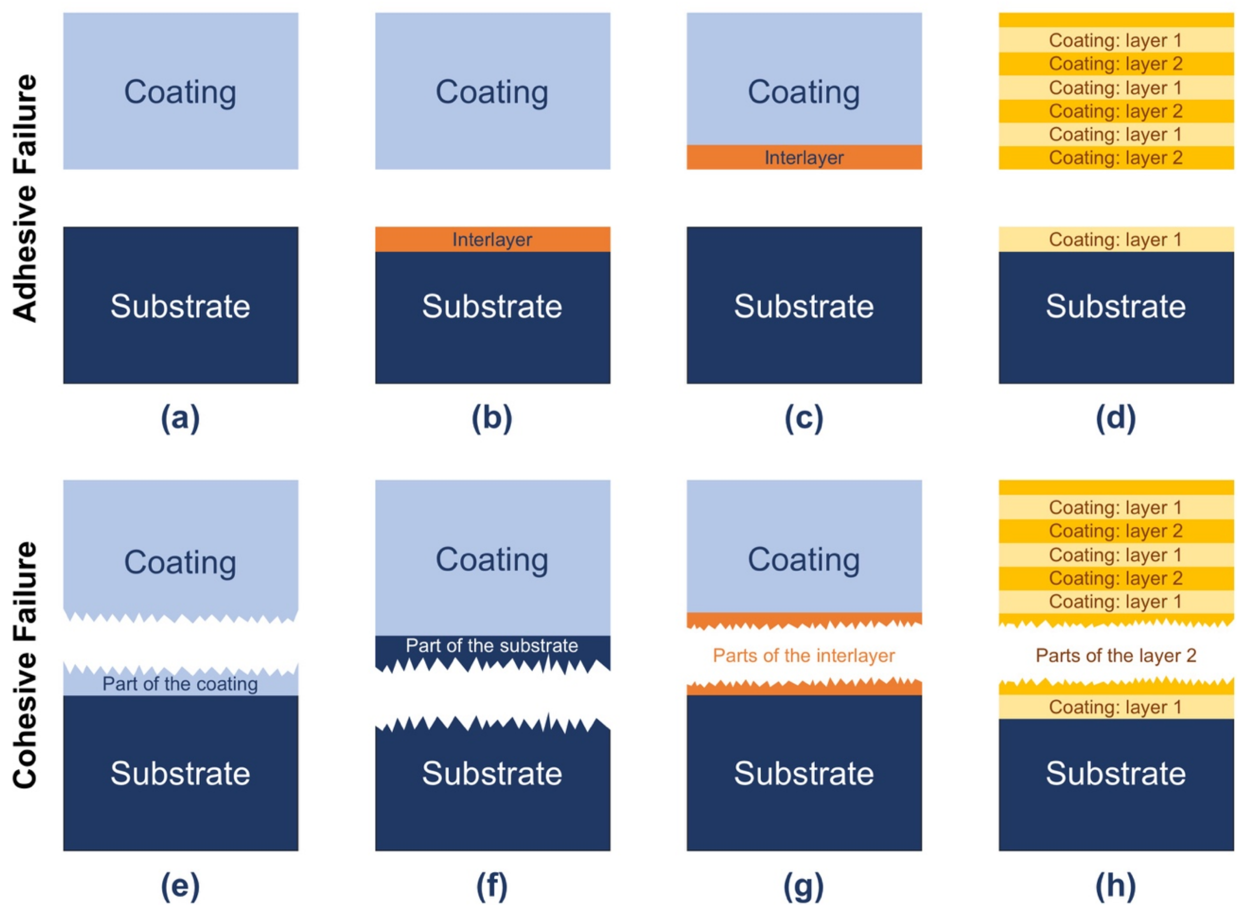

Fig. 1.6 - Adhesive and cohesive failure events occurring in deposited protective coatings.

For protective coatings it is necessary to have good adhesion after the deposition and during all service life of the tool, machine part or product.

1.3.3.2. Factors Affecting Adhesion

Residual stress in thin films and coatings significantly influences on the apparent adhesion. The nature of stresses usually comes from the difference of thermal processes in

depositing films and substrate, or from the growth processes and conditions. The residual stress can be tensile or compressive and can result in microdeformation and curvatures of the substrate coating interface possibly followed by adhesion failure of the film. Microstructure, morphology and mechanical properties of the film material determine the capability to distribute applied stress and to endure internal ones. That is why in case of large difference in the properties of two materials it may be beneficial to produce gradual interfacial zone. Physical and mechanical properties of the substrate surface and near-surface zone are important for good adhesion. The lattice mismatch between substrate and deposited material may produce additional stress causing decrease in apparent adhesion. The material should have a high fracture toughness. The surface roughness may have impact on the adhesion, as well as flaws at or near the interface area often may be the determining factor in adhesion. Flaws at the interface may appear from the surface of the substrate, incomplete contact between the film and the substrate, or defects growth. These can decrease the fracture toughness of the material and also create points of high local stress. Other defects in the films structure as nodules, pinholes, voids and porosity also have an effect on the apparent adhesion, usually negative.

The nodules in deposited films can be formed by growth on surface features such contaminations or other large particles, or by droplets and clusters evaporated or sputtered from the sources of material.

1.3.3.3. Adhesion Failure Mechanisms

There are many factors and mechanisms promoting adhesion failure, with mechanical or chemical nature. Very often several reasons may be involved at the same time.

1.3.3.3.1. Spontaneous Failure - Adhesion Lack or High Residual Stress

The film may peel off spontaneously with no any load or stress applied. High compressive residual stress in the film cause its blistering from the surface, while opposite, tensile stress, may result in microcracking and flacking (see Fig. 1.7) [49]. Often this type of adhesion failure due to the residual stresses may happen just after the deposition after removing the samples from the deposition chamber and cooling them down because of the different thermal expansion coefficients.

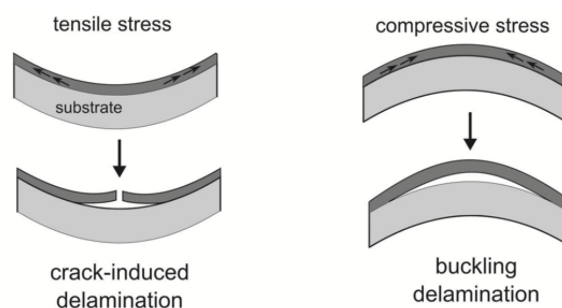

Fig. 1.7 - Thin film failure under high residual tensile or compressive stress. Microcracking and peeling of a “flake” from a surface, under tensile film stress (left). Blistering of a film under compressive stress leaving a void (right).

If the film adhesion strength is high but the fracture strength of the substrate near the surface zone is relatively weak, the failure may go through the substrate and not at the interface - cohesive failure (as shown in Fig. 1.6 (f)). Regions of localised high residual stress due to the growth discontinuities or nonhomogeneous growth (near to steps and defects in the film) can lead to the localised adhesion failures appearing as pinholes. The film stress may vary through the depth profile of the film. If the high residual stress in the film or coating is being generated during deposition, usually it can be limited by reducing the film thickness, changing the film composition, structure, deposition technique or parameters [49].

1.3.3.3.2. External Loads and Fatigue Processes

When the external mechanical force is applied to the coating it generates mechanical stresses. Depending on the nature of applied load, tensile or compressive stresses and shear may appear. If an external stress is applied to the surface of a film, it will appear at the interface as a tensor force with both tensile/compressive and shear components. The components of stress depend on the mechanical properties of the film and substrate materials [49,51]. If the substrate deforms under the load the stress tensor will be further complicated. Even though one application of the stress doesn't lead to the adhesion failure, the cyclic application of a stress, which is called fatigue, may ruin the film or adhesion. It may be thermal, chemical or mechanical influence. Fatigue failure usually happens by the flaws generation, continuous cracking and their expansion, propagation or by changes in the mechanical properties [49].

1.3.3.3.3. Corrosion and Oxidation

Corrosion and oxidation may happen due to the subsequent processing, such as chemical etching or contaminations, aggressive environment during tool service, as well as from resulted heating at the air atmosphere. These chemical reactions of materials at the interface from new compounds, usually with poor mechanical strength. Moreover, they may provoke a volume expansion and, thus, wedging at the interfaces [49]. Corrosion may penetrate from the surface of the film to the substrate and interfaces from the pinholes in the film, though the cracks or by grain boundaries in columnar structures.

1.3.3.3.4. Diffusion Toward or Away from the Interface and Reactions at the Interface

Diffusion of species to the interface can weaken the interface. Gas precipitation or diffusion of lattice defects form voids at interfaces, which impact on adhesion loss [49]. Diffusion away from the interface can decrease local density, form porous, voids and, as result, cause loss of adhesion. The diffusion may be initiated or accelerated by increase of the environmental temperature or heating while the film is in service. Reactions at the interfaces between materials or diffused elements can weaken the involved areas by voids and microfracturing. New compounds may have different mechanical properties, as undesired brittleness and weak fracture

strength, which decrease the adhesion. Also, they can cause volume expansion leading to the increase of internal stresses and possible cracking, local delaminations or drop in the apparent adhesion.

1.3.3.4. Ways for Adhesion Improvement

Good adhesion is determined by a large number of factors, many of which are difficult to control. The development of processes, which should lead to the good adhesion, is often based on an empirical manner with consideration of some factors which are mostly give an improvement in adhesion and which factors may cause a degradation of adhesion.

1.3.3.4.1. Selection of Substrate and Film Material

For the best adhesion the substrate and film materials should have good chemical bonding. If the film has a high elastic modulus it can lead to high total residual stresses. This may be adjusted by control of the deposition parameters or decrease of the total thickness which is often the easiest solution unless the thick films are required.

For metallic substrates, which is usually the case for many applications and tools for mechanical machining, the adhesion to metal films should be good if the surface was cleaned from the contaminations and surface barrier layers. Then deposited film will easily alloy with the substrate. Elevated temperatures of the surface may help to improve the adhesion by increased interfacial diffusion unless such process doesn't lead to undesired effect of diffusion processes discussed above (adhesion weakness).

Metallic substrates usually may have oxide layer on the surface or other contaminations. They should be cleaned mechanically, chemically or (and) by in-situ cleaning inside the deposition system (e.g. plasma etching).

1.3.3.4.2. Adhesive, Graded or Barrier Layers

Often the best solution to obtain good adhesion and desired film on the substrate is to deposit previously an additional thin film (usually 5-50 nm thick) with good bonding both to the substrate and to the main film.

Sometimes the transition from the substrate to the film may be designed in a form of film with graded properties like composition, density, yield strength. This may be done by using additional targets to change elemental composition of vapour phase, by the layered composition of the targets or reactive gasses conditions.

In some cases, diffusion barriers may be used at the interface to reduce diffusion [49].

1.3.3.5. Adhesion Evaluation

Adhesion tests are generally very difficult for analytical study and more often they are used for comparative evaluation. The testing of coatings should be performed under the stresses similar to those faced just after the deposition and then during post-processing, storage and service, including environmental stress (e.g. time, temperatures, chemical surrounding,

mechanical fatigue etc.). It could happen that different tests give different values and even different failure mechanisms. The difficulties in tests reproducibility and large number of adhesion evaluation methods make it even more complicated [49]. The best test of adhesion is the evaluation of real coatings and their behaviours under the real processing, storage and service.

Adhesion tests may be grouped by the methods of stress application to the film/coating: mechanical pull (tensile, peal) tests; mechanical shear tests; scratch, indentation, abrasion and wear tests; mechanical deformation; stress wave tests [52]; fatigue tests; non-destructive methods with infrared microscopy or SEM, acoustic imagining [53], scanning thermal microscopy [54] and many others. Brief summary of the main adhesion test types is shown in Fig. 1.8.

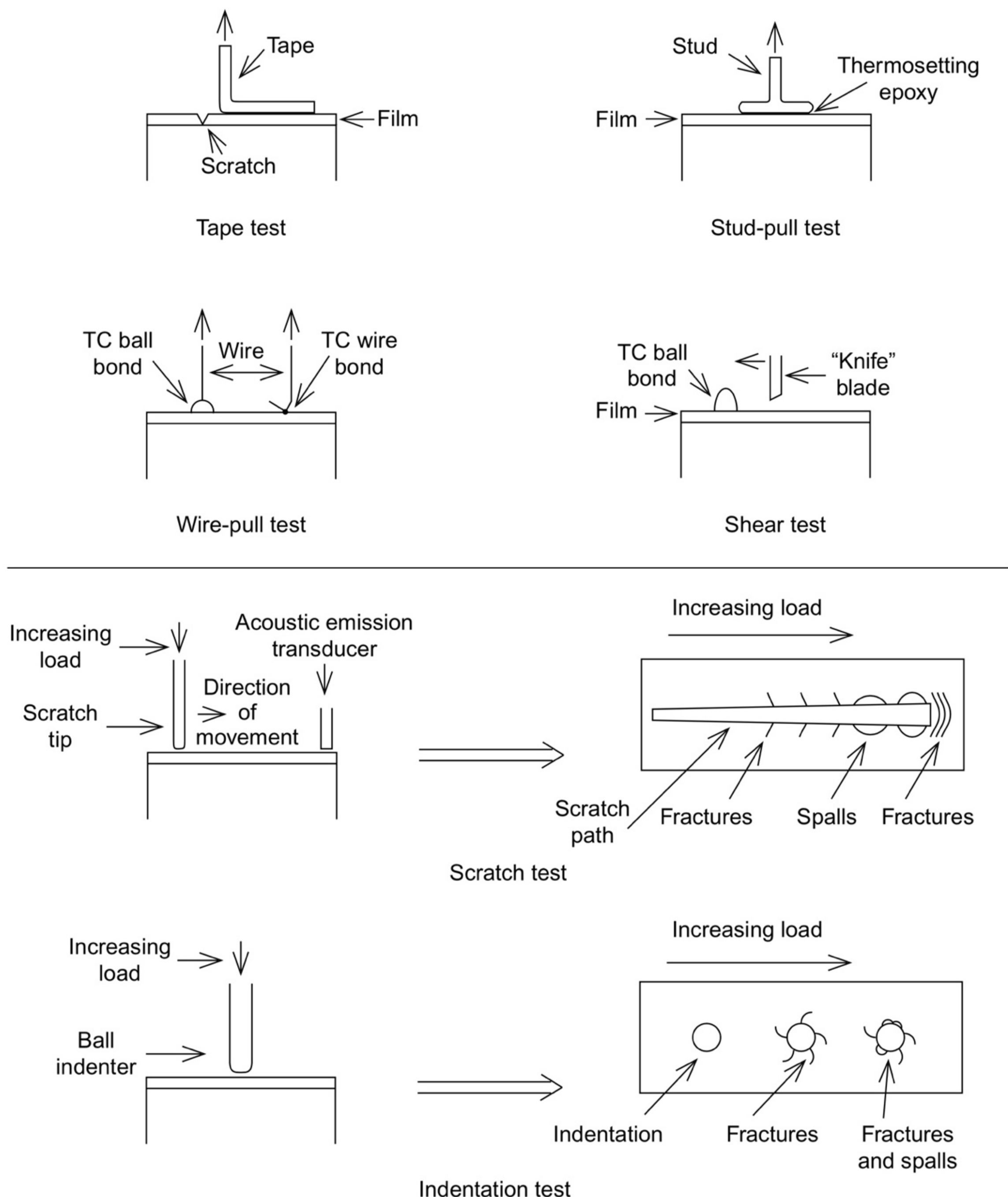

Fig. 1.8 - Adhesion Tests. As taken from [49].

1.4. Types of Modern Protective Coatings

Based on principal properties and functionality, protective coatings may be grouped mainly into hard coatings, coatings with enhanced thermal stability, coatings with high oxidation and corrosion resistance, thermal barrier coatings. High hardness is essential for cutting tools coatings. In addition to usually extended tools' life time it helps to achieve smooth high-quality surface and shape of machined parts. Hard materials with hardness H ≥ 40 GPa and H ≥ 70 GPa are classified as super- and ultrahard materials respectively. Since many well-done up-to-date review-papers on hard coatings have been already written so far [26,55–61], there no needs to duplicate them within this work, but some overview and introduction will be provided. Hard coatings are the most efficient in providing protection from deformation and wear. But often hard materials may be brittle and prone to cracking, which is why for protective coatings, it is crucial to have both high hardness and toughness. And only a mixture of several parameters leads to a high wear performance and long lifetime of cutting tools under extreme conditions.

1.4.1. Diamond

Diamond is the intrinsically hardest material because of its strong nonpolar covalent C-C bonds and the high coordination number of 4. It belongs to ultrahard materials with H = 70-100 GPa [26]. Diamond exhibits the highest room temperature thermal conductivity of $\sim 20\ \mathrm{W/cm \cdot K}$ and extremely low coefficient of thermal expansion of $\sim 0.8 \times 10^{-6}\ K^{-1}$ at 300 K. At room temperature it's inert toward attack of acids and alkalis and is resistant to thermal shock. Topography of diamond surface may be customised from extremely smooth with coefficient of friction as low as 0.1 in air to very rough with protruding edges, depending on the extent of polishing and orientation of the crystallographic planes [55]. Because of these properties, diamond promises tremendous application in the field of tribology especially as a protective coating for cutting tools. Polycrystalline diamond films are best synthesised by chemical vapour deposition (CVD) techniques (but not limited to) [62,63], the most common are hot filament-assisted CVD (HFCVD), direct current plasma-assisted CVD (DC PACVD), microwave plasma CVD (MPCVD) and combustion flame-assisted CVD (CFACVD) [55]. However, most of the metals and ceramics have much higher thermal expansion coefficient than a very low one of the diamond coatings. This often may cause residual stress and further spallation of the coatings. Thus, it limits number of workpiece materials for diamond coated cutting tools. Tungsten carbide (WC) has the closest coefficient of thermal extension to that of diamond, which allows diamond films deposition on WC substrates in almost stress-free conditions. Nevertheless, the diffusion of cobalt contained in WC tools promotes higher graphitisation at the diamond-carbide interface. This induces coating delamination during the machining. To reduce such effect and improve adhesion, the deposition of an interlayer with specific composition, dopants, multilayer architecture of coatings, surface etching and other surface treatment techniques may be applied

[64–69]. This also should help in case of diamond coating deposition on the surface different from WC, with higher coefficient of thermal expansion.

1.4.2. Diamond-Like Carbon

Diamond-like carbon (DLC), as follows from the name, exhibits some of the properties intrinsic to diamond. Among them the most important for cutting tools application are hardness of super- and ultrahard level, high wear resistance and low coefficient of friction (~0.1). Most DLC films are structurally amorphous and can be synthesised by plasma-based PVD and CVD methods. Deposition method and type of carbon source can influence substantially the structural chemistry of the resultant films, which leads to large variations in their properties. Since 1970s, DLC films have been well developed and discussed [70–72]. Structurally they made of sp^2- and sp^3-bonded carbon atoms and may be classified depending on the structure and hydrogen content as well as presence of other dopants. DLC coatings with lower hydrogen percentage (≤40%) and higher proportion of sp^3 bonding in the structure have higher hardness. Thereby, hydrogen-free tetrahedral amorphous carbon (ta-C) with highest sp^3 content (80-88%) has ultrahardness of 80 GPa [70]. DLC films are not only hard but also smooth, and furthermore their tribological properties may be manipulated easily by introducing dopants such as nitrogen, silicon, etc. [73]. It also helps to achieve high-quality shapes of machined surface or cutting edge: clean, smooth, without chipping or rounding (see Fig. 1.9).

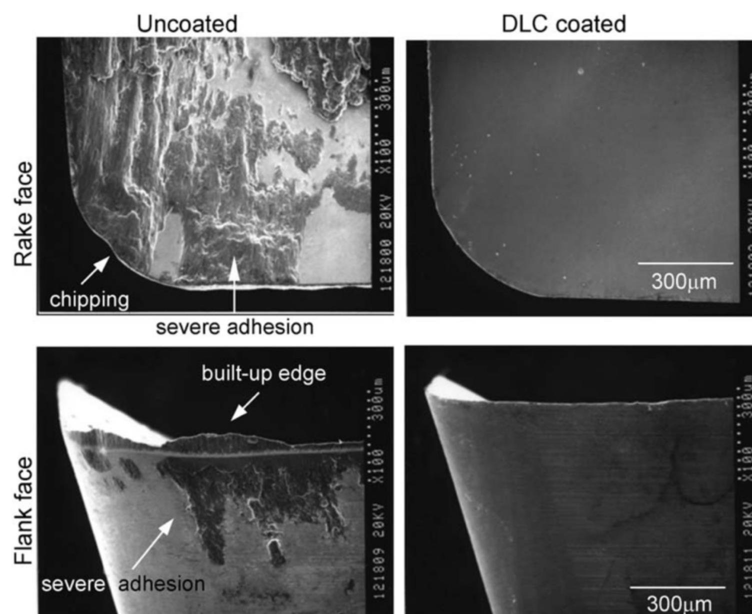

Fig. 1.9 - SEM micrographs of rake and flank face after the dry milling test for $AlCu_{2.5}Si_{18}$ alloy. As taken from [71].

However, it is quite difficult to deposit thick coatings (2 µm and more) because of delamination due to the internal stress, as well as there are limitations on substrate choice to have adherent film. Moreover, such coatings are prone to graphitise at temperatures above 300°C with further decrease of their hardness [55]. In other words, if the outer layer of DLC is turned in graphite, when tool is in service, it should decrease both friction and wear rates [74].

Nevertheless, not only ultrahardness is necessary for protective coatings in cutting tools, and other types of coatings may win in such a competition.

1.4.3. Transition Metal Nitrides, Carbides and Borides

Transition metal (TM) nitrides (TMN), carbides (TMC) and borides (TMB) are largely employed as hard protective coatings in the cutting and forming tool industry. They attract interest due to exceptional properties they shown, such as high hardness, chemical inertness, electronic properties from insulation to superconductivity, high melting point and thermal stability under harsh environments (oxidation, radiation). Such properties are mainly due to the variety of chemical bonding. Transition metals belong to d-block of the periodical table (groups 3-12) and most of them form one or more stable ions which have incompletely filled d-orbitals. Transition metal compounds with nitrogen, carbon or boron can take such chemical bonding state where ionic, covalent and metallic bonding co-exist. So, for example, in case of titanium nitride (TiN), metallic bonds exist between Ti-Ti. On the other hand, ionic character is due to charge transfer occurs between Ti and N, while substantial covalent bonds are existed as well [75]. Such mixed bonding has been also observed and well established in TiC and TiB_2 [76,77], the hardest binary compound among transition metals. Bondings directly determine material properties like melting point, surface energy, thermal expansion, bulk modulus, etc., so high melting point and high hardness of the nitrides, carbides and borides can be also attributed to the mixed character of bonds [77]. Transition metals have smaller atomic volumes than group 1 and 2 of metals in the periodic table and can pack together more closely, which results in higher densities and hardness. Closer packing assumes stronger bonding, so more energy is required to melt or boil transition metals. Based on prevailing bonding type in TM nitrides, carbides and borides Holleck [48] ranged their properties from low to high level, some of them are shown in Fig. 1.10. Depending on the priority properties and suitable deposition technique, one may select the coating which fits the best.

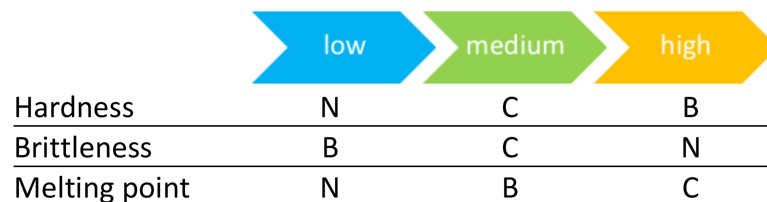

Fig. 1.10 - Properties of transition metal nitrides (N), carbides (C) and borides (B) [48]. Published in [2].

The first industrial CVD coated tool coating on cemented carbide was TiC in 1969, and in 1980 TiN become the first PVD coating. Lower temperatures of coatings in PVD process made possible the deposition on steel tools [1]. Since 1970s-80s and until now TiN, TiC, TiB_2, CrN and ZrN are the most frequently used among binary coatings.

TiN has been the most widely studied TMN protective coating and it's still widely used since the late 1960s. However, it has some limitations and hardly overcomes modern challenges:

thermal stability and oxidation resistance. Under high temperature, an oxide layer may be formed on the surface, which develops stress in the coating, high enough to damage or destroy the protective layers. For TiN it happens at a temperature above 500°C. L. Shizhi et al. [78] reported TiN hardness enhancement up to 70 GPa by Si addition. The films were deposited by plasma chemical vapor deposition (PCVD) from a mixture of $TiCl_4$, $SiCl_4$ with excess of hydrogen and nitrogen at a temperature of 560°C. However, several months after the preparation of samples and publication of the paper, the decrease of hardness was observed. S. Veprek discussed possible reasons in his review [26]. Later, in their joint research [79] they obtained TiN nanocrystals in amorphous Si_3N_4 matrix prepared by PCVD with stable hardness ≥50 GPa and resistance against oxidation in air up to 800°C.

1.4.4. Ternary and Quaternary Compounds

To overcome new modern challenges of extreme conditions new more complex compositions of coatings, as **ternary and quaternary compounds** have been proposed, which exhibit some superior and specific properties. An important place belongs to Al-containing TMN ternary compounds of $TM_xAl_{1-x}N$ type, where TM is transition metal, such Ti, Cr, Zr, Nb, Hf, Ta, V, etc. The most popular are Ti-Al-N and Cr-Al-N systems, remaining to be "state-of-the art" coatings for a long time and well-discussed in research and review papers [80,81]. Their exceptional hardness and oxidation resistance is mainly caused by supersaturated solid-solution of hexagonal B4-structured AlN in cubic B1 structure of TiN, with the following large volume mismatch, elastic strain energy and solid solution strengthening [80]. The mechanical and chemical properties of $TM_xAl_{1-x}N$ coatings usually improve with increase of Al fraction, but up to a certain critical content. If Al percentage is higher, then supersaturated cubic structure transforms into a mixture with hexagonal B4 phase, which causes a drop of hardness, wear resistance and even oxidation resistance.

$TM_xAl_{1-x}N$ coatings form a dense Al_2O_3 oxide layer on the top of the film, which effectively impedes oxidation of hard protective coating. In Ti-based films this layer is mixed with TiO_2, which limits the oxidation resistance effect. From this point of view, $Cr_xAl_{1-x}N$, where both Cr and Al form protective oxides, has an advantage of Al_2O_3 + Cr_2O_3 protective top layer and, hence, exhibit significantly better oxidation resistance at elevated temperatures.

Metastable supersaturated films, which $TM_xAl_{1-x}N$ systems are, exhibit phenomena of age-hardening caused by decomposition with annealing temperature or time. More significant increase of hardness occurs in Ti-Al-N system then in Cr-Al-N due to the different interaction of resulted precipitations with dislocations [80]. This particular feature may have a high potential for efficient enhancement of tool lifetime.

Recently, groups of T. Polcar and A. Cavaleiro performed the study of Cr addition to Ti-Al-N system and its influence on thermal resistance, oxidation stability, tribological and cutting

performance by the deposition of quaternary Ti-Al-Cr-N coatings [82,83]. Fig. 1.11 taken from their research shows the comparison of Ti-Al-N and Ti-Al-Cr-N films wear performance at room temperature and at 650°C. As seen here, the coating which demonstrates relatively lower wear resistance at room temperature (Ti-Al-Cr-N system) in comparison to another one (in this case, Ti-Al-N system) then can exhibit much higher wear performance at elevated temperatures of real conditions of the cutting tools work.

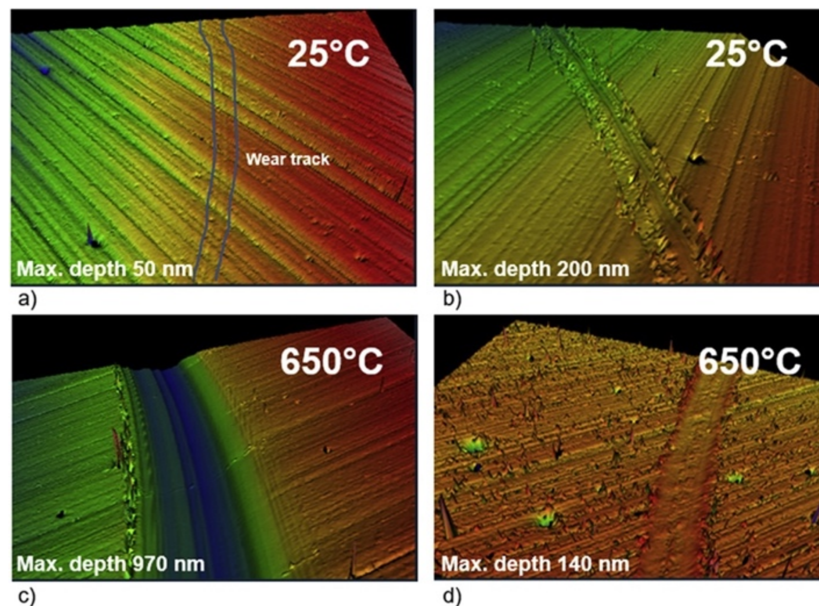

Fig. 1.11 - 3D profiles of the wear tracks of $Ti_{0.47}Al_{0.46}N$ and $Ti_{0.28}Al_{0.31}Cr_{0.51}N$ films. As taken from [82].

Other ternary coatings which combine superior properties of transition metal carbides and nitrides are transition metal carbonitrides (TMC_xN_{1-x}). The most famous are TiC_xN_{1-x} coatings where x ranges from 0 to 1. Usually they are deposited as solid solution of fcc TiN and fcc TiC. TiCN structure may be described by TiN matrix with substitution of N atoms by C atoms, which lead to distortion strengthening and increased resistance to dislocation movement [84]. Depending on deposition method and deposition conditions the film may also be composed of a mixture of TiN, TiC and C_3N_4, as in research of T. Sampath Kumar et al. [85]. Transition metal nitride contributes to the strengthening and hardening of coatings, while carbon forms graphite lubricating layer during work and, thus, substantially reduces wear rate. S.-H. Jhi et al. [30] studied electronic mechanism of hardness enhancement in transition-metal carbonitrides. On this base also other ternary and quaternary carbonitride coatings with transition metals and other specific dopants exhibit better mechanical and chemical properties than their binary analogous and may be employed as protective ones, but their application should be evaluated from the CRMs and costs effectiveness point of view: CrCN [86–88], CrSiCN [89–91], CrBCN [91], HfCN [92], VCN [93], etc.

In quaternary and higher-order coatings based on transition metal nitrides, carbides, borides, carbonitrides and other types the selection of each element means some special task for improvement of coatings. Aluminium mainly helps to increase oxidation resistance by Al_2O_3 layer

on the surface, or hexagonal lattice of AlN may be used for distortion of structure and strengthening. Silicon very often introduced in nitride coatings to form hard nanocomposite materials where amorphous Si_3N_4 surrounds hard metal nitride grains, or similar multi-layered configuration may be applied. Refractory metals (Nb, Mo, Ta, W, Re) significantly improve thermal stability of the coatings and allow to work under extreme conditions and high speed.

1.4.5. High Entropy Alloy Coatings

A. Greer [94] in 1993 stated "the confusion principle" of the crystallisation possibility lowering by increase of alloying elements number. Later such materials were separated into a new class of high-entropy alloys (HEAs) by J. Yeh et al. [95] and B. Cantor et al. [96] in 2004. HEAs are mostly identified as alloys which contain at least five principal elements with concentration of each between 5 and 35 at.% and possible inclusion of minor elements to modify final properties [95,97]. Entropy-based definition describes HEA as an alloy with high entropy of $S^{SS,ideal}$>1.61R, where SS ideal is a solid solution with the maximum possible value of configurational entropy. However, modified definitions and alternatives are existed and the discussion about which one fits the best is still open. Four "core effects" of HEAs are: the high-entropy effect which may favour single-solution phases over competing intermetallic compounds; the lattice distortion effect, resulted from the different atom sizes that make up crystal lattices of complex, concentrated phases, which may contribute to the hardening; the sluggish diffusion effect; the "cocktail" effect – in each case, properties depend on material composition, microstructure, electronic structure and other features in complicated and sensitive ways [98]. HEAs may be fabricated as protective coatings, usually deposited by magnetron sputtering or laser cladding. Because of the great diversity of possible involved elements into the composition, HEA coatings have high opportunity to contain critical raw materials. However, CRM consumption in this case is pretty low.

1.4.6. Thermal Barrier Coatings

High amount of heat is generated in the cutting zone during machining. There are three different zones from where the heat flux come into the cutting tool: the primary shear zone (plastic deformation and viscous dissipation), the secondary shear zone (frictional and plastic shearing energy), and the frictional rubbing of the cut surface on the tool insert flank. The diffusion of heat into the workpiece or tool body influences negatively on lifetime and work performance. There are many coatings with functionality as thermal barrier applied to metallic surfaces to operate at elevated temperatures, but most of them are existed for cases with no direct high mechanical load applied, such as gas turbines or aero-engine parts. In case of cutting tools, the influence of coating in heat distribution from working interface is unknown or very poorly studied. It is not clear whether coatings influence the cutting process by an insulation effect (lower heat flux transmitted into the substrate), or rather by a tribological effect (lower level of heat generated by friction) [99].

It is quite difficult to perform in-situ or ex-situ experimental study of thermal barrier coatings or to find thermal properties data in the literature due to the lack of standard methodology to quantify these properties in the case of very thin layers. That is why most of the existed approaches based on simulation methods. J. Rech et al. [99] proposed an analytical solution of heat transfer modelling to characterise the influence of a coating on the heat flow entering into the tool substrate. He showed, that coatings don't have any capacity to insulate a substrate in continuous cutting applications, but in applications with a very short tool-chip contact duration, such as high-speed milling, coatings keep a large amount of heat in the interaction zone, which may improve the wear resistance of the tool. This result is in accordance with the computational and experimental investigations made by F. Du et al. [100] and J. Rech et al. [101]. Also, it was shown that the larger the coatings thickness is, the more influence it has on the heat transfer. Moreover, it has been pointed out that the heat flux transmitted to a substrate is much more influences by the tribological phenomenon at the cutting interface than by thermal barrier properties of the coating [99].

M.A. Shalaby et al. [102] reports that the increase of pure alumina ceramic tool performance in proportion to the cutting speed can be attributed to the thermal barrier properties of ZrO_2 tribo-layer induced at high cutting speed (temperature). In case of SiAlON ceramic (Si_3N_4+Al_2O_3) they pointed out the high performance due to the high amount of mullite (Al-Si-O) tribofilm formed on the tool face, a phase that has a reduces thermal conductivity and serves as a thermal barrier layer. W. Song et al. [103] reports thermal barrier contribution to the wear resistance of the cemented carbide tool coated by Ti–MoS_2/Zr. J.J. Gengler et al. [104] investigated the thermal transport for Si-B-C-N ceramic films and concluded that their properties are ideal for thermal barrier applications for high-temperature protective systems of aircrafts, as well as surfaces of cutting tool and optical devices.

1.5. Concepts for the Enhancement of Protective Properties

1.5.1. Nanostructural Approach

Nano- and microstructural approach is a base of another method to overcome modern challenges and enhance significantly protective properties of coatings. One of them is based on grain size refinement and Hall-Petch strengthening [26,105]. It was found experimentally, that material usually exhibits higher hardness when the grain size reduces. Empirically it was defined, that most of the materials reaches highest values of hardness and related properties when the grain size approaches to nanoscale values around 10 nm (see Fig. 1.12). This phenomenon was named Hall-Petch strengthening effect. The most recognised explanation is briefly based on increase of grain boundaries volume when grain size decreases. In turn, grain boundaries impede dislocation movement and activation, which have positive influence for hardness and strength of material. The opposite happens when the grain size remains to decrease to values smaller than

10 nm when the maximum hardness was reached. Overgrown volume of boundaries and small grains cause loss of material hardness. This phenomenon has been termed as the reverse or inverse Hall–Petch relation/effect. Thus, the grain size refinement allows to control and optimise mechanical and tribological properties by selection of the deposition conditions (deposition time, targets power or cathodes current, bias voltage applied to the substrate, temperature, pressure, gasses flow, etc.) and elemental composition.

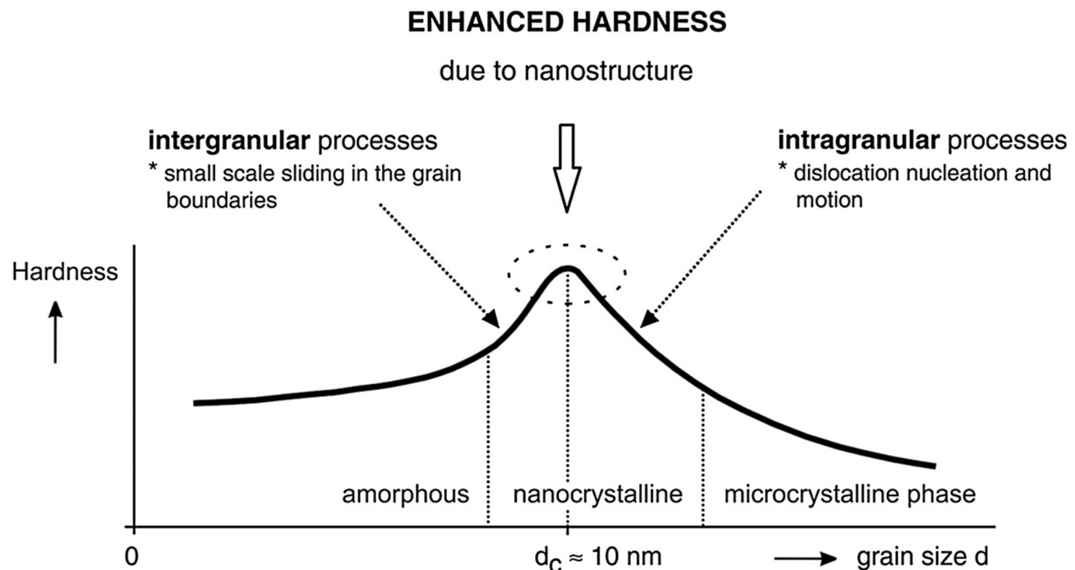

Fig. 1.12 - Schematic illustration of Hall-Petch strengthening effect: hardness as a function of grain size (d). As taken from [38].

1.5.2. Nanocomposites

Nanocomposite coatings are materials containing nanocrystals distributed in the amorphous matrix. The optimum thickness of amorphous intergranular media separating nanocrystals ranges up to 1-3 nm, which is enough to contain several atomic layers. Nanocomposite structure is usually formed by the segregation of one phase at the grain boundaries of another one. This hampers grain growth and promotes the formation of nanostructure [9]. In a couple with small grain size and crucial role of grain boundaries in strengthening and hardening of the material, this leads to the fabrication of the protective coatings with high wear performance. Hard nanocomposite coatings, which are in the scope of the protective coatings for cutting tools, generally may be classified in two groups: 1) nc-Me_1N/a-Me_2N (hard phase/hard phase composites); 2) nc-Me_1N/Me_3 (hard phase/soft phase composites), where Me_1 = Ti, Zr, W, Ta, Cr, Mo, Al, etc. are the elements forming hard nitrides, Me_2 = Si, B, etc. and Me_3 = Cu, Ni, Ag, Au, Y, etc. [38]. The most used and interesting for cutting tools are Ti-Al-Si-N with nc-$(Ti_xAl_{1-x})N$ + a-Si_3N_4 phases [106–108], Cr-Al-Si-N of nc-$(Cr_xAl_{x-1})N$ + a-Si_3N_4, TiZrSiN of c-(Ti,Zr)N solid solution + a-SiN_x [109], nc-TiC + a-C [110,111], Ti-Si-N [112,113], Ti-Si-B-C [114–116], Ti-Si-B-C-N [117], AlTiN-Ni [118], ZrN/SiN_x [119], nc-W_2N/a-Si_3N_4 [120], (Zr–Ti–Cr–Nb)N [10,14], Mo_2BC [121], nc-AlN/a-SiO_2 [122]. Nanocomposite hard coatings are well discussed in the most recent and fundamental reviews of J. Musil [38], S. Veprek et al. [123,124], A.D. Pogrebnjak et al. [9,59], C.S. Kumar et al. [125].

1.5.3. Multilayer Architecture

Multilayer architecture is one of the most efficient and promising approaches nowadays for hardness and toughness enhancement of the protective coatings. There are several ways of their design: set of films deposited in a special order according to their functionality (e.g. substrate > adhesion film > superhard film > oxidation resistant film), alternating films with similar crystal lattice for epitaxial growth, hard crystalline films with thin amorphous layers, alternating TMN, TMC or TMB films, nanocomposites, HEA coatings etc. Many scientific groups over the world work on this topic and many papers have been published in order to review and evaluate the recent progress in this area, for the last decade as well [9,38,126–129]. Among the most recent and interesting multilayer solutions for protective coatings are TiN/TiAlN [130,131], TiAlN/TaN [132], Ti(Al)N/Cr(Al)N [82], TiAlN/TiSiN [133], (TiAlSiY)N/MoN [134], CrN/AlSiN [135], CrAlSiN/TiVN [136], AlCrN/TiAlTaN [137], AlCrN/TiVN [138], TiVN/TiSiN [139], TiSiC/NiC [140], TiN/MoN [11,12], TiN/WN [141], TiN/ZrN [142], Zr/ZrN [143], Ta/TaN [144], CrN/CrCN [86], CrN/MoN [145,146], AlTiCrSiYN/AlTiCrN [147], TiCrAlN/TiCrAlSiYN [148], (TiZrNbHfTa)N/WN [149], multilayer hard/soft DLC coatings [150].

At least three significant benefits of multi-layered coatings should be mentioned. The first is the possibility to build one-dimensional nanocomposites – coatings with nanoscale thickness of film/films and following enhancement of mechanical and tribological properties [26]. The second is the adjustment of grain size by changing bilayer thickness in the coatings, since the grain sizes decreases in the thinner layers, as was reported in many works. The third but the main feature of multilayer design of coatings by itself is the ability to resist to the external forces and cracks and to interrupt their propagation toward the substrate on the interlayer interfaces. This prevents a direct impact of the destructive factors on workpiece material of cutting tools (Fig. 1.13 [126]).

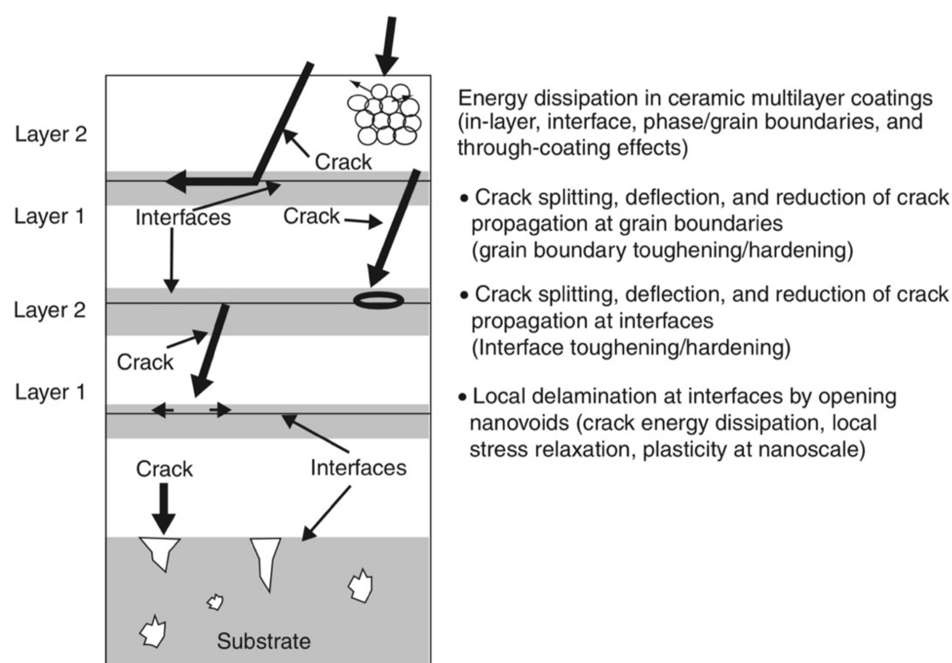

Fig. 1.13 - Toughening and strengthening mechanisms in multilayer coatings. As taken from [126].

Another necessary aspect of protective coatings deposition for cutting tools, which was mentioned briefly in this Thesis earlier, concerns the **adhesion to the surface**. Often the mixture of the substrate material and desired coating requires special study to achieve satisfying results in adhesion. The most common solutions may be additional interlayer between the tool and main protective coating (adhesive layer) or calibration of deposition conditions, elemental composition, substrate surface treatment and they are an objective for the specific study [151]. Related to this, but not limited to, is the problem of **residual stresses** in the coating. They may influence adhesion, hardness, wear resistance or thermal stability, etc., as well as may appear during deposition or with time. Detailly the nature and presence of residual stresses in coatings were reviewed by G. Abadias et al. [152] and in other works earlier [153].

Many protective coatings against wear and corrosion, which may be applied for cutting tools, haven't been considered here due to the huge variety of their types and infinite number of specific tasks. However, some general principles and tendencies were discussed, as well as more information is available in specialised papers and reviews [1,9,61,154–158]. Although chemical vapour deposition and physical vapour deposition are two main groups of **methods of protective coatings fabrication**, it is suggested to look deeply into thematic papers and reviews to learn about certain techniques [159,160] or find details of deposition methods in research papers regarding specific material and structure.

1.6. Multi-Layered CrN/MoN TMNs Protective Coatings

It is well known that various surface modification techniques (ion implantation, surface oxidation, ablation, protective coatings, etc.) [13,26,161,162] are widely used nowadays to satisfy the needs of engineering, industry and business, in materials with desirable properties for an acceptable price. Hard coatings are the most efficient in providing protection from deformation and wear [38,58,163–168]. However, often hard materials may be brittle and prone to cracking, that is why for protective coatings, it is crucial to have both high hardness and toughness. Nitride films based on transition and refractory metals are largely employed as hard protective coatings in the cutting and forming tool industry, as they exhibit high hardness, high melting temperatures and chemical inertness, resulting in thermal, chemical and physical stability under harsh environments (high operational velocities and temperatures, oxidation, radiation).

TiN has been the most widely studied TMN protective coating, and it is still widely used since the late 1960s [42,168–177]. Nevertheless, it has some limitations and hardly overcomes modern challenges. The weak point of such coatings is thermal stability and oxidation resistance. Under high temperature, an oxide layer may be formed on the surface, which develops stress in the coating, high enough to damage or destroy the protective layers. For TiN, it happens at the temperature above 500°C [175,177].

Currently deployed research strategies are focused on the improvement of coatings toughness by synthesising multicomponent systems [178–180] and/or tailoring their architecture through interface control (e.g., in superlattices) [176,181,182].

To produce a new coating with superior hardness, toughness and wear resistance it is proposed to employ mainly two approaches and get the benefit of this combination: Hall-Petch strengthening based on the effect of grain size control and multilayer design of the films [26]. The first assumes the increase of hardness values when the grain size reduces up to around 10 nm. The second approach is a multilayer architecture of coatings which benefit from the synergistic effect of individual layer properties. It improves the protective properties of the multilayer films by reduction of cracks propagation towards the substrate by the deflection of cracks on the interlayer interfaces. The design of multilayer coatings consisting of alternating layers with different composition (soft and hard phases) allows reducing internal stresses and brittleness while high values of hardness from 30 to 45 GPa are maintained [17,82,142,183–191]. Additionally, by control of individual layers thickness in coatings, it is possible to predetermine the grain size in coatings: the thinner layers are, the smaller grains may be obtained.

The substitutional defects may occur along the interfaces between adjacent layers in multi-layered films when some of the elements of one layer enter the crystal lattice of the adjacent one, replacing its atoms. This process results in the generation of strain energy proportional to the shear modulus of the material. The layers with different shear modulus prevent the movement of dislocations. Firstly such type of model to describe hardness enhancement was proposed by J.S. Koehler [192] and then approved and followed by many experimental and theoretical works, as well as by review papers [26,34,193–198]. Additionally, deviations or redistribution of dislocations and cracks at the grain boundaries help to increase the resistance of coatings. The multilayer structure reduces the influence of sublayer cracking and allows the use of such coatings under large dynamic loads. The alternation of nanometre-scale layers with different physical-mechanical characteristics allows to change significantly the properties of multilayer coatings, such as concentration of internal stresses or crack propagation, and, hence, to increase the fracture toughness of such material [26,36,199]. However, some works have been published recently where the enhancement of hardness and toughness in multilayer thin films is considered mainly due to the grain rotation for the nanocrystals and grain boundary sliding for larger grains [200,201].

Multilayer design of the coatings also allows benefiting from the combination of outstanding properties of different materials used in the deposition of individual layers in the films [137,166,199,202–205]. It has been recently reported that TiN/MoN multi-layered coatings demonstrate successful enhancement of mechanical properties [11,185,206–209]. One of the promising multilayer systems should be the combination of chromium and molybdenum nitrides [185–188,210–214].

Chromium nitride exhibits high thermal stability (more than 600 °C) [215–220] in comparison to titanium nitride and typically produces low friction in engineering contact conditions. While the hardness of CrN is on the same level as TiN, it demonstrates higher corrosion and wear resistance, and extremely strong adhesion to the metal surface.

Molybdenum nitride is the hardest superconductive metal nitride (28-34 GPa) but still has been less studied. The diversity of possible phases with a wide range of stoichiometry and lattice structures (cubic γ-$Mo_2N_{1\pm x}$, tetragonal β-$Mo_2N_{1\pm x}$, hexagonal δ-MoN and metastable MoN_x phase of NaCl-B1-type cubic structure) makes it interesting for the current research [189,190,213,221–223].

Such features of MoN in a couple with good adhesion and low wear rates will complement the properties of single-layer CrN coatings, in particular the oxidation resistance [222,224–228].

It is worth mention that the study of CrN/MoN multi-layered system in already published works is very limited [186,228–233] and does not disclose the potential of the coatings.

Objectives of the Thesis

This research is aimed to create **novel multi-layered CrN/MoN coatings with enhanced protective properties allowing to increase the lifetime of tools, machine parts and products.** For reaching the declared goal and for understanding the main regularities of the formation of microstructure and further properties of considered CrN/MoN protective coatings, the following objectives have been established.

Increase of Tools' and Products' Lifetime by Multi-Layered CrN/MoN Protective Coatings

Fabrication of multi-layered nanocomposite CrN/MoN films by vacuum arc evaporation of Cr and Mo cathodes in a nitrogen atmosphere

Elemental and structural characterisation of deposited coatings, investigation of their mechanical and tribological properties

Study the dependence of structure and protective properties of CrN/MoN coatings on their individual layer thickness

Study the effect of the negative bias voltage applied to the substrate and nitrogen pressure during deposition of CrN/MoN coatings on their structure and protective properties

Evaluate the effectiveness of the multilayer architecture approach to enhance mechanical and tribological properties of CrN/MoN nanocomposite protective coatings and find optimal deposition conditions

Estimate the position of designed CrN/MoN protective coatings among reported competitors and discuss their role in critical raw materials problem solution and sustainable circular economy

Chapter 2.

Experimental and Characterisation Techniques

Do not trust (do not use) a black box! This is one of the key-messages to be delivered to the reader of the Thesis. There are plenty of characterisation techniques in material science available in the world nowadays. The researcher has many options how to perform study: send sample to the laboratory, perform experiments together with an expert or technician, blindly trust in results obtained by a colleague or from collaboration, or do everything by himself.

It is hard to avoid any of mentioned cases since each technique is a complex system which may require months of years of total dedication to learn it and achieve experience enough for correct acquisition of data and its interpretation. However, it is essential to know basic principles of characterisation techniques and features of their applications to the materials and samples to be considered. There are dozens of books and guides for each technique, but some brief summaries of experimental techniques used in this research and specific methods useful for analysis of multilayer structures, thin films and coatings are given in this chapter.

This should help to understand obtained results, correctly interpret data and minimise probability of errors, not correct explanations or considering artefacts as true results. Also, it gives an opportunity to select the most suitable techniques for materials characterisation, optimise research and achieve more informative results.

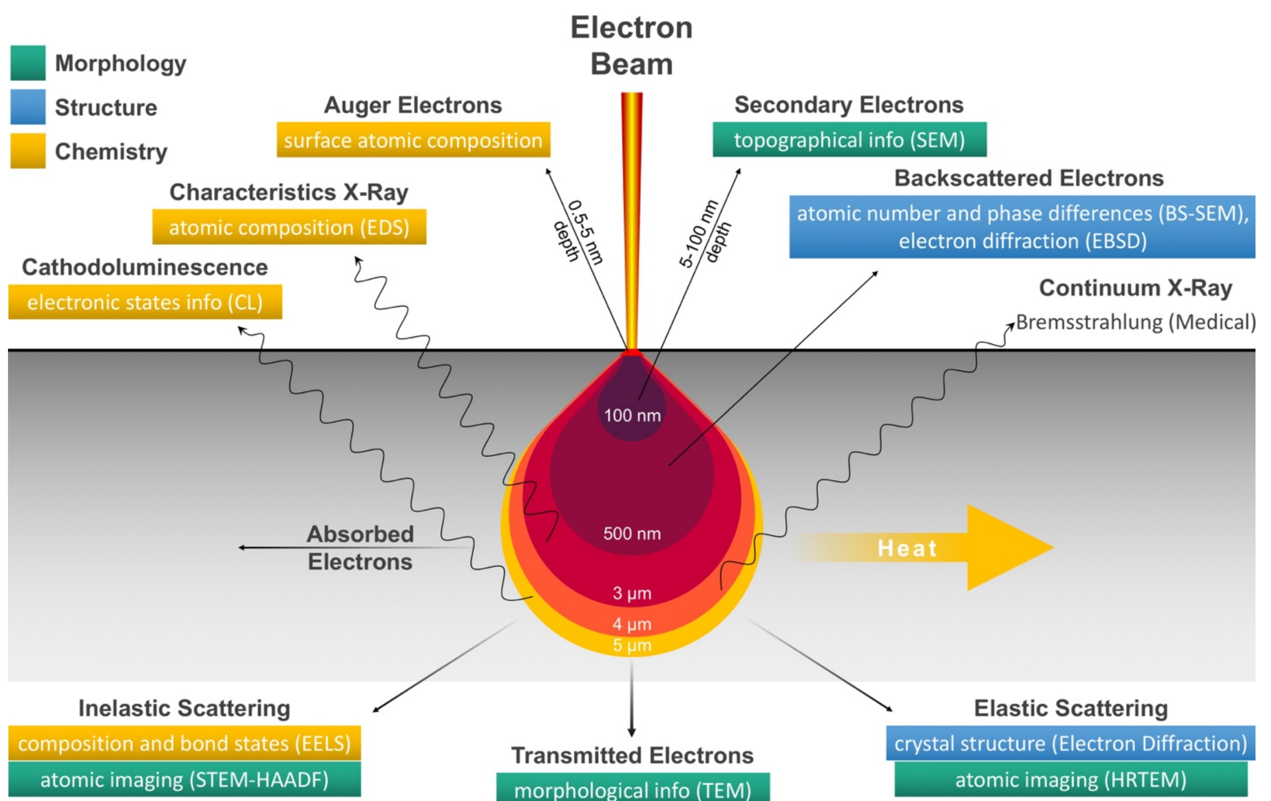

Fig. 2.1 - Electron beam interaction with matter, interaction volume scheme (based on [234]).

2.1. Scanning Electron Microscopy

2.1.1. Electron Beam Interaction with Matter

Scanning electron microscopy is a general type of electron microscopy, a powerful imaging technique that uses focused high-energy electron beam to scan across the sample surface and form an image by collecting emitted secondary (SE) or/and backscattered (BSE) electrons. When the electron beam hits a surface many types of interactions of high-energy electrons with the matter occur (see Fig. 2.1).

As seen, results of such interactions of electron beam with the matter may be employed by various advanced experimental techniques to study properties of the materials morphology (scanning and transmission electron microscopies), structure (backscattered electron detecting mode in SEM or electron probe microanalyser (EPMA), electron backscatter diffraction (EBSD)) and chemistry (Auger electron spectroscopy (AES), cathodoluminescence, energy-dispersive X-ray spectroscopy (EDS), wavelength-dispersive X-ray spectroscopy (WDS)).

The most interesting products of primary electron interaction with the matter and atoms for the chapter of scanning electron microscopy are secondary electrons and backscattered electrons. The process of primary beam interaction with an atom to produce secondary and backscattered electrons is shown schematically in Fig. 2.2.

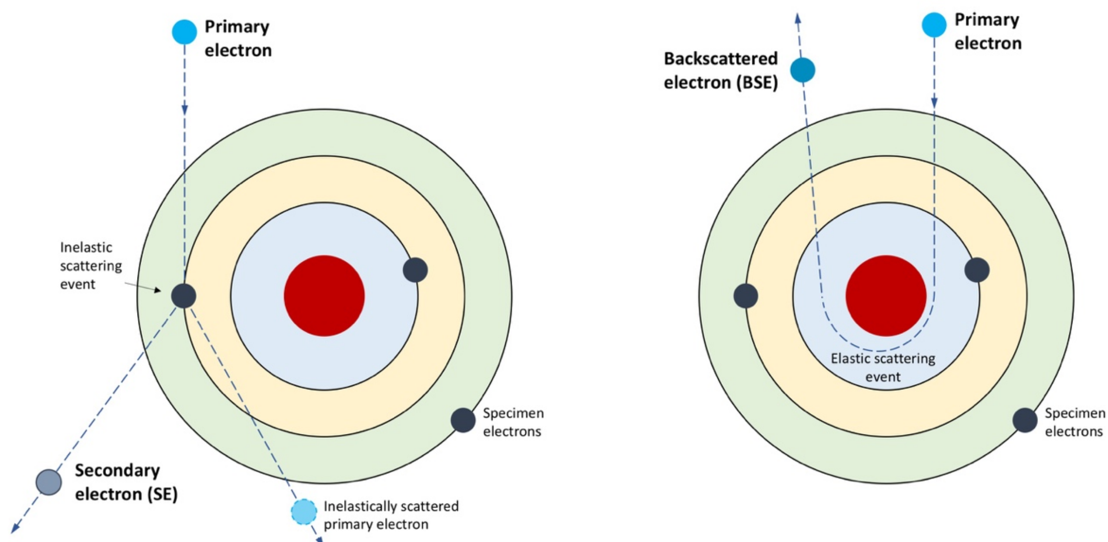

Fig. 2.2 - Schematic model of secondary electrons (SE) and backscattered electrons (BSE) emission (left and right sides, respectively).

2.1.2. Basic Parts of Scanning Electron Microscope

A schematic illustration of typical elements of the scanning electron microscope system is shown in Fig. 2.3. It includes the electron gun containing electron source and accelerating anode, set of electromagnetic lenses for electron beam focusing, specimen stage and certain detectors to collect the specific signals emitted from the studied material. Modern SEM instruments are usually equipped with variable condenser and objective lens aperture, which are metal strips with

a variety of pinhole sizes to choose from. This can be used depending on the specific needs to refine the beam, adjust resolution and depth of field, minimise charging.

All mentioned parts are placed in a vacuum to produce an acceptable mean-free path for electrons greater than the length of the electron column, avoid possible arcing between the filament (cathode) and the anode plate, avoid oxidation and damage of the filament, avoid collisions between the electron beam and stray particles, which may result in diffusion of electrons as well as in contamination of column elements from volatilisation events. For these proposes the electron column is always maintained at high vacuum. The vacuum of 10^{-5} Pa is usually required for electron column in SEM, while the pressure in the sample chamber may vary depending on the measurements needs and type of the material. The vacuum in sample chamber is necessary to prevent scattering of electrons and absorption of X-rays emitted from the sample to be collected

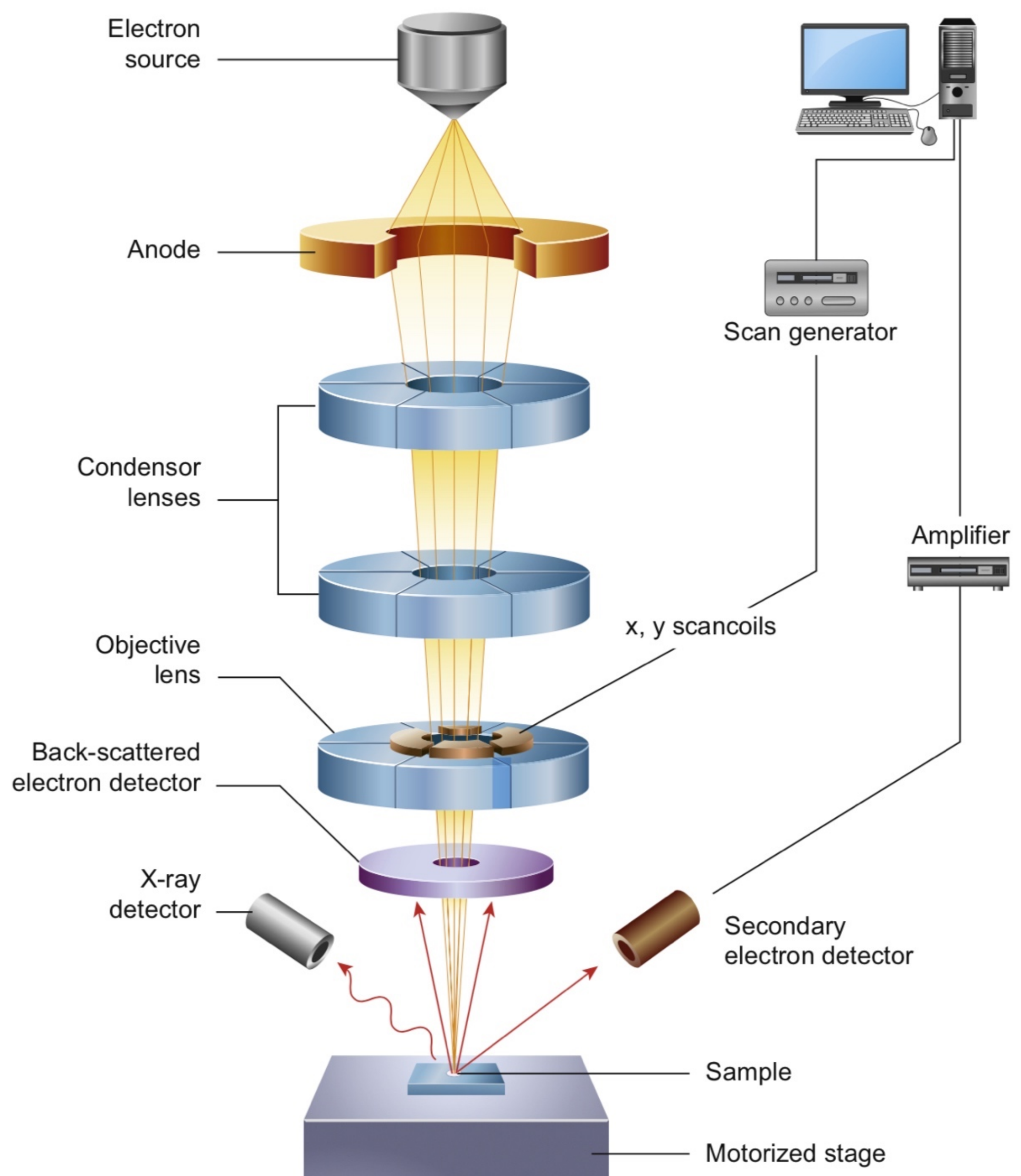

Fig. 2.3 - Schematic diagram of the core components of a scanning electron microscope (SEM). As taken from [235].

by analysers when exposed to the electron beam. The sample chamber is separated from the electron column by single or multiple limiting apertures and valves. In case of multiple apertures, it is possible to operate SEM while the column is at high vacuum, but the sample chamber is at low vacuum conditions or so-called wet mode (about 0-3000 Pa). The latter type of microscope is named environmental SEM (ESEM) for the ability to operate at near to the environmental conditions.

During the sample loading, the chamber is isolated from the electron column, and the pumping occurs after the sample is loaded and the chamber is closed. Modern SEM systems may have a special specimen-delivery system (load-lock sample exchange system) avoiding the direct sample placement from the outside and, thus, improving the vacuum quality in the chamber, decreasing vacuum pumping time after the sample is loaded and increasing the number of studied samples.

2.1.3. Electron Sources for Scanning Electron Microscopes

There are two main types of electron-emitting sources for electron microscopy: thermionic and field emission. The scheme of their comparison is shown in Fig. 2.4.

In thermionic sources, the filament (or crystal) is heated by the applied current to the temperature when the outer orbital electrons have enough energy to overcome the work function barrier and escape from the solid surface. The most common materials for thermionic sources are tungsten metal filament and lanthanum hexaboride (LaB_6) or cerium hexaboride (CeB_6) crystals. The latter two solid-state crystal sources have 10 times higher brightness and much longer lifetime than tungsten but require a higher vacuum. In turn, the tungsten filament is cheaper.

As the electrons in the thermionic source are emitted in all directions, it is necessary to focus them at one spot. Wehnelt cap (or cylinder) is used for this. Negatively biased of 200-300 V in respect to the filament, Wehnelt cylinder surrounds the source producing a repulsive electrostatic field that localises emitted electrons at the tip above the aperture of the cap. The anode is used to create a voltage difference with electron source (cathode) which serves to accelerate electrons.

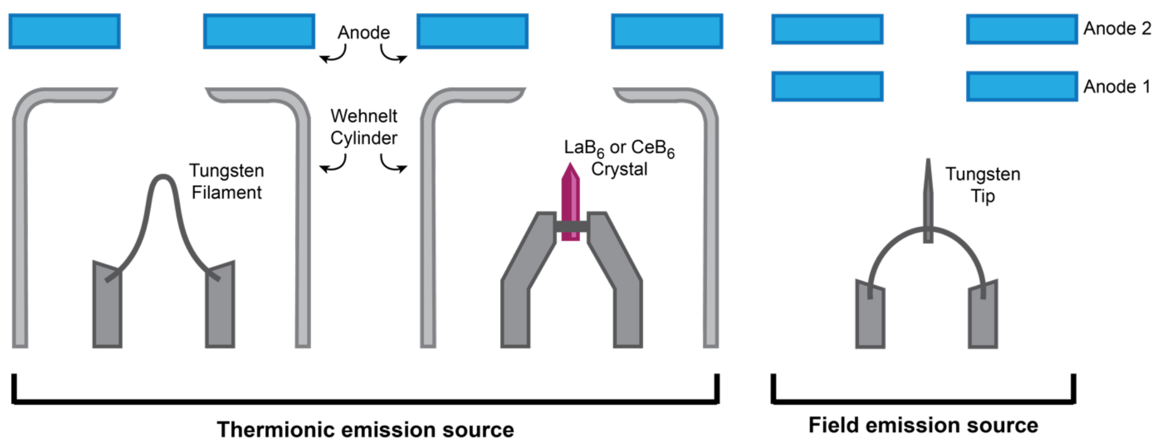

Fig. 2.4 - Illustrative comparison of thermionic and field emission types of electron emitting sources. As taken from [236].

In field emission sources (field emission guns or FEGs) a strong electrostatic field of 10^5-10^8 V/cm is used to cause electron emission. This field decreases the work function barrier of the cathode, necessary for escape of electrons. This phenomenon is called Schottky effect. When the field is high enough there is no barrier, and the electron emission process begins. This tunnelling effect doesn't require temperature activation and may occur even at room temperature but require ultra-high vacuum. Usually, the tungsten wire with a sharp tip used in field emission sources. First anode with applied extraction voltage of 3-5 kV serves to release electrons from the source. The second anode accelerates the electrons, while the accelerating voltage determines their speed and energy. Both anodes also act as electrostatic lenses, focusing the beam into a small initial crossover [237]. Because such electron sources don't require heating, they often may be called cold FEGs (CFEGs).

The third type of electron source is a hybrid of previous two, which is thermally assisted field emission source, also called Schottky field emission gun (Schottky FEG), or thermal-field (TF) source, or field-assisted thermionic emission, which combines the benefits of thermionic and field emission sources. The tungsten tip in a large electrical field is heated, mixing both thermionic and field emissions. This type of source requires lover vacuum than cold FEGs, bug higher than thermionic electron emission sources. Tungsten tip or filament is coated with zirconium oxide, which lowers the work function and facilitates the thermal emission of electrons when the source is heated. Usually Schottky sources have shorter lifetime than CFEGs and worse image quality under certain conditions, but generally they have better stability [236,238]. Three different types of electron emission sources are compared in Table 2.1.

Table 2.1. Comparison of thermionic emission, cold field emission and Schottky field emission sources (taken from [238]).

Characteristics	W (thermionic)	Cold FE	Schottky FE
Brightness, A/cm^2 sr	10^6	10^9	5×10^8
Energy spread, eV	2	0.25–0.5	0.35–1.0
Cathode temperature, K	2800	300	1800
Vacuum, Pa	10^{-3}	10^{-8}	10^{-7}
Current stability	1%/1h	5%/15min	0.4%/1h
Probe current	10 pA–2000 nA	1 pA–20 nA	1 pA–200 nA
Lifetime	100 h	>1 year	>1 year

2.1.4. Image Formation in Scanning electron Microscopes

SEM image formation process includes the collection of signals from secondary emitted or backscattered electrons specific type of detector in each moment of time while the focused primary electron beam is scanning the selected area of the specimen surface. Electron beam scanning is controlled by a scan generator (shown in Fig. 2.3) which gives corresponding command to the set of scan coils (deflection coils) placed before the objective lens (final lens) to deflect the electron beam in *x* and *y* scanning directions (see Fig. 2.5). Point by point, line by line,

this process occurs until the whole area of the specimen is covered by the beam. Signal from the detector is amplified and synchronised with the scan generator. In previous generations of SEM systems the signal was then transferred to the cathode ray tube (CRT) screen (such image formed by lines of scans is called a raster), while in modern systems the signal is just transmitted to the computer and in digital form analysed by specialised software and the corresponded image is shown on the screen.

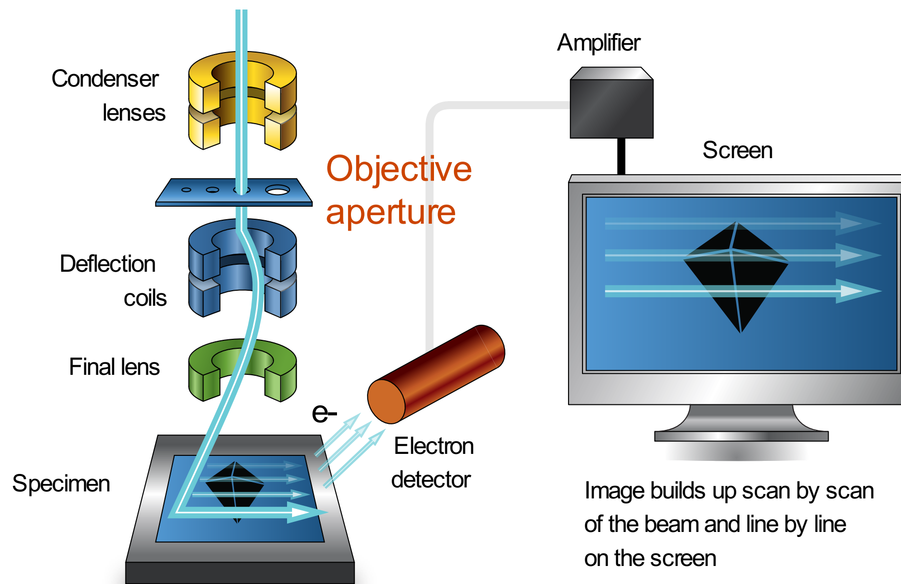

Fig. 2.5 - Principles of image formation in SEM. Adapted from [239].

2.1.5. Energy Distribution and Detection of Electrons in SEM

2.1.5.1. Secondary and Backscattered Electrons Energy Distribution

The most energetic particles produced by the primary electron beam interaction with the matter are backscattered electrons. They are a result of elastic interactions, and most of them have energies close to or slightly lower than the values for the primary electron beam (E_0) since they can be immediately deflected through the large angle after entering the sample and leave it with no energy losses. Other primary electrons undergo several scattering events while travelling through the specimen before they leave it, or till they lose all of their kinetic energy. In metals, they could become conduction electrons. The lowest limit of energy for electrons to be considered as backscattered is 50 eV [240]. The energy distribution spectra for electrons after the primary electron beam interaction with matter in SEM is shown in Fig. 2.6.

When the high-energy electron interacts with the specimen inelastically, it can eject the loosely-bound electron from the outer shell of an atom. If the excited electron moves towards the surface of the sample, and if after all possible collisions it has energy higher than the work function E_W needed to remove electrons from the surface of a material, it can escape. Majority of the secondary electrons have an average kinetic energy of 2-6 eV and the escape depth for them is very small: around 1 nm for metals and 10-20 nm for insulators, which have a lack of electrons to

cause collisions and inelastic scattering with secondary electrons on their way out from the sample.

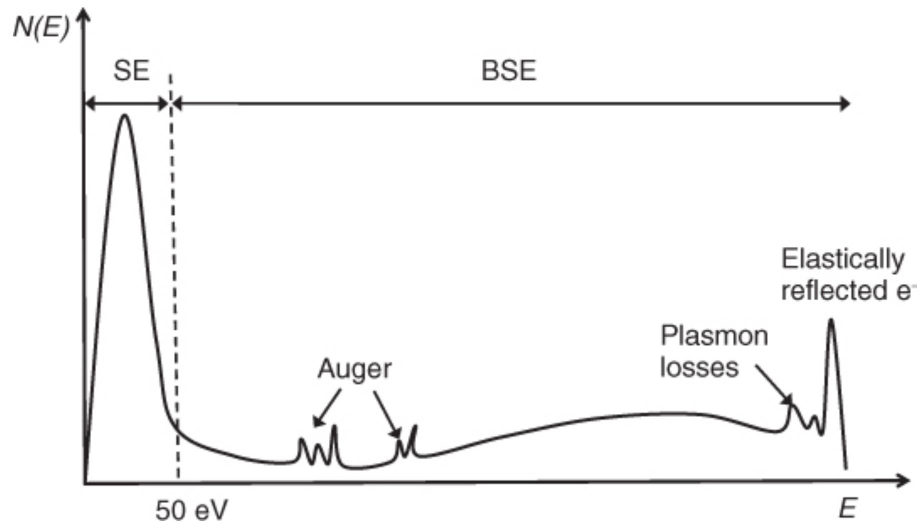

Fig. 2.6 - Energy spectrum N(E) (arbitrary units) of electron emission, showing secondary (SE), backscatter (BSE), Auger electrons regions. As taken from [241].

2.1.5.2. Everhart-Thornley Detector for Secondary and Backscattered Electrons

The most widely used detector of electrons in SEM is the Everhart-Thornley detector named after their designers Thomas E. Everhart and Richard F.M. Thornley proposed it in 1960. This detector is capable of detecting both secondary and backscattered electrons. The Everhart-Thornley detector is placed inside the chamber next to the specimen located on the holder directly below the final objective lens, as shown in Fig. 2.3, Fig. 2.5 and Fig. 2.7. It is a scintillator-photomultiplier system built in the form of a tube with its front end facing the specimen surface at an angle of around 30° [240].

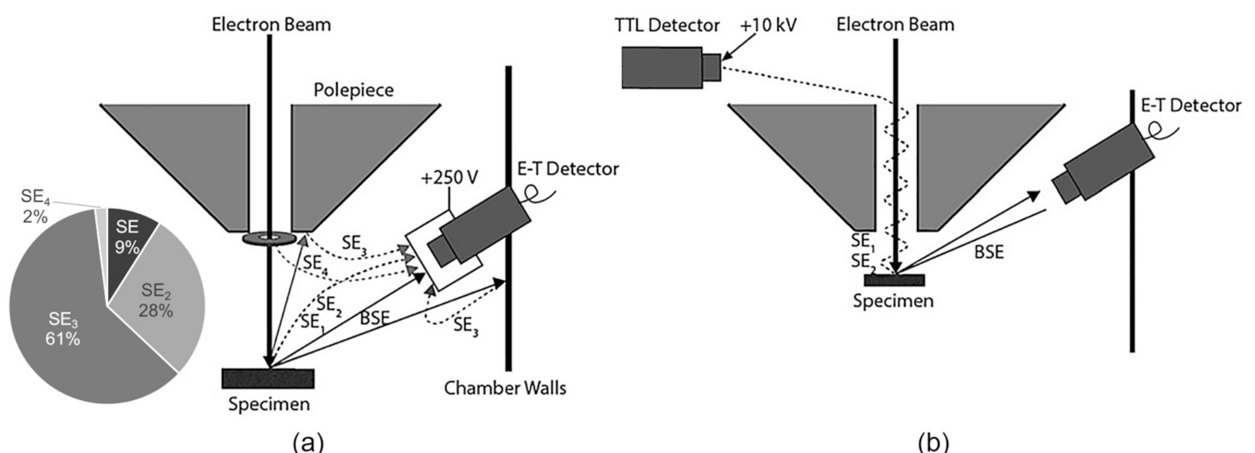

Fig. 2.7 - Generation of secondary electrons and the position of SE detectors.
Everhart-Thornley detector only (a) and in combination with through-the-lens (TTL) detector (b).
The figure is based on the images taken from [242].

The Everhart-Thornley detector is shown schematically in Fig. 2.8. A Faraday cage made of copper mesh which covers the face of the detector may have the bias voltage varied from −100 to +300 V. Positive bias is used to attract the majority of low-energy secondary electrons including

those having initial directions away from the detector. It is possible to tilt a sample toward the detector if needed to increase the rate of the collected secondary electrons. The negative bias of −50 to −100 V applied to the Faraday cage will reject all secondary electrons, and only line-of-sight backscattered electrons will be collected. The electrons collected by Faraday case strike the scintillator made of a doped light-emitting plastic, Eu-doped crystalline CaF_2 or other phosphorescent materials. As the energy of such electrons is not significant to have effective output from the scintillator, its surface is coated by a thin metal film where the positive bias of 10-12 kV is applied to accelerate secondary electrons on their way to the scintillator. Photons emitted from the scintillator by accelerated secondary electrons then pass through the light guide and quartz window isolating the vacuum chamber of SEM with the specimen from the parts outside.

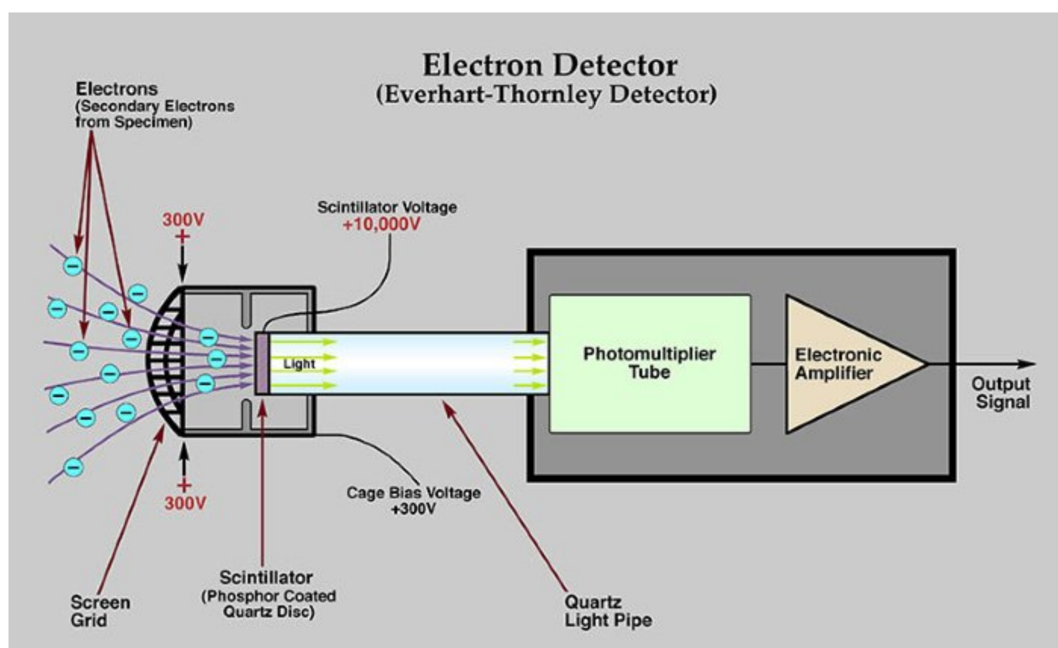

Fig. 2.8 - Scheme of Everhart-Thornley detector for secondary and backscattered electrons. As taken from [243].

The photons hit the thin layer of photocathode placed at the front of the photomultiplier tube outside of the specimen chamber. The photocathode converts the light back into the electrons, which then travel through the set of dynode electrodes. Each dynode accelerates incoming electrons and emits from 2 to 10 secondary electrons for every electron that collides with the electrode surface. Therefore, this dynode system serves as an electron multiplier: up to 10^6-10^8 gain in signal is achieved without an appreciable increase in noise [242]. The electric signal then is further amplified by a preamplifier, the last part of the Everhart-Thornley detector. After the detector, the signal passes an amplifier for further strengthening and then goes to the video and image processing device for the conversion from analogue to the digital type suitable for computer operations.

As the Everhart-Thornley detector is placed on the side of the specimen, the surface features of the specimen will result in highlighting or shadowing of corresponding zones. This creates an image contrast easy for interpreting. In a couple with edge effect for secondary

electrons SEM images in SE mode taken with Everhart-Thornley detector give detailed information about surface topography of the sample.

2.1.5.3. Origin of Secondary Electrons Detected in SEM

It should be noted that secondary electrons in SEM chamber have different nature of their origin and may be classified into 4 groups (see Fig. 2.7, left). The first group (SE_1) is a direct product of primary electron beam interaction with the specimen in SEM chamber, emitted from the top surface of several nanometres depth from the area exposed to the electron beam. The other three groups (SE_2, SE_3, SE_4) are the products of backscattered electrons interaction. SE_2 are emitted from the specimen by backscattered electrons within the sample, in contrast to SE_1 produced by the primary beam. SE_3 and SE_4 are produced not from the specimen but from SEM chamber walls or objective pole piece (SE_3) and final aperture (SE_4) after the hitting by backscattered electrons coming from the specimen.

As one may see from the pie chart (estimated for Au specimen) in Fig. 2.7, the main fraction of secondary electrons collected by Everhart-Thornley detector is actually not emitted directly from the specimen after the interaction with the primary beam (SE_1) but secondary electrons produced by BSE upon striking the chamber walls or pole piece (SE_3) [242]. In this way, SE signal collected by the Everhart-Thornley detector has a significant contribution from indirect secondary electrons (SE_2, SE_3, SE_4) and, thus, increases backscattered electrons component. Therefore, they degrade the resolution of the resulted SE-formed SEM-image.

It comes from larger interaction volume for BSE than for SE1, atomic number effect on BSE yield (for specimen areas with material with a larger atomic number the higher degree of elastic scattering results in higher BSE yield and higher emission of indirect SE), inhomogeneous density, porosities or cavities in the material. In other words, in case of the image of particles with different elemental composition the increase of SE signal may not be due to the higher SE1 generation at a few nanometres of surface close to the probe (where the key information for SE mode of SEM-images about the specimen topography is collected) but by indirect secondary electrons generated by backscattered electrons with higher yield in areas with larger atomic number.

2.1.5.4. Through-the-Lens (TTL) Detector

A placement of secondary electrons detector inside SEM column above the objective lens as shown in Fig. 2.7 (right) avoids a registration of low-resolution signal of indirect SE_3 (the main component of secondary electrons detected in the specimen chamber as seen from Fig. 2.7, left), SE_4 and low-energy and line-of-sight BSE. This detector is actually the Everhart-Thornley detector but called a through-the-lens (TTL) detector due to its location in SEM column. TTL detectors may be installed in field emission microscopes equipped with an immersion or snorkel objective lens, where the strong magnetic field of the lens extends to the surface of the sample placed on the

short working distance. In this configuration, secondary electrons SE_1 and SE_2, going towards the objective lens (the maximum intensity of secondary electrons is in direction normal to the specimen surface), are trapped by the magnetic field and then move by spiral up through the lens due to the axial velocity component and Lorentz force generated by the magnetic field and applied to the electrons. After the objective lens is passed, these secondary electrons are collected by the Everhart-Thornley detector placed within the SEM column.

SE_2 component dependent on BSE yield is still present in the collected signal and degrade the secondary electrons image resolution by addition BSE contrast. However, SE signal is effectively separated from SE_3, SE_4 and BSE component, which makes TTL-registered signal clear of noise and rich in contrast in comparison to the signal collected inside the specimen chamber by Everhart-Thornley detector. The reduction of BSE direct and indirect components makes TTL detector especially useful for imaging of pits, cavities or voids.

TTL detector assumes short working distances which applies some limitation to the sample and dimensions of studied areas. However, both Everhart-Thornley and through-the-lens detectors may be used simultaneously to maximise a benefit.

As was mentioned in the description of Everhart-Thornley detector (Chapter 2.1.5.2 and Fig. 2.8), a positive bias of 10-12 kV is applied to the coated by a thin metal film surface of the scintillator to accelerate secondary electron. This potential may misalign the primary electron beam of low energy used in SEM at high magnification and resolution. This effect may be compensated by the Wien filter placed directly above the objective lens. Its magnetic field neutralises the perpendicular electric field from the TTL detector, thus keeping the electron beam exactly on the optic axis [242].

2.1.5.5. Detection of Backscattered Electrons

Backscattered electrons emitted from the specimen have significantly higher energy than any of the secondary electrons present in the SEM chamber (see Fig. 2.6). Therefore, it is quite easy to separate these two types of electrons by applying a small negative bias of up to −100 eV to the Faraday cage of the Everhart-Thornley detector and collect only backscattered electrons. However, in standard configuration, when the Everhart-Thornley detector is placed on the side of the beam and the specimen, it is not possible to achieve a maximum of BSE collection efficiency, since the maximum probability of BSE emission is in the direction along the primary electron beam and is normal to the surface of the specimen.

Thus, a separate BSE detector located as close to the electron beam as possible is needed. It could be possible with a retractable Everhart-Thornley detector that can be moved closer to and above the specimen surface and, in this way, increasing the number of collected backscattered electrons. However, it is more common to use a BSE detector fixed directly below the pole piece and above the specimen for maximum efficiency [242].

2.1.5.5.1. Solid-State BSE Detector

The solid-state BSE detector (SS-BSD) is the most common solution for BSE-signal collection available on the market. The structure of the solid-state backscattered electrons detector is shown in Fig. 2.9. It is a diode consisting of a p-n junction connected to the two semiconducting electrodes (Si/Ge doped with boron/gallium and arsenic/phosphorus/antimony for p- and n-types respectively) [242].

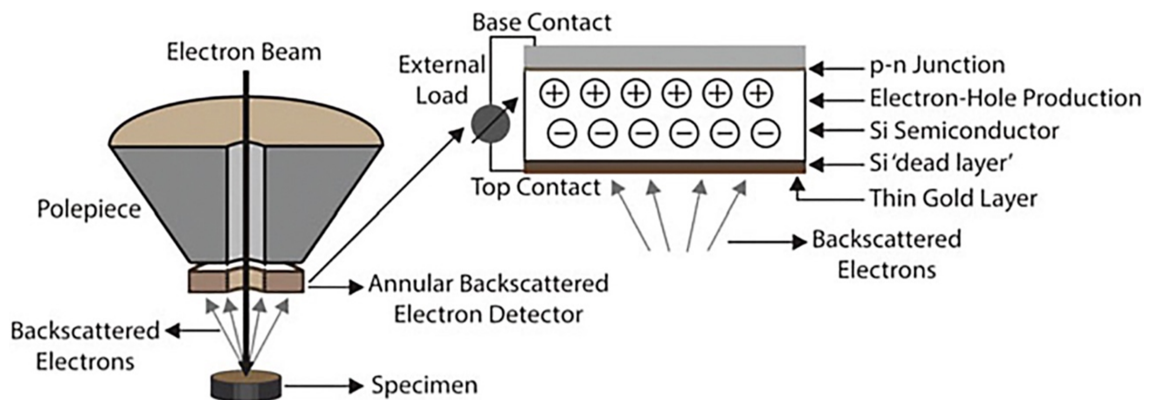

Fig. 2.9 - Scheme of solid-state backscattered electrons (SS-BSE) detector and its location in SEM. As taken from [242].

When a high-energy BSE strikes the detector, it interacts with the electrons of Si layer and scatters inelastically ejecting electrons from the valence into the conduction band of Si leaving behind a hole. As a result, an electron-hole pair is created. Both surfaces of the detector are coated with a thin layer of gold to apply the bias voltage. If a potential is applied, the electrons that jumped into the conduction band and the produced holes are separated and collected. In that manner, the current can be measured.

The energy required to create electron-hole pair in Si is about 3.6 eV. Therefore, the number of electron-hole pairs generated by BSE can be easily calculated. The current measured by SS-BSD is proportional to the number of backscattered electrons hitting the detector. In this way, the contrast observed in the backscattered image is formed. Areas of the specimen with higher average atomic number produce more backscattered electrons and, thus, appear brighter in the image.

The outer thin layer of Au absorbs low-energy secondary electrons, and they are not detected as well as X-rays produced from the specimen don't affect the performance of SS-BSD [242]. By the same reason, the low-energy backscattered electrons can't be detected, which lowers the sensitivity of the solid-state detector and makes it not suitable for low voltage SEM operations.

Solid-state detector can be designed in two or more segments when their signals are collected separately for further addition or subtraction, which may bring more compositional or topographical information on the resulted images, respectively.

2.1.5.5.2. Scintillator BSE Detector

A scintillator type of BSE detector is also available. It works on the same principle as the Everhart-Thornley detector and has a scintillator, light guide and photomultiplier. It can be mounted below the objective lens with a hole for the electron beam passing or can be designed as a retractable detector.

The scintillator BSE detector has a large size in comparison to the thin SS-BSD plate, which may limit imaging of the specimens at short working distances. But such design allows to maximise the BSE efficiency and, thus, to have faster response time and rapid scan rates. It is also possible to detect low-energy backscattered electrons, which means that the scintillator detector is more sensitive than the SS-BSD.

2.1.5.5.3. Channel Plate Detector

Another type of detector is a channel plate detector composed of a large number of parallel electron multiplier tubes of a few millimetres in length and 2-100 micrometres in diameter. The schematic design of the channel plate detector is shown in Fig. 2.10.

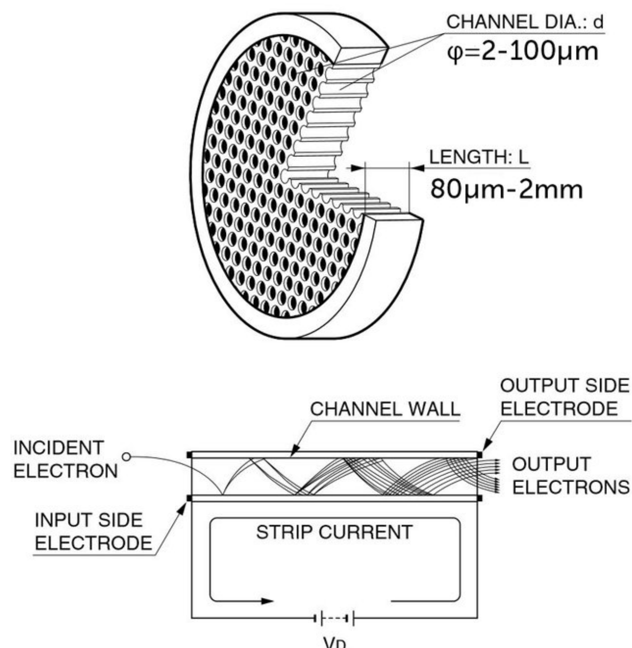

Fig. 2.10 - Design of multi-channel plate detector. As taken from [244].

High voltage is applied to the ends of capillaries to accelerate electrons. This thin detector is placed between the sample and the objective lens. The high-energy electrons emitted from the specimen enter the end of the microscale tube and hit the walls that emit secondary electrons which are further accelerated and excite new electrons by new collisions with the walls. This acts as a multiplier and produces a cascade of secondary electrons at the end. This detector is able to catch the signal from both SE and BSE [242] and can be employed for low-energy electrons produced in low-voltage and low-current SEM operations.

2.1.6. Samples Preparation for SEM

2.1.6.1. Sample Preparation for Topographical Study of the Surface

The methods of sample preparation for SEM are varying through the diversity of possible materials: metals, ceramics, minerals, semiconductors, powders, polymers, biological materials, liquids and others. As hard metal nitride coatings are studied in this PhD Thesis, only the methods of sample preparation for SEM suitable for such materials (metals, ceramics, metal nitrides, hard coatings) will be observed in this Chapter.

When the preparation of the specimen for SEM is considered, the requirements come both from the specimen and SEM parameters. The first step is to make sure that the sample fits in the sample stage and chamber. Usually, the sample could be up to 50×50 mm^2 in dimensions, but for high-end microscopes designed for ultra-high resolution and magnification the working distance may be small or the specimen is even must be placed within the bore of the lens (e.g. for immersion lenses) which restricts the size of the sample to a few nanometres.

In case of hard coatings, this may require the careful cutting of the sample using techniques that don't contaminate or damage it. The sample may be cleaned in acetone or other appropriate solvent using an ultrasonic bath. A final wash can be performed by ethanol or isopropanol to remove the contaminated acetone and any remaining contaminations. The attention should be paid to the fact that the chosen solvent should not damage or modify the surface (or deposited films and substrates in case of coatings). If there are any doubts regarding the material interaction with the cleaning solvent or if the surface contains fine particles that can be easily removed, the best solution will be just to bring the sample for SEM analysis without any initial sample preparation. Also, before the specimen is placed in the SEM chamber, it should be cleaned by high-pressure inert gas flow or air blower to remove microparticles of dust which may appear on the surface of the sample.

For the mounting of the sample onto the sample stub, the conductive paint or carbon tape is used usually. If a nonconductive paint or resin is used to hold the sample, a stripe of the conductive paint or tape should be applied to the sample to create a conductive path to the ground through the sample stub. It is necessary to ensure the drain of the incoming electrons from the beam and to avoid the charging effect. If the sample contains a nonconductive fraction as some ceramics or metal-ceramic composites, a thin layer of the conductive film should be deposited. It is relatively easy to apply the coatings but almost not possible to remove them if they interfere with the imaging or microanalysis in SEM. Therefore, it is better to perform image acquisitions without the coatings first [245].

Another approach to avoid the charging effect is to lower the vacuum level in the chamber, which introduces positively-charged molecules there. At the near to the sample surface are they interact with accumulated electrons and neutralise them. In this way, the charging effect is

removed. It works for nonconductive samples without conductive coating at pressures starting in the range 10-50 Pa [245]. However, such air molecules in the vacuum chamber, depending on the other parameters, such electron beam accelerating voltage and type of the objective lens, may reduce the quality of the obtained image due to the interaction with the primary electrons.

The considered methods are good for the morphological and topographical study of the sample surface mostly in SE mode of SEM-imaging, where all shapes of the as-deposited surface are under analysis.

2.1.6.2. Preparation of the Sample for Microstructural Study in SEM

For the microstructural study, both SE and BSE modes and their combination may be used. In addition to the microstructural analysis, which may be performed on the surface of the coating, of great interest is the study of cross-sectional samples. Generally, such samples can be prepared by the three main approaches.

The easiest way is just to break (to fracture) the sample by bending, which works well for thin or brittle substrates. For thick metal substrates, the initial sawing from the bottom side may be needed. For brittle silicon wafer substrates, which are widely used for deposition of films and coatings for further microstructural analysis, the cleavage of the sample is possible by diamond scriber or another sharp and hard tool. In this manner, the study of microstructure on the cross-sectional fracture surface occurs.

Another approach assumes the preparation of cross-section by cutting the sample with some sort of saw, abrasive cutting, shearing or another method. A slow-speed diamond wheel cut-off saw is suggested to avoid damage of the sample during the sawing operation by overheating, deformation, delamination or chipping.

For further steps, depending on the size, it may be needed to embed the sample in a mounting material. There are many materials available on the market for cold or hot mounting, such as epoxy, phenolic, Bakelite or melamine. They could be conductive or not. Conductive materials are much more expensive. The mounted sample should have the height which fits the SEM sample height limit.

The surface of the mounted sample is polished using abrasive materials in a sequence of decreased grit. The first step is a coarse grinding with an abrasive of 60-180 grit to remove damages of the cutting process. Then abrasive papers with increased grit number (smaller abrasive particles) are used to finish the grinding with 600-grit. These steps should be performed in wet conditions (better with continuous water flow) to prevent the heating and to clean the particles removed from the sample. The further polishing must be performed on polishing cloths with diamond suspensions of 30-0.05 μm grains. The final polishing may be done with alumina or silica suspension or with electropolishing. The final result of the careful grinding and polishing will be a flat, scratch-free surface with high reflectivity, as a mirror [245].

The third approach is the preparation of the precise cross-section with the focused ion beam (FIB). It allows cross-section sample dimensions from 100-200 μm to 1 μm or less in width and 10-30 μm in depth with the location accuracy of better than 20 nm [245]. This method doesn't require any additional polishing of the sample, and the analysis usually may be performed immediately after the cutting at the same vacuum chamber of the dual-beam FIB system with electron and ion beam columns.

2.1.7. Experimental Details

The morphology of the surface and the cross-section observations were performed by scanning electron microscopy (SEM), using JEOL JSM-7001F Schottky Emission Scanning Electron Microscope, Quanta 200 3D microscope and FEI Quanta 400 FEG Environmental SEM (ESEM). Cross-section samples were prepared by cutting of coatings and substrates with further hot mounting into conductive epoxy resin and, finally, by grinding and polishing.

2.2. X-Ray Spectroscopy Techniques for Microanalysis in SEM

As seen from Fig. 2.1, there are more products of the electron beam interaction with the matter than just secondary and backscattered electrons used in SEM for topographical and microstructural analyses (see Chapter 2.1 about SEM).

One of these products are X-rays emitted from the atom of the material when the incident electron ejects an electron from one of the internal orbitals and the electron from the higher energy level orbital takes its place with the release of the energy in the form of an X-ray photon. The energy of electron transition between those two levels is a unique value specific for each material. This is discussed in more details in Chapter 2.3.2 and is shown in Fig. 2.23.

Due to the dual wave-particle nature of X-rays, they are characterised both by the energy (E) and the wavelength (λ), which are inversely proportional ($E(keV) = 12.4/\lambda(Å)$). Therefore, by collecting the signal of characteristic X-rays in conjunction with their energy or wavelength, the information about the elemental composition of the specimen may be obtained. It should be noted that considered X-ray spectroscopy techniques may be employed not only with SEM but with transmission electron microscopy for nanoscale analysis basing on similar principles.

2.2.1. Energy-Dispersive X-ray Spectroscopy

Energy-dispersive X-ray Spectroscopy (EDS, EDX, EDXS or XEDS) technique is based on the collection of X-ray photons emitted from the specimen during electron beam bombardment and measuring its energy and intensity distribution. Then the received data is analysed to identify elements and elemental concentration from the peaks on the obtained spectrum. EDS-detector is incorporated in the SEM column. This enables the microchemical analysis on the determined region of the specimen and its direct fitting to the topographical or microstructural SEM-image.

There are two main types of X-ray detectors for EDS analysis: lithium-drifted silicon Si(Li) solid-state detector and, later, solid-state silicon drift detector (SDD).

2.2.1.1. Lithium-Drifted Silicon Si(Li) Solid-State Detector

Lithium-drifted silicon Si(Li) solid-state detector is the most used EDS detector in the past but is still very common in the labs, proposed by Fitzgerald in1968 [246]. EDS-detector must collect only X-rays which come directly from the specimen. For this reason, the detector needs to be placed as close as possible to the sample to get a maximum of the efficiency. Additionally, a collimator tube is installed at the entrance of the detector. The typical working distance is 20 mm from the specimen. Usually, the EDS detector has a retractable mechanism which allows to approach it to the sample only when EDS measurements are needed. The most common configuration of the EDS detector in SEM is shown schematically in Fig. 2.11. The main feature of the Si(Li) detector distinguishing it from other types just by the external appearance is the container with liquid nitrogen (Dewar) needed for Si(Li) crystal cooling.

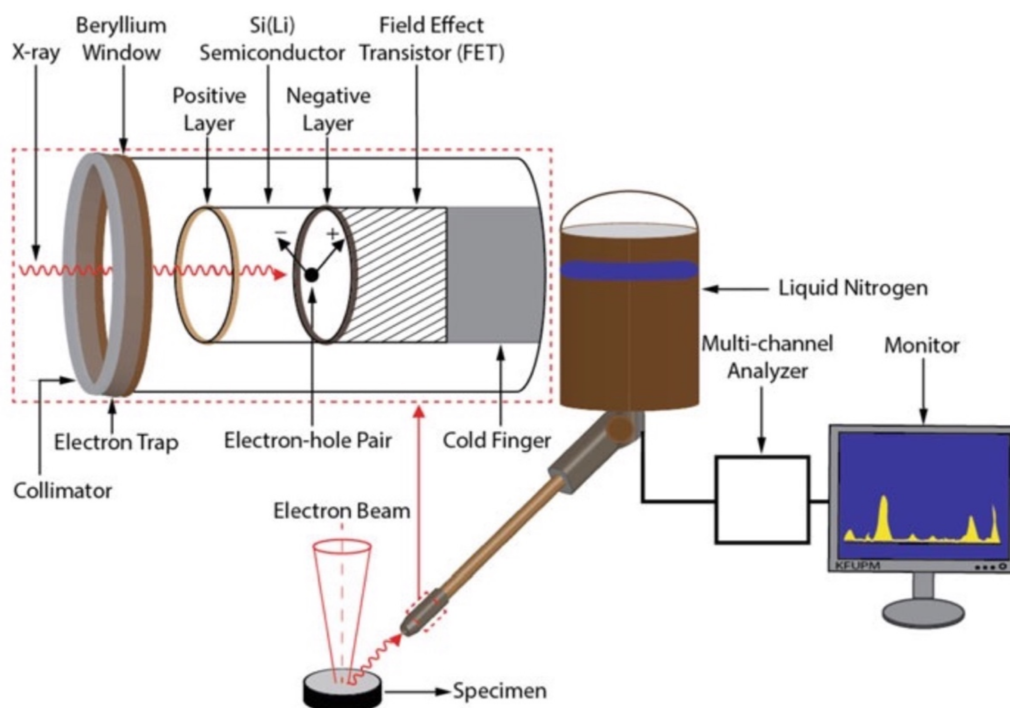

Fig. 2.11 - Scheme of typical lithium-drifted silicon detector for EDS. As taken from [247].

Pure silicon crystal has all valence bands filled by electrons, and all conduction bands are empty. Thus, there are no excess electrons available for charge transport as well as no holes in the valence band. Such material is called an intrinsic semiconductor. It will not conduct current in the applied field unless electrons are introduced to the conduction band with holes left behind by the absorbed external energy. For this reason, intrinsic semiconductors serve very well for radiation detectors [248].

However, it is very hard to obtain sufficiently pure silicon to achieve a good intrinsic semiconductor in practice. To compensate some small level of impurities and reduce defects in the Si lattice, lithium is added into the crystal. Lithium (n-type dopant) is applied to the surface of

p-type silicon and diffuses into the crystal forming the p-n junction. The boundary of such p-n junction is the intrinsic semiconductor with the thickness of a few micrometres. If the reverse bias electric field is applied, the intrinsic region may be extended to a few millimetres, which is adequate for a detector material after the rest of the p-type material is removed. The disadvantage is that at room temperatures when the field is applied, the Li ions are mobile and pulled toward the biased electrode. That is why it is allowed to operate such type of detectors only at near the liquid nitrogen temperatures [248].

A pair of permanent magnets is placed after the collimator. They deflect any incoming electrons and protect in this way the resulted X-ray spectrum from possible background artefacts. The lithium-drifted silicon crystal is mounted on a cold finger connected to liquid nitrogen stored in the dewar. Since the detecting crystal is light-sensitive, it is necessary to filter any possible incoming radiation. Moreover, the detector chamber is usually needed to be sealed under vacuum to avoid contamination from the specimen and to help with keeping a stable low temperature of the detecting crystal. For all three tasks, a beryllium window was the best candidate for many years due to its high mechanical strength. However, it was necessary to use a quite thick window of around 8 μm, which absorbs low-energy electrons (less than 1 keV) and doesn't allow to detect light elements such as carbon, nitrogen, oxygen, boron, etc. Later, many of ultrathin solutions were developed to enable light elements detection: organic film Formvar coated with gold, or polymer covered with a thin layer of evaporated Al and supported with Si grid at the detector side to withstand the pressure of more than 100 Pa in the SEM chamber. The latter solution is a standard nowadays and can transmit low-energy X-rays (≈100 eV) which is a proffered choice for light elements analysis [247]. Modern EDS analysers detect elements from beryllium to uranium. However, H, He and Li are not detected due to the lack of electrons to produce characteristic X-rays.

Work principles of Si(Li) detector and p-n junction are shown in Fig. 2.12. X-rays emanating from the specimen pass through the protective window and are captured by the photoelectric absorption in Si single crystal and the X-ray photon is annihilated in the process. The incident X-ray photon with an energy hν is first absorbed by a silicon atom and an inner shell electron with an energy $h\nu - E_c$ (E_c = 1.84 keV for silicon) is ejected. This photoelectron then scatters inelastically while travels towards the detector and knocks electrons from the valence band into the conduction band (CB), leaving holes behind in the intrinsic semiconductor. The mean energy required for the generation of one electron-hole pair for a Si crystal is 3.86 eV. The photoelectron will produce such electron-hole pairs until all its energy is dissipated. The silicon atom left in an excited state after the X-ray photon annihilation also releases energy in the form of an Auger electron or a silicon X-ray when the electron from a less tightly bound state fills the vacancy. The Auger electron then scatters inelastically and also creates electron-hole pairs. The silicon X-ray may be reabsorbed to initiate the process again, or it can be scattered inelastically

[248]. Therefore, all energy of the original photon is deposited in the detector, unless some dose of generated radiation during the scattering process (K_α silicon X-ray) escapes the detector resulting in the artefact known as the escape peak.

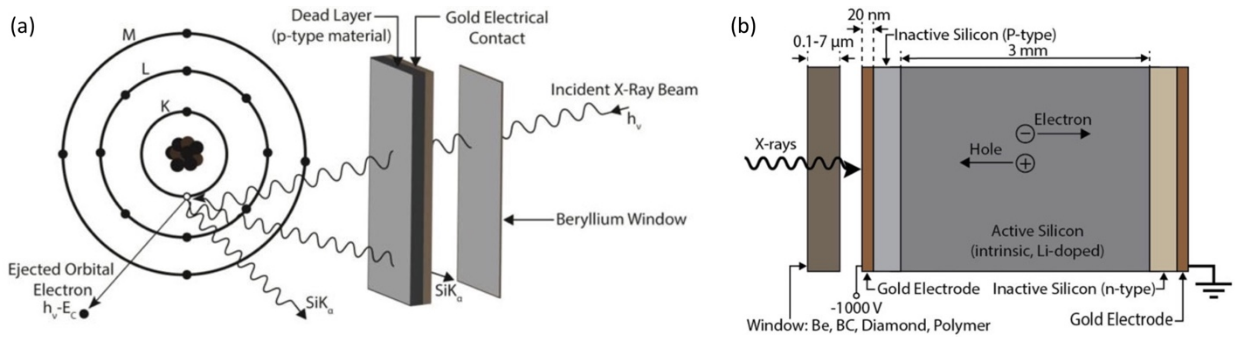

Fig. 2.12 - Working principles of Si(Li) detector. As taken from [247].

Under the bias applied to the faces of the detecting crystal, the holes and electrons produced by the incoming X-ray are separated and collected on the electrodes. The charge and number of pulses can be counted, and the X-ray photon energy can be calculated by multiplying by 3.86. The result is the energy of the characteristic X-ray, and the element can be identified. The charge received from the X-ray photon is extremely small, and the noise minimisation, as well as the further amplification and processing, are needed.

The Si(Li) crystal is connected to a FET at the rear end (Fig. 2.11), which acts as the preamplifier to increase the signal strength, signal-to-noise ratio and to convert the charge pulse into the voltage steps [247]. The process of the charge-to-voltage conversion is shown in Fig. 2.13. The size of a voltage step is proportional to the energy of the incident X-ray. Then in modern EDS systems the voltage signal goes to a high-speed pulse-stream digitizer, and once the signal is in a digital form, it is passed to the computer where a variety of pulse processing techniques is employed for the noise reduction, increasing the count rate performance and for the data conversion in the form convenient for the further analysis and interpretation [248].

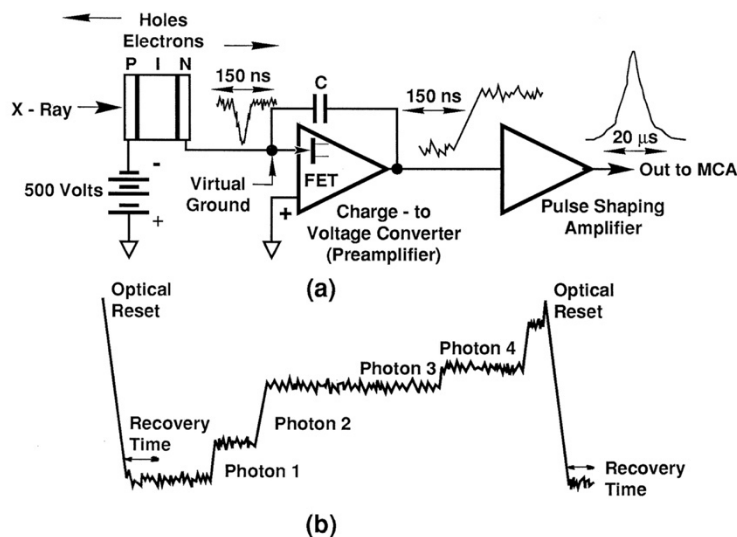

Fig. 2.13 - Charge-to-voltage conversion process. (a) Representation of the detector charge- to-voltage converter and pulse-shaping amplifier from an electronics perspective. (b) Output of the charge-to-voltage converter after the detection of a series of x-ray photons. As taken from [248].

2.2.1.2. Silicon Drift Detector

Most of the modern EDS systems nowadays use the silicon drift detector (SDD), which was first manufactured in the 1980s for radiation physics. The development of advanced fabrication methods led to a liquid nitrogen-free EDS SDD to replace the Si(Li) detector with better performance and productivity in SEM. The structure of SDD used in SEM is shown schematically in Fig. 2.14. This device is based on concentric rings and is composed of a volume of fully depleted high-resistive silicon, in which a strong electric transversal field (parallel to the surface) drives the electrons generated by X-rays towards a small collection anode. This transversal field is caused by a set of increasingly reverse-biased ring electrodes. The collection electrode together with the integrated field effect transistor converts the current into a voltage [249]. While only one surface is structured and functionalised to transport and collect the charge, the opposite side is made of unstructured shallow implanted junction and serves as the radiation entrance window with homogeneous sensitivity over the entire detector area [238,249,250]

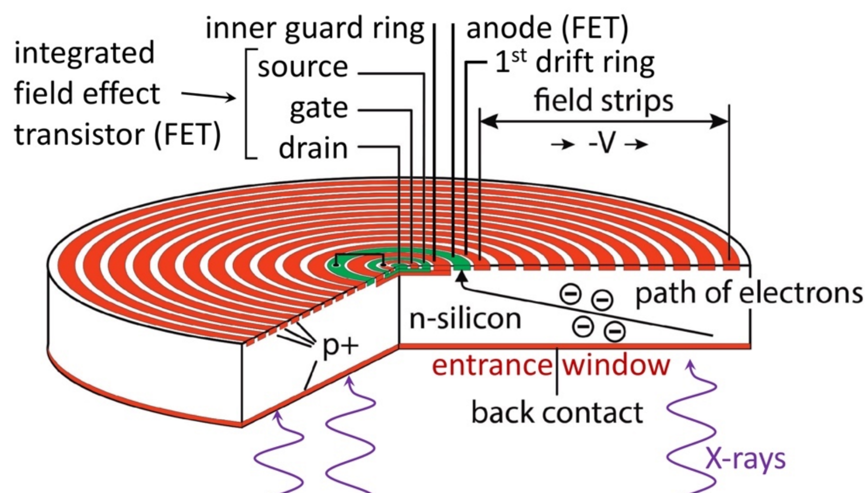

Fig. 2.14 - Schematic operation of a silicon drift detector with integrated FET preamplifier. Based on the figure taken from [251].

2.2.2. Wavelength-Dispersive X-Ray Spectroscopy (WDS)

Until 1968, when the energy-dispersive spectrometers were first introduced to SEM, the wavelength-dispersive spectrometer was used almost exclusively for X-ray spectral characterisation and is still the principal mode of X-ray measurements for the electron probe microanalyser [248]. Later, the fitting of WDS spectrometers to SEMs allowed much more precise positioning of the specimen to the electron beam and, thus, better selection of the area to study or performing elemental composition mapping.

The main advantage of the WDS is the significantly higher energy resolution (2-20 eV for WDS in comparison to 70-130 eV of EDS, depending on the element [238]) and much higher count rate with no loss in the energy resolution. The comparison of EDS and WDS spectra is shown in Fig. 2.15. Usually, the process of WDS spectra acquiring is longer than for EDS, since a full spectrum is taking sequentially for all range of wavelengths. WDS can work with higher

count rates than EDS allows to detect elements with much lower concentration. Both X-ray data may be acquired by EDS and WDS techniques simultaneously.

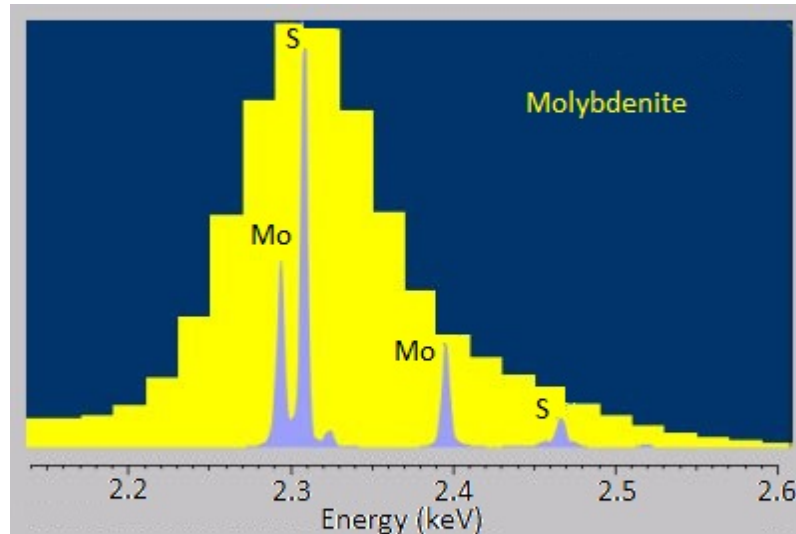

Fig. 2.15 - Comparison of EDS and WDS resolution: overlapped X-ray peaks in EDS are well separated in WDS scan. As taken from [252].

2.2.2.1. Working Principles of WDS

The working principle of WDS is based or X-ray diffraction condition defined by Bragg's Law (nλ= 2dsinθ, where n is an integer showing the order of the reflection, λ is the X-ray wavelength, d is the interplanar distance, θ is the angle between the incident X-ray and diffraction plane). This is well described in Chapter 2.3.2 of this work.

Electron beam usually accelerated by a voltage of 10-30 kV strikes the specimen material and characteristic X-rays, also used in EDS analysis, are produced from the specimen. Some part of the emitted X-rays moves towards the WDS system and goes to the diffraction crystal with a well-defined d-spacing. Only the X-rays with the exact and specific wavelength (thus, selected energy line of interest) will be diffracted and directed to the detector which is precisely adjusted at the symmetrical position relatively to the "incident bean - diffraction plane" configuration.

For all conventional WDS systems developed for SEM since the 1970s, it was necessary to keep all three main components, the sample (X-ray source), the diffraction crystal, and the detector, on the same circle in order to satisfy Bragg's Law in the focussing configuration. This circle is known as the Rowland circle. The schemes of the main circle-based WDS geometries are shown in Fig. 2.16 (a-c). The yellow area represents all X-rays emitted from the sample by the interaction of the electron beam with the sample. The blue area represents the subset of X-rays that will collide with the diffractor. The red area represents the X-rays that are reflected by the diffractor. X-rays emitted by the specimen in SEM originate from a very small interaction volume (can be considered as a point-type source) and diverge from the origin equally in all directions. Since the flat diffractor (shown in Fig. 2.16 (d)) doesn't focus the X-rays onto the detector, the X-ray count is going to be very low. This makes Rowland circle-based design with the flat diffraction crystal very unpractical and moves towards the design with curved crystals.

There are two main types of bent crystals: Johann (Fig. 2.16 (c)) and Johansson (Fig. 2.16 (a, b)) diffractors. They both have layers of diffracting crystals curved to twice the radius of the Rowland circle. The difference between them is that only the Johansson diffraction crystal has the surface finished to the radius of the Rowland circle. Therefore, it ensures its fully focusing geometry and that all X-rays diffracted from all area of the crystal are focused onto the detector. Both crystals move along the Rowland circle simultaneously, keeping the angle θ to the incident X-rays and the X-ray detector moves through the angle 2θ. Nowadays, all these positioning operations are performed routinely, reliably and easily with computer automation.

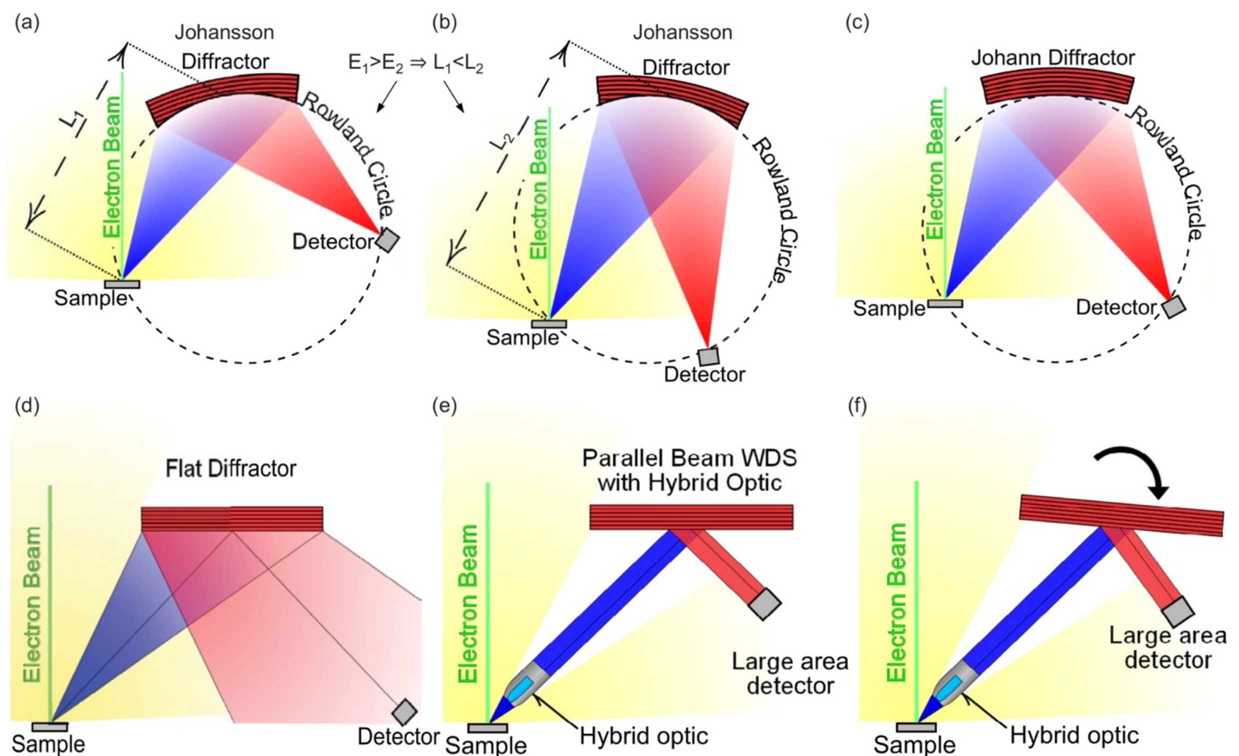

Fig. 2.16 - Diagrams of various WDS diffraction geometries. As taken from [253].

The limited space within the spectrometer causes a limited range of Bragg angles to use. The typically available θ angle range in WDS systems is around 70°. Thus, the maximum X-ray wavelength being diffracted is less than a double of interplanar distance in the analysing crystal [247]. To cover the full range of elements to be detected and to keep a high angular (thus, wavelength and energy) resolution a set (usually a pair) of diffracting crystals is used. The most commonly used crystals for shorter wavelength (higher energy) from heavy elements are ionic solid lithium fluoride (LiF) and organic crystals pentaerythritol (PET) and thallium acid phthalate (TAP). For lighter elements with lower energy and longer wavelength, the diffractor with larger d-spacing is needed. This type of pseudo crystals is generally named as layered synthetic microstructure (LSM). They are available in a range of different d-spacings, such as 6, 8 or 20 nm, and optimised for different elements [238]. The pseudo crystals are usually produced by deposition of alternating layers of crystal lattices with lighter and heavier elements to maximise

scattering efficiency and to obtain desired d-spacing [247,254]. However, such layered diffractors for light elements are particularly difficult to produce with the Johansson geometry [253]. As a result, typical commercial WDS systems with the Rowland circle usually have layered diffractors (LSM) with Johann geometry and crystalline diffractors with Johansson geometry.

As shown in Fig. 2.16 (a, b) the distance from the source (the sample) to the crystal (or from the diffracting crystal to the detector, as these distances are identical) placed on the Rowland circle varies depending on the diffracting angle θ: $L_1 < L_2$. Since the X-ray intensity falls quadratically as a function of the distance between the sample, diffractor and X-ray detector $I \sim 1/L^2$ [253], the collection of low energy X-rays from light elements (e.g., O K_α) is less efficient relative to high energy X-rays from heavy elements (e.g., Fe K_α).

The modern alternative to the Rowland circle technique compensating the divergent nature of X-rays emission from the specimen is the X-ray optics which transforms the divergent X-rays near the sample into a parallel beam. In this way, the Rowland circle geometry is not required anymore, and the spectrometer design becomes significantly easier, the system is reduced in size, the diffractor can be flat, which is also much easier in production, the detector can be placed at almost any distance with no loss in the X-ray signal. The WDS system with the parallel beam optics is significantly more sensitive, particularly at low energies, in comparison to the traditional solutions with the Rowland circle. The design of WDS with parallel beam is shown in Fig. 2.16 (e, f). Commercial WDS with parallel optics become available in the market since the late 2000s. There are two types of optical technologies for collimating diverging X-rays - grazing incidence and polycapillary focusing optics. For low energies (<~2.5 keV), the first type has greater efficiency, while the latter one is much more effective at higher energies (>~2.5 keV) [253]. This results in two WDS spectrometer designs: one for low energy spectrometry (grazing incidence optics) and one for high energy spectrometry (polycapillary optics). Additionally, the third type was implemented which is the compromise between choosing high or low energy spectroscopy: hybrid optics which incorporates both a grazing incidence and polycapillary optics. Fig. 2.16 (e, f) shows a parallel beam WDS system equipped with hybrid optics. However, the same scheme is accurate for grazing incidence and polycapillary optics.

2.2.2.2. X-rays Detection

The most common X-ray detectors used in WDS systems are gas proportional counters of two types: gas flow counter and sealed counter. They generate an electronic signal proportional to the numbers of X-rays interacting with a gas. The principal scheme of gas flow proportional counter (FPC) is shown in Fig. 2.17. Diffracted X-ray photons enter the counter through a thin window made of Formvar, cellulose nitrate or stretched polypropylene films to isolate the gas atmosphere of the detector from the vacuum in the microscope and spectrometer. Then the X-ray photons are absorbed by atoms of the counter gas and a photoelectron is ejected. Usually, the gas used for FPC as an ionisation medium is P10, the mixture of argon and methane (90%

Ar, 10% CH_4) [248]. In this case, approximately 28 eV is absorbed per electron-ion pair created. Photoelectron will heat other atoms of gas unless all energy is absorbed. Therefore, the number of pairs is proportional to the X-ray energy, and the charge of ejected electrons can be collected. However, the charge of a few hundreds of electrons (e.g., for Mn Kα with the energy of 5.895 keV the number of electrons created directly by a single photon absorption is about 210 [248]) is very small to bring a sufficient signal for the detector. That is why the positive potential is applied to the collecting anode. The voltage is high enough to accelerate electrons ejected in the primary events to ionise gas atoms and perform secondary ionisation to reach a desirable level of the collected charge, which is by several orders higher by magnitude to the initial charge of primary ejected electrons. The applied potential lies in the range of voltage values named "proportional region" where the collected charge remains proportional to the energy of the incident X-ray photon.

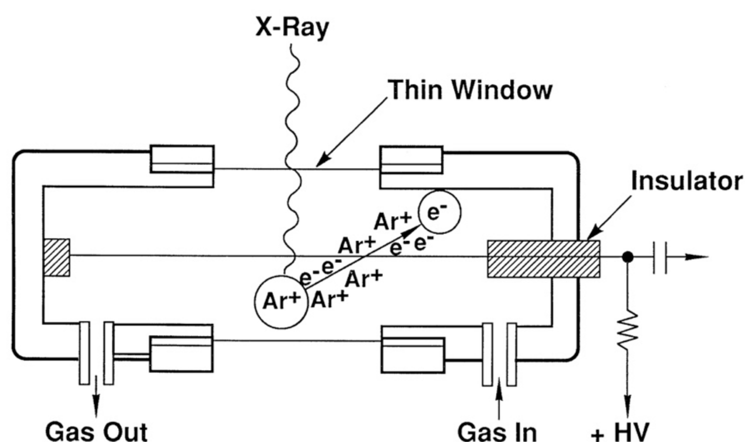

Fig. 2.17 - Principal scheme of a gas proportional counter used in WDS. As taken from [248].

It is also possible that the X-ray photon just will pass through the gas unabsorbed, especially in case of high energy X-rays. The third option is that the X-ray photon with the energy higher than 3.206 keV can eject an Ar K electron with L-shell electron replacing it. In this scenario, the new photon is produced, which then can produce another photoelectron with a further set of ionisations of Ar gas atoms, or the Ar Kα X-ray can just escape through the window from the detector, reducing the total received signal. Also, instead of the Ar Kα X-ray photon, the excess of energy can be converted into emitted Auger electron, which also can perform further ionisation.

Another type of detector, which is mostly used for high-energy X-rays, is a sealed proportional counter (SPC) with a thicker window (in comparison to FPC) made of beryllium, Mylar or other material [247]. The ionisation gas in the detector chamber is usually xenon (Xe), krypton (Kr) or Xe-CO_2 mixture. For shorter X-ray wavelengths they have a higher quantum counter efficiency (the percentage of input pulses detected) than argon-filled detector. However, the increase of the gas pressure to 2-3 atm (3×10^5 Pa) can improve the efficiency of the latter [248].

2.2.3. Practical Applications of EDS/WDS Techniques for Thin Films and Coatings Characterisation

2.2.3.1. Qualitative and Quantitative Analyses

The experimental data acquired with EDS and WDS techniques may be shown for further interpretation in many different ways, as well as it can be characterised by different levels of accuracy. The EDS or WDS analyses and gained data are classified into two the most general types: qualitative and quantitative. In statistical language, the quantitative data is the data which can be measured in values or counts and be expressed as numbers, while the qualitative data is measured in some characteristics or types and represented by a name, symbol or a number code [255]. Often in the elemental composition analysis the data acquired with accuracy level not enough for serving as exact numbers for quantitative analysis is still valuable and may be used for qualitative interpretation. The role and difficulty level of the elemental X-ray spectroscopy are often underestimated. There are more references in the literature to quantitative analysis. However, qualitative analysis is the first stage in the analysis of the materials with unknown constituents, as well as in case if the known sample was exposed to some treatment, modification or unexpected processes when the elemental composition and constituents may be different from the forecast. Then the superaccurate quantitative analysis will bring wrong results if the elemental constituents of the sample have been identified improperly.

Qualitative analysis is a powerful tool in X-ray microanalysis. Often a "rough" elemental identification with the classification of their concentration into major, minor or trace categories without exact numbers is enough to solve many tasks. The definition of such categories is not strict and may vary depending on the sample, tasks or technique features. Generally, it is widely accepted to assume major components as the elements with a mass fraction more than 10 wt.%, minor components with mass a fraction from 1 to 10 wt.% and trace elements those have fraction less than 1 wt.%. As EDS and WDS techniques have a different approach to the identification and count of the characteristic X-rays signal, they have individual and specific features for proper qualitative and quantitative elemental analysis. Many details for the correct EDS/WDS analysis and its better understanding are well written by J.I. Goldstein et al. [256]. The following subchapters of EDS and WDS techniques applications for characterisation of thin films and coatings are dedicated to the approaches of elemental composition data appearance as an overview of opportunities available for the final user - material science researcher.

2.2.3.2. EDS or WDS Spectra of the Analysed Area

X-ray spectrum is the most common form of the visualisation EDS or WDS data acquired from the selected area of the specimen. An example of an EDS X-ray spectrum is shown in Fig. 2.18. It can be obtained from a very small zone, irradiated by electron beam (spot analysis) or from a larger selected area. The signal collected from the X-rays emanating from the area of

interest of the specimen forms a pattern when the vertical axis shows the intensity of photons and the horizontal axis shows the energy of photons in case of EDS. In WDS spectrum the horizontal axis typically has units of wavelength, sinθ or millimetres of diffracting crystal movement. Also, in modern software, these units can be automatically transformed into X-rays photon energy units, and WDS patterns can be compared with the EDS spectrum, as was demonstrated in Fig. 2.15. However, the nonlinear relation between photons energy and wavelength (E~1/λ) should be noted, which results in peaks asymmetry and loss or distortion of some details of WDS peaks.

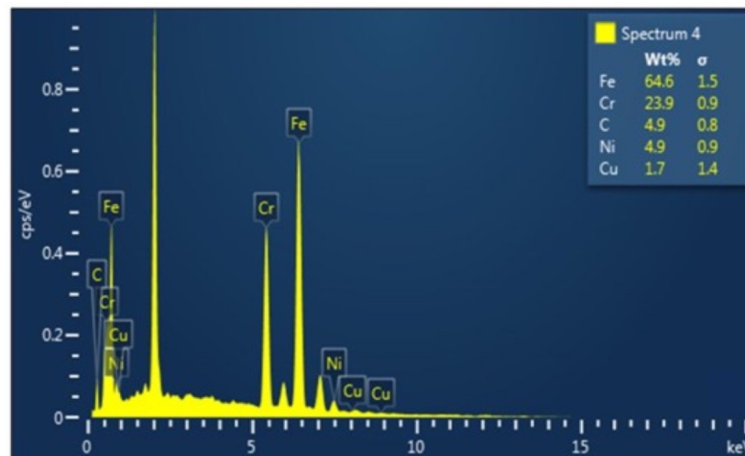

Fig. 2.18 - EDS spectrum obtained from intermetallic layer between welding seam and SUS304 stainless steel showing the presence of various elements. As taken from [257].

All modern software systems for X-ray microanalysis have a function for automatic qualitative and quantitative analysis, but it is always suggested to confirm manually the suggested identification of elements, especially low-intensity peaks representing minor or trace constituents. It is important to know the concept of a family of X-ray peaks appearing from the same type of atoms but as a product of electron transition from all possible shells or subshells to replace ejected electron. As WDS has better energy/wavelength resolution and higher peak-to-background ratio than EDS, more members of the X-ray peaks family can be detected and must be confirmed in the resulted pattern to avoid misidentification of minor or trace elements. The complexity of the family structures increases with the increase of the atomic number. The neglect of a presence of some lower energy members of the same X-ray peaks family may result in ascribing these peaks to other elements which are not present or falsify the fraction of another lighter constituent when its peak of main interest is overlapped with members of another X-ray peaks family. There are existed several types of X-ray peaks tables or plots developed so far, to make the process of X-ray microanalysis more convenient for the analyst: e.g. very detailed table organised by Bearden in 1967 with the list of 25 L-family peaks, which is too detailed for EDS spectra, but could be useful for high-resolution WDS systems, or more simplified information published by Fiori and Newbury in 1978 in a graphical form of plots for all X-ray peaks observed in high-quality EDS spectra [258].

2.2.3.3. Thin Film or Coating on a Substrate, Multi-Layered Structures

If a film or coating deposited on a substrate should be exposed to EDS or WDS, the thickness of the specimen becomes an important factor. If the thickness of the film or coating is less than the depth of electron beam interaction volume with the matter of sample, then X-rays both from the deposited material and substrate will be generated. If X-rays emitted from the substrate are not completely absorbed by the specimen on the way out from the surface they will contribute to the resulted X-ray spectrum and, therefore, the elemental composition from the acquired data will be influenced by the substrate.

As the depth of electron beam interaction with the matter depends on the beam energy, the decrease of acceleration voltage up to some values when the energy is still sufficient to excite all of the characteristic X-ray peaks of interest would help. Usually it is $U > 1.25(E_{EB}/E_C)$ [259]. In this way, the signal will be obtained with less depth, and the substrate may be avoided. Also, X-ray peaks of the same family but from an electron shell requiring lower excitation energy may be considered to decrease electron beam energy. If such an approach doesn't work and the substrate is still present, it is possible to take a series of spectra with a set of different acceleration voltage values as 5, 10, 15 or 20 keV. By careful analysis of the peaks' evolution, it would be possible to obtain the elemental composition of the film or coating with a high degree of accuracy. The additional elemental composition of the substrate obtained separately, if possible, or in some cases from the backside of the sample, would help in the evaluation. In this case, the identification of thin film thickness is also possible, but definitely, it is not the easiest method and not the best solution [259]. X-ray reflectivity may be suggested as a better and more accurate solution to identify the thickness of thin films with low roughness.

The same issue of electron beam interaction volume happens with multi-layered thin films. However, it is absolutely impossible to identify the elemental composition of each layer individually exposing the specimen to the electron beam from the top side of the sample. Only the first layer could be accurately evaluated using explained approaches of an integral average elemental composition of several layers may be obtained. For the detailed elemental composition of each layer or study the transition from the deposited film or coating to the substrate, the elemental depth profiles obtained on the cross-sectional specimens could be used.

2.2.3.4. Line Scans and Elemental Depth Profile Analysis

In a line scan, the electron beam travels linearly along a selected line on the specimen, and the X-ray signal is counted at each point of the scan in relation to the probe position. It is possible to control the number of points for the scan, dwell time per point and number of passes. This type of scan is usually used to study elemental variations in impurities, precipitates and grain boundaries. It could be very useful for the cross-sectional study of thin films and coatings, for building elemental depth profiles from the surface of the coating to the substrate. Such elemental

depth profile of layered structures gives information (most likely qualitative) about the elemental composition of each layer and allows to evaluate the thickness of individual layers. Some examples of EDS line scan and elemental depth profile are given in Fig. 2.19.

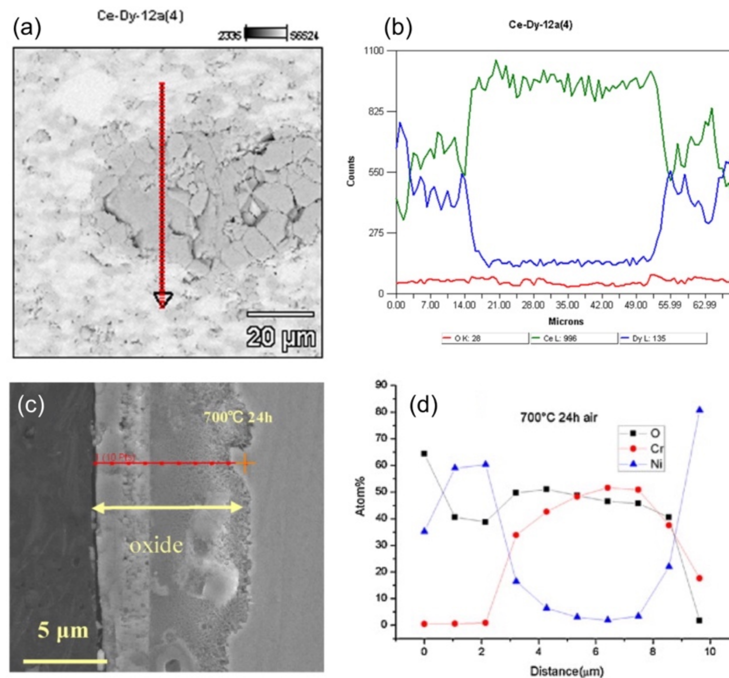

Fig. 2.19 - Examples of EDS scan lines and elemental depth profiles:
(a, b) EDS line-scan performed along Ce-rich area of Ce-DY oxide surface [260]; (c,d) SEM-image and EDS line-scan profile on cross-section of oxide film grown on Inconel 600 at 700° for 24 h oxidation under dry air [261].

2.2.3.5. Elemental Mapping

EDS or WDS maps show the distribution of elements on the selected area of the specimen surface visualised as a colour two-dimensional plot. Area of interest is scanned by the electron beam and the X-ray energy/wavelength spectra with the further calculation of elemental distribution is acquired and stored for each point of the map. The number of points (pixels), dwell time for acquiring data from each point and the number of passes can be selected by the user, controlling in this way the final resolution and quality of the X-ray elemental map. An example of EDS elemental mapping results appearance is shown in Fig. 2.20.

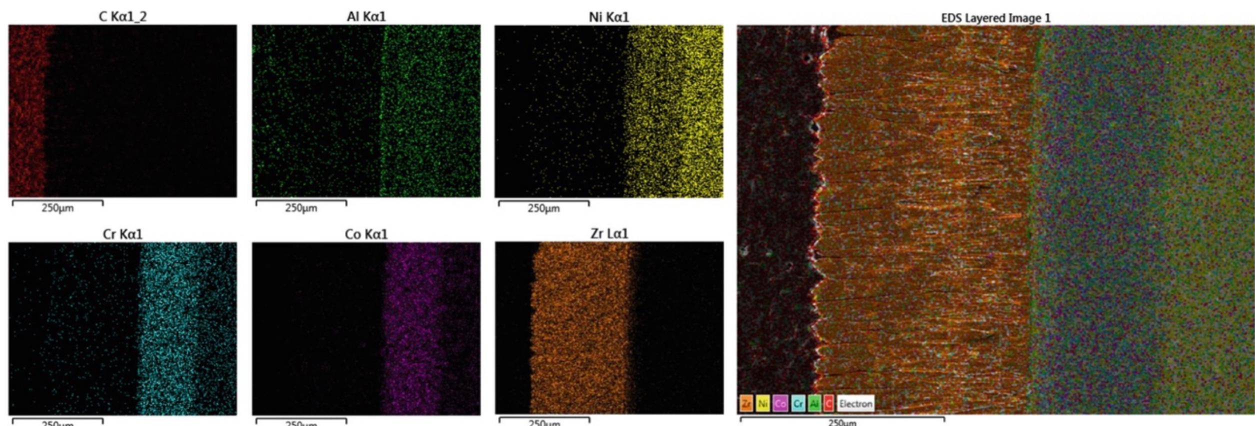

Fig. 2.20 - X-ray map showing elemental distribution within the thermal barrier coating (TBC) sample.
The last (right) window shows layered elemental distribution map, a combination of the previous six maps [247].

Usually, X-ray maps of elemental distribution are shown in multiple colour windows simultaneously, where each window corresponds to one of the elements of interest predetermined previously by spot or area EDS/WDS elemental analysis. In each window, the brighter zones indicate a higher concentration of the corresponded element. Also, such maps may be combined into one to show elemental composition distribution for selected elements, or even combine all scanned elemental maps together, as shown in the right window in Fig. 2.20. Despite the acquiring of EDS spot scan usually is a relatively fast procedure, the process of obtaining EDS map could take some time from a few minutes to a few hours, depending on the number of points to be scanned, beam dwell time, number of passes, dimensions of the selected area and, thus, resulted resolution and quality. In these conditions, the electron beam stability becomes very important, and the image drift during multiple or even single scans at extremely high magnification can appear producing smeared and distorted EDS/WDS-mapping images.

Therefore, it is difficult to achieve high-resolution and good detection limits during X-ray mapping as a compromise of time and quality. Thus, this impedes the registration of minor and especially trace constituents in X-ray elemental distribution maps. It is possible to obtain high-resolution maps of elements with WDS techniques but at the expense of time [247].

2.2.4. Experimental Details

The elemental analysis was obtained by energy-dispersive X-ray spectroscopy (EDS) using Quanta 200 3D microscope and FEI Quanta 400 FEG ESEM and by wavelength-dispersive X-ray spectroscopy (WDS) using an Oxford Instruments INCA WAVE WDS spectrometer unit attached to the above mentioned JEOL JSM-7001F and by INCAEnegy+ software module. Most of the EDS analyses of multilayer films were performed on cross-section samples acquiring integral spectra from the large area of all layers contained in the coating, keeping an equal number of MoN and CrN layers. Electron beam energy used in elemental composition analysis by EDS was 10 keV. The WDS scanning was performed successively by $K\alpha_1$ lines for Cr, N, O elements and by $L\alpha_1$ line for Mo using 10 kV high accelerating voltage, probe current of 20 nA and magnification in range ×1000÷5000. This technique is complementary to the energy-dispersive spectroscopy (EDS) or can run independently. The WDS spectrometers have significantly higher spectral resolution and enhanced quantitative potential.

The calculation of electron beam penetration depth in thin films was done using Equation (2.1) [262]:

$$x = \frac{0.1{E_0}^{1.5}}{\rho}, \tag{2.1}$$

where E_0 is the energy of incident electrons in keV; ρ – density of the material in g/cm^3.

2.3. X-ray Diffraction

2.3.1. Introduction

X-ray diffraction (XRD) is one of the most common and powerful tools of micro- and nanostructure characterisation. It is a non-destructive method and, in many cases, doesn't need any special preparation of the sample for being examined. It may be applied for a very broad range of samples - powders, thin films, nanoparticles, bulk materials, organic and inorganic materials, single-crystals, polycrystalline or amorphous materials. Despite the simplicity of X-ray diffraction basics, there are many approaches to the structure characterisation developed so far, while each of them has its specific features. Techniques and equipment for XRD data acquisition, as well as algorithms and software for its interpretation, are still constantly improving.

2.3.2. Basics of X-ray Diffraction

X-rays are electromagnetic ionising radiation of short wavelength ranging from 0.1 to 10 Å, discovered by Wilhelm Conrad Röntgen on 8th of November 1895, for which he received the first Nobel Prize in Physics 6 years later, in 1901: "in recognition of the extraordinary services he has rendered by the discovery of the remarkable rays subsequently named after him" [263].

The radiation with a wavelength of around 1 Å is used for the atomic and crystallographic structure study as it best fits the atomic sizes scale. As seen from Fig. 2.21, they belong to the class of soft X-rays.

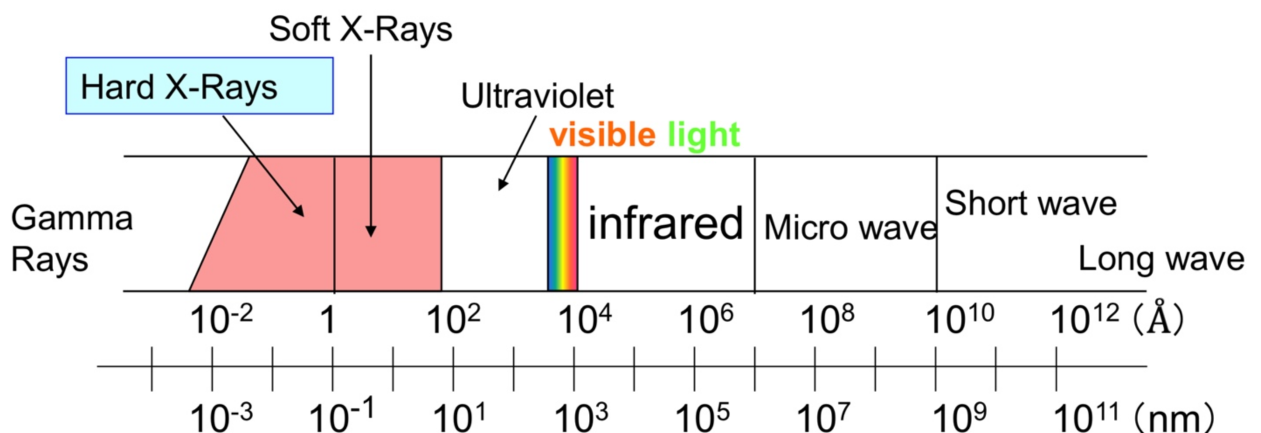

Fig. 2.21 - Electromagnetic spectrum.

As X-rays has a dual wave-particle nature, in addition to the wave motion character, it behaves as a particle that has energy inversely proportional to its wavelength ($E(keV) = 12.4/\lambda(Å)$). They are at the short wavelength, high energy end of the electromagnetic spectrum. Only gamma-rays can carry more energy. While most of the gamma-rays are created by nuclear decay, X-rays are generated by energy transitions that happen when electrons hit a target. Two different atomic processes are involved in X-rays generation, creating white (continuous X-rays, Bremsstrahlung X-rays) and characteristic X-rays ($K\alpha_1$, $K\alpha_2$, $K\beta$).

X-rays with a wavelength in the range suitable for crystallography studies (~0.8-2.3 Å) are generated mainly by three groups of devices: X-ray tubes and rotating anodes (laboratory X-ray sources) and synchrotrons. Electrons emitted by the heated filament (acting as a cathode) and accelerated by high voltage in a vacuum, bombard a target (anode). The most common materials for the anode are Cu, Mo, Co and other metals depending on the specific needs. Almost all of the energy from the electrons is transformed into heat after the bombardment, and only a small amount of the energy is converted into X-rays (ex. for Cu anode the generation efficiency is around 0.1%: $E=1.1\times10^{-9}ZV$, where Z - atomic number and V - applied voltage).

The loss of energy by electrons occurs due to the collisions with atoms via multiple events. As a result of the deceleration of their speed, white X-rays are emitted, which is a continuous spectrum of X-rays (see Fig. 2.22). The higher the accelerating voltage of the X-ray source, the shorter the minimum wavelength that can be obtained.

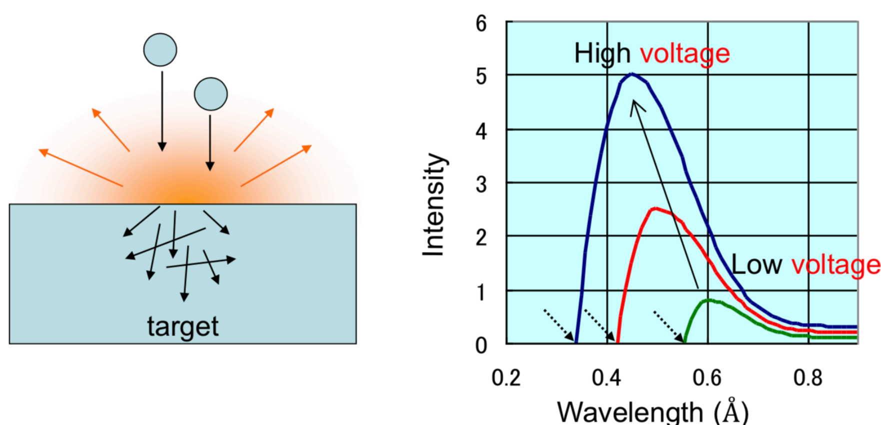

Fig. 2.22 - Generation of continuous white X-ray spectrum [264].

An accelerated electron with the energy higher than a certain threshold level depending on the anode material can eject an electron from one of the inner electron shells of the metal atom. In result, another electron from a higher atomic level drops to the vacant level emitting X-ray photon with energy characterised by the difference between those two levels, which is a unique value specific for each material (characteristic X-rays). An example is shown in Fig. 2.23 for a copper atom.

Higher released energy leads to the shorter wavelength of the X-ray. Depending on the shell type of the vacancy and electron from a higher atomic level, several discrete peaks for corresponding wavelengths will be formed. These characteristic lines are called by the electron shell where the vacancy was created (K, L, M, ...). When the two orbitals involved in the electron transition are adjacent (e.g. from L- to K-shell), the line is called α. If they are separated by another shell (M-shell to K-shell), the line is called β. As seen, β-transition releases more energy than α. Therefore, β-line has a shorter wavelength and is on the left side from α-line on the X-ray spectrum. The transition of an electron from L-shell to K-shell occurs from 2p orbital, which is split into two energy levels (L_{II} and L_{III}) with a very small difference (for copper $\Delta E(L_{II}-L_{III})$ = 0.020 keV),

and two wavelengths of the emitted X-rays are very similar ($K\alpha_1$ = 1.540593 Å, $K\alpha_2$ = 1.544414 Å). This means that $K\alpha_1$ and $K\alpha_2$ may appear on the spectrum as a simple peak labelled Kα, and only a high-resolution spectrum will show a doubled. The intensity of the $K\alpha_2$ peak is almost half of the intensity of $K\alpha_1$ peak, which is determined by the probability of the outer electron to fill the vacancy. For Kβ line it is approximately 0.2-0.3 of the $K\alpha_1$.

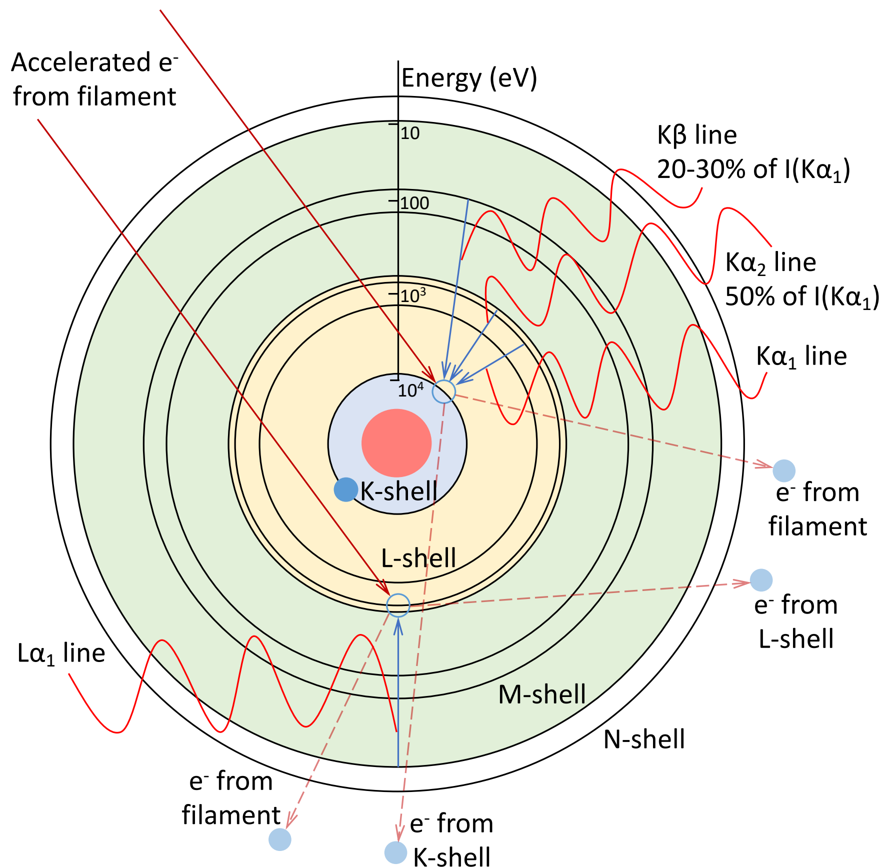

Fig. 2.23 - Characteristic X-rays generation process. Schematic model for a copper atom with electronic energy levels.

The intensity of the characteristic X-rays is proportional to $i(V-V_0)^n$, where i and V are tube current and voltage, V_0 - excitation voltage, n is a coefficient dependent on V and, in case if V is over $3V_0$, $n = 1$. For white X-rays, the intensity is proportional to iV^2Z, where Z is an atomic number of anode material [264]. Therefore, the ratio between both intensities depends on the tube voltage and other parameters of a certain X-ray generation system. The spectrum of White and Characteristic (Kα, Kβ) X-rays for Molybdenum cathode is shown in Fig. 2.24. In case of diffractometer with the copper anode (V_0 = 8.86 kV) and typical operating voltage of 40 kV, the Kα is approximately 90 times more intense than the white radiation of a similar wavelength [265]. All instrumentals setups are optimised to use Kα radiation and $K\alpha_1$ in case of high-resolution optics and measurements.

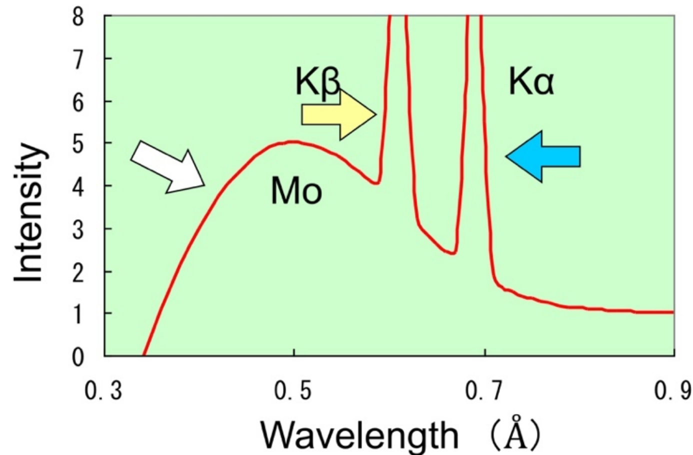

Fig. 2.24 - Spectrum of White and Characteristic (Kα, Kβ) X-rays. As taken from [264].

When emitted X-ray penetrates into the material, different events of interaction with matter occur (see Fig. 2.25). Depending on absorption characteristics of the medium, its thickness and density, some part of the incident X-ray beam may pass through the sample with no losses and changes (transmitted X-rays). Collisions of the rest of the beam with the medium lead to the absorption of the X-rays (transfer of energy from the photon to the absorbing material) or scattering (in which the X-ray photon is "redirected" by interaction with the scattering material). The major part of the absorbed energy at the end is released as heat dissipated through the sample to the environment.

Incident X-ray may eject an inner electron and form a vacancy which then should be filled by an electron of the outer orbital followed by the emission of secondary X-ray (fluorescent) that leaves the atom. This phenomenon of initial X-ray absorption with the emission of fluorescent X-ray and high-energy electron is called the photoelectric effect. Also, instead of X-ray emission out of the atom, the photon may be absorbed by an outer shell electron resulting in the emission of an Auger electron.

An inelastic collision of X-ray photon with an electron on the orbital is called Compton scattering. In this process, a part of the energy from photon is transferred to the ejected electron (Compton electron), which will typically interact with other atoms producing secondary ionisation. The incident X-ray photon after collision with the electron changes direction and loses energy. As a result of losing energy, scattered X-ray has greater wavelength than the initial one and scatters relatively to the higher angle. The Compton scattering contributes to the overall background in the measured X-ray data.

Thomson scattering (or Rayleigh, coherent, classical scattering) occurs when the X-ray photon interacts with the orbital electron or the whole atom with no change or transfer of internal energy between the scattering atom and the X-ray photon (elastic collision). This only changes the direction of the X-ray photon and the wavelength is the same. Scattering is mainly in the forward direction and occurs without the loss of energy. This is the primary effect which makes X-ray diffraction possible and is called the diffraction phenomenon.

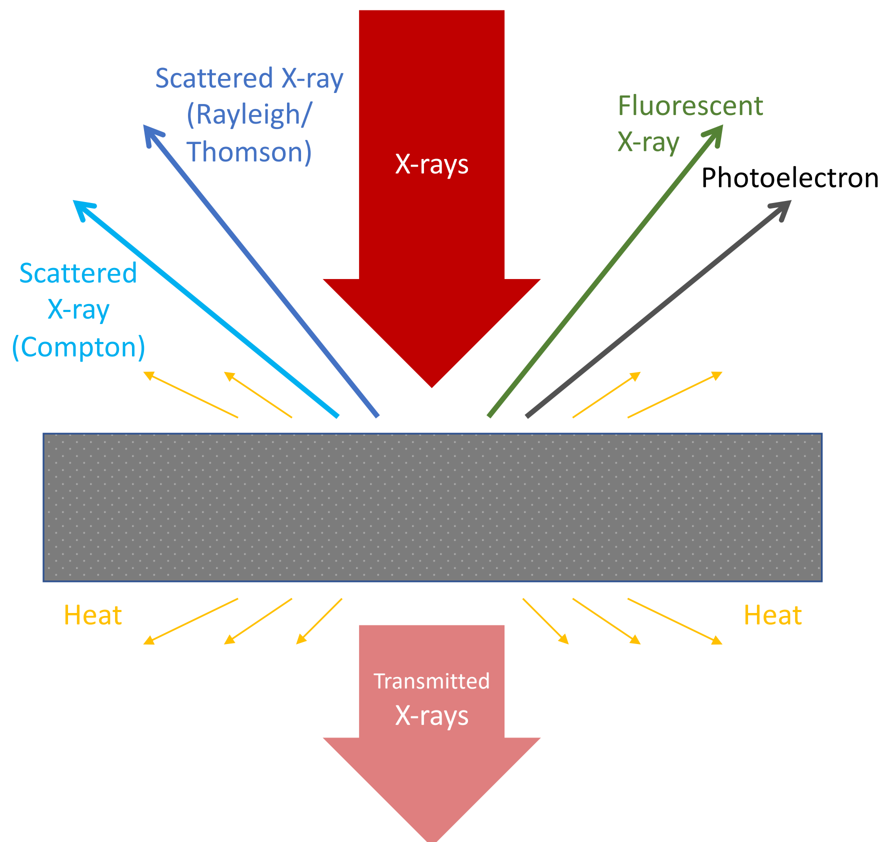

Fig. 2.25 - Interaction of X-rays with matter.

The easiest and basic way to the structural characterisation in powder diffraction is by Bragg's condition (Bragg's law), which describes the principles of X-ray diffraction in terms of a reflection of X-rays (the type of Thomson scattering considered earlier) by sets of lattice planes. Lattice planes are crystallographic planes, simplistically formed by periodically placed atoms of the certain material. The orientation of the planes is described by Miller indices *hkl*. They are placed parallel to each other, separated by the same distance d_{hkl} named interplanar spacing or interplanar distance, lattice spacing (see Fig. 2.26).

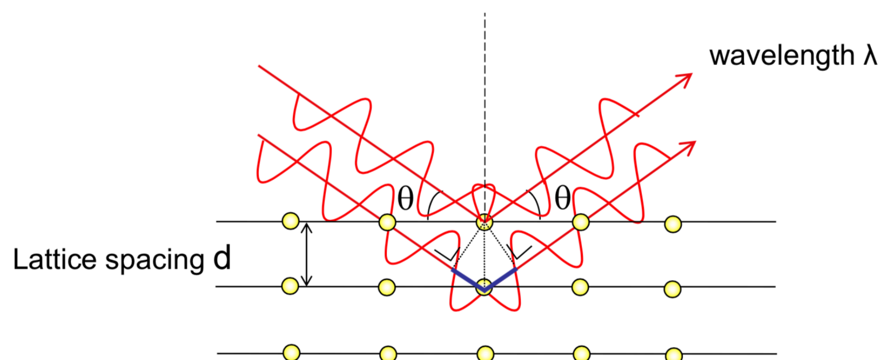

Fig. 2.26 - Simplified illustration of Bragg's condition for the family of crystallographic planes spaced by the distance *d*.

Bragg analysis considers incident X-rays emitted by a source and reflected at the lattice planes like visible light by the mirror surface. At the screen of the X-rays detector, the maximum

signal is only achieved when both waves stay in phase, thus when the constructive interference occurs. The path length of AB+BC should be an integer (whole number *n*) of wavelengths (λ), or *nλ*. For all other angles corresponded to the fractional n, the reflected waves will be out of phase and the distractive interference occurs. Thus, sharp intensity peaks appear from the sample only at special angles where AB+BC = nλ, with no intensity in between.

It is seen geometrically that AB and BC are equal to each other and to the distance d multiplied by the sine of the reflected angle θ, or dsinθ. Consequently,

$$n\lambda = 2d\sin\theta, \tag{2.2}$$

which is the Bragg's condition.

Therefore, knowing the wavelength of the used X-rays and the positions of the diffraction angles from the peaks registered on the measured diffractogram it is possible to calculate the interplanar distance d. For powder diffraction and polycrystalline materials, the diffractogram of broad diffraction angle will show a complete spectrum of their crystallographic planes, which gives information about crystal structure and allow to obtain lattice parameters of certain material. A great database with thousands of diffraction spectra exists, and the experimental pattern obtained from the studied sample may be compared to the database for further interpretation and characterisation.

The demonstrated-above derivation of Bragg's law is very simplified and idealised. Despite leading to the correct solution, it has serious drawbacks. In real experiments, X-rays are reflected not by planes but are scattered by electrons at the orbitals bound to the atoms. Crystal planes are not like shiny optical mirrors, but contain discrete atoms separated by regions of much lower electron intensity. Moreover, atoms in one plane may not lie exactly below atoms in the plane above [266].

Simplified illustration for more generalised case of Bragg diffraction is shown in Fig. 2.27, where the atom of the lower plane is shifted from the vertical line position. For the constructive interference the phase shift nλ should be equal to the distance AB+BC. As line AD is perpendicular to the AB, and CD is perpendicular to BC, AB = BDcos(180°-(α + θ)) and BC = BDcos(α - θ). Thus, nλ = BD(-cos(α + θ)) + cos (α - θ)). As cos(α+θ) = cosαcosθ - sinαsinθ and cos(α-θ) = cosαcosθ + sinαsinθ, our equation transforms to nλ = BD(2sinαsinθ). Geometrically, d = BDsinα. With this, the already known Bragg's equation follows: nλ = 2dsinθ.

The assumption of specular reflection was used to derive the Bragg's condition, but it was concluded experimentally. For crystalline materials. the destructive interference will eliminate intensity in all directions except where the Bragg's law is respected (Equation (2.2)). This no longer works for amorphous materials where X-rays will be scattered in many directions leading to a large bump distributed in a wide range of angles instead of high intensity narrower peaks when the constructive interference occurs.

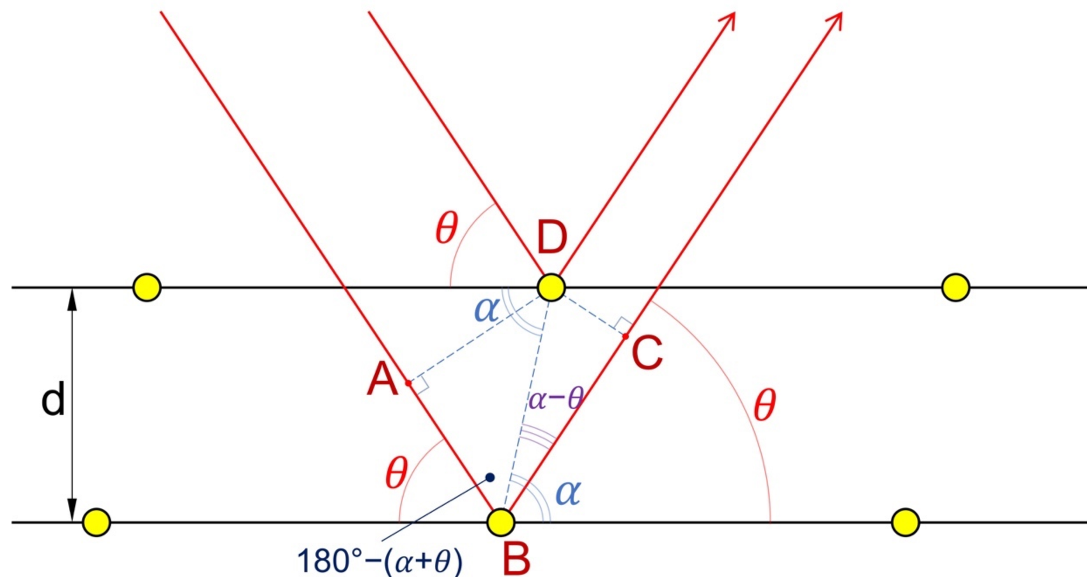

Fig. 2.27 - Illustration of Bragg X-ray diffraction geometry in the general case where scattering takes place at the position of atoms in consecutive planes.

2.3.3. X-ray Diffraction Modes

2.3.3.1. θ/2θ Symmetrical Mode

This is the most common and simplest method of X-ray diffraction measurements based on Bragg's law. From Bragg's condition, it is seen that incident angle ω and (or) X-ray wavelength λ may vary. As the X-ray beam used in laboratory equipment source has a fixed wavelength, ω angle can be changed. In mode $\theta/2\theta$ the incident angle ω is positioned at θ, while the detector on the diffraction beam side is placed simultaneously at angle 2θ and counts the intensity I of the diffracted beam (see Fig. 2.28). With the change of source and detector position at the selected range, the diffraction pattern can be taken.

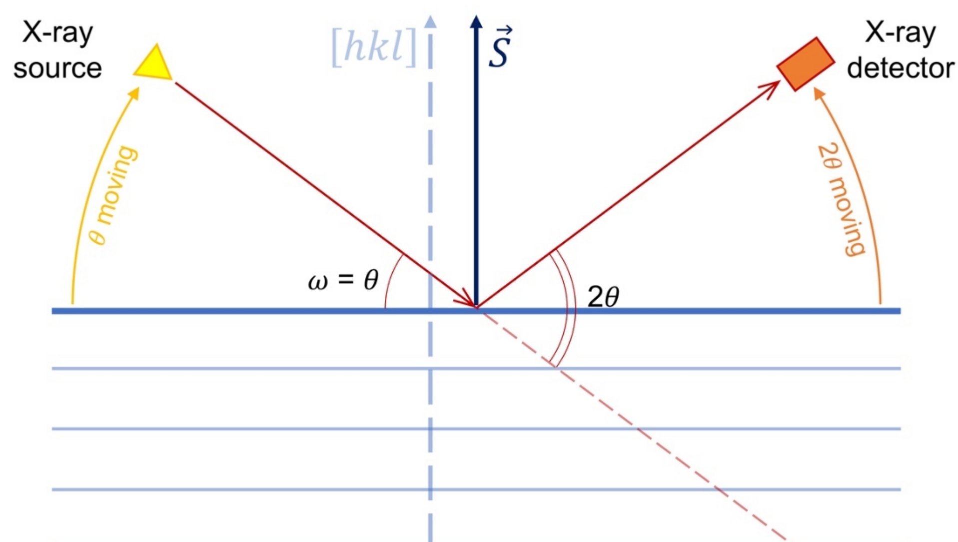

Fig. 2.28 - Geometry of symmetric θ/2θ X-ray diffraction scan.

Based on the geometry shown in Fig. 2.28 it is possible to detect Bragg reflections corresponded to the diffractions of each family of the atomic planes which satisfy Bragg's

condition ($n\lambda = 2d\sin\theta$), thus each interplanar distance. In $\theta/2\theta$ mode the diffraction angle ***s*** always stays at the same position and when it is perpendicular to the surface the diffraction from the planes parallel to the surface of the sample is observed. This method is good for qualitative analysis, identification of crystal structure and reflectivity experiments.

In case if the diffraction planes are inclined from the surface of the sample (e.g. thin films, single crystals etc.), the diffraction vector may be adjusted (tilted) to perform the measurements. This may be done by two approaches shown in Fig. 2.29, depending on the facilities of the diffractometer, either by incline of source-detector arms (a) or by tilting the sample (b).

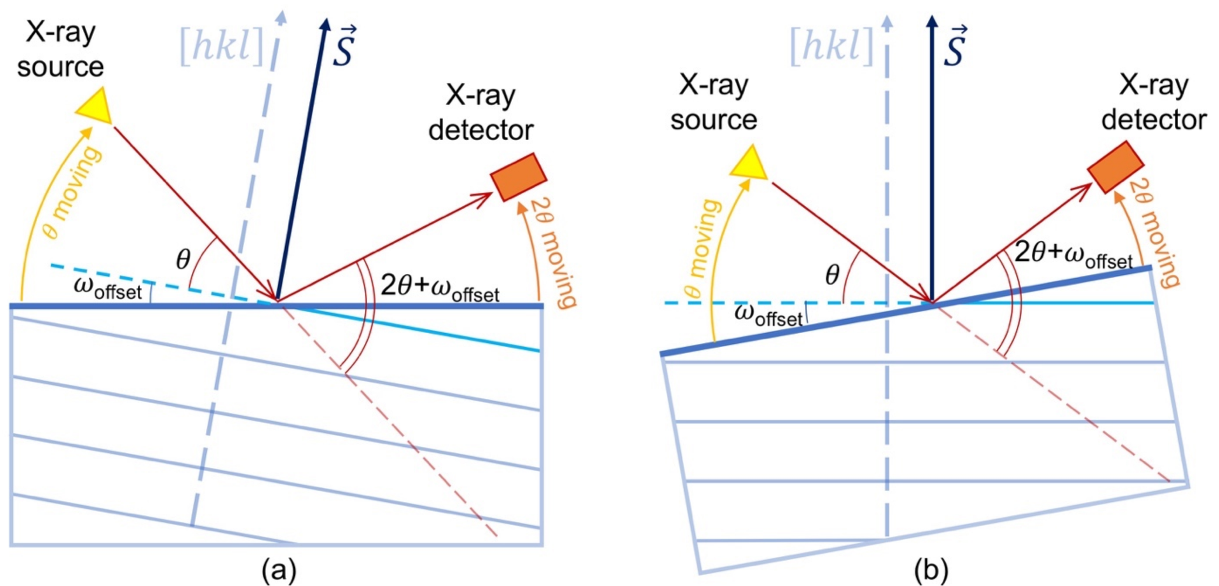

Fig. 2.29 - Geometry of asymmetric X-ray diffraction scans with ω-offset (a) or sample tilting for angle ω-offset (b).

It should be noted that the penetration depth of the X-ray beam depends on the incident angle and decreases when the angle becomes smaller. Therefore, if the incident angle of X-rays is just above a critical angle of the total reflection (usually 0.2°-0.8°, depending on the material), only the zone close to the surface will be exposed.

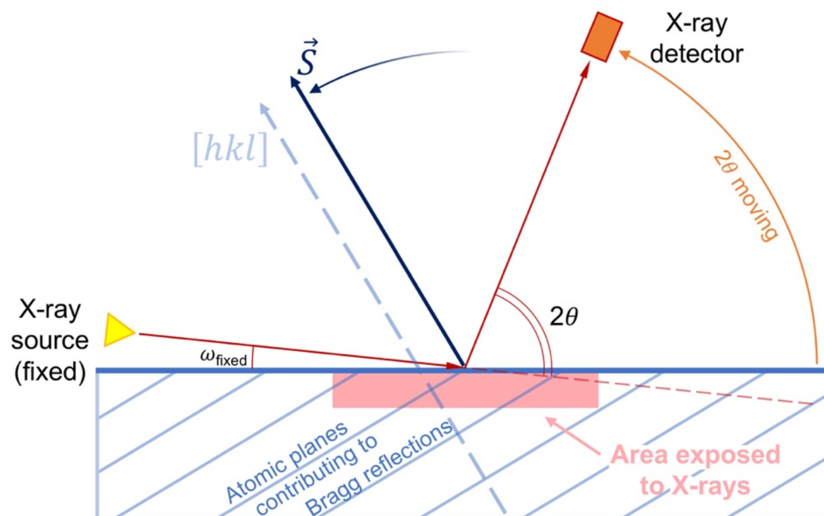

Fig. 2.30 - Geometry of X-ray diffraction in grazing incidence mode (GIXRD).

When the X-ray source is fixed and only the detector arm of the goniometer moves (2θ scan), the diffraction pattern of the surface zone will be registered (see Fig. 2.30). This mode is called Grazing incidence X-ray diffraction (GIXRD or GID). It helps to avoid the contribution of the substrate to the resulted diffraction pattern when thin films are being measured or may provide information just from the top layer of multi-layered or graded structures. If XRD patterns are taken at several values of the fixed incident angle, it allows obtaining depth-sensitive measurements. More generalised name of such method, when the incident angle is fixed and just the detector moves, is 2θ scan or asymmetric scan mode.

The important note is that in this mode the diffraction vector position always changes with a movement of the diffractometer, thus the atomic planes contributing to Bragg reflection changes during 2θ scan.

2.3.3.2. In-plane Mode.

Goniometers of the modern laboratory X-ray diffractometers may allow obtaining information not only from the atomic planes placed parallel to the surface or tilted for some small or large angle, when the diffraction vector ***s*** is always out of the sample surface plane (out-of-plane) but also from the atomic planes perpendicular to the surface, i.e. the diffraction vector lies on the surface (in-plane). It is possible in case when the goniometer arm with the detector is able to perform movements within the plane parallel to the surface ($2\theta_\chi$, see Fig. 2.31).

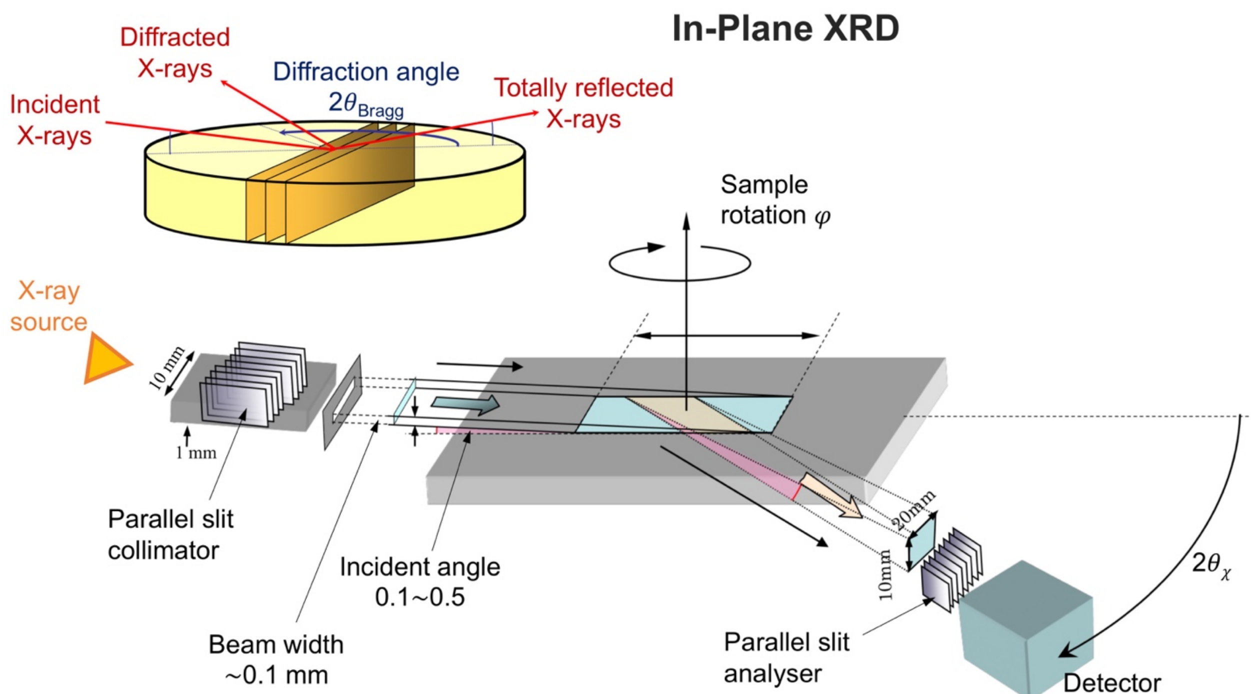

Fig. 2.31 - In-plane geometry of X-ray diffraction measurements. Adapted from [264].

In this mode, the incident angle of X-ray source ω is set to the angle close to the total reflection of X-rays. The detector is placed at the same symmetrical angle θ = ω in the plane normal to the surface and moves by angle χ horizontally ($2\theta_\chi$). To maintain the same position of

in-plane diffraction vector, the sample holder also has to perform rotation (φ) by half of the detector position change ($\Delta\varphi = \theta_\chi$). Similarly to GIXRD scan, it is possible to obtain depth-sensitive measurements by changing the incident X-ray beam angle ω.

2.3.4. Experimental Details - Equipment

The X-ray diffraction analysis was performed using two diffractometers with Cu radiation: initial θ/2θ-scan measurements for part of the samples were done with Panalytical X'Pert Pro Multipurpose Diffractometer, and the main measurements, including asymmetric and in-plane modes, were done with high-resolution X-ray diffractometer Rigaku SmartLab.

Panalytical X'Pert Pro unit was equipped with PW3373/00 (Cu LFF DK292308) X-ray tube generator operated at U_{acc} = 40 kV and I_{emis} = 30 mA in the line focus mode with 12.0 mm length and 0.4 mm width. The XRD patterns were acquired by exposing samples to Cu-Kα X-ray radiation, with characteristic wavelengths $\lambda_{K\alpha1}$ = 1.5405980 Å (mainly) and $\lambda_{K\alpha2}$ = 1.5444260 Å, the ratio of intensities $K_{\alpha1}/K_{\alpha2}$ = 0.5. The data were collected over the range 2θ from 10° to 95° with the step size 2θ = 0.017° and the scan speed 2°/min, using the X'Celerator scanning detector. The fixed divergence slit of 0.5° was used together with the beam mask of 5 mm and all scans were carried out in continuous mode. Incident and receiving soller slits were 0.04 rad., receiving slit was 0.1°.

Rigaku SmartLab at the Institute of Physics for Advanced Materials, Nanotechnology and Photonics (IFIMUP) has 9kW rotating Cu anode, operated at U_{acc} = 45 kV and I_{emis} =200 mA. Rotation helps to achieve a stable and homogeneous flow of X-rays from the anode under such high voltage and current, which is almost not possible for the same exposed zone of the static Cu target in the sealed X-ray tube (see Fig. 2.32 for comparison).

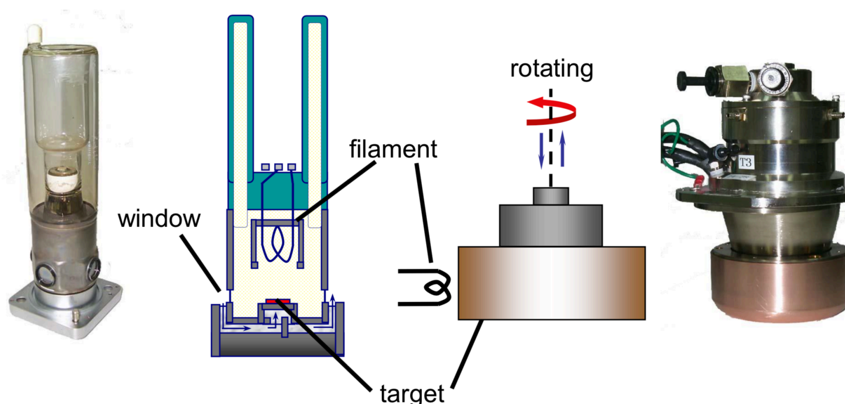

Fig. 2.32 - X-ray sources used in modern X-ray diffractometers. As taken from [264].

Emitted X-ray radiation beam mainly consists of $K_{\alpha1}$ ($\lambda_{K\alpha1}$ =1.540593 Å), $K_{\alpha2}$ and $\lambda_{K\alpha2}$ = 1.544414 Å and K_β ($\lambda_{K\beta}$ = 1.392250Å) lines with their intensity ratio 100:50:20 respectively.

Spectra were acquired by using various optics, scan speed and scan step, applying the parallel beam in line focus mode with 8.0 mm length and 0.4 mm width.

For symmetrical θ/2θ scans taking in continuous mode, the diffraction angular range was from 30° to 100° with the step of 0.01° and scan speed 0.3°/min. Asymmetric 2θ GIXRD scans were performed in the same angular range and step, but the scan speed was 0.5°/min, incidence angles ω were 0.4°, 0.8° and 1.2°. In-plane XRD 2θχ/φ scans were taken in the angular range 32-84°, with the step of 0.024° and scan speed 0.5°/min.

SmartLab diffractometer is equipped with patented by Rigaku CBO (Cross Beam Optics) unit which allows switching between conventional Bragg–Brentano para-focusing (BB) and parallel beam (PB) optics. In BB optics the X-ray source, the sample, and the receiving slit must be on the same focusing circle (see Fig. 2.33 a), the sample must be equidistant from the source and the receiving slit and θ/2θ scanning mechanism is needed. This regime is the most popular for powder X-ray diffraction and, indeed, is good for identification of trace phases, due to high intensity and high angular resolution. However, BB optics is very sensitive to the sample surface flatness, thus may give an error to the measurements if the sample is not flat (actually, should follow the shape of the focussing circle - slightly bent). Systematics errors of the measurements also may be caused by sample displacement, transparency, absorption effect, axial divergence, which makes BB optics limited and inaccurate when single crystals, rough surfaces, thin films and coatings are considered, or when some specific, not θ/2θ, scanning mode is needed. Therefore, for multi-layered coatings studied in this research PB optics were used (see Fig. 2.33 b).

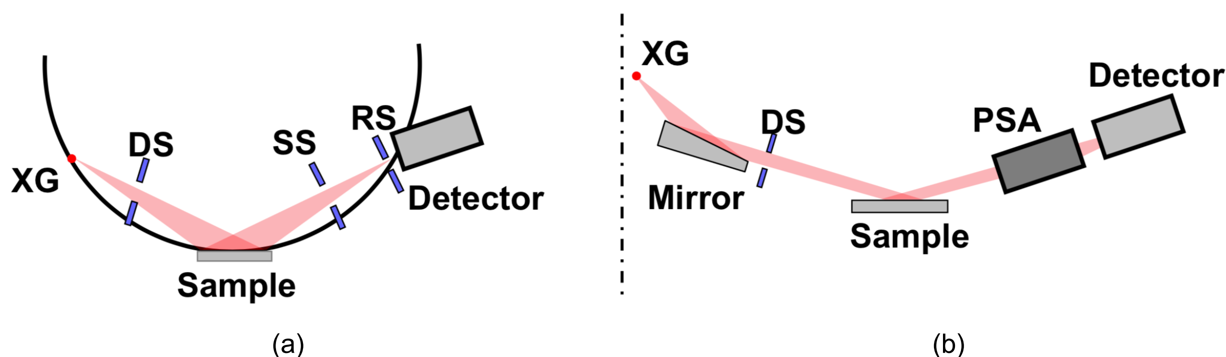

(a) (b)

Fig. 2.33 - Schematic geometry of (a) Bragg–Brentano para-focusing (BB) and (b) parallel beam (PB) optics. As taken from [264].

Parallel beam (PB) of X-ray radiation in CBO of SmartLab diffractometer is formed by a parabolic multilayer mirror. A multilayer mirror is an artificial lattice with alternating thin-film layers of heavy and lighter elements [267]. When X-rays of a certain wavelength are incident at an angle which satisfies the Bragg's condition for *d*, which is the thickness of bilayer structure in the mirror, X-ray diffraction occurs. Selection of the X-ray wavelength and monochromation can be obtained by this way [268]. Multilayer mirror is shown schematically in Fig. 2.34 (a). In the actual parabolic multilayer mirror of the CBO unit, the periodic thickness of the multilayer *d* continuously increases in the direction from the X-ray source to keep Bragg's condition because the diffraction angle close to the source is higher than it is far away from the source. A multilayer mirror of this type is

called a graded multi-layered mirror (Fig. 2.34 b). Due to the extremely high-level requirements to the synthesis technology of continuously varying of *d* value, K-α_1 and K-α_2 radiation are difficult to separate, so K-α radiation includes both characteristic radiations, while K-β radiation is almost excluded, but still present at a low level.

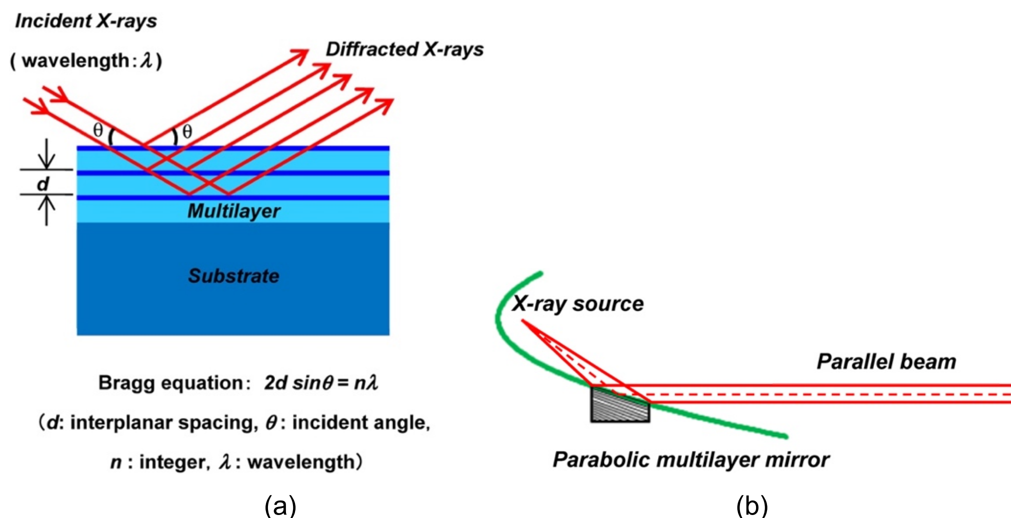

Fig. 2.34 - Multilayer mirrors in optics for X-ray diffractometers. As taken from [268].

Although PB configuration of optics helps to avoid many errors inherent in BB optics configuration, axial divergence and sample misalignment may be an issue. Axial divergence, or umbrella effect, caused by the vertical divergence of the incident X-ray makes the profile asymmetric (see Fig. 2.35), particularly pronounced at low 2θ. Closely spaced soller slits may minimise it, but at the cost of reduced intensity.

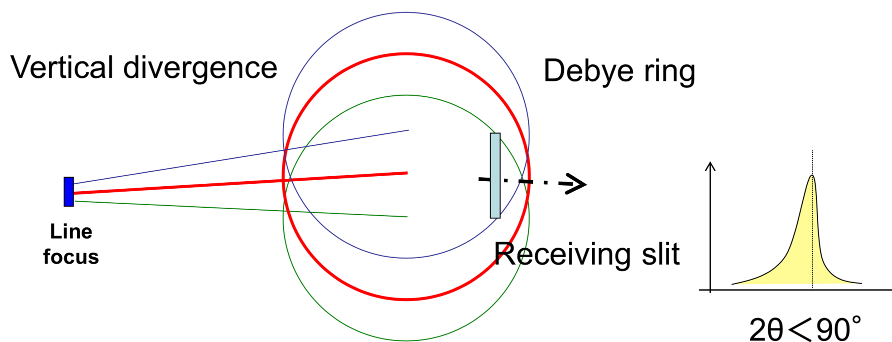

Fig. 2.35 - Umbrella effect. As taken from [264].

The correction of sample displacement/misalignment can be done just by the correct and accurate procedure of sample alignment. In Rigaku SmartLab, the alignment procedure is automated and depends on the type of the sample and experimental tasks. For precise X-ray diffraction analysis of thin films and coatings the sample should be well aligned to the goniometer system and X-ray beam. Special alignment procedure designed for such tasks was used. The dialogue window of its configuration is shown in Fig. 2.36.

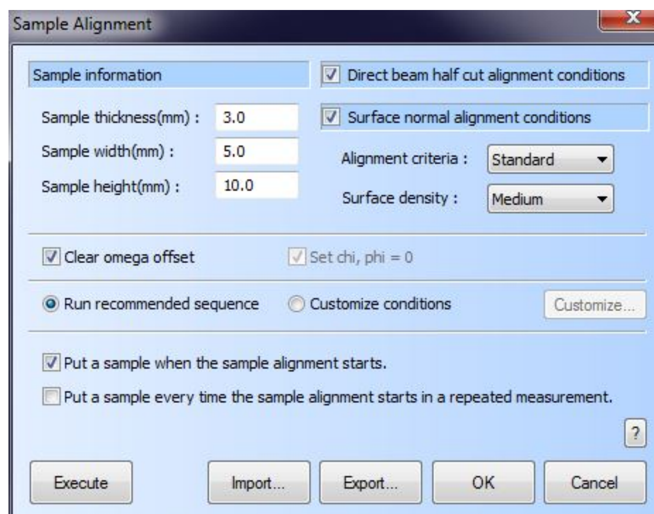

Fig. 2.36 - Window of sample alignment configuration.

Direct beam half-cut alignment is the basic procedure of the alignment. With Z-scan (high scan) the position at which the incident X-ray beam is blocked and reduced to 50% intensity by the sample is determined (Fig. 2.37a). Then, at identified Z-axis position, the omega scan is performed keeping the detector coupled with X-ray source at one line for direct beam conditions. This will determine the omega position (profile peak position) at which the incident X-ray beam is parallel to the sample surface (Fig. 2.37b). This sequence should be repeated and finalised by another one Z-scan at smaller scanning range and scan-step. After the alignment has been completed, the sample surface must be parallel to the incident X-ray beam and coincidental with the centre of rotation of the goniometer axes (Fig. 2.37c). When a precise sample alignment is required by the application, the surface normal alignment should be executed.

During the procedure of surface normal alignment 2-theta/omega axes drive to the scattering angle 2θ determined by the sample surface density, usually from 0.2 to 0.6, and ω-axis scan is performed to determine the position (profile peak position) at which the incident angle of the X-ray beam on the sample surface equals half of the 2-theta scattering angle (Fig. 2.37d). Then the determination of the position (profile peak position) at which the sample surface coincides with the centre of rotation of the goniometer axes at a defined ω angle by Z-scan occurs. These two steps were repeated 2 times (corresponds to the standard alignment criteria but may be repeated up to five times until the alignment results converge, which is the precise alignment criteria). After the alignment has been completed, the incident and exit angles of the X-ray beam on the sample surface are identical and equal to half of the scattering angle. The sample surface also coincides with the centre of rotation of the goniometer axes [269].

Described above is the general sample alignment sequence. Although only an example of the medium resolution parallel beam/RS optics is shown here, the basic alignment sequence is the same for other optics.

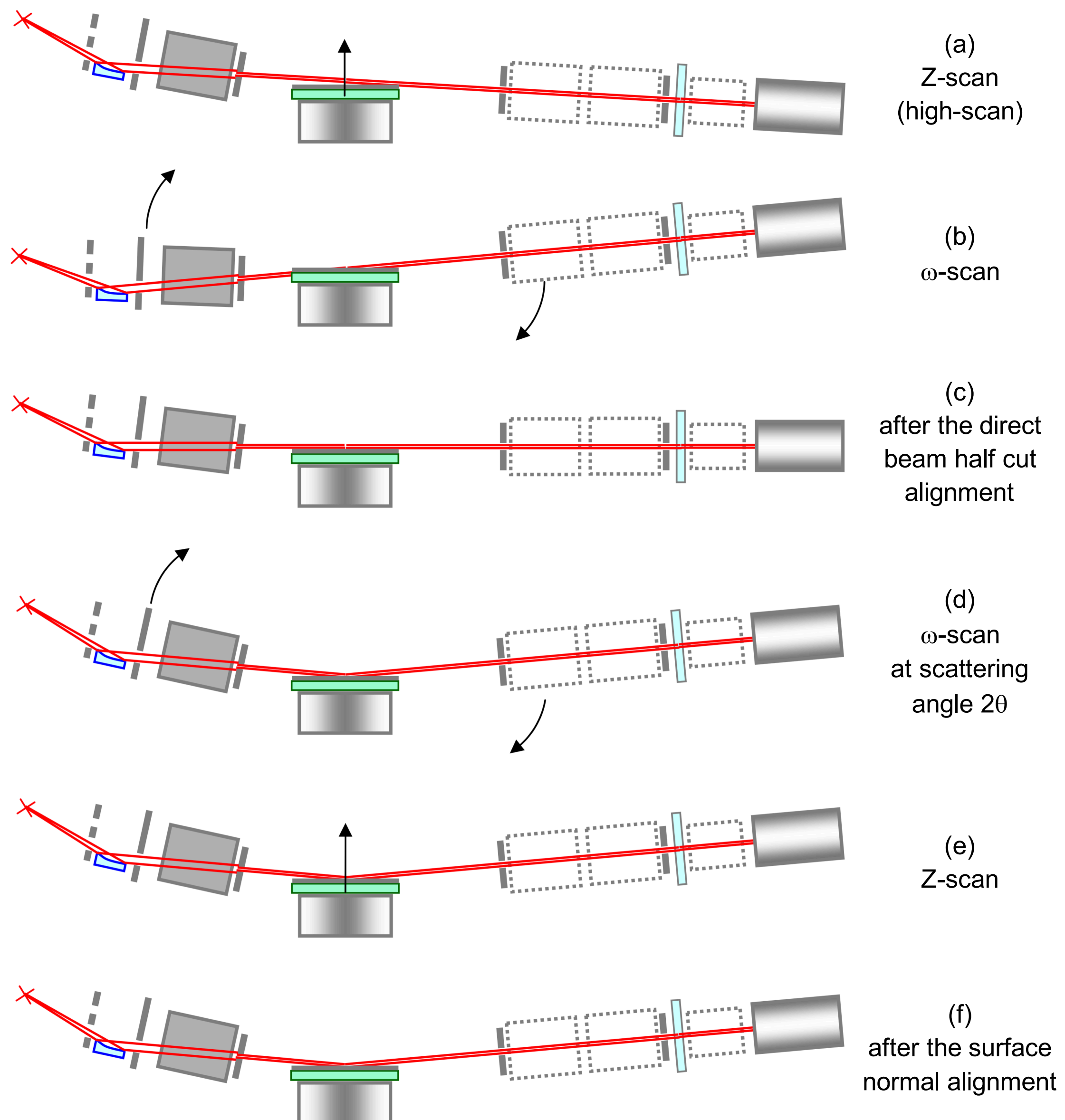

Fig. 2.37 - Sample alignment sequence for thin films and coatings for Rigaku SmartLab [269].

2.3.5. X-ray Diffraction Data Analysis Methods and Software

Phase identification was done with reference to ICDD Powder Diffraction Files No. 00-006-0694 for Cr (bcc), No. 00-042-1120 for Mo (bcc), No. 00-011-0065 for CrN (fcc), No. 00-035-0803 for β-Cr_2N (hexagonal), No. 00-025-1366 for γ-Mo_2N (fcc) and No. 00-025-1368 for β-Mo_2N (tetragonal) [270]. The phase identification, profile fitting, determination of peaks positions (their deconvolution, if necessary) and values of full width at half maximum (FWHM) were performed using the Crystal Impact's software "Match!" and Rigaku SmartLab Guidance.

The evaluation of crystallites sizes was carried out using the Scherrer Equation (2.3) [271]:

$$d = \frac{K\lambda}{\beta \cos \theta}, \tag{2.3}$$

where d is a mean size of the ordered (crystalline) domains, which may be smaller or equal to the grain size, in Å; λ is an X-ray wavelength, in Å; β is a line broadening at half the

maximum intensity (FWHM) in radians; θ is the Bragg angle, in radians; K≈0.89 is a dimensionless shape factor depending on (hkl) Miller indexes. Any additional factors, such as instrumental effects, microstrain, solid solution inhomogeneity or any other factors which can contribute to the width of a diffraction peak besides crystallite size were not considered while performed these calculations.

2.3.6. Residual Stresses Measurements

In a contrast to many other methods, X-ray diffraction-based approach is a non-destructive method to measure residual stresses. When the stress is present the lattices are strained, which results in changes in lattice parameter and d-spacing values. Uniform strain affects d-spacing and shifts diffraction peaks positions, and non-uniform strain can additionally change the peak shape, as shown in Fig. 2.38.

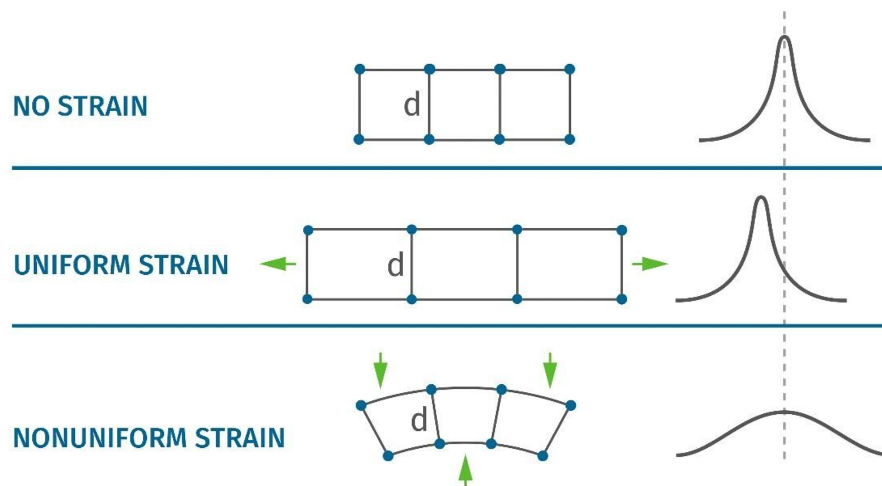

Fig. 2.38 - Strain and stress effects on the diffraction peaks. As taken from [272].

The calculations are based on the strain values obtained from the diffraction data and on the elasticity theory. The strain ε can be measured by XRD if the unstrained interplanar spacing d_0 is known, when d_n is a strained interplanar spacing:

$$\varepsilon_z = \frac{d_n - d_0}{d_0}. \tag{2.4}$$

This equation (2.4) gives the information from the XRD measurements taken at conventional θ/2θ mode when the diffraction vector is normal to the surface. By tilting the sample, the measurement of planes at an angle ψ is possible and the calculation of strain along that direction can be performed:

$$\varepsilon_{\phi\psi} = \frac{d_{\phi\psi} - d_0}{d_0}. \tag{2.5}$$

From Hooke's law and elasticity theory, assuming that the stresses are biaxial, the stresses can be evaluated by the following equation [273]:

$$\sigma_\phi = \frac{E}{(1+\nu)\sin^2\psi}\left(\frac{d_\psi - d_n}{d_n}\right), \tag{2.6}$$

where ν is Poisson's ratio, and E is Young's modulus for the material.

The most widely used method for residual stresses calculation by XRD is named the $\sin^2\psi$ method. A set of asymmetric XRD 2θ scans was made at several fixed ψ angles (as GIXRD) assuming zero values of φ and χ angles [273–275], and then the calculated interplanar distances are plotted vs $\sin^2\psi$ values. By the obtained line (see Fig. 2.39) the stress can be determined qualitatively and quantitatively. A zero stress is assumed at $d=d_n$, when the line crosses the Y-axis.

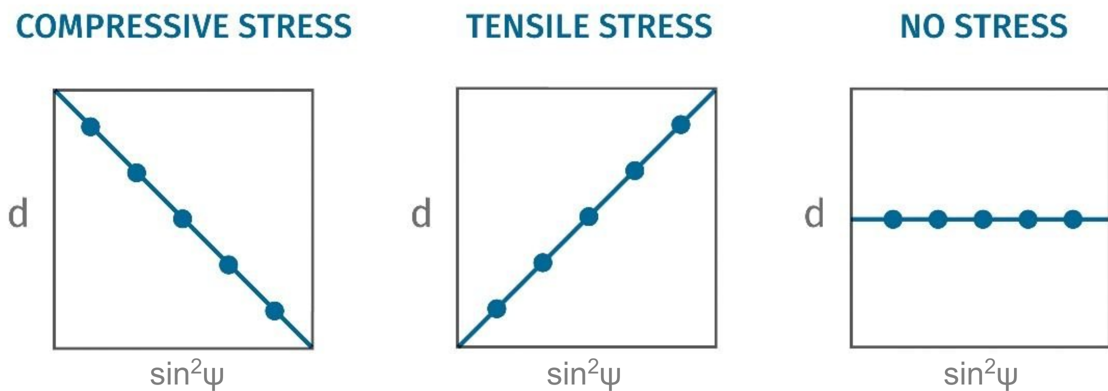

Fig. 2.39 - Examples of d-spacing vs $\sin^2\psi$ plots for residual stresses evaluation. As taken from [272].

Thus, the stress is given by

$$\sigma_\phi = \frac{m}{d_0}\left(\frac{E}{1+\nu}\right), \tag{2.7}$$

when m is the slope of the plotted line and d_0 is the value of unstrained interplanar distance, which both can be obtained from the equation of the plotted trend line.

The scheme of the experiment is shown in Fig. 2.40. Since the diffracted X-ray beam signal is collected mostly from the top layers of the deposited coatings (GIXRD instead of θ/2θ mode with ω offset), the method gives an advantage in the peak deconvolution process in contrast to the conventional integral XRD pattern with overlapped peaks corresponding to the similar crystal structure of the phases from the layer of the multilayer coating. The angle ψ was calculated as $\psi = \theta - \omega$ for each diffraction peak.

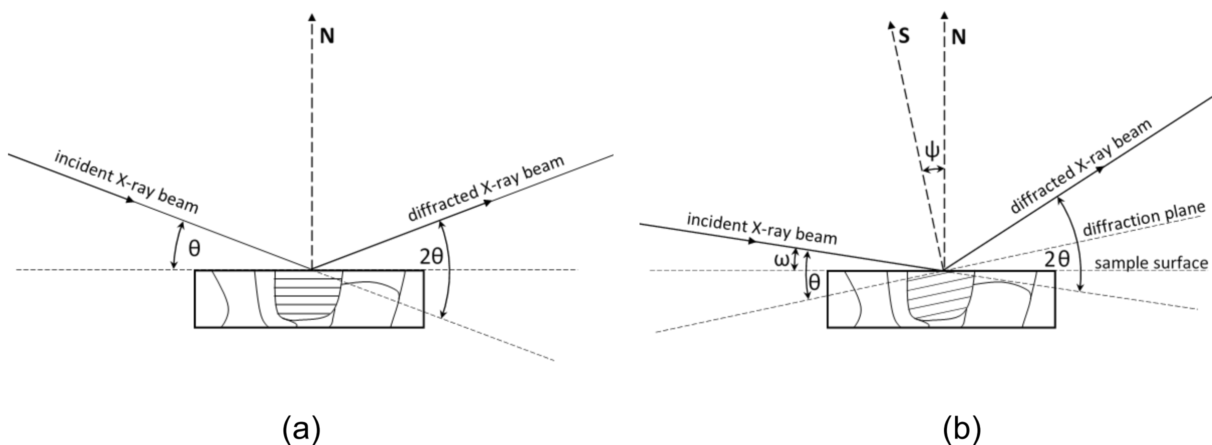

Fig. 2.40 - X-ray diffraction analyses: (a) conventional symmetric θ/2θ scan, (b) asymmetric 2θ scan with fixed position of the X-ray source. Published in [214].

2.4. Electron Backscatter Diffraction

2.4.1. Introduction to the Electron Backscatter Diffraction Technique

Electron Backscatter Diffraction (EBSD) technique has become a standard characterisation method for bulk materials in the last two decades [276–278]. The lateral resolution of modern EBSD systems operated in a field emission gun (FEG) SEM allows to determine structural elements as small as 20 nm in diameter [278–280] and, thus, enables the application of this technique to thick films and protective coatings, which widely occurs nowadays. EBSD technique is based on capturing the patterns on phosphor screen formed by backscattered electrons diffracted from lattice planes of crystalline specimens. Transmission or scanning electron microscopes are usually used as a source of the focused electron beam with facilities to observe a sample by standard means when equipped with a special EBSD detector for analysis.

In backscattering, a primary electron from the incident beam travels close to the nucleus of the atom and changes its trajectory by the force of the electrostatic field of the positive nucleus. This event is named an elastic scattering. Elastically backscattered electrons have the same energy as incident electrons and, thus, emerge from deeper layers of the subsurface zone of the sample. Depending on the size of the atomic nuclei, the fraction of backscattered electrons differs – the higher size, the higher number of backscattered electrons. The number of backscattered electrons escaped from the material depends significantly on the inclination angle of the incident electron beam. Fig. 2.41 shows the Monte Carlo simulation of backscattered electrons emission and escape for aluminium with an incident beam energy of 15 keV at various inclination angles with 200 trajectories. This qualitatively reveals the increase of backscattering rate and escape of BSE in the direction of the incident electron beam. More extensive simulations with 25 thousands of trajectories show that the ratio N_{BSE}/N_B changes from 0.129 to 0.242 and 0.531 with the change of tilt angle from 0° to 45° and 75° respectively, where N_B is the number of electrons entered the specimen from the incident beam and N_{BSE} is the number of those electrons that subsequently emerge from the surface of the specimen as backscattered electrons [281].

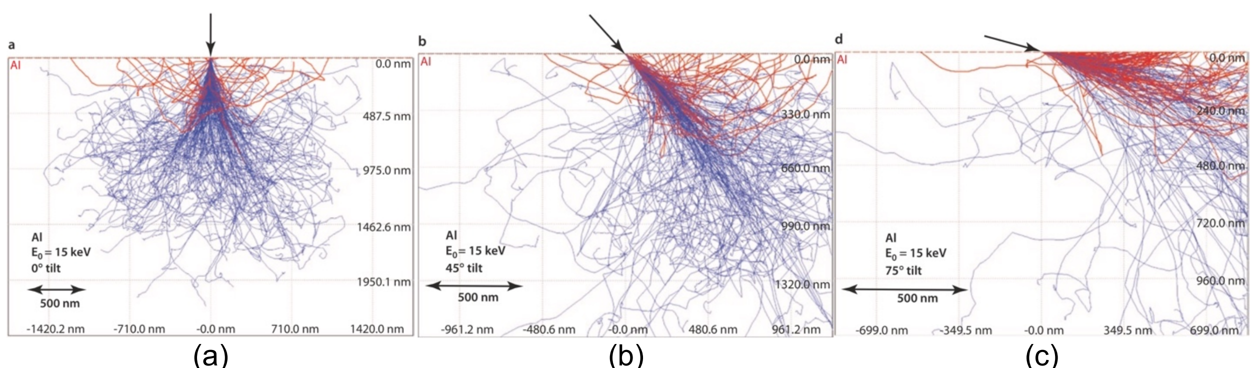

Fig. 2.41 - Monte Carlo simulation of backscattered electrons emission and escape from aluminium at various tilt angles of the incident electron beam. The simulation was performed for the electron beam with energy E0 = 15 keV and tilt angles of 0° (a), 45° (b) and 75° (c). As taken from [281].

In most of the modern scanning electron microscope-based EBSD analysis systems, the specimen placed in the sample holder is tilted typically by 70°, which in turn gives 20° between the incident electron beam and the specimen surface, as shown in Fig. 2.42 (c, f). Such orientation of the specimen ensures a sufficient number of backscattered electrons emerging from the surface towards the EBSD detector. Generally, Fig. 2.42 (a-c) schematically demonstrates the positioning of electron beam interaction volume in the matter and the paths of backscattered electrons at different inclination angles of the specimen. Fig. 2.42 (d-f) additionally shows the intensity distribution for backscattered electrons depending on the orientation of the sample.

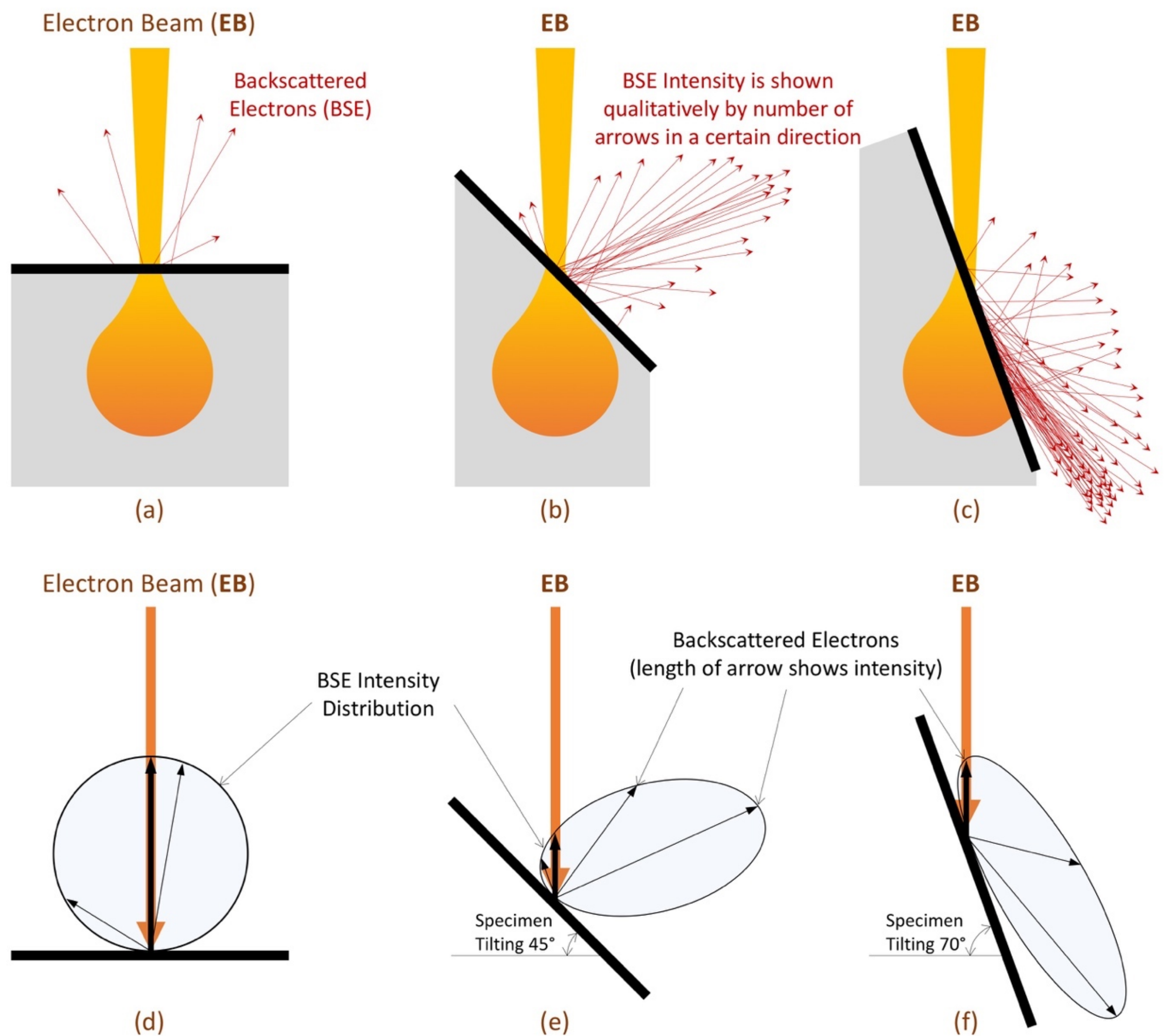

Fig. 2.42 - Emission and escape of backscattered electrons from in SEM depending on tilting angle of the specimen. Adapted from [240].

Backscattered electrons escaped from the surface of crystalline material under certain conditions may form diffraction patterns called Kikuchi patterns, firstly discovered by Shoji Nishikawa and Seishi Kikuchi in 1928, on the phosphor screen of the EBSD detector (see Fig. 2.43). They consist of Kikuchi lines and bands diffracted from the lattice planes and arranged to each other in a unique way inherent to the specific crystal structure type and crystal orientation.

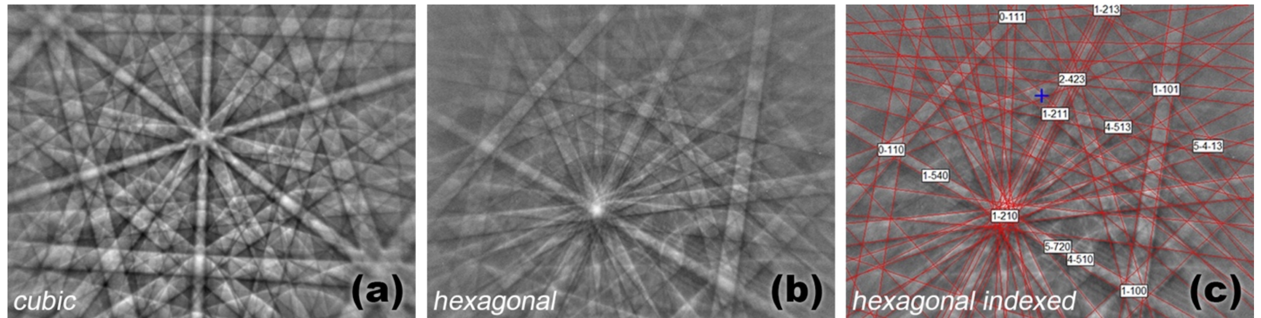

Fig. 2.43 - Examples of Kikuchi patterns. EBSD patterns were obtained from cubic (a) and hexagonal (b, c) crystal systems [282].

The process of EBSD patterns formation may be described by two steps (see Fig. 2.44). Firstly, the primary electron beam enters the material at angle *α* and quasi-elastic incoherent scattering of these electrons occurs. The electron beam travels inside the material a distance of r/sinα until it has reached a maximum depth *d* below the surface of the sample from where backscattered electrons may come out. Length *r* defines approximately the spatial resolution of the EBSD technique for selected material, accelerated voltage and incident angle of the electron beam. Incoherently scattered electrons emerge from a very small volume in the crystal and have large directional distribution as shown in Fig. 2.42 and Fig. 2.44.

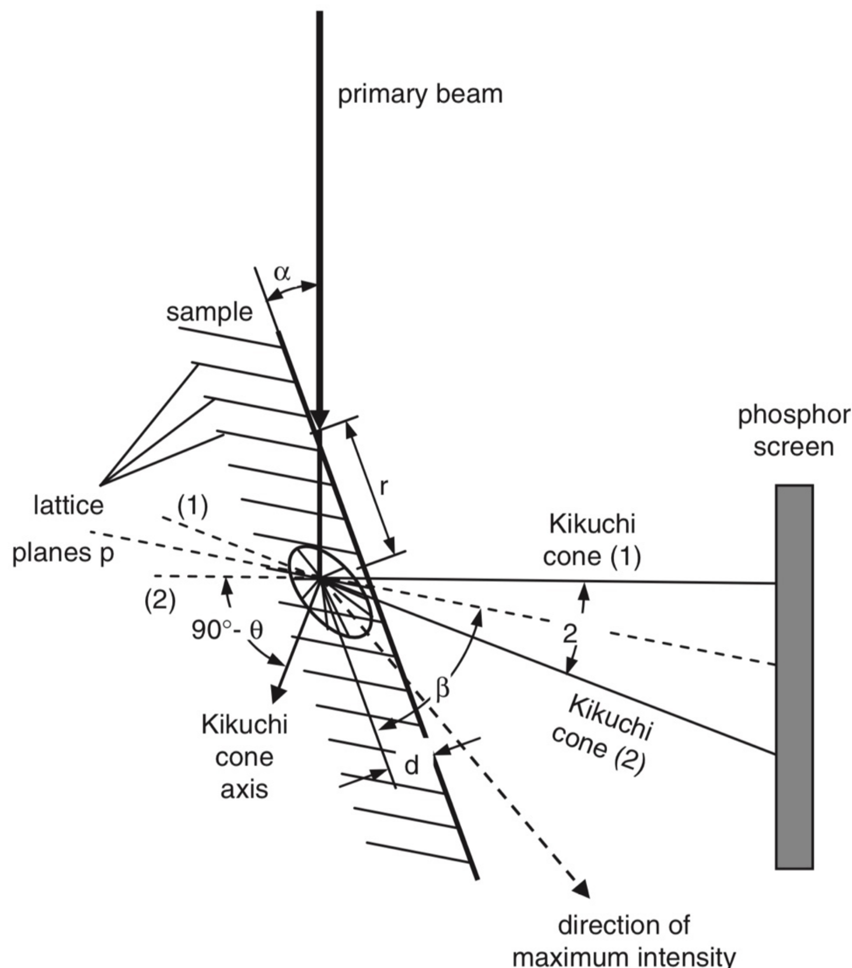

Fig. 2.44 - Scheme of EBSD pattern (backscatter Kikuchi pattern) formation. As taken from [283].

For the next step, this can be considered as a secondary source of electrons. There are always some electrons from this point-type source arriving at Bragg condition at every set of the

nearby lattice planes (Fig. 2.45). They form pairs of cones with a large opening angle of 180° − 2θ and the cone axis are perpendicular to the diffracting lattice planes [283]. According to the Bragg's law and a typical accelerating voltage of electrons for EBSD analysis in SEM of 15-30 kV, the diffraction angle supposed to be small. For 20 kV and interplanar spacing of 0.2 nm the Bragg angle is 1.24°, for 5 kV (some high-resolution EBSD technique) the diffraction angle is about 2.48°. Therefore, obtained cones (Kossel cones, or Kikuchi cones) are very large. They cut an observation plane (e.g. phosphor screen in case of EBSD detector) positioned tangentially to the propagation sphere of the electrons in almost straight and parallel pairs of Kikuchi lines [283].

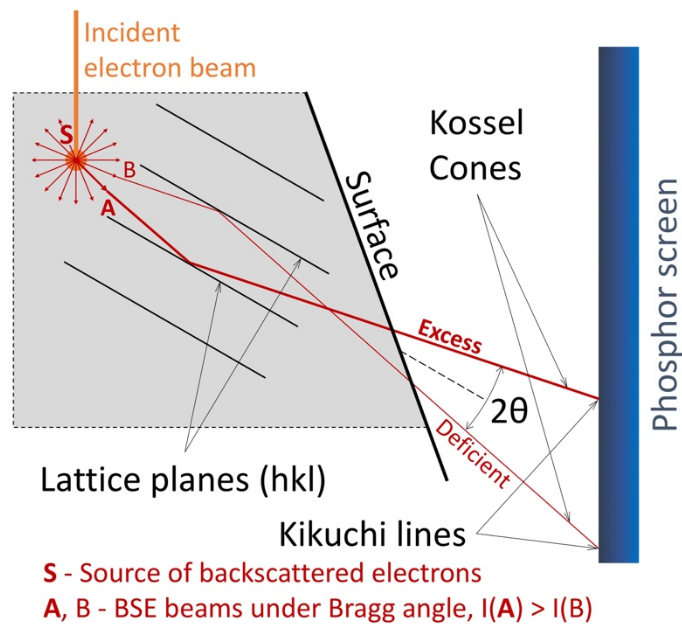

Fig. 2.45 - Origin of Kikuchi lines from EBSD. Based on [284].

The cones leave the surface approximately at the angle *β*, which corresponds to the orientation of diffracting planes family. The path length of the coherently scattered electrons (second step) until they are evacuated from the material is *d/sinβ*. For the angle *β* equal to the incident electron beam angle *α* the intensity of electrons flow is maximum, in the reflection direction of the primary beam (see "direction of maximum intensity in Fig. 2.44) [283]. As seen from Fig. 2.45 the path *A* of electrons is closer to the direction of maximum intensity, while path B brings less intensity of electrons, therefore they will result in cones of electrons with different intensities. In turn, Kikuchi lines with different intensities will be registered on the phosphor screen: excess line is brighter, and the deficient line is darker. The area between those two lines is also illuminated on the analyser screen and called Kikuchi bands. Their occurrence at EBSD patterns is not an easy process which still has several explanation theories so far. They are well discussed and reviewed in the literature, e.g., by S. Zaefferer [283] who concluded that the phenomenon of Kikuchi bands formation can only be explained on the basis of the Bloch wave theory and incoherent scattering process based on thermal diffuse scattering.

Although EBSD patterns are formed by backscattered electrons, the signal doesn't come from the whole BSE interaction volume (1-2 μm depth), but just from the top few nm. Therefore,

the EBSD technique may have a very high resolution of less than 20 nm, depending on other conditions and acquisition parameters.

For EBSD analysis running in SEM system, the acquisition of Kikuchi patterns occurs point-by-point for the full selected region of the specimen with a defined step, exposure time and other parameters. When the automated run of collecting EBSD patterns is finished, all data necessary for further analysis is received. With modern EBSD data analysing software, in most of the cases, it is possible to obtain a complete characterisation of the microstructure of the specimen: phase distribution, texture strength, grain size, boundary properties, misorientation data and much more.

2.4.2. Experimental Details

The electron backscatter diffraction (EBSD) analysis was carried out using the unit of EDAX EBSD forward scatter detector system and high-resolution DigiView III camera attached to FEI Quanta 400 Field Emission Gun (FEG) Environmental SEM (ESEM). The DigiView is a versatile high-resolution digital camera. The CCD sensor with a resolution of 1.4 megapixels (1392×1040) has a particularly high quantum efficiency, peaking in the blue-green spectrum for use with an optimised phosphor screen coating, resulting in higher sensitivity for EBSD applications. Noise is significantly reduced using a single-stage Peltier cooling system that does not require a cooling fan. The DigiView EBSD camera is designed to serve a wide range of EBSD applications [285]. Electron beam accelerating high voltage was 15 kV, spot size 5, aperture number 3. Low-vacuum mode with a pressure of 20 Pa was used. Exposure time was 0.1 s per point with step a size of 0.05 μm, gain 12, binning 4×4 (effective CCD resolution 348×260, hexagonal scanning grid. Binning the CCD makes the camera effectively more light-sensitive, which leads to the increase of achievable frame rates (less exposure time for each point while brightness is maintained at the same level). Hexagonal grid instead of standard square analysis grid in traditional SEM imagining, which doesn't provide a constant point-to-point distance between all adjacent measurements and leads to the artefacts in the determination of the grain shapes and statistical analysis of triple grain junctions, allows an optimum measurements density of an area and precise grain boundary reconstructions.

The experiment was performed on polished cross-sections of multilayer films with 5.3×15 μm^2 are selected for the analysis at each sample of Series 1. It should be noted that the diffraction patterns (Kikuchi patterns) were observed only for CrN layers in all samples. After discussion with experts, it was concluded that MoN layer may not give EBSD signal due to the features of cross-section samples preparation (polishing stage) related to the difference in hardness of CrN (harder) and MoN (softer) phases, which may damage the surface of the last one.

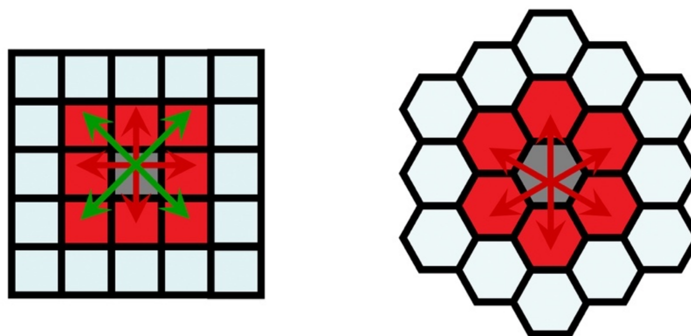

Fig. 2.46 - Comparison of square and hexagonal scanning grids for EBSD analysis [286].

The calculation of the grain size values, as well as other analyses of EBSD data, was performed using specialised Analysis System software “OIM (Orientation Imaging Microscopy) Analysis” of EDAX TEAM™ (AMETEK, Inc.). The grain tolerance angle of 5° was used for grains determination. Grains at edges of scans were not included in statistics.

2.5. Transmission Electron Microscopy

Transmission electron microscopy is a very powerful tool for material science as a technique with the highest spatial resolution for imaging and local diffraction. Thus, it fits nicely for analysis of internal micro- and nanostructure of the specimen, characterisation of particles, fibres, thin films and interfaces in multi-layered structures, imaging of atoms [235]. However, the final quality, magnification and resolution of the image depends on many factors as electron beam stability, electromagnetic optics and used parameters, surrounding environment, quality of the sample preparation, its elemental composition and structure etc.

2.5.1. Basic Parts of Transmission Electron Microscope

A schematic illustration of key components of a transmission electron microscope (TEM) is shown in Fig. 2.47. It comprises the electron gun, electrostatic and electromagnetic lenses of illumination before and image-formation systems after the specimen, specimen stage, transmitted electrons detection and image recording systems. The microscope usually may be equipped with additional analysing systems and detectors, e.g. for X-ray microanalysis by EDS or WDS. The latter is used very rarely as a practical microanalytical solution.

2.5.1.1. Electron Sources for TEM

Electron sources employed in TEM systems are actually the same types as used in SEM and already discussed in Chapter 2.1.3 about the sources for scanning electron microscopy: thermionic sources (tungsten, LaB_6 or CeB_6), field emission (tungsten tip) and Schottky field emission guns (tungsten tip or filament coated with zirconium oxide). Tungsten thermionic source is the worst for TEM in most respects and nowadays is almost not used. Table 2.2 contains most of the important characteristics for all mentioned electron sources. Please, note that all values are given for 100 kV accelerating voltage and, thus, some characteristics are different from those presented in Table 2.1 in the chapter dedicated to the scanning electron microscopy.

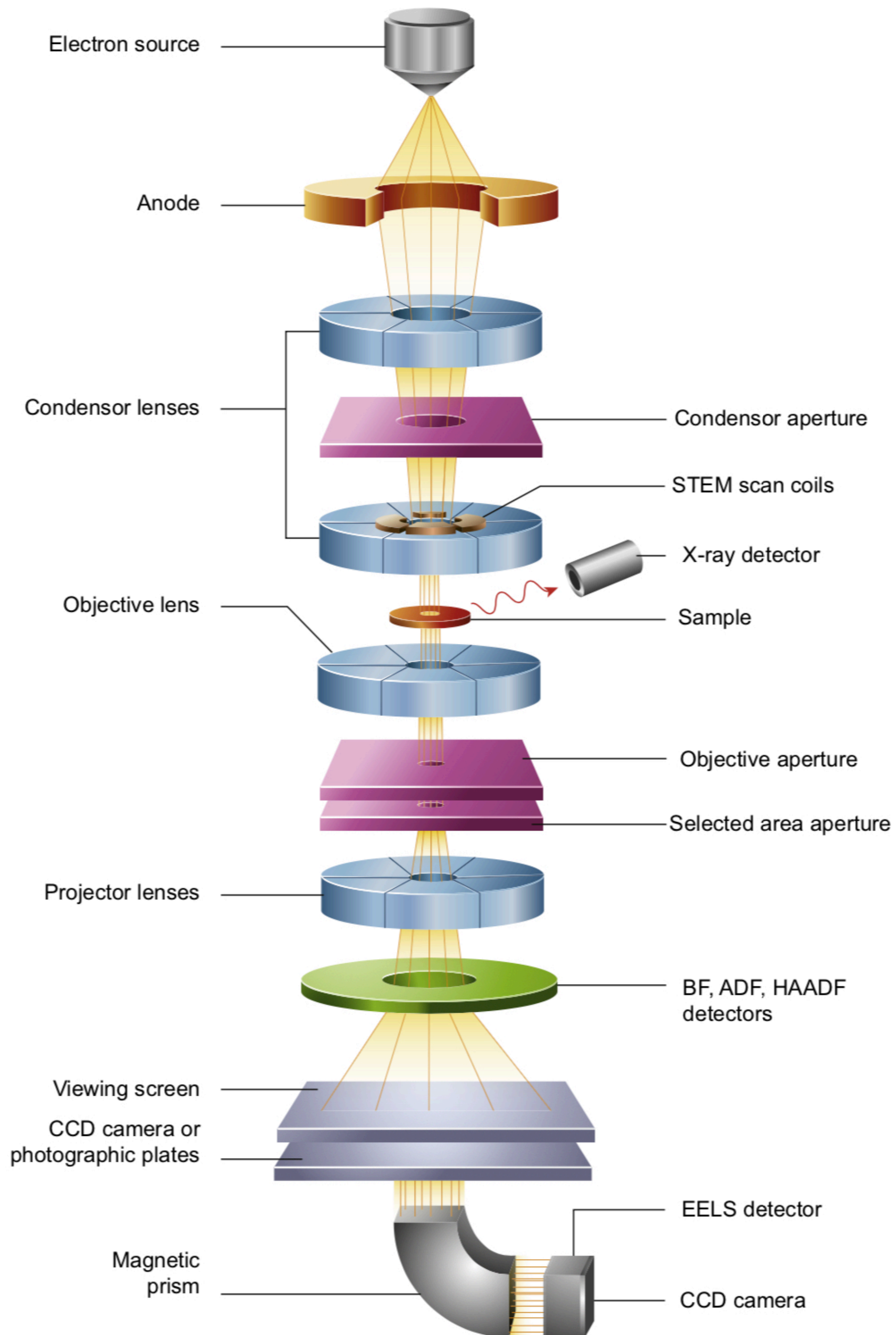

Fig. 2.47 - Basic Components of Transmission Electron Microscope (TEM). As taken from [235].

LaB_6 electron source has increased brightness, higher coherency and longer life in comparison to tungsten. It also should be operated under higher vacuum, which improves most aspects of TEM performance as well [287]. Depending on the main tasks and applications required from the TEM device, one of three main electron sources may fit the best. In field emission sources the current density and brightness are much higher, so for the applications that

need a bright coherent source (analytical electron microscopy (AEM), high-resolution transmission electron microscopy (HRTEM), electron holography etc.) they are the best solution. Cold FEGs have highly spatially coherent beam and the resulting energy spread is the smallest available without monochromator [287]. This is very important for electron energy loss spectroscopy (EELS) or for ultra-high-resolution scanning transmission electron microscopy (STEM) imaging and X-ray analysis with the brightest and the smallest probe. For routine work Schottky gun is more stable and easier in operation. In case of daily work with relatively low magnification TEM imaging (up to ×100k) LaB_6 sources may be better than FEGs, since the latter have too small crossover size to illuminate the specimen with no loss of current density and intensity of the image. However, with modern software and automatic computer control of many processes, FEG TEM systems give the optimal analytical performance and best high-resolution imaging [287]. Emitted electrons are then accelerated to the working energies by the voltage of 80-300 kV. Such electron beam is able to pass through up to 1 μm of material. The typical accelerating voltage for routing imaging is 200-300 keV, while lower energy about 100 keV is used for the analysis of very light elements to reduce specimen damage [235].

Table 2.2. Characteristics of the Principal Electron Sources for TEM (data is for 100 kV acceleration voltage) [287].

	Units	Tungsten	LaB_6	Schottky FEG	Cold FEG
Work function, Φ	eV	4.5	2.4	3.0	4.5
Richardson's constant	A/m^2K^2	6×10^9	4×10^9		
Operating temperature	K	2700	1700	1700	300
Current density (at 100 kV)	A/m^2	5	10^2	10^5	10^6
Crossover size	nm	$> 10^5$	10^4	15	3
Brightness (at 100 kV)	A/m^2sr	10^{10}	5×10^{11}	5×10^{12}	10^{13}
Energy spread (at 100 kV)	eV	3	1.5	0.7	0.3
Emission current stability	%/hr	< 1	< 1	< 1	5
Vacuum	Pa	10^{-2}	10^{-4}	10^{-6}	10^{-9}
Lifetime	hr	100	1000	> 5000	> 5000

2.5.1.2. Electron Optics and Imaging Systems

The electron beam passes a set of electromagnetic lenses on his way to the specimen and, thus, transmitted, to the detectors where the image is formed. Condenser lenses and aperture focus the electrons into a beam of controlled diameter and convergence which then goes through the specimen. Additional lenses (usually a pair of scan coils) are installed before the specimen for the beam alignment, its control for STEM mode, or for special diffraction techniques etc.

The combination of the objective lens and the specimen stage is a very important component of the microscope. The objective pre-field, not shown in the figure, serves to form the final electron beam, which could be a parallel beam or a crossover of larger or smaller spot size. Special stigmator is placed behind the objective lens to correct aberrations.

Special stage is used to deliver the specimen holder into the correct position. The stage provided X-Y orthogonal axes movements in the specimen plane in a range ≈1 mm from the

centre position. There is eucentric goniometer available in TEM, and it allows to tilt and rotate the specimen (angle may be limited by the pole pieces of the objective lens) in such manner that every part of the specimen can be examined at a variety of angles while the area of interest is always adjusted so that it stays illuminated and in focus. Most of the specimen holders are designed for dimensions of specimen up to 3 mm in diameter and 200 μm thickness. Some objective lenses with wide-gap objective lenses allow up to 5 mm in size, but the requirement of electron transparency for the specimen still exists [235].

Transmitted electrons are focused by the objective lens and form the diffraction pattern and first image. Then the image or diffraction pattern is magnified onto the detection system by projector lenses. The image can be monitored live on a phosphor screen or a wide-angle camera. All modern TEM systems are equipped with digital electron detection systems. The most commonly used are the charge-coupled device (CCD) detectors, where the signal of incident electrons, firstly converted into light, is conversed to an electron charge of an array of separated MOS capacitors (pixels) which then is recorded into a digital image.

2.5.2. TEM Imaging Concepts

Many TEM data viewing modes have been developed so far to obtain as much as possible information from the specimen. There are many books published and dedicated to each of such techniques as they have their own features and details to operate. Basically, there are two main TEM modes: diffraction pattern (DP) mode and imaging mode. The basic principles of electron optics functions and electron beam trajectories for these two main modes are schematically shown in Fig. 2.48. Only some basic techniques of TEM diffraction and imaging modes, which then are used in the experimental part of this Thesis research, will be discussed in this Chapter.

2.5.2.1. Selected Area Electron Diffraction (SAED) Mode

Electrons elastically scattered from certain atomic planes of the specimen change their direction but do not change their wavelength. Constructive and destructive interferences of coherent elastically scattered electrons will produce beams of high intensity at specific angles to the incident electron beam, in a similar way to the X-ray diffraction. This characterises crystal structure of the specimen and specific diffraction planes orientation. Such diffracted electron beams may be focused by the electron optics to form an electron diffraction pattern, as shown in Fig. 2.48 (left). The diffraction pattern will contain electrons from the whole illuminated area of the specimen. Usually a diffraction pattern from smaller specific areas is required.

For this, there are two ways of the illuminated area size reduction: converging the electron beam to make it smaller or cut some part of the electron beam flow by introducing a special aperture. The first approach of beam converging destroys the electron beam parallelism and, hence, ruins the quality and sharpness of the resulted pattern. Moreover, high-intensity beam in some cases is undesirable, e.g. it may saturate the CCD camera [288].

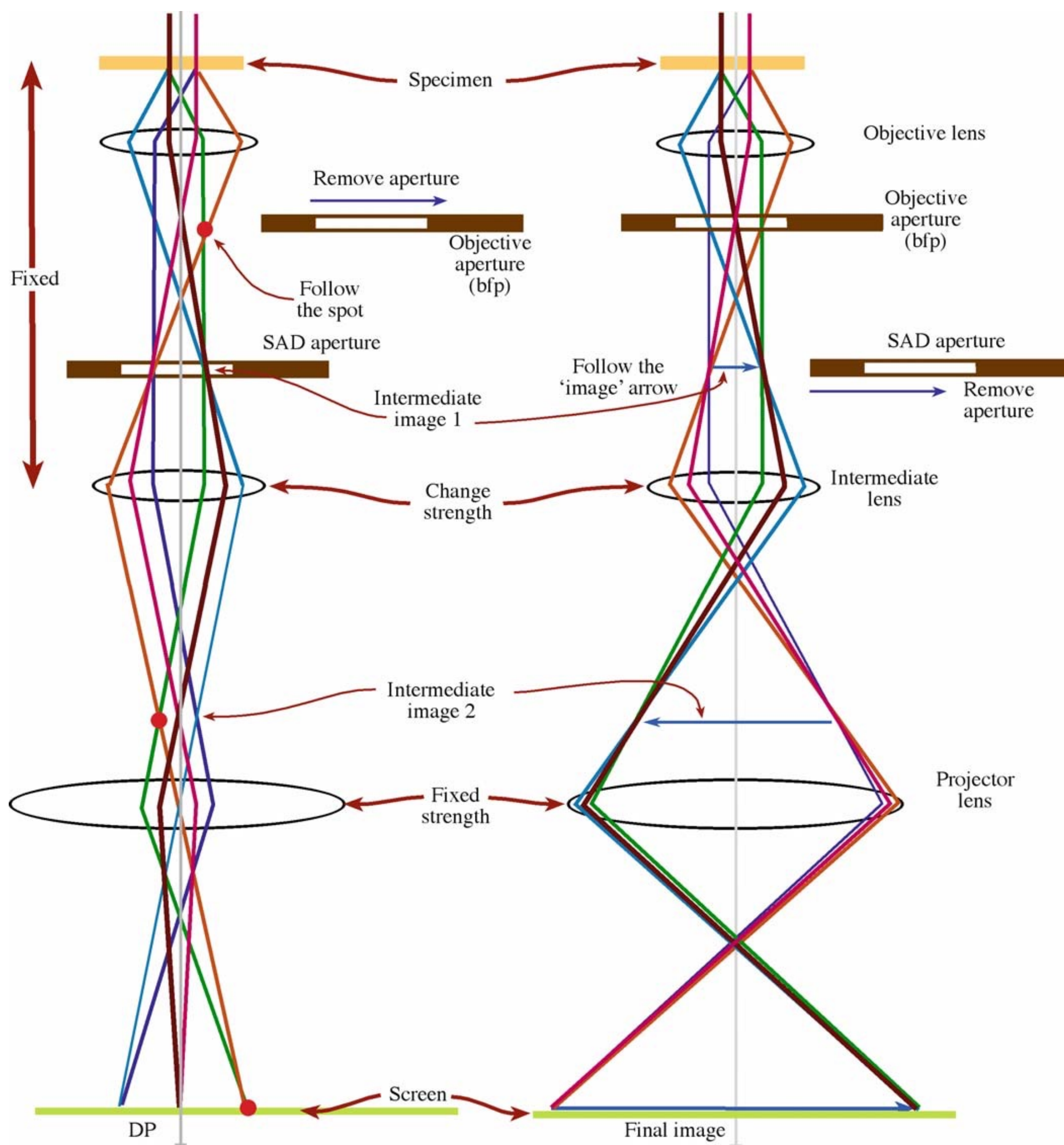

Fig. 2.48 - Schemes of electron optics and electron beam trajectories for diffraction pattern (DP) and imaging TEM-modes (left and right figures respectively). As taken from [288].

The second approach of using selected area aperture is the standard method to obtain the diffraction pattern, which is called selected area electron diffraction pattern (SAED, SAD or SADP). SAED aperture is placed in one of the image planes of an imaging lens and creates a virtual aperture at the plane of the specimen, since it is not possible to insert a physical aperture at the specimen plane (see Fig. 2.49) [288]. Under these conditions, when the SAED aperture is inserted and the objective aperture is removed, all electrons outside of the selected area will be blocked by the diaphragm at the image plane and they will not contribute to the resulted diffraction pattern. Some examples of SAED patterns are shown in inserts of Fig. 2.50. Central bright spot corresponds to the directly transmitted electron beam and the rest of the points are electron diffraction beams resulting in the specific patterns characteristic for each material, phase and crystal structure.

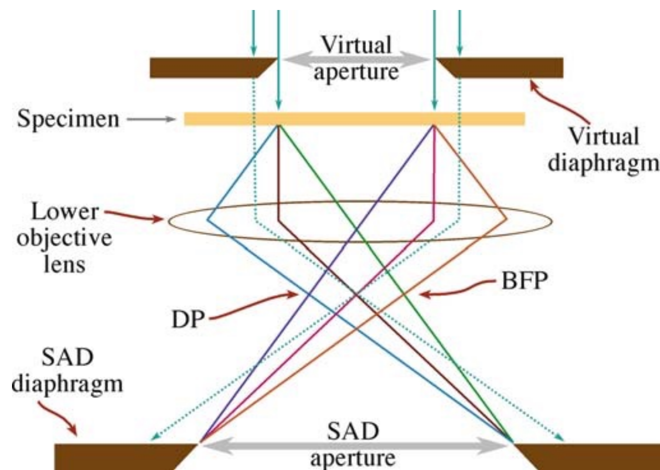

Fig. 2.49 - Formation of a virtual aperture in the plane of the specimen by an aperture in the image plane. As taken from [288].

Detailed analysis of electron diffraction patterns can give information about the crystallography of the selected area of the specimen, such as lattice type, point group, lattice parameters, crystal orientation, phase composition and their orientation relationships [235]. SAED pattern analysis directly correlates with images or chemical information obtained by the other TEM techniques in the same area of the specimen.

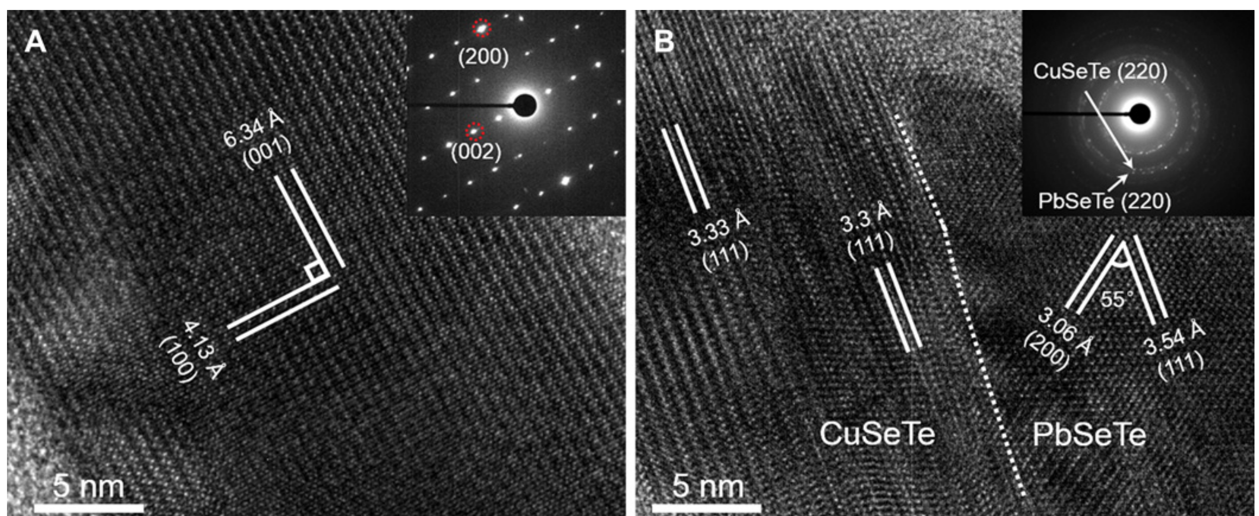

Fig. 2.50 - HRTEM images and SAED patterns (insets) of AgCuSeTe and CuSeTe/PbSeTe nanowires. As taken from [289].

2.5.2.2. Bright-Field and Dark-Field TEM Imaging

Electrons travelling through the thin specimen are transmitted directly (unscattered) or scattered either elastically or inelastically and move at some angle to the axis of the electron beam. When an image is formed in TEM, the central spot or scattered electrons are used. By inserting an objective aperture positioned in the back focal plane (see Fig. 2.48, right) scattered electrons can be blocked and the bright-field (BF) image will be formed only by unscattered electrons, as shown in Fig. 2.51 (a).

Zones of the specimen where the electrons are actively scattered give fewer electrons to the BF-image and, thus, appear in darker contrast. Locally increased electron scattering, particularly inelastic scattering, coming from microstructural features of the specimen, such as grain boundaries, dislocations, increased thickness, density or atomic number, can be recognised

by darker areas of BF TEM-image. Strong elastic Bragg scattering also appears dark, which can be used for the identification of changes in grains orientation and grains boundaries [235].

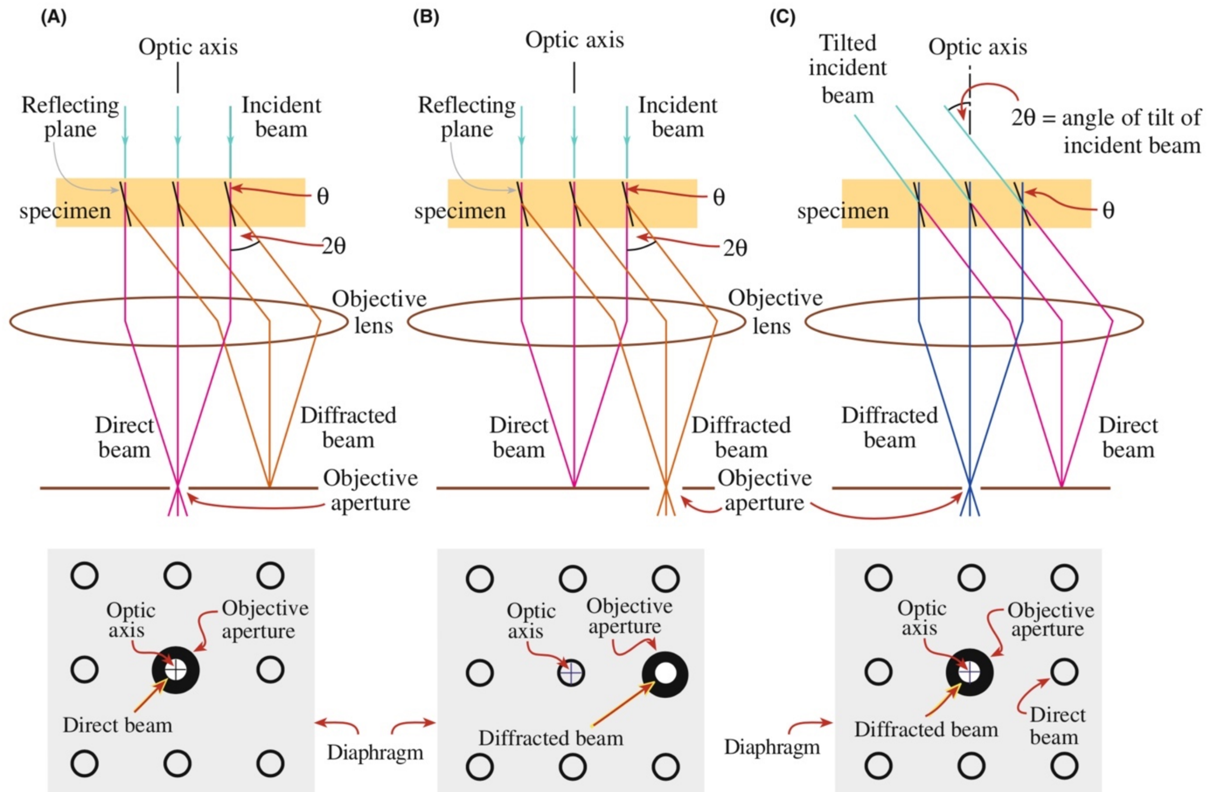

Fig. 2.51 - Ray diagrams showing how the objective lens and objective aperture are used in combination to produce BF (a), displaced-aperture DF (b) and centered DF (c) TEM-images. As taken from [288].

When the objective aperture placed in the back focal plane is adjusted so that it blocks unscattered electrons, the dark-field (DF) image is formed by scattered electrons (see Fig. 2.51, b). DF-images are used to show the regions of the specimen, which generate specific electron scattering that passes the aperture and appear bright in the image [235]. There is one more approach to form DF-image called centred dark-field (CDF) imaging, when the electron beam is tilted in such manner that the beam of the scattered electrons goes towards the central on-axis position as shown in Fig. 2.51 (c) [288]. This method was aimed to avoid aberrations and astigmatism influence on the electrons travelling off the optics axis when the aperture is displaced to select the scattered electrons. As modern TEM systems have small spherical aberrations and effective mechanisms of their corrections, there is no need nowadays anymore in CDF mode, and images are taken in displaced-aperture dark-field (DADF) mode, which is easier to operate.

2.5.2.3. Scanning TEM

Scanning TEM (STEM) images require more complex objective-lens optics than in conventional TEM. Two pairs of scan coils are used to incline the electron beam in the specific direction and the condenser lens (usually the third in the illuminating system) after them aligns the beam parallel to the optics axis. In this way, the focused electron beam can scan across the specimen area.

The image formation process in STEM is fundamentally different from the static-beam mode of TEM discussed earlier. The BF electron detector collects the direct beam signal, which varies in intensity depending on the electron prone position and specific features of the illuminated area. Then this intensity data is recorded for each point in correspondence to the position of the electron beam (scan coils) and, thus, the BF-image is formed.

For dark-field STEM image, the scanning approach is the same, but the signal is recorded from the scattered electrons, instead of the direct beam in BF-STEM. This is usually performed by the annular detector, which surrounds the bright-field detector and, in this way, can collect all incoming scattered electrons [288].

2.5.2.4. High-Resolution TEM

The high-resolution TEM (HRTEM) technique nowadays has reached the point resolution below 0.5 Å [290,291] and, thus, allows direct imaging of the atomic structures of the sample or even to resolve individual atoms of a crystal, study point defects, dislocations, stacking faults, precipitations, grain boundaries etc. If specimens are ultrathin (100 nm or less) the elastic scattering prevails over inelastic. HRTEM uses both the transmitted and the scattered electron beams. The contrast in HRTEM-images is formed by the interference of modulated electron waves outgoing from the sample at very low angles [235,292]. Some samples of HRTEM-images (not at the maximum magnification or the highest resolution) are shown in Fig. 2.50.

2.5.3. X-ray Analysis in TEM

X-ray analysis approaches in TEM are very similar to EDS/WDS used in SEM. The difference is that the spatial resolution of TEM-EDS is much higher due to the very small electron beam interaction volume restricted by the thickness of the electron transparent TEM specimen (up to 200 nm). Characteristic X-rays are emitted from a very small zone of the specimen, which gives a very local chemical composition of the material with an accuracy of approx. 0.1 wt%. TEM-EDS includes spot-analysis, line-scan, 2D mapping and EDS tomography (3D elemental distribution map) by tilting the specimen [235].

2.5.4. Thin Films or Coatings Specimen Preparation for TEM

Specimen preparation is a very broad topic. At first, it is necessary to understand what kind of information is needed to obtain from the specimen. In case of hard thin films or coatings it is possible to study the sample through the plan view (through the surface plane), look parallel to the surface at the cross-section of the sample, or look at surface at glancing angle in case of reflection electron microscopy (REM). The first two approaches are the most interesting, and especially the cross-section view is in a focus of multi-layered coatings study.

High-quality of the specimen prepared for TEM is essential for obtaining correct, reach and clear information from TEM signal. The specimen should be thin enough to be electron transparent and to allow enough transmitted electrons to flow onto the screen or CCD. This

thickness parameter depends on the electron beam energy and the average atomic number of the specimen. Usually, for a steel sample and 100 keV electron beam, it is recommended to prepare specimens with thickness less than 200 nm. Generally, for TEM, the thinner the specimen is better. In cases of HRTEM, the thickness must be less than 50 or even 10 nm to obtain ultra-high resolution and clear image easier for interpretation. Other dimensions of the specimen, additionally to the thickness, are also restricted usually to the disk of 3 mm in diameter to fit in a specimen holder. Depending on the holder type these dimensions may be extended in one line up to 10 mm.

Basically, there are two approaches available for thin films and coatings preparation for TEM observation: mechanical preparation of thin self-supporting disk with the following final thinning by electropolishing or ion milling, or specimen preparation by focused ion beam (FIB). The first method is much difficult process which could take up to several days to prepare only one sample by an experienced specialist. The second method is much faster and usually provides better quality of the specimen. FIB is expensive equipment and is not available at every specimen-preparation laboratory. However, nowadays it becomes much more common and often used for thin cross-section specimens of multi-layered thin films or coatings. It should be noted that both methods require correspondent knowledge base and experience either to prepare the specimen mechanically or to operate FIB instrument.

2.5.5. Experimental Details

More detailed characterisation of microstructure by high-resolution transmission electron microscopy (HRTEM) was performed using JEOL-ARM 200F with an accelerating voltage 200 kV, equipped with EDS analyser. Thin cross-section samples for HRTEM were prepared by focused ion beam technique using JEOL JIB-4000 with Ga^+ ions. Thin carbon film was deposited prior to the ion etching to prevent damage of samples.

2.6. Secondary Ion Mass Spectroscopy

2.6.1. Basic Principles of Secondary Ion Mass Spectroscopy

Secondary ion mass spectroscopy (SIMS) is a destructive analytical technique where the material is sputtered from a surface of the solid specimen by ion beam and generated secondary ions are analysed in a mass spectrometer [293,294]. The ion bombardment is usually performed with noble gasses, such as Ar or Xe, or by high-energy heavy metal ions of gold or gallium. This high-energy ion beam hit the sample surface and the two main scenario of ions interaction with the matter can occur: an elastic scattering of the primary ion by the surface atom, which is a subject of study for ion scattering spectroscopy, or the primary ion penetrates the surface, inelastically interacts with the surrounding atoms and become embedded in the solid. Its high kinetic energy is transferred to lattice atoms or molecules, their bonds may be disrupted, and they can be expelled from the surface as individual atoms and molecules, or as atom clusters and

molecular fragments (see Fig. 2.52). For approx. 10 keV-energy ion beam the disruption occurs only in a few atomic or molecular layers deep [295]. SIMS is the most sensitive beam technique with the detection limits in the range 10^{14}-10^{15} cm^{-3} when the background interference is very small. The lateral and depth resolution is usually 100 µm and 5-10 nm [293], but in special cases it can be reduced up to 0.5 µm of lateral resolution and up to 10^{-4} percent of a monolayer [295]. Removed particles may be neutral or ionic with multiple charges (e.g., aluminium sputtered with argon yields Al^+, Al_2^+, Al_3^+, Al_2^+ and Al_3^+ [294].

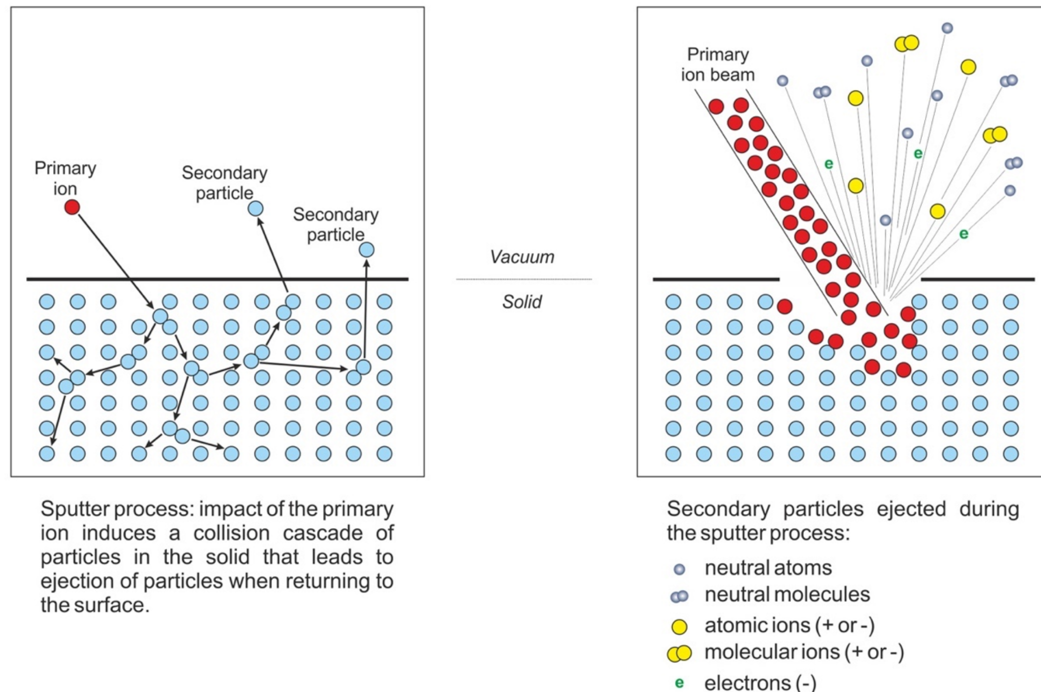

Fig. 2.52 - High-energy ion beam interaction with the matter in SIMS. As taken from [296].

All principal steps of SIMS analysis are shown in Fig. 2.53. Secondary ions are focused by an ion lens and transferred within a continuous high vacuum and through the energy filter into a mass spectrometer, where they are then sorted and counted based on their mass-to-charge ratio (m/Z) using a quadrupole or a time-of-flight (ToF) mass spectrometer and one of the ions detectors. There are three main modes of SIMS analysis and types of final results: surface spectroscopy (static SIMS), surface imaging and depth profiling.

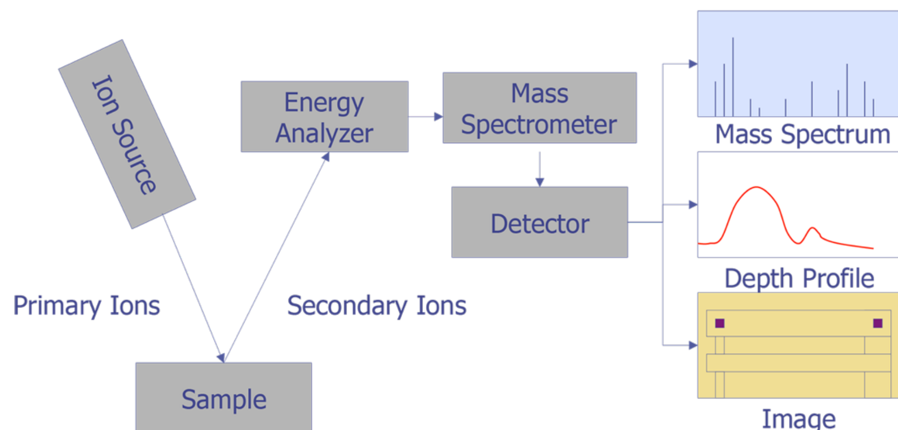

Fig. 2.53 - Principal blocks of secondary ion mass spectroscopy analysis. As taken from [297].

2.6.2. SIMS Operation Modes

2.6.2.1. Surface Spectroscopy

In static mode the analysis of the original non-modified surface composition is performed: very low primary ion current densities are used for bombarding the specimen with sputtering rates of fractions of monolayer per hour and, thus, low secondary ion current density. In this way, static SIMS is a truly surface analysis technique with negligible damage to the surface and detection limits as low as 10^{-8} monolayer [298].

2.6.2.2. Surface Imaging

For SIMS surface imaging, a finely focused ion beam scans the sample surface as the electron beam in SEM and the signal of secondary ions is recorded in correspondence to the probe position. As an alternative, a direct imaging SIMS mode is available: a full area of interest on the specimen surface is exposed to the ion beam of a large diameter, and then secondary ions filtered by energy or (and) mass with energy/mass analysers are delivered to a relatively large two-dimensional detector to form an image of the bombarded region on the sample [299]. The direct imaging, also named ion microscopy or stigmatic imaging, requires from the ion optics and mass spectrometer the transportation of selected secondary ions to the detector with no loss of the lateral position information. The lateral resolution of the scanning surface imaging SIMS is much higher than of the direct imaging (approx. up to 20 nm and 1μm respectively) [300].

It is also possible to obtain 3D images (image depth profiles) when the images are acquired as a function of sputtering time. Direct imaging mode usually has by several times or magnitudes higher sputtering rates in comparison to microbeam scan. Therefore, its depth resolution is more compatible with the lateral scales, while the latter provides a better combination of image features [300].

2.6.2.3. Depth Profiling

Unlike static SIMS for surface spectroscopy, high primary ion current densities are applied in SIMS depth profiling to provide a successive excavation of the correspondent top surface layers [301]. By acquiring the spectra in continuous relation to the time during the sputtering, the in-depth elemental distribution can be obtained. For this, it is necessary to know the sputtering rate of the experiment. It may be calculated from the measuring, e.g. by profilometer, the crater depth, formed during the primary ion beam sputtering of the material from the sample.

2.6.3. Secondary Ions Transfer

In order to remove disrupted ionised atoms and molecules of the specimen from the surface, a potential difference between the sample and the first lens (immersion or ion extraction lens) is created. Usually, the lens is grounded, and the sample is held at a high positive or negative potential (e.g. ±4.5 kV, ±10 kV or other). If the sample is an insulator, it may be coated

with a thin layer of gold or carbon to achieve stable potential difference and secondary beam current.

Positive or negative secondary ions (depending on the polarity applied to the sample) released from the specimen towards the immersion lens move to the second electrostatic lens (transfer lens) which focuses the secondary ions onto the spectrometer entrance slit and forms a real magnified image of the bombarded area of the sample in the plane of the field aperture (see Fig. 2.54) [302,303]. The immersion and transfer lenses constitute together a system named an ion microscope. Often there could be several transfer lenses, e.g. three, producing the image in the field aperture plane at different magnifications. However, only a single user-selected lens can be active at the same time.

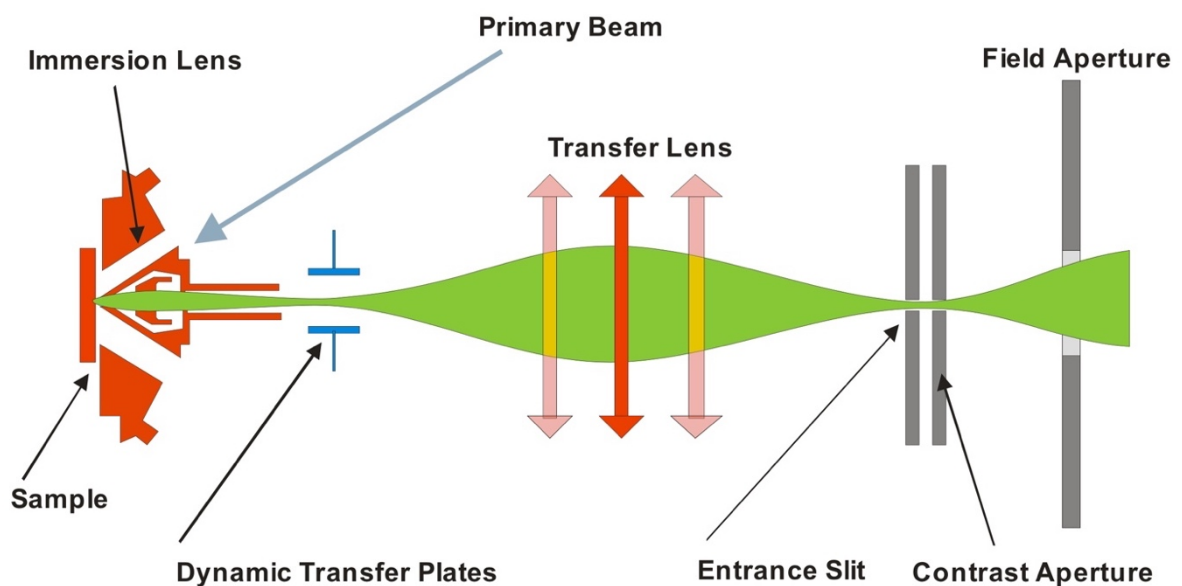

Fig. 2.54 - Secondary ions transfer from the specimen to the spectrometer. As taken from [302].

If the primary beam spot is large, the secondary ion beam can be off-axis. This results in aberrations at the entrance slit of the spectrometer and impedes clear energy and mass separation. Dynamic transfer plates are used to deflect all incoming secondary ions back on axis to pass through the centre of the transfer lens. In this mode, it is not possible to form a direct image of the surface, but the high mass resolution is achieved for any size of the incident ion beam [302]. At the same position as the entrance slit the contrast aperture is placed. Smaller aperture diameter cuts off ions with off-axis energy components which reduces image aberrations and improves spatial resolution, but it also lowers the intensity of secondary ions.

2.6.4. Secondary Ions Energy and Mass Analysis

2.6.4.1. Secondary Ions Energy Analyser

As the initial secondary ion beam contains ions with a wide range of energy, the incoming ions pass through the energy analyser and energy window to allow just ions with selected energy to reach the mass spectrometer (see Fig. 2.55, top left scheme). The inner and outer spherical sector electrode has a voltage of opposite polarity with a magnitude of about 10% of the

secondary ions accelerating voltage. The polarity of the electrodes depends on the polarity of the secondary ion beam. When the beam passes the electrodes, the trajectory of ions is bent with dispersion by their energy: the lower energy ions are deflected more strongly in comparison to the high energy ions appearing near to the outer side of the energy slit, while low energy ions move towards the inner jaw [303]. Therefore, by selecting the size and the position of the energy window it is possible to permit the entrance to the mass analyser only for the secondary ions with filtered energy.

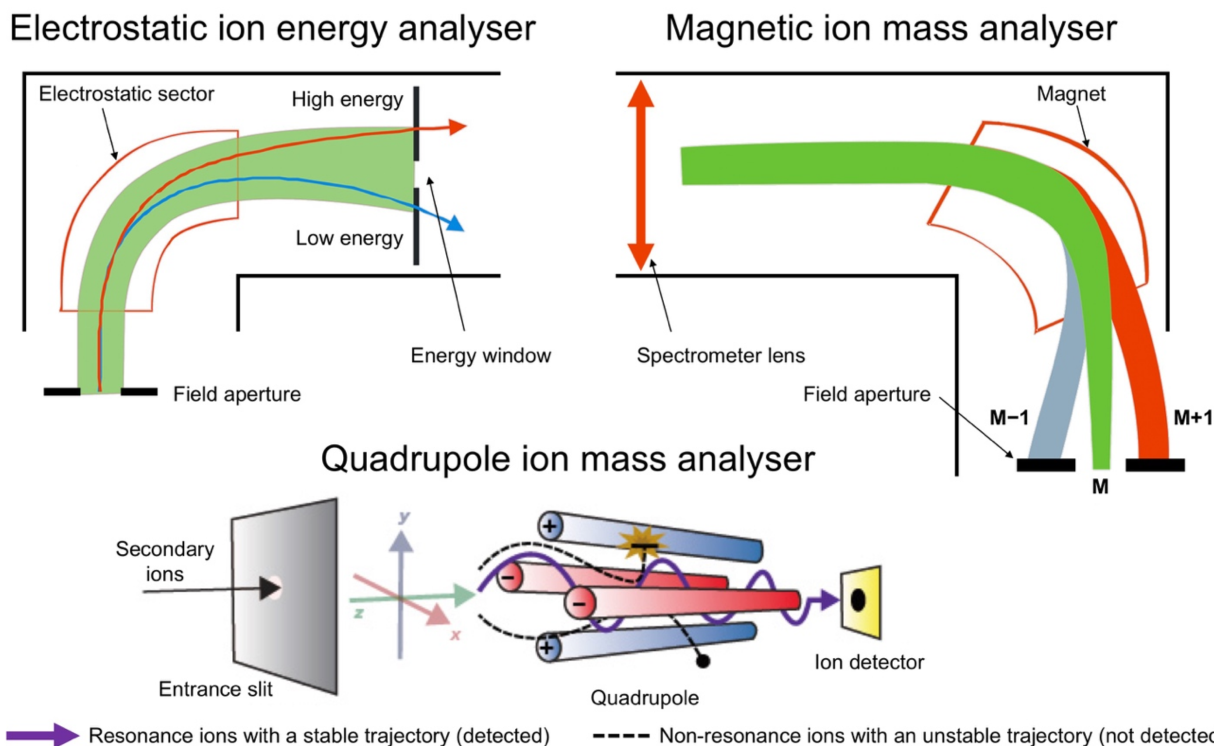

Fig. 2.55 - Energy and mass analysers typical used in SIMS systems. Adapted from [302] and [304].

As it was explained earlier, the ion bombardment of the sample produces ions of atoms, molecules and atomic or molecular clusters. Monoatomic ions have higher energy spectrum. Thus, by adjusting the position of the energy window to high energies, it is possible to remove low energy ionic particles and obtain the beam of mainly monoatomic ions for further operations in mass-analyser. Alternatively, the voltage offset technique may be used to achieve a similar result. When the energy slit is fixed at the central position, the secondary ions accelerating voltage is reduced by the offset of, usually, 30-100 V [305]. The energy analyser deflects low energy ions by a larger angle, and most of the multiatomic ions are intercepted by the inner jaw of the energy slit [303].

2.6.4.2. Secondary Ions Mass Analysers

There are two types of secondary ions mass analysers used in dynamic SIMS instruments: magnetic sector and quadrupole devices. Time-of-flight (ToF) mass analyser is also widely employed in SIMS systems, but since it uses a pulsed incident ion beam with much lower sputtering rates such systems serve for dynamic spectroscopy very rarely, however, work successfully with surface sensitive static SIMS mode [306].

2.6.4.2.1. Magnetic Sector Mass Analyser

Magnetic sector-based mass analysis is the most common in SIMS systems. When the ion beam passes through a magnetic field the ion trajectories are influenced by Lorentz force. If the magnetic field vector is aligned perpendicular to the velocity of the ions, the magnetic Lorentz force is also perpendicular to the velocity and to the magnetic vector, which results in a circular (or arc) ion motion as shown in Fig. 2.55, top right.

The deflection, or arc radius (r), of ions with a certain mass-to-charge ratio (m/q) depends on the acceleration voltage (V) and the magnetic field magnitude as described by the following equation [302,303,307]:

$$\frac{m}{q} = \frac{B^2 r^2}{2V}. \tag{2.8}$$

Therefore, ions which are not selected by the accelerating voltage (V) or magnetic field (B) will collide either with the side of the analyser wall or with the exit slits. And only the ions with selected mass-to-charge ratio will pass through the exit of the mass analyser to the ion detectors. The magnet pole entrance and exit faces in modern mass spectrometers are oriented at a non-normal angle to the optics axis. The fringing fields in this configuration provide a focusing of the ion beam in the vertical direction as it passes through the sector [303]. The exit pole face is adjusted so that the beam is rotated to produce an ion image normal to the optics axis. The combination of electrostatic and magnetic sectors provides a double focusing instrument. A magnetic analyser itself produces chromatic aberrations into the ion beam with dispersed energies and reduces mass resolution. However, the energy dispersion of the electrostatic sector placed before compensates further energy dispersion of the magnet. In such way, high mass resolution can be achieved.

2.6.4.2.2. Quadrupole Mass Analyser

Quadrupole mass analyser is another type of mass analyser broadly used in dynamic SIMS and other kinds of analysis. It consists of four parallel rods that have fixed DC and alternating RF components of the potential applied to them (see Fig. 2.55, bottom). The two pairs of opposite rods have the potential of ±(U+Vcos(ωt)) with different polarity [308]. The ions motion along the middle of the quadrupole rods depends on the electric fields. Their trajectory is very complex and shown in the figure just simplified and schematically. For a given set of voltages and frequency, only the ions with the selected mass-to-charge ratio have a stable oscillation and pass through the quadrupole filter. All other m/z values and ions have unstable oscillation and strike the rods. The alternating frequency and the ratio between the alternating and direct voltages usually are remained constant while the mass spectrum is scanned by the voltage scan [303]. The mass range and resolution of the instrument is determined by the length and diameter of the rods [308]. For typical SIMS quadrupole analyser the rods are 1 cm in diameter and 20 cm long [303].

2.6.5. Secondary Ions Detectors

Modern SIMS instruments are equipped with more than one detector, usually there are four detectors. However, there are could be eleven or more, some of them can be used simultaneously [302,303]. The most used are electron multiplier and Faraday cup ion counting detectors and one or two combined plates consisting of an array of miniature electron multipliers of lead glass for ion image detection in SIMS instrument.

The ion counting electron multiplier is the most sensitive detector. The principles of its work are similar to the multiplier system of the Everhart-Thornley detector considered in Chapter 2.1.5.2 dedicated to SEM as this design of multiplier is widely used for counting of particles (electrons, neutrals, ions etc.) in many different techniques. The incident ion strikes a dynode and secondary electrons are produced and then accelerated and multiplied by the further collisions with the next dynodes, and the resulted pulse signal of a secondary electrons cascade is then recorded for further analogue or digital processing.

The Faraday cup is just an electrode with a shape of a cup from which the electrical current is measured when a charged particle (electron or ion) hits the collector connected to the ground through the resistor. The deep cup shape helps to prevent loss of secondary electrons that would alter the current measurement [302,303].

2.6.6. Experimental Details

The method of secondary-ion mass spectrometry (SIMS) analysis was performed using SAJW-05 spectrometer equipped with Physical Electronics argon ion gun and QMA-410 Balzers quadrupole mass analyser. Two levels of ion beam energy of 5 and 1.72 keV were used for the acquisitions with exposure time of 2.5 h and 4.5 h respectively.

2.7. Rutherford Backscattering Spectrometry

2.7.1. Basic Principles of Method

Rutherford backscattering spectrometry (RBS) is the most commonly used non-destructive nuclear technique for the quantitative analysis of the elemental composition, thickness and elemental depth profiles of thin films, coatings or solid samples near the surface region [309]. In contrast to the usually destructive SIMS method, which uses secondary ions removed from the sample material by high-energy heavy ions bombardment (see Chapter 2.6), RBS results are based on the measurement of the kinetic energy loss of the primary high-energy (typical 0.5-2.5 MeV [309]) beam of light ions, such as H^+ or He^+ (α-particles), elastically backscattered from near the surface region of the sample.

When monoenergetic ions of the incident beam collide with the specimen atom, the energy is transferred from the moving particle to the stationary one. The resulted energy and the energy loss of the scattered ions depend on the masses of the incident ions and the target atoms and provide the characteristic of the specimen atoms. When energy and mass of the incident and

backscattered ions are known or can be measured, the atomic mass and, thus, the element of the target cab be identified.

The energy transfer in fully elastic collision of two isolated particles can be described by the principles of conservation of energy and momentum [310]. The kinematics of the considered process is shown in Fig. 2.56 along with the equations of energy conservation and conservation of momentum in parallel and perpendicular projections relative to the incident ion beam.

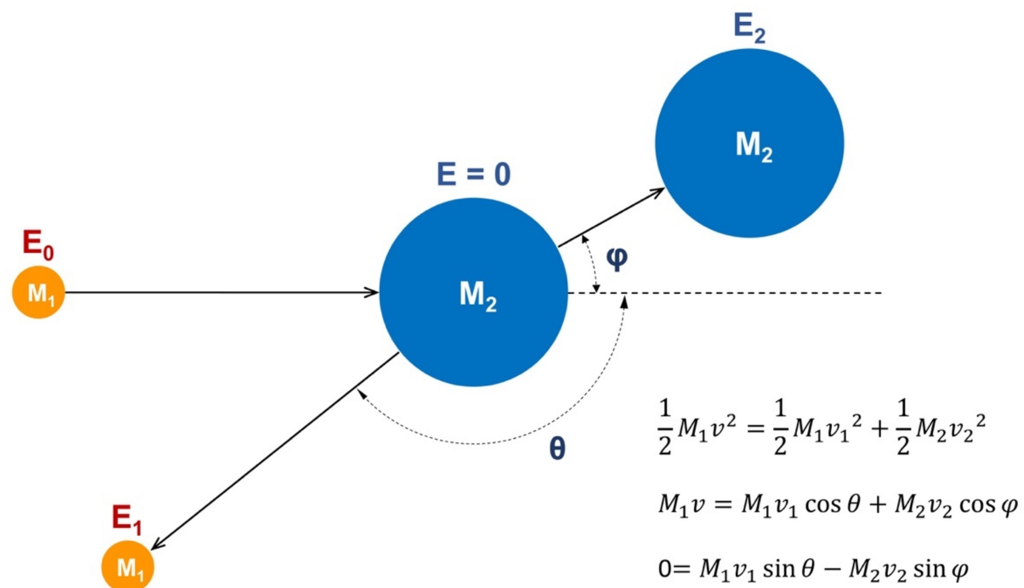

Fig. 2.56 - Kinematic scheme of elastic collisions.

From the equations shown in Fig. 2.56 the ratio of particle velocities is derived by eliminating φ and then v_2:

$$\frac{v_1}{v} = \frac{\pm\left({M_2}^2 - {M_1}^2\sin^2\theta\right)^{1/2} + M_1\cos\theta}{M_2 + M_1}. \tag{2.9}$$

Then the ratio of energies of backscattered ions to the incident ions for $M_1<M_2$, where the plus sing should be used, is

$$\frac{E_1}{E_0} = k = \left[\frac{\left({M_2}^2 - {M_1}^2\sin^2\theta\right)^{1/2} + M_1\cos\theta}{M_2 + M_1}\right]^2. \tag{2.10}$$

The ratio of energies $k = E_1/E_0$ is called kinematic factor and it shows that the energy of the elastically scattered ions depends only on their mass, mass of the target atom and the scattering angle. To achieve the larger as possible difference in the energy and to eliminate the influence of the angle the scattering angle should be 180°. Such configuration gave to the method its name of backscattering spectroscopy. This will give the maximum energy resolution for the experiment, especially it is appreciated if the target contains several elements with a small difference in the atomic number. In practice, the experimental RBS geometry is adjusted for the scattering angles about 160-170°, mostly because of the detector size [309,310].

The equation of kinematic factor k is given to calculate the energy loss only for ions backscattered by atoms at the surface of the target. However, the ion beam penetrates the sample and the ions may be scattered from the depth of the sample, from any point along the beam path. The of the ions is much narrow in comparison to the electrons interaction volume with the matter (see Fig. 2.57), they don't lose much energy when collide with electron clouds and their direction of motion is hardly to change [311].

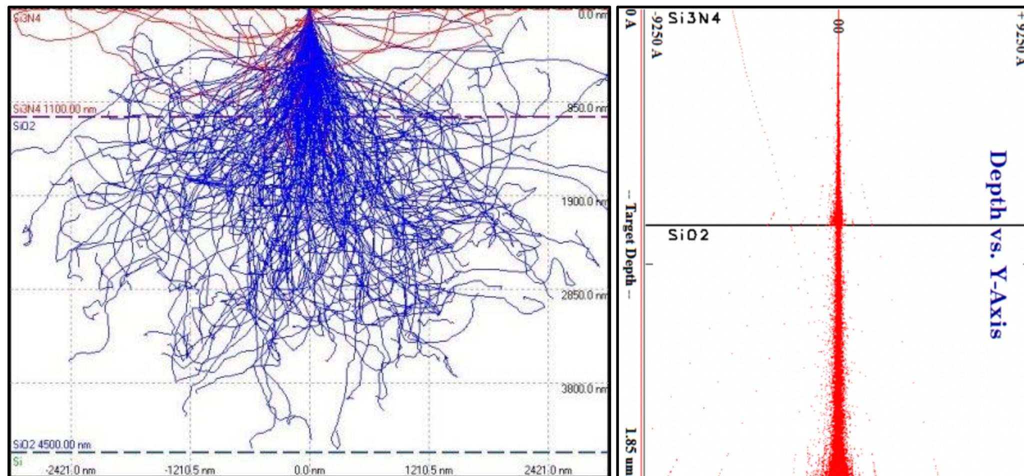

Fig. 2.57 - Pathway of 18 keV e^- and He^+ striking a Si_3N_4 layer with a SiO_2 substrate [311].

In the RBS region of ions energy their trajectory is a straight line (unless the ions are backscattered), along which the ions lose their energy primarily through the excitation and ionisation of atomic electrons (electronic energy loss) [309]. The ion loses the energy on both pass towards the sample atoms and when passes the matter of the sample backwards the detector. The energy loss per unit path length, dE/dx, is called stopping power or stopping cross-section. Relatively close to the surface such energy losses have linear relation to the depth of the scattering event [312]. These additional energy losses contribute to the peak broadening to side of lower energies (to the left). An example of RBS spectra is shown in Fig. 2.58.

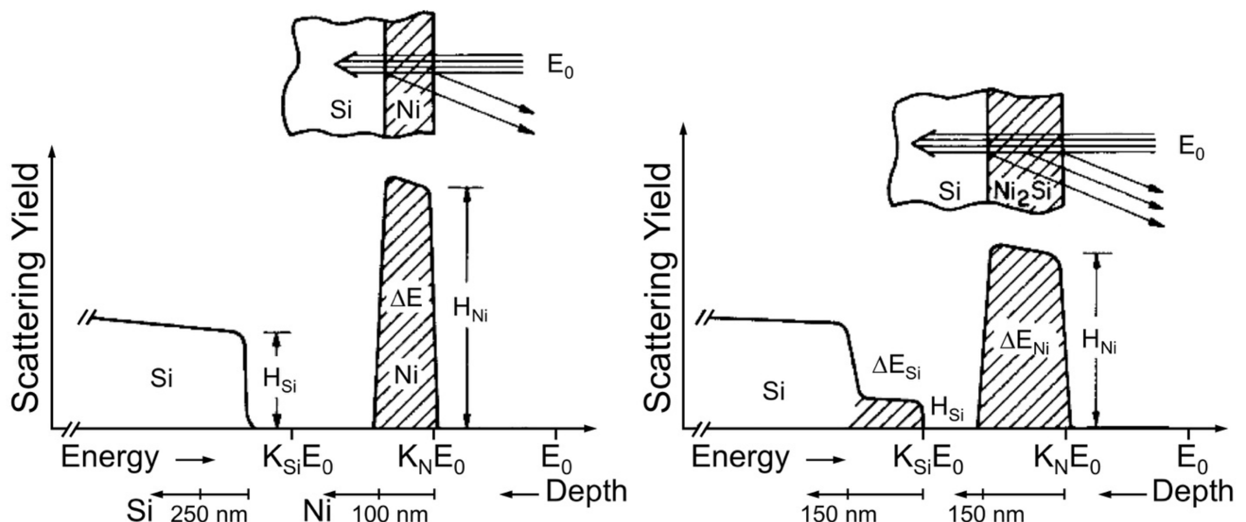

Fig. 2.58 - Schematic backscattering spectra for MeV $^4He^+$ ions incident on 100 nm Ni film on Si (left) and after reaction to form Ni_2Si (right). Depth scales are indicated below the energy axes. As taken from [313].

100 nm Ni film was deposited on Si substrate. The front side of the Ni peak corresponds to surface atom of the film and to the energy $K_{Ni}E_0$, where K_{Ni} is a kinematic factor for $^4He^+$ ions backscattered at 170°, E_0 is an energy of the primary ions. ΔE of the peak is a signal from ions backscattered from the full depth of the film. Front of the second energy growth correspond to the energy of ions backscattered by Si and shifted by the energy loss of the ions passing through the Ni film towards the substrate and backward. After reaction the film has changed the composition to Ni_2Si and its thickness has been increased due to interdiffusion. This is seen also from the broadened ΔE peak for Ni. The front of the Si signal appears at higher energy, $K_{Si}E_0$, which is an evidence that Si is present now at all thickness of the film up to the surface layer. The step ΔE_{Si} corresponds to Si in the Ni_2Si film. It is also possible to estimate Ni/Si concentration ratio in the silicide based the ratio of the products of signal height H and energy with ΔE and scattering cross-sections as shown by the following equation for two elements A and B uniformly distributed within a film [313]:

$$\frac{N_A}{N_B} = \frac{H_A \Delta E_A \sigma_B}{H_B \Delta E_B \sigma_A}. \quad (2.11)$$

Despite the nature of energy spectra from backscattered ions in RBS is described by kinematics of fully elastic collisions and the interpretation is straightforward, for multielemental compounds, gradual or multi-layered structures on bulk materials the analysis is much more complex and needs attention, experience and deep knowledge of the method.

Nowadays most of tasks for RBS analysis may be solved using modern software, which is based on the simulation of the RBS spectrum and their fitting to the experimental data using corrections and special algorithms. One of the most widely used program is SIMNRA, as well as other open access or commercial solutions from the equipment suppliers are available.

2.7.2. Instrumentation: Ion Beam and Detectors

2.7.2.1. Ions Sources

Ion beams suitable for RBS are produced in an ion source and then accelerated, mass- and charge-filtered and transported to the specimen. One of the most widely used general-purpose ion source is duoplasmatron and it is very common in RBS systems and well suited for this task [309]. Basic elements and working principles of duoplasmatron are shown schematically in Fig. 2.59 (a).

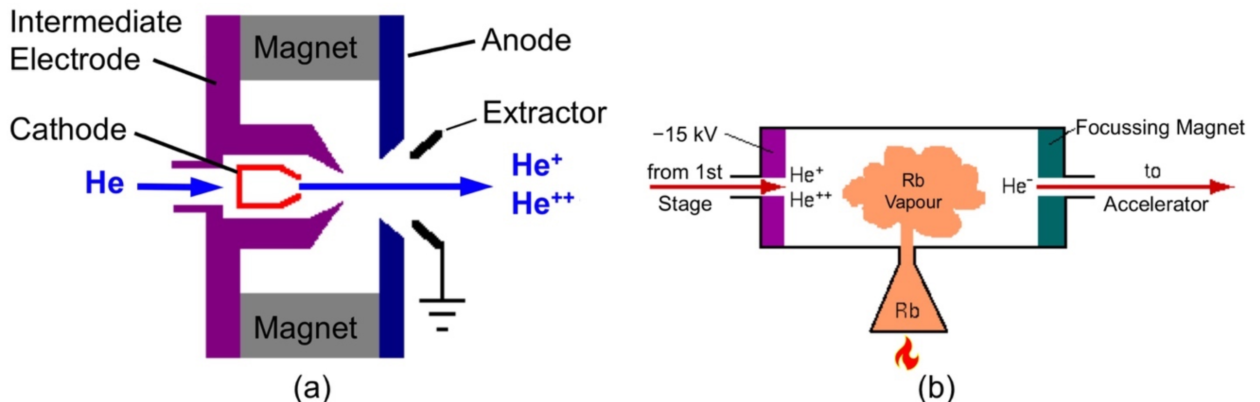

Fig. 2.59 - Ions Generation for Rutherford Backscattering Spectrometry: (a) illustration of duoplasmatron, (b) conversion of positive Helium ions H^+ and H^{++} into negative H^- by passing through hot alkali metal vapor. Adapted from [314].

A gas, e.g. helium, is introduced at low pressure to the interior of the hollow cathode. A potential difference of several hundred volts is applied between the hollow cathode and anode. In such way, plasma is produced by an arc [315]. The duoplasmatron contains two types of plasma: cathode plasma and anode plasma which are close to the cathode and anode respectively. Hot filament emits electrons which ionize the helium or other introduced gas. The discharge is maintained close to the axis by a conical intermediate electrode at floating potential. A magnetic field produced by electromagnetic coils help to focus electrons and concentrate plasma close to the axis. A part of the plasma passes between the opened edges of intermediate electrode and expands in a second chamber [315]. The extractor electrode produces an electric field which pules out positively charged ions through a small aperture. The duoplasmatron can produce ions of both polarities. To extract negative ions the axis of discharge should be displaced from the axis of extraction hole, which allows extraction of negative ions concentrated in the periphery of the plasma [315]. However, to obtain negative ions of helium, the most inert of the inert gasses, which may be required by accelerator type (e.g. tandem accelerators) or for negative ions bombardment, positively charged ions of helium can be directed to pass through hot alkali metal vapour, which converts H^+ into He^-. This process is shown schematically in Fig. 2.59 (b) with Rubidium used for illustration, but all of the alkali metals have sufficient reducing power to form He^- [314].

2.7.2.2. Ion Beam Accelerators

Produced ions then should be accelerated to obtain high-energy ion beam, which is usually about 1-2 MeV for conventional RBS experiments. For these purposes the most used devices are Van de Graaff and Cockroft-Walton electrostatic accelerators. They can be designed as a single-ended or tandem configuration (tandem Van de Graaff or Cockroft-Walton type Tandetron) [309].

An example of two-stage tandem Van de Graaff particle accelerator is shown schematically in Fig. 2.60. Rapidly moving belt of insulating material transports positive electric charge to the high-voltage terminal and negative ions are accelerated towards the positively

charged outer surface of the high-voltage terminal. In the two-stage tandem configuration ion beam can receive a double of the accelerating energy since at the middle of the accelerating tube, near the high-voltage terminal, ions change their polarity by passing through the stripping gas or stripping film losing electrons and then, holding a positive charge, they are accelerated out from the high-voltage terminal of positive polarity. Nowadays in many Van de Graaff accelerators belts are replaced by Pelletron charging chains which provide more stable, longer and efficient work with reaching much higher accelerating potential [316].

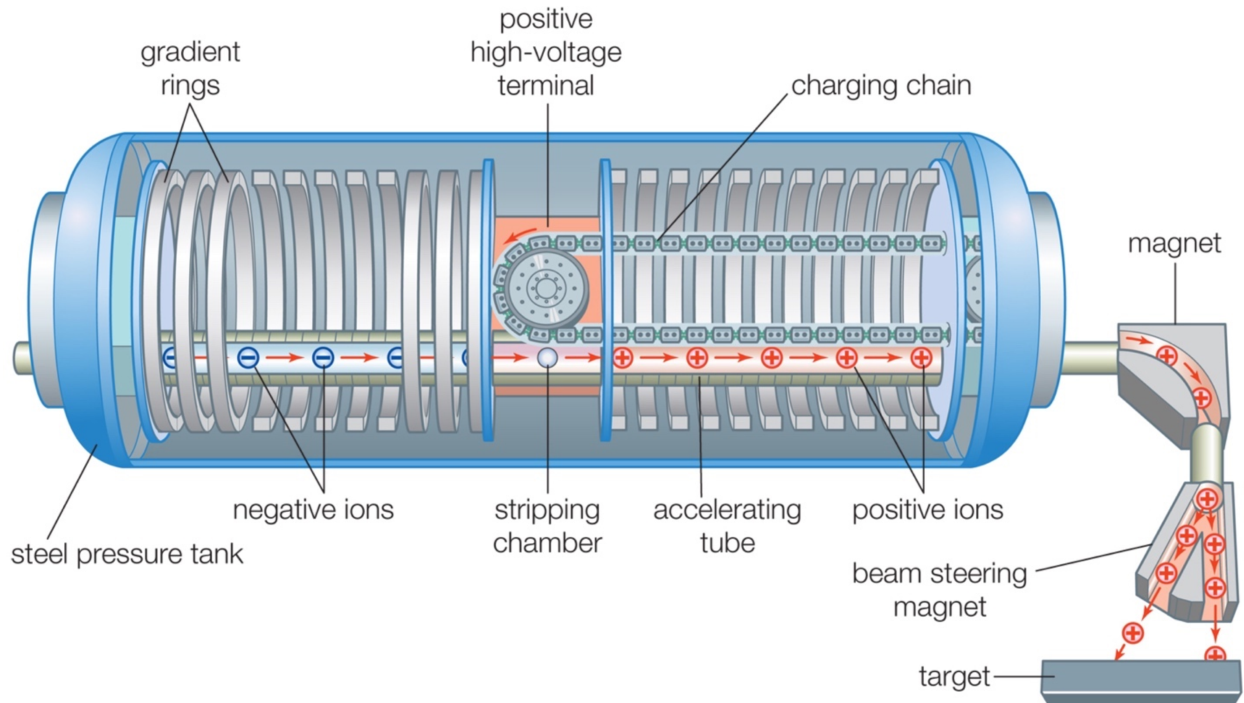

Fig. 2.60 - Two-stage tandem particle accelerator. As taken from [317].

Cockcroft-Walton accelerator is based on the gradual high voltage of spherical cascade generator or voltage multiplier circuit applied to the set of electrodes along the accelerating tide [316]. Each system has own pros and cons. The main advantage of Cockcroft-Walton type accelerators is that they don't have moving parts and, hence, there is no wear or need to clean the dust from the Van de Graaff belts etc. [309]. On the other hand, Van de Graaff (or Pelletron-updated) accelerators more easily can reach much higher ion beam energies: 20-40 MeV in contrast to 1-4 MeV produced by Cockcroft-Walton type [317]. This may be important is case if the same ion beam line is used for other experimental techniques, which usually happens since the accelerating device, its operation and maintenance is a costly and experts needed procedure.

Before the accelerated ion beam reaches the specimen it should be mass- and charge-selected to extract ions suitable for material analysis since accelerators normally produces ions in several charge states. Filtered ion beam then enters a UHV environment and directed towards the target by electrostatic or magnetic lenses [309].

For general analysis the ion beam strikes the specimen at normal angle. If structural information is needed to be extracted (RBS and channeling) the specimen can be rotated for desired incident angle by moving a special rotating sample stage.

2.7.2.3. Detecting of Backscattering Ions

The best scattering angle for RBS to achieve the maximum of mass resolution is 180°, as seen from Eq. (2.10). However, due to the dimensions of the detector, in practice the scattering angle is about 170°. Usually, solid-state detectors, either a silicon surface-barrier (SSB) detector or a passivated implanted planar silicon (PIPS) detector, are employed for detection of backscattered ions. For conventional RBS experiments with 1-2 MeV He^+ or H^+ ions the PIPS detector has better energy resolution [309].

2.7.3. Experimental Details

Rutherford backscattering spectrometry (RBS) experiments were performed with 1.4 MeV He^+ ion beam produced by Van de Graaff type AN–2500 HVE (High Voltage Engineering Europa B.V.) electrostatic accelerator. He^+ ions were ionised by the radio-frequency ion source located on a high-voltage terminal and accelerated by a large potential gradient distributed within the accelerating vacuum tube towards the grounded end. The specimen was exposed to the He+ ions at normal angle of the incidence beam.

Spectra were collected with a silicon surface-barrier detector with an energy resolution of 15 keV installed at 170º to the beam direction. Elemental concentration through the depth profiles and layers thickness were determined by computer simulation in specialised software SIMNRA 6.0 assuming the bulk density of 5.8 g/cm^3 and 9.2 g/cm^3 for CrN and MoN respectively.

2.8. Hardness Measurements

For thin films and protective coatings, and in many other fields of material science and engineering, hardness usually means indentation hardness (unless another type is needed and specified) because of their relative simplicity, reproducibility and standardisation. Depending on the mode of load application during hardness measurements, hardness tests can be classified as shown in Table 2.3.

Table 2.3. Classification of hardness tests

Direction of load application	Fixed load; variable indentation		Variable load; fixed indentation	
Normal to surface of specimen	Static load	Dynamic load	Static load	Dynamic load
	(a) Brinell (b) Meyer (c) Vickers (macro- and microhardness) (d) Rockwell regular (e) Rockwell superficial (f) Knoop (microhardness) (g) Nanohardness (Vickers and Berkovich indenters)	(a) Shore scleroscope (b) Poldi	(a) Monotron; (b) Wood-hardness tool	
Parallel to surface of specimen	(a) Herbert pendulum (b) Bauer drill (machinability test) (c) File test		(a) Mohs' scale of hardness	

The basic idea of hardness measurement is to indent the material to be studied by other materials with known hardness and measure the resistance that tested material demonstrates. The material of indenter, aiming to impact and penetrate into the surface of tested material, should be much harder than the testee. The usual method to evaluate the hardness at the end comes to the forming of indentation footprint with area *A* by applying specific force *F*. Known value of force *F* divided by the footprint area *A* gives the hardness value *H* = *F*/*A* [25]. Further, most of the existed methods of indentation hardness tests differ by the geometric shape of the indenter, which is usually chosen among whose footprint area can be easily calculated: ball (sphere), pyramid, cone or other, shown in Fig. 2.61.

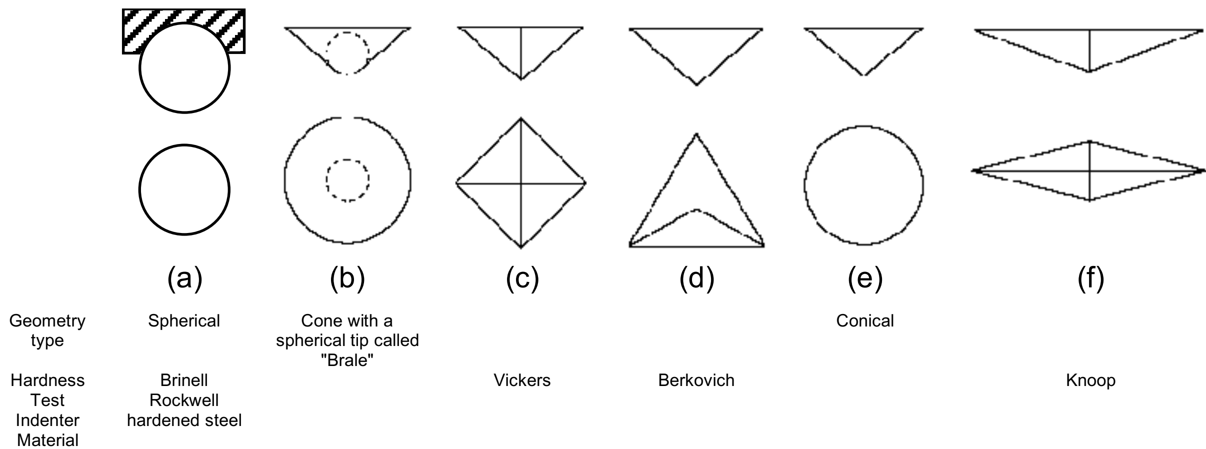

Fig. 2.61 - Main types of indenter tips (schematically). Adapted from [318].

2.8.1. Brinell Hardness

Brinell Hardness was the first widely accepted standard method of quantitative determination of indentation hardness, proposed by Dr. J.A. Brinell in 1900. The indentation is performed by standard spherical ball indenter into the surface of the material with a define static load applied for a standard period of time. The Brinell hardness number (BHN) is defined as the ratio of the applied load, P in kilograms, to the curved surface area of the elastically recovered indentation, A_S in square millimetres. In order to determine the Brinell hardness number of a material, it is necessary to know the curved surface area of the indentation in the test piece. When the dimensions of standardised ball-shaped indenter are known, as well as applied load, it is possible to derive geometrically the equation only with the load P, the spherical ball diameter, D; and the diameter of the indentation d involved, or depth of indentation *h*, as shown below and in Fig. 2.62 [27].

$$BHN = \frac{P}{A_S} kg/mm^2 = \frac{2P}{\pi D\left[D - \sqrt{D^2 - d^2}\right]} = \frac{P}{\pi Dh} \tag{2.12}$$

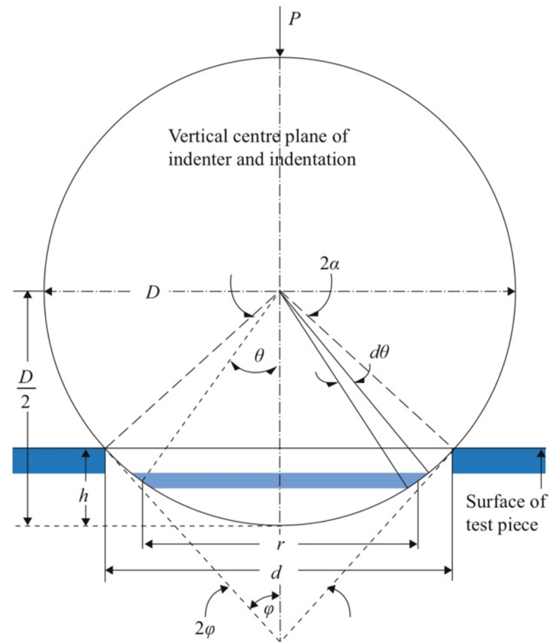

Fig. 2.62 - Scheme for derivation of Brinell hardness number (BHN)
Shows that an indentation of diameter *d* with depth *h* is formed after the indenter ball with diameter *D* has penetrated into the surface of test piece under an applied load, *P*. The included angle between the tangents drawn to the edge of a Brinell indentation is 2φ. As taken from [27].

There are two reference sizes of spherical indenters for standard Brinell hardness tests: 5 and 10 mm. Additional indenters with diameters of 1.25, 2.5 and 7 mm are existed, but they are not considered to be used for standard Brinell test. The standard applied load in such measurements is usually varies between 3000 kg for 10 mm indenter and 750 kg for 5 mm indented to 500 kg with 10 mm diameter of spherical indenter, depending on the properties of studied material, as well as loading time is also in range from 10 to 30 seconds. The general rule is that the combination of test load and ball diameter should be such that the diameter of the indentation lies within the range of 25-60% of the ball diameter [319].

2.8.2. Meyer Hardness

In Brinell hardness test the diameter of the indentation (rarely, the depth) should be measured after the release of applied force. At this step, after the load is removed, the indentation is recovered elastically and usually will take a shape of a spherical cup but with a curvature radius higher than the real ball-shaped indenter. The harder the material, the larger is the difference. It is suggested to consider rather the diameter of indentation than the depth, as it is less affected by elastic recovery effect as well as gives more accurate results because of larger dimensions. Thereby, it is assumed and accepted that the elastic recovery doesn't in general influence the Brinell hardness.

In case of Meyer hardness, the ratio is calculated from the load and the projected area of the elastically recovered indentation, oppositely to the surface area of indentation in Brinell method. Meyer hardness test may be performed using the same setup as Brinell hardness, but

is not so broadly used and common as the first one, although it is more rational and gives more fundamental measure of indentation hardness [27].

2.8.3. Rockwell Hardness

Rockwell hardness test is the most widely used method of quantitative study of the indentation hardness, nowadays. This testing method is based on the measurement of the increment of indenter penetration depth into the metal forced by a primary and a secondary static loads (minor load and major load respectively).

The indenter usually is made from hardened steel with shape of a spherical ball or may be a diamond with shape of a cone having a spherical tip, called the "Brale". In standard measurements, initially it goes into the surface under minor static load of 10 kg to form a very shallow indentation up to a certain depth, which is considered as a zero datum. Then a major static load of 50, 90 or 140 kg is applied, enlarging the indentation depth by the total static indentation loads of 60, 100 or 150 kg respectively.

Application of the initial minor static load helps to arrange a good contact between the indenter and the surface of the sample, set and hold the position of the indenter tip and, thus, eliminate or reduce errors caused by slight imperfections or defects of the surface, reduce factors of "ridging" or "sinking in" affecting indentation.

The diameter of the standard steel ball indented for Rockwell test is 1.588 mm, and steel ball indenters with larger diameters of 3.175, 6.35 or 12.7 mm are existed and usually may be used for softer materials. The radius of spherical tip of Brale indenter is 0.2 mm and the include angle of its diamond cone is 120°.

It is necessary to keep the indenter tip with no damage, since the chipped or cracked or blunted indenter would bring errors to the measurements of hardness. The spherical shape of the used in Rockwell hardness test helps to minimize the damage of the indenter under the load by removing the sharpness of the head of the cone.

2.8.4. Vickers Hardness

Vickers hardness tests is a widely recognised and accepted method of hardness measurements capable for quantitative determination of indentation hardness under constant static load applied for a very broad range of materials, from very soft to extremely hard, with no needs to change the indenter or load, which distinguishes it from Brinell or Rockwell hardness tests.

The basic principles of Vickers hardness test operation are the same as for Brinell hardness test and the Vickers hardness scale is identical with that of the Brinell [27]. The key difference is in the type of the indenter. In the case of Vickers hardness test the standard indenter is a square-based pyramid made of a diamond with an included angle of 136° between opposite faces which produces a square indentation on the surface of the sample.

Depending on the purpose of the test, relative hardness and dimensions of the sample, the load may be selected among 1, 2.5, 5, 10, 20, 30, 50, 100 and 120 kg for Vickers hardness tester. In many cases the most appropriate applied load is 30 or 50 kg for macro-scale bulk materials.

Similar to the Brinell hardness number, the Vickers hardness number (VHN, or VPN), or the diamond pyramid hardness (DPH, or DPN) is determined as the ratio of the applied load *P* to the surface area of the elastically recovered pyramidal indentation A_s. Like the Brinell hardness, the Vickers hardness can be expressed and calculated as follows:

$$VHN = \frac{P}{A_S} kg/mm^2 = 1.854 \frac{P}{D^2}. \quad (2.13)$$

where *P* is the applied load in kg, A_s is the lateral area of elastically recovered pyramidal indentation in the test specimen in mm^2, and D is the average diagonal length (arithmetic average of the lengths of two diagonals of the square indentation, D1 and D2) of square indentation in mm.

One may observe no difference between the Vickers and Brinell hardness measurements and corresponded hardness numbers for certain materials with relatively low values of hardness. Indeed, they are practically identical when the hardness values are up to 300 kg/mm^2. Then, for harder materials, the method matters (see Fig. 2.63). Beyond the hardness values of about 300 kg/mm^2 the Brinell hardness shows lower numbers than the Vickers test with true values of the indentation hardness.

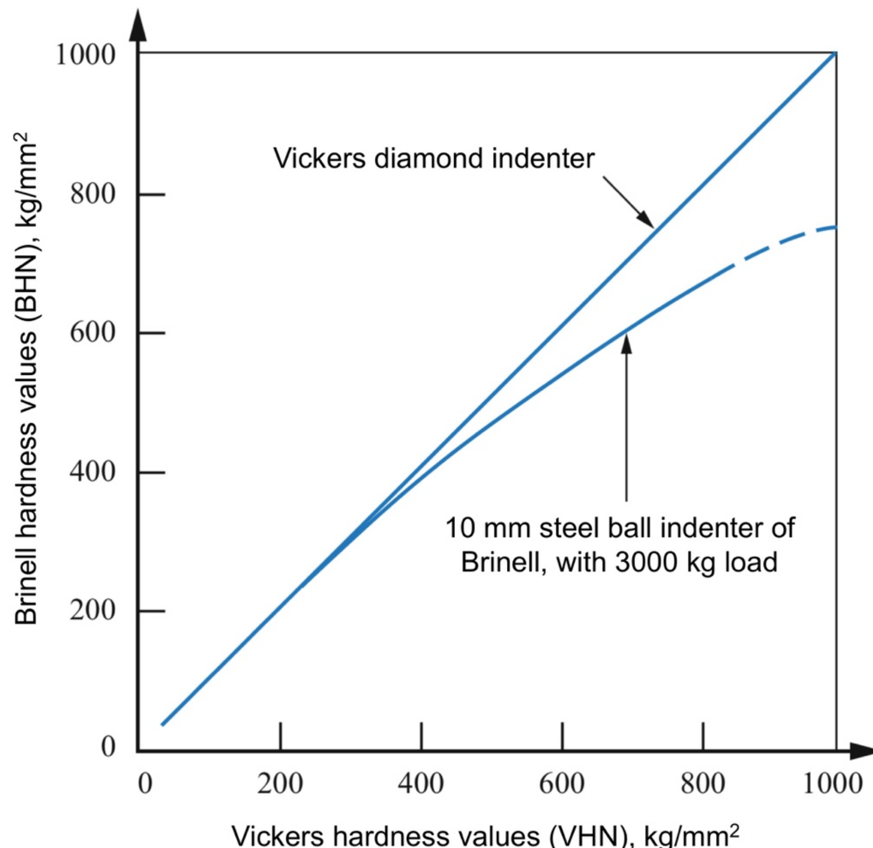

Fig. 2.63 - Illustration of the divergence of Brinell from Vickers hardness number at high hardness values. Adapted from [27].

Lower values of Brinell hardness are produced due to the distortions of the steel ball indenter during indentations with harder materials (VHN ≥ 300). This effect increases with the growth of hardness of materials to the and becomes more remarkable: VHN of 1300 is equivalent for BHN of 850. While Brinell hardness curve starts to show unacceptable values above 600 Brinell, the Vickers hardness curve remains almost straight at all range of values, which passes Vickers test to be a reliable hardness measurement method.

2.8.5. Indentation Depth and Load Aspects of Hardness Measurement for Coatings

National Burau of Standards reported that for each indentation on the specimen with the thickness less than the "critical" value a spot of altered surface was visible on the surface opposite to the indentation surface. The material plastically deforms over an appreciable distance below the surface of indentation. The ASTM specified that the hardness measurements on thin sections or soft materials can't be considered as reliable if the compression or indenter mark or bulge is observed on the reverse side of the specimen after the indentation.

It is recommended and widely accepted that the thickness of the sample should be at least ten times the depth of the indentation [27]. Therefore, the indentation hardness is influenced not only by the hardness of the material at the point of indentation, but also by the mechanical properties of the material below the indentation point up to at least ten times of the indentation depth.

Described requirements of the indentation depth are absolutely applicable for the coatings. When the coating is thinner than the ten times of indentation depth the effect of the substrate occurs in the hardness measurements. If the substrate is harder than the coating, it may cause a noticeable reduction in the depth of indentation for fixed values of loads or increase the amount of applied load to reach needed indentation depth.

Since it is not possible to increase the fixed thickness of the coatings after the deposition, the rule of penetration depth may be formulated in other way: the indentation depth should not exceed 10% of the coating thickness to avoid the influence of the substrate. The above statement is true irrespective of whether the coating is harder or softer than the substrate [319–321]. Thus, the intrinsic hardness of the coating with thickness of 10 μm has limit of 1 μm for the indentation, which is a microhardness test. Furthermore, coatings of 1-2 μm thick or submicron level will require the indentation of nanoscale range.

If the hardness values were obtained in such way that the indentation depth exceeds 10% of the coating thickness and it is not possible to avoid it with the available facilities the values should be reported as composite hardness of the coating-substrate system [319]. Later on, if necessary, the intrinsic hardness of the coatings may be distinguished from the composite hardness values by using various mathematical models developed so far [322–324].

As discussed and shown above, due to the dimensional requirements of the specimens the thickness of the coatings or some mechanical properties of samples, various values of the indentation loads may be applied, and various values of indentation depth may be desired. Thereby, indentation hardness tests are divided by the load and penetration ranges to macroindentation tests with indentation loads from 2 N to 30 kN, microindentation, when loads are in range from 0.2 N to 2 N and penetration depth is more than 0.2 µm, and nanoindentation, when indentation depth doesn't exceed 200 nm. Hardness classification by ISO 14577-1 [325] and corresponded hardness measurement methods are summarised in Table 2.4. From such classification and corresponded penetration depths and shapes of indenters it follows, that hardness tests may serve of characterisation of materials at different levels of structural dimensions, as shown in Fig. 2.64.

Table 2.4. Hardness Testing Scales Based on ISO 14577-1 and Corresponded Measurement Methods [325,326]

	Macroindentation	Microindentation	Nanoindentation
Scale	macroscale	microscale	nanoscale
Load (L), N	2<L<30000	L<2	not specified
Penetration depth (h), µm	not specified	h>0.2	h<0.2
Hardness test methods	Brinell, Meyer, Vickers, Rockwell, Shore Durometer, International Rubber Hardness Degree	Vickers, Knoop	nanoindentation tests with Berkovich or cube corner indenters and Oliver Phar calculations

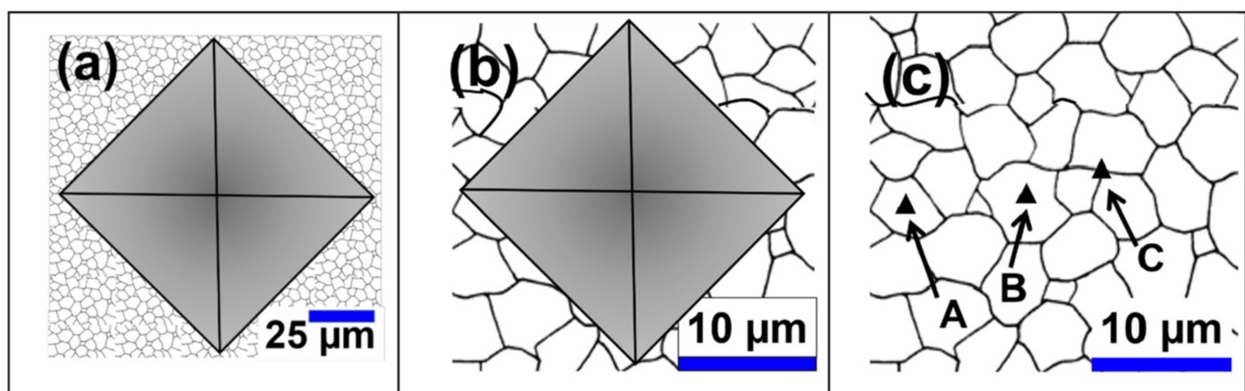

Fig. 2.64 - Scheme of indentation hardness of a polycrystalline material at macro- (a), micro- (b) and nanoscale (c) Note that the scale in (a) is different to be able to visualize all the indented area [326].

2.8.6. Knoop Hardness (Microhardness)

Knoop indenter is a diamond indenter introduced by the National Bureau of Standards [327,328] specially for microhardness testing in a couple with Tukon tester. The Knoop indenters is made in the form of a pyramid with rhombic-shaped base. It has an included longitudinal angle (opposite to the longer diagonal of the base) of 172°30′ and an inclusive transverse angle (opposite to the shorter diagonal of the base) of 130°0′. The indentation from Knoop indenter has rhombic shape with perpendicular longitudinal and transverse diagonals of 7:1 ratio. This results

in a state of plane strain in the deformed region [27]. The depth of Knoop indentation is $h \cong l/30$, where l is the longitudinal diagonal length.

The Tukon tester usually may apply an indentation load from 25 g to 10 kg or even 50 kg depending on the model, to extend the measurements for Vickers macrohardness as the standard Vickers indenter may be used in such tester. There are more microhardness testing machines now available in market, as Leco microhardness tester, Buehler Micromet, and others with loads from 1 or 10 g to 1 kg and more.

The Knoop hardness number (KHN) is defined as the ratio of the applied load P to elastically unrecovered projected area of the indentation A_{up}:

$$KHN = \frac{P}{A_{up}} kg/mm^2 = \frac{P}{0.07028 l^2} = 14.24 \frac{P}{l^2}, \quad (2.14)$$

where P is an applied load in kg, A_{up} is a projected area of elastically unrecovered indentation in the test piece in mm^2 and l is the length of longitudinal or longer diagonal of rhombic-shaped indentation imprint.

There is some elastic recovery of the indentation after the release of applied load always present in most of the materials. Referring to the special shape of Knoop indenter with ratio of 7:1 of longitudinal and transverse diagonals, the elastic recovery mainly occurs along the transverse (shorter) diagonal. Thus, longitudinal diagonal may be considered as elastically unrecovered and suggested to be solely used to express precisely the elastically unrecovered projected area of the indentation A_{up}. Knoop microhardness test involves significantly smaller indentation area and lower volume of the deformed zone in comparison to Vickers hardness test. This results in in related advantages of Knoop test such as hardness measurement of microscale structures in material, products with small dimensions, single crystals, cutting edges, thin sheets of materials, coatings and surfaces. It allows also to measure hardness of very hard and brittle materials, whose tendency for fracture is proportional to the volume of the stressed material.

On the other hand, Knoop hardness test is slower than Rockwell test, usually requires special preparation of the specimen for the experiment (polishing of the surface to eliminate defects and scratches for accurate measurement, grinding of the back side of the sample and careful mounting to keep the specimen surface normal to the vertical axis of the indentation)), may have influence of personal error during the measurements, which is not an issue for Rockwell test.

2.8.7. Nanohardness or Nanoindentation

The first difference with macro- or microindentation tests is that in the nanoindentation machines the displacement h and the load l of the indenter when it is forced into and drawn back from the material are continuously controlled and recorded with high precision. It is possible by using the high-resolution technique of instrumented indentation testing (IIT), also known as continuously-recording indentation test.

The hardness, the principal mechanical property determined by nanoindentation, is defined as the applied maximum load divided by the projected area of contact surface of the indenter under the load:

$$H_{nano} = {}^{P_{max}}\!/_{A_{pc}}, \tag{2.15}$$

where P_{max} is the applied maximum load and A_{pc} is the projected area of contact surface at the load. Knowing the indentation depth corresponding to the maximum load, the size of the projected contact area under full load can be determined from the depth of impression and geometry of the indenter.

There are two main types of indenter shapes used for nanoindentation (but not limited to): Berkovich and cube corner [326,329].

Berkovich indenter is an equilateral triangular-based pyramid made of diamond. The angle between the pyramid face and the indentation vertical axis is 65.27°, whereas in four-sided Vickers pyramid this angle is 68°. For small-scale indentation experiments, like nanohardness test, the geometry of three-sided pyramid of Berkovich indenter has an advantage in respect to the Vickers indenter, because three edges of Berkovich indenter can be ground to meet at a single sharp point, while a four-sided pyramid ends at a "chisel edge" (a line) rather than a point [27].

The cube corner indenter is also a three-sided pyramid (precisely the corner of a cube) with centre-line-to-face angle of 35.26°, which makes it sharper than Berkovich indenter. Such kind of indenter displaces more than three times the volume of the Berkovich indenter under the same load and, thus, develops much higher stresses and strains in the near-contact zone. This produces small well defined micro-cracks around indentation imprint in brittle materials which may be used for fracture toughness estimation at relatively small scale [27].

Besides the discussed indenters, there are existed other solutions for nanoindentation with various shapes of indenter, such as spherical, conical, sphero-conical indenters, used much less frequently and mostly for some specific tasks. Knoop indenter with two different face angles may be employed to study anisotropy of the specimen surface by the measurements of the unequal lengths of the rhombic-shaped residual imprint diagonals.

There are some high-end nanoindentation solutions with picoindenters for installation in SEM or TEM systems from Bruker and other companies present in market nowadays. In addition to nanoindentation on the microscopic samples at the selected area of specimen they allow to perform in-situ measurements with direct observation, video recording and possible nano- and microstructural studies.

In case of Berkovich indenter the projected contact area $(A_{pc})_{Berkovich}$ geometrically may be expressed as follows [27]:

$$\left(A_{pc}\right)_{Berkovich} = \frac{1}{2}aL = \frac{\sqrt{3}}{4}a^2 = \frac{\sqrt{3}}{4}\left(2\sqrt{3}h_c \tan 65.27°\right)^2 = 24.494h_c^2 \approx 24.5h_c^2, \quad (2.16)$$

where a is the length of each arm of equilateral triangular indentation imprint, L is the perpendicular distance from the base of the triangular imprint to the apex, h_c is the contact depth of penetration into the specimen under the load.

Therefore, the expression to calculate the Berkovich hardness can be transformed to

$$H_{Berkovich} = \frac{P_{max}}{24.5h_c^2}. \quad (2.17)$$

During the nanoindentation experiment the indenter penetrates the sample until a prescribed maximum load L_{max} is reached and the corresponded penetration depth h_{max} is achieved. When the indenter is unloading from the sample, the displacement is also continuously recorded until the zero load is reached and the final (residual) penetration depth of the indenter h_f is measured. Therefore, the load-unload curve of nanoindentation may be obtained (see Fig. 2.65).

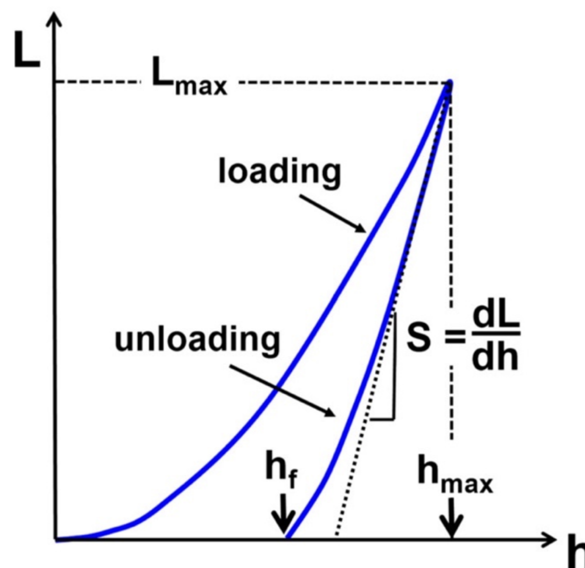

Fig. 2.65 - Example of load-displacement curve obtained from the nanoindentation experiment [326].

When the indenter is withdrawn, only the elastic part of the displacement is recovered. Such wise, the elastic properties of the material may be easily separated from the plastic [27]. The slope of the upper portion of the unloading curve denoted as $S = dL/dh$ is called the elastic contact stiffness, or simply contact stiffness. The values of h_c, the contact depth of penetration of the indenter under the maximum load, vary depending on the geometry of the used indenter.

As the penetration depth of the indenter in nanoindentation is limited up to 200 nm by the definition of nanoindentation, corresponding dimensions of indentation imprint, contact area and contact depth also have submicro- and nanoscale values. The only way for precise observation of such small areas and parameters is by scanning electron microscopy (SEM), which is costly, time consuming procedure, not practical and may be not present among available facilities of the laboratory or department. Fortunately, the methods of contact depth h_c determination and

projected contact area A_{pc} calculation directly just from the unloading part of the load-displacement curve have been developed.

The most widely used method to determine the projected area of contact surface and, hence, accurately calculate hardness H and elastic modulus E from the indentation load-unload curve, with no needs of direct observation of indentation area by microscope, was developed by Oliver and Pharr in 1990s with some advanced refinements later in 2004 [330,331].

They found that the unloading curve usually fits very well to the power-law relation derived from the elastic contact theory:

$$L = \beta\left(h - h_f\right)^m \tag{2.18}$$

where β and m are empirically determined power-law fitting parameters and h_f if the final displacement after the complete unloading determined from the curve fit. The power-law index m is always more than 1 and lies in the range of 1.25-1.51 depending on the material [27,330]. The fitting of unload curve in such way is the first step of the method. At the second step the contact stiffness S should be found by the differentiating the unload curve fit (Equation (2.19)) at the maximum indentation depth:

$$S = \left(\frac{dP}{dh}\right)_{h=h_{max}} = \beta m(h_{max} - h)^{m-1} \tag{2.19}$$

The third step is to calculate the contact depth h_c, which is usually smaller than the total penetration depth h_{max} due to the elastic contact. The deformation scheme of an elastic-plastic sample during and after the indentation [330] is shown in Fig. 2.66, where the behaviour of the Berkovich indenter is simplified to be represented by a conical indenter with an equivalent half-included angle φ = 70.296°, which gives the same projected area-to-depth ratio [27].

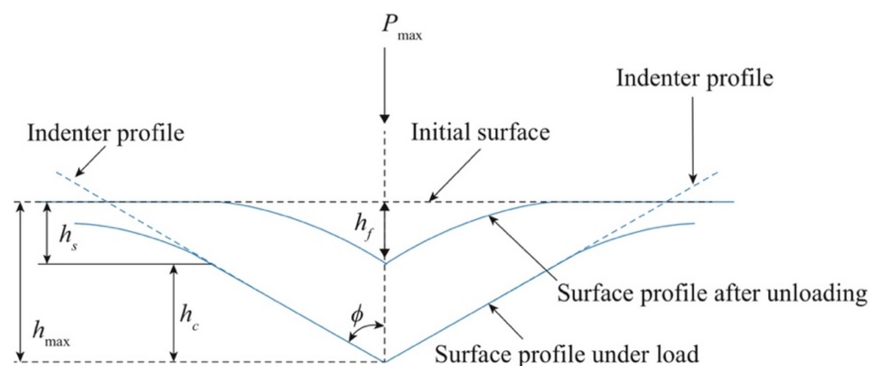

Fig. 2.66 - Schematic representation of deformation pattern of an elastic–plastic sample during and after indentation showing parameters characterizing the contact geometry. As taken from [27].

This model assumes that the "pill-up" of material (the movement of the indented material around the indenter above the original surface plane) at the contact periphery is negligible. The "sinking in" of the material (the movement of the indented material around the indenter below the original surface plane) occurs and its amount in elastic model is giving by [332]

$$h_S = \chi \frac{L_{max}}{S}, \quad (2.20)$$

where χ is a constant that depends on the geometry of the indenter. For Berkovich, Vickers and cube corner indenters the value χ = 0.75 is used for analysis [27,326,329,332].

According to the discussed equations and scheme shown in Fig. 2.66, the contact depth h_c can be estimated as follows:

$$h_c = h_{max} - h_s = h_{max} - \chi \frac{L_{max}}{S}. \quad (2.21)$$

Finally, when "sink-in" predominates in the elastic model, and "pile-up" and displacement arising from the compliance of the testing machine are neglected, the projected contact area for an ideally sharp Berkovich indenter may be calculated as $(A_{pc})_{Berkovich} = 24.494h_c^2$ with known value of contact depth (Equation (2.21)) [27].

In the reality the Berkovich indenter is not perfect. Experience shows that the face angles of the Berkovich indenter can be made with high accuracy, but for the indenter tip it is impossible to achieve in practice the indenter tip with infinitely sharp radius, as the ideal Berkovich indenter should have. Usually the radius of the tip of a new Berkovich indenter is in the range 50-150 nm [333]. And even if the manufacturing process was careful, the indenter tip is usually blunted or may have other defects in an as-produced state or after a few nanoindentations. Such corrections may be applied to the Oliver and Pharr method by introducing polynomial indenter shape functions with empirically defined fitting parameters from the indentation tests on the materials with known elastic modulus.

Materials with low ratio of the yield stress to elastic modulus and little or no capacity for work hardening ("soft" metals that have been cold-worked prior to the indentation) exhibit large "pile-up" effect which leads to an underestimation of the contact area (up to 50%) and overestimation of the nanohardness. This error usually increases with increase of the indentation depth. If from the h_f/h_{max} ratio (h_f/h_{max} >0.7 or close to 1, when the degree of work hardening is small) or from other independent information about the properties of the material, "pill-up" is suspected, indentations should be examined by imaging techniques for the measurements of true contact area and calculation of the correct hardness [27].

There are other factors influencing results of the nanoindentation measurements, such as the machine compliance, when the frame of the testing machine may deflect under the load applied on the specimen. Such displacement is included in the total displacement on the load-unload curves and, thus, the stiffness dL/dh has contributions both from the machine and the test piece. This contribution from the instrument may cause a significant effect and must be calibrated and deducted from the displacement.

Most of the modern instruments for nanohardness measurements are automated and can be controlled from a computer with specially supplied software. Many of necessary corrections,

adjustments and calibrations also may be performed automatically via the software under the careful human control.

Nanoindentation technique allows to calculate also the elastic modulus, or Young's modulus, of the material, another important parameter to evaluate mechanical properties of the material, especially important for characterisation of hard protective coatings.

2.8.8. Experimental Details

The hardness and Young's modulus (elastic modulus) were measured by micro-indentation method using the NanoTest instrument from Micro Materials Ltd company. The NanoTest system has unique pendulum design which combines superior vibrational stability with the ability to carry out a wide range of measurements (see a principal scheme of the NanoTest^{TM} instrument in Fig. 2.67).

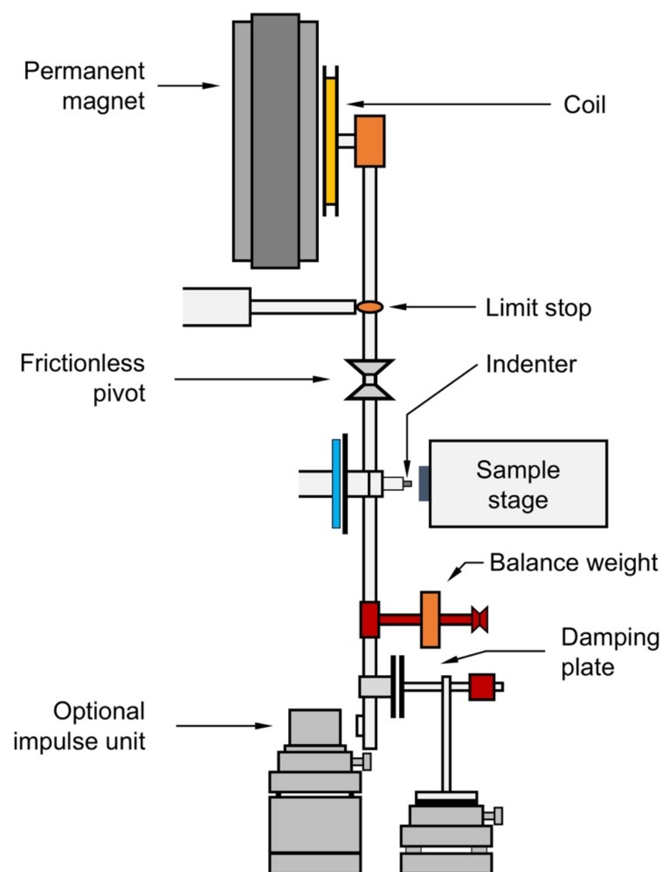

Fig. 2.67 - Principal scheme of NanoTest^{TM} instrument for micro- and nanoindentation. Adapted from [334].

The MML Nano Test equipment is a static system that functions with a horizontal loading mechanism. The pendulum can rotate on a frictionless pivot. A coil is mounted on the top of the pendulum near to a permanent magnet. When a current is present in the coil, it is forced toward the magnet. Consequently, the opposite side of the pendulum with the diamond indenter moves toward the sample, into the surface of test piece. The parallel plate capacitor, one plane of which is attached to the indenter holder, changes the capacitance when the indenter moves with the capacitor plane. The capacitance is measured by the bridge circuit instrument and, thus, the

information about the displacement of the diamond indenter is obtained. The sample in the holder can be moved in 3D-configuration by three DC motors driving with micrometre steps. The limit stop, positioned manually with a micrometre, defines the maximum outward movement of the diamond, and also the operating orientation of the pendulum, when a load is applied. The equilibrium position of the pendulum with no current in the coil and, thus, zero load for indenter, is adjusted with balance weights, movable in horizontal and vertical directions [335].

The equipment is well protected against significant thermal drift, ambient air flow and acoustic disturbance. It is equipped with a Nano-K bench top vibration isolation platform. Depth calibration, load calibration, and frame compliance experiments were performed before the actual measurements to obtain accurate values of load and depth. The tip radius of the Berkovich indenter was 20 nm [336]. The SEM image of the Berkovich indenter is shown in Fig. 2.68.

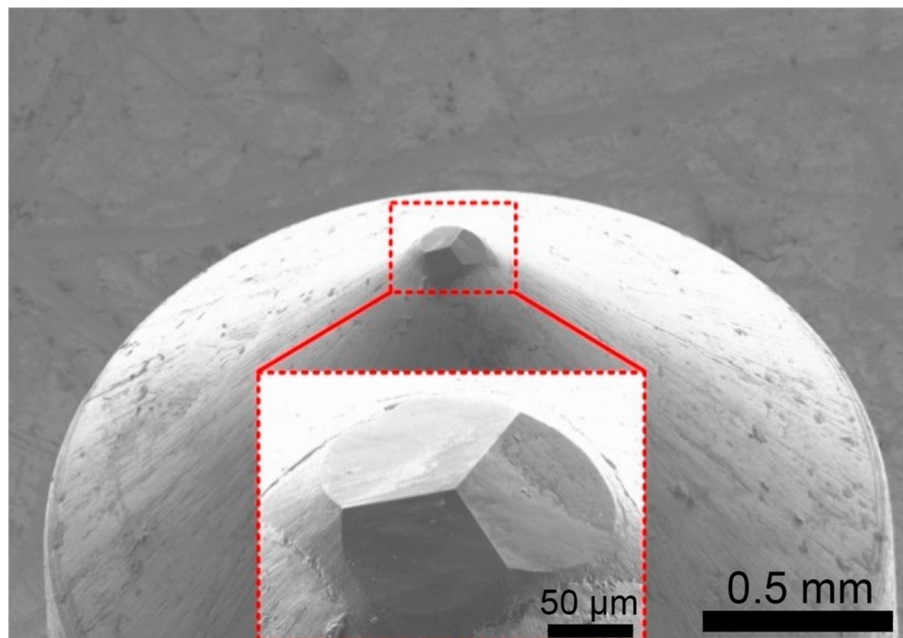

Fig. 2.68 - Scanning electron microscopy (SEM) images of Berkovich indenters by HITACHI S-4800 (Tokyo, Japan). The inset shows the enlarged images of the indenter tip. As taken from [337].

For the measurements, the samples were mounted on the stage firmly with a special glue to avoid any movement during the experiments. On each sample, up to 10 indentations oriented in one line (the location was chosen randomly) with the interval of 50 µm were performed. The experiments were performed at room temperatures (25°C). The NanoTest instrument has Berkovich indenter with an apex semi-angle (Θ = 65.27°) and effective cone angle (α = 70.3°) and uses the method of depth sensing indentation with the collected data analysis performed by supplied software using Oliver-Pharr method. The projected contact area at a contact depth hc with a Berkovich indenter corresponds to $24.5hc^2$. The measured data was collected in “Depth Vs Load Hysteresis” mode with an acquisition process controlled by penetration depth. The maximum penetration depth was in the range 0.6-1.3 µm, but not deeper than 10% of coating thickness. The maximum load has reached the values of 600 mN.

2.9. Tribological Tests and Measurements

2.9.1. Basic Principles of Tribological Tests for Protective Coatings

One of the key properties of protective coatings is low wear of the coatings and coated tools. Wear is identified as an alteration of a solid surface by progressive loss or progressive displacement of material due to relative motion between that surface and a contacting substance or substances a solid surface, generally involving progressive loss of material, due to a relative motion between that surface and a contacting substance or substances [338]. To describe and evaluate wear it is important to know the nature of relative motion responsible for the wear and then select the correct type of wear test designed to imitate a "working conditions" in the most realistic way. One of the most widely used tribological test methods reproduces sliding motion, which is characterised by continuous contact between the two samples in tribological contact [339]. Common tribological test geometries involving sliding motion are shown in Fig. 2.69.

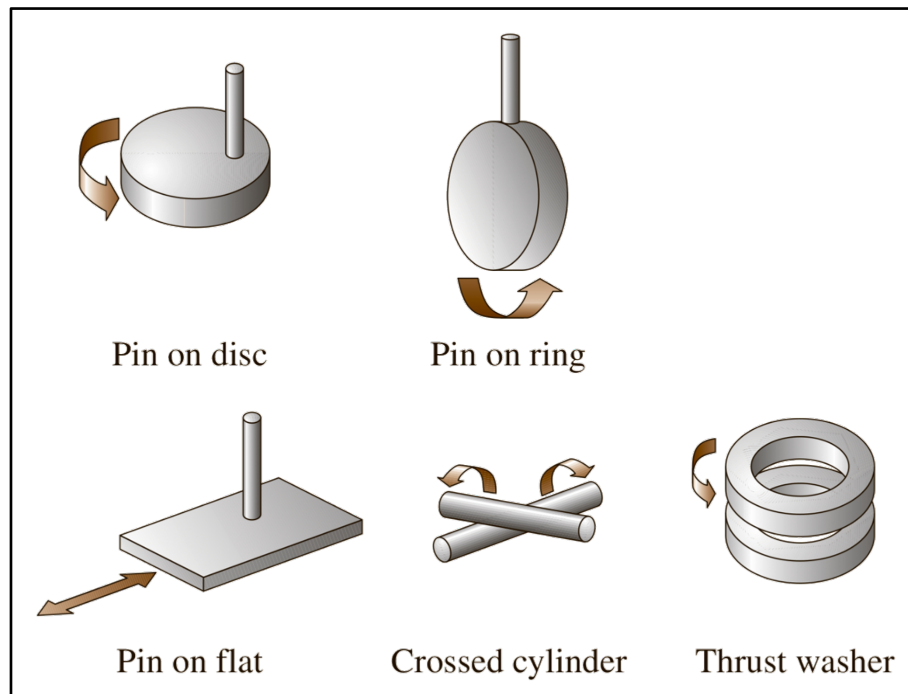

Fig. 2.69 - Examples of test geometries used for tribological tests involving sliding motion. As taken from [339].

Pin-on-disc and reciprocating geometries are used most often, but in many applications balls are used instead of pins [339]. A typical scheme of ball-on-disc test is shown in Fig. 2.70. It is usually consisted of a rotating disc mounted horizontally and a stationary ball (or pin in case of pin-on-disc test) pressed onto the disc. The load is applied parallel to the axis of rotation. This configuration can used under dry or lubricated conditions, with additional heating, cooling, cryogenic or vacuum setups. Typically, the radius of ball's track on the disc is fixed, and after the first full rotation, the counterbody enters the wear track produced during the previous turn. But, if needed, this can be avoided by a continuous variation of the radius during the test [340].

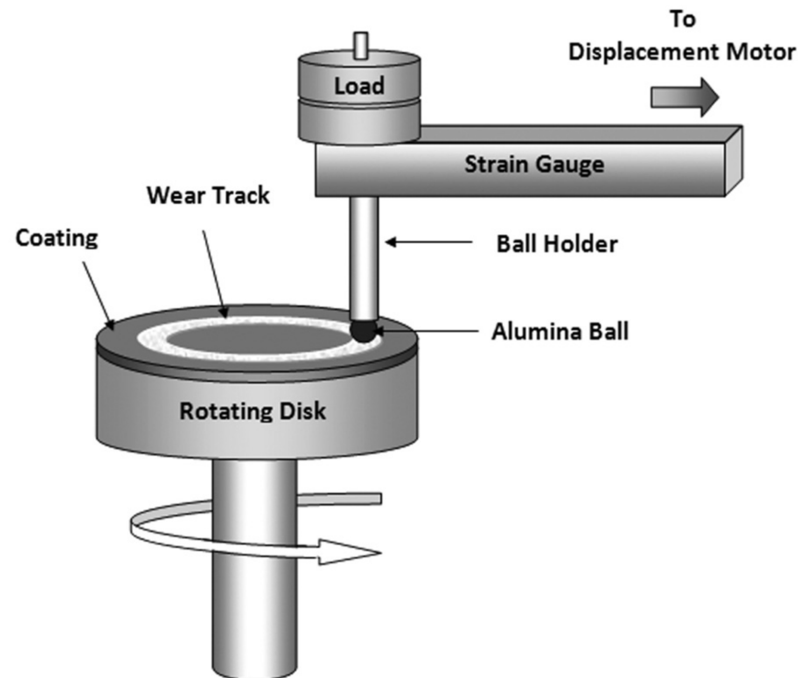

Fig. 2.70 - Schematic drawing of ball-on-disk wear test. Adapted from [341].

Friction measurement is usually done by torque transducers or load cells either on the rotating or the stationary specimen. Wear is typically determined as a volume or weight loss of the counterbody or coating after a certain sliding distance [340]. The wear track on the disc can also be evaluated to get additional information about nature and mechanisms of the wear.

2.9.2. Experimental Details

Tribological tests and measurements were performed in air with the ball-on-disk scheme by spherical Al_2O_3 counterbody using CSM Instruments tribometer friction machine. The sintered certified aluminium oxide ball (static element) has diameter of 10 mm and R_a = 0.03 μm. The normal load was 6 N and linear sliding speed was about 0.15 m/s. The wear rate was evaluated using the results of the ball-on-disk experiment performed at dry friction conditions on a distance of 200 m. It was calculated as wear volume divided by sliding distance and normal load [38,342].

Chapter 3.

Methods of CrN/MoN Films Fabrication

3.1. Thin Films and Coatings Deposition Techniques

When the fabrication of thin films and coatings of a nanometre or a few micrometres is considered, the main two groups of fabrication methods are physical vapour deposition (PVD) and chemical vapour deposition (CVD), as shown in Fig. 3.1. Both include many specific techniques and even some hybrid approaches with PVD and CVD elements are existed. Depending on the requirements to the product and properties of used materials the most adequate method and technique may be selected. Both PVD and CVD have advantages, drawbacks and unique applications. CVD methods usually have higher deposition rates and allow easily perform deposition on any type of the surface features and shapes, which is harder to achieve by PVD (line-of-sight deposition). On the other hand, CVD methods are based on reactions of toxic and expensive precursors very often generating hazardous by-products.

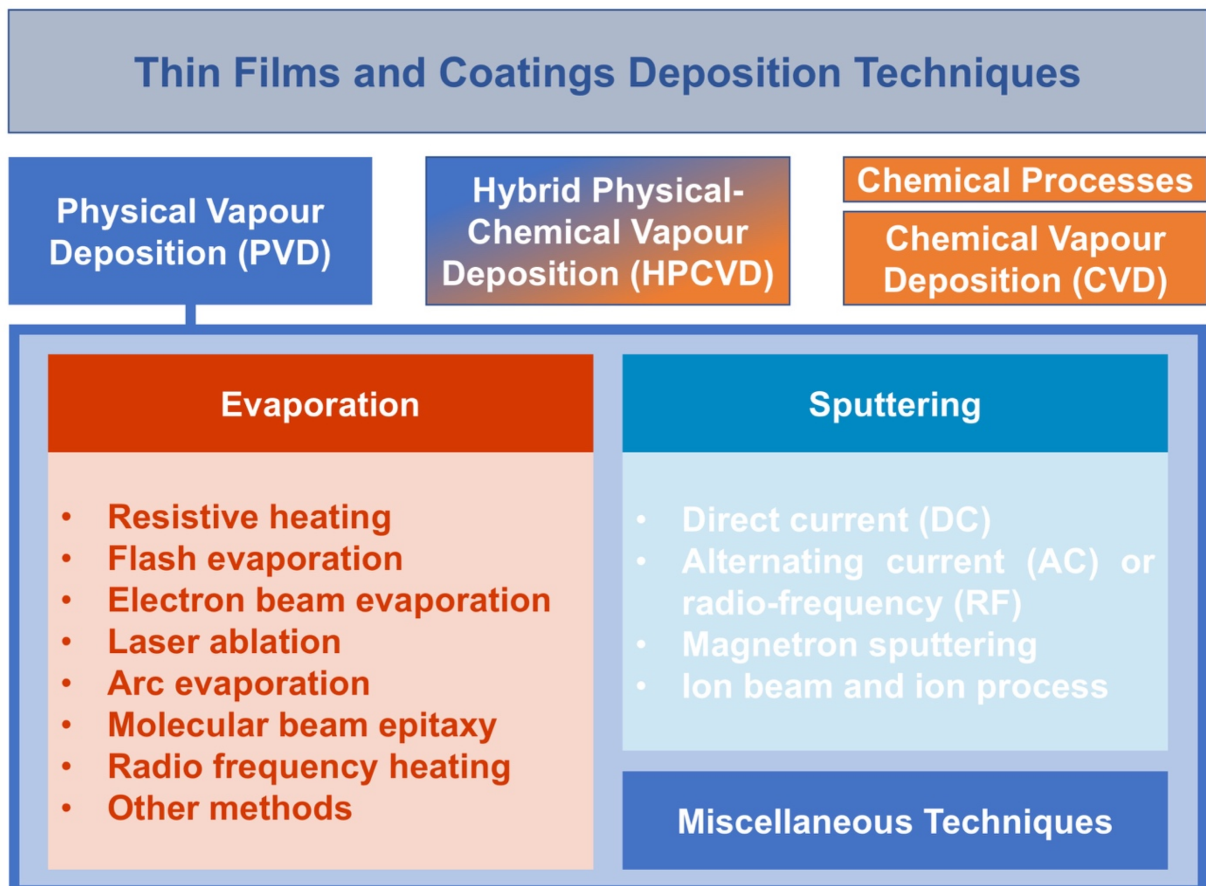

Fig. 3.1 - Classification of physical vapour deposition techniques and their place among thin films and coatings deposition methods.

Another disadvantage of CVD process in comparison to PVD is that they usually require much higher temperatures and it always heats the substrate. Despite it doesn't cause a damage for the most of metallic substrates by itself, it leads to much higher thermal residual stresses in

the deposited thin films and coatings and their further deadhesion or destruction. All above-mentioned factors in a couple with the possibility of up to atomic level control of chemical composition and the need to produce multi-layered structures lead to the decision to use PVD processes of metal nitride-based protective coatings fabrication.

In physical vapour deposition the film or coating is obtained in vacuum by condensation of material from a vapour phase of neutral or ionised atoms of metals. Depending on the method how the vapour phase was obtained, the basic PVD processes are grouped into two general categories, evaporation and sputtering, while each one of them includes many techniques and specifications, as schematically shown in Fig. 3.1.

3.2. Physical Vapour Deposition: Sputtering

When a solid surface is bombarded by high-energy ions, surface atoms of the solid are scattered backward due to the collisions between the surface atoms and the energetic particles as shown in Fig. 3.2 [343]. This phenomenon is called "back-sputtering" or simply "sputtering". The term "impact evaporation" is also used to describe the same process.

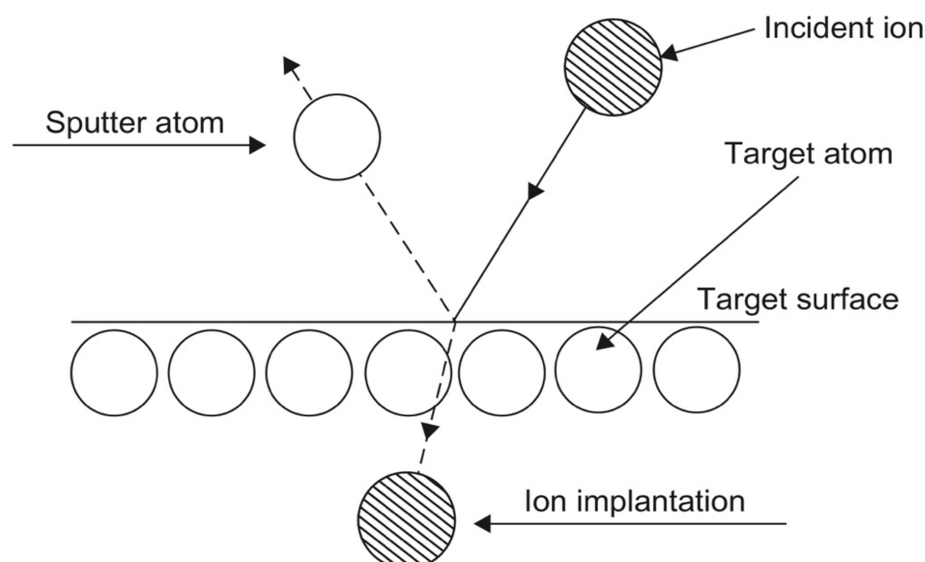

Fig. 3.2 - Physical Sputtering Processes. As taken from [343].

3.2.1. Direct Current and Radio-Frequency Sputtering

The simplest sputtering system is the direct current (DC) diode sputtering, which is composed of two electrodes enclosed in a vacuum chamber equipped with pumping system and gas supply (a typical scheme is shown in Fig. 3.3(a)). A voltage is applied to the electrodes. The target of the material to be sputtered, or cathode, has negative potential. The substrate and substrate holder plate serve as an anode and can be grounded, floating or biased. The vacuum chamber, which also may serve as an anode when the sample is grounded, is filled with a sputtering gas, typically argon, at low pressure. An electric field formed between the electrodes generates an electric current in the rarefied gas, due to the presence of electrons and ions formed

by processes such as ionisation by cosmic rays, thermionic emission, and collisions between particles [344]. The accelerated electron moving towards the anode collides with an atom of the sputtering gas and generates an ion and new electron. Thus, two electrons will move to the anode and one ion will move towards the cathode. If electrons travel a distance long enough, they may reach high kinetic energy to cause a new ionisation before their collision with the anode. Ions of the sputtered gas are accelerated towards the cathode and if they have high enough kinetic energy they will cause the emission of secondary ions, which, in their turn, can be accelerated towards the anode and generate new collisions with the sputtering gas atoms causing a cascade effect. Above a threshold breakdown voltage, depending on the selected sputtering gas, pressure in the chamber and cathode material, a stable discharge will be established keeping the plasma in an equilibrium condition. When this occurs, the atoms of the target materials are randomly ejected from the surface together with secondary electrons after collisions with high-energy ions and some of them hit the substrate (anode) condensing and forming a thin film.

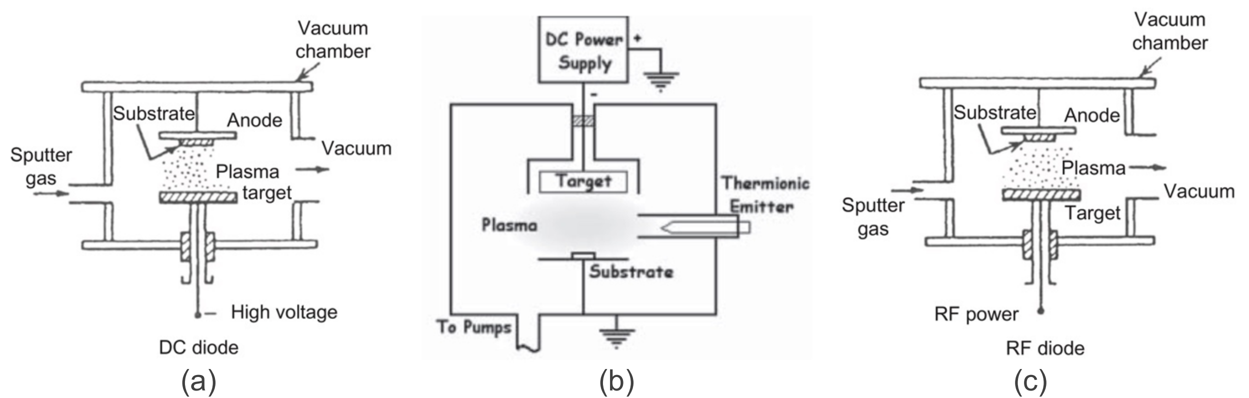

Fig. 3.3 - DC and RF sputtering systems. As taken from [343] and [345].

Typically, DC sputtering is characterised by low deposition rates due to the low plasma densities [344]. In order to increase the ionisation of plasma in DC sputtering, a heated filament is introduced between two electrodes to emit electrons directly into the plasma, independently of the target, as shown in Fig. 3.3(b) [345]. Higher electron density gives more control of the ion energy and flux, which results in higher deposition rates. However, such triode sputtering systems are not common nowadays due to the drawbacks, such as scaling up problem, interactions of the filament with reactive gas, which cause its rapid erosion.

DC sputtering is suitable only for conductive materials. If the target is an insulator or material with pour conductivity, then the glow discharge will not be sustained due to the immediate collection of a positive charge from the incoming ions on the exposed surface. For such cases DC power supply has to be replaced by radio-frequency (RF) power supply. In this way, during the first half of each cycle the potential difference accelerates ions to sputter the target and, in the second half cycle, the electrons are directed towards the target surface and prevent the formation of a positive charge barrier. Since the power is divided between the two electrodes in

RF sputtering, the effective power at the cathode is typically only 50% of the power delivered in DC sputtering. Therefore, it usually brings lower deposition rates at equivalent DC and RF processes. Also RF is generally more complicated system requiring matching network to match the impedance of the system to reduce reflected power and the RF power supplies are more expensive [345].

In addition to the sputtering gas, a reactive gas, such as oxygen or nitrogen, can be introduced into the chamber to react with sputtered atoms and form deposited films of oxides or nitrides, respectively. Comparing DC and RF reactive sputtering, it should be noted that DC sputtering has more difficulties to overcome. It is due to the possible formation of a dielectric compound layer on the target, which leads to the charging of the surface of the target and to the decrease of the sputter yield. There are many factors affecting the sputter yield drop: sputter yield for compounds is usually lower than for pure metals; higher emission of secondary electrons leading to the decrease of the plasma impedance; decreased potential difference between electrodes results in lower ions energy; insulating film deposits on all surfaces, including the anode and it can't conduct electrons away from the plasma anymore [345].

The major problems of the described sputtering systems are low and nonuniform plasma density following by sputter yield / deposition yield rate and nonuniform film thickness, which limits their use in the applications where high uniformity of the films is required (electronics, optical coatings industry, etc.) [345].

3.2.2. Magnetron Sputtering

Magnetron sputtering is another family of sputtering techniques. The common configuration is a planar magnetron which has architecture similar to DC and RF diode sputtering systems consisted of two electrodes but with a set of permanent magnets behind the cathode. Magnets are arranged in a such way as to create a region of magnetic field directly above the target, as seen in Fig. 3.4 (b). Under the applied magnetic field the secondary electrons leaving the cathode surface experience a Lorentz force and start to move in a circular path, which results in a cycloidal path, as shown in Fig. 3.4 (a), when the electric field decreases linearly away from the cathode [345]. Thus, under the electric and magnetic fields electrons are concentrated and allowed to move at the area above the cathode surface ionising sputtering gas atoms. In this way, the ion density increases significantly when the magnetic field is applied. Thus, the sputtering yield and deposition rate are notably enhanced. Also, this configuration allows the sputtering at lower pressures than for conventional DC and RF sputtering. As a high power is delivered to the cathode, it heats significantly and requires a cooling system, which is typically a water or another cooling agent flowing around the magnets behind the cathode.

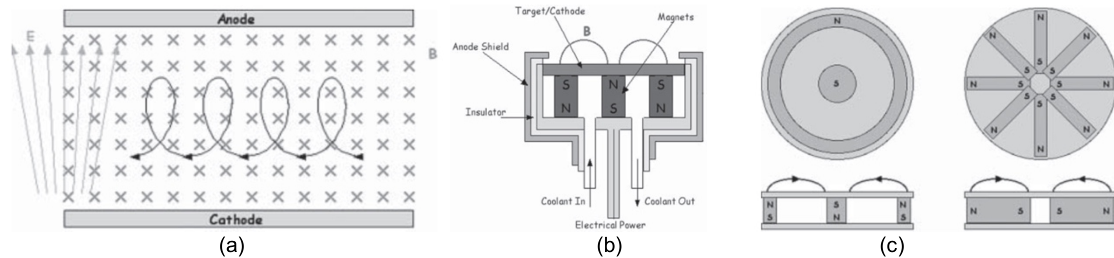

(a) (b) (c)

Fig. 3.4 - Magnetron Sputtering. As taken from [345].

A couple of common magnet arrangements are shown in Fig. 3.4 (c). Under the electric field between the cathodes and magnetic field oriented radially and near to the surface zone the drift path for electrons moving along the surface has a circle shape, resulting in a high-density plasma region along this path. This cause a preferential sputtering of the target around a circular region known as "racetrack" and typical target utilisation of only 20-45% [345].

There are many modifications of magnetron sputtering systems to overcome some drawbacks, such as racetracks, or to improve fabrication process and characteristics of the deposited films: cylindrical post magnetrons and cylindrical hollow magnetrons (the latter ones allow to deposit films on three-dimensional substrates and improve target utilisation rates up to 90%), unbalanced magnetrons to increase ion bombardment of the growing films, which makes them denser and preferentially orients the crystallites, high-power pulsed magnetron, which provide regions with both the process gas and sputtered species highly ionised for high degree control over the deposition process, high ion energy, films density, deposition rates, etc. [345].

3.2.3. Ion Beam Sputter Deposition

Another type of sputtering systems is ion beam sputter deposition (IBD), where a relatively focused beam of accelerated ions (typically, inert gas (Ar, Kr, Xe) or O_2 and N_2 if oxides and nitrides are to be grown) hits the target of the material to be deposited. Schematic drawing of typical ion beam sputter deposition technique is shown in Fig. 3.5 (a). The generation of the primary particles from the ion source, the generation of film-forming particles at the target and thin film growth on the substrate are spatially separated. Thus, it is possible to control and modify the energy distribution of the film-forming particles (and thin film properties) by changing ion beam parameters (ion species and energy) and geometrical parameters (ion incidence angle and emission angle) [346].

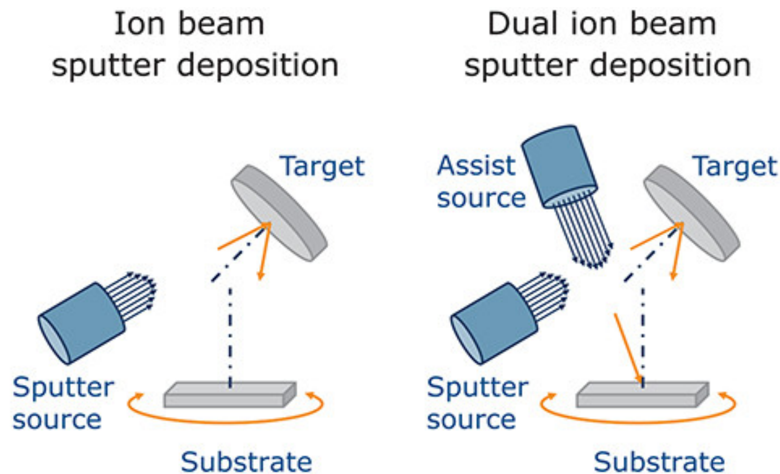

Fig. 3.5 - Ion beam (a) and dual ion beam (b) sputter deposition techniques, as taken from [346].

3.3. Physical Vapour Deposition: Evaporation

Evaporation is a large group of physical vapour deposition techniques, which includes many approaches with involved thermal process how the material can be transferred from the source to the substrate. In contrast to sputtering, where target surfaces usually are maintained at room temperatures and atoms are ejected through the impact of gaseous ions (momentum transfer), evaporation methods assume thermal energy transfer to atoms in a liquid or solid source (heating) such that their temperature is raised to the point when they either efficiently evaporate or sublime [347].

3.3.1. Resistive and Induction Heating

The simplest and the most commonly used method of thermal evaporation is resistive heating, where the source material is heated by a high direct current (10-100 A) passing through the filament, boat or crucible usually made of refractory metals, as shown in Fig. 3.6 (a,b) [348]. Crucibles of quartz, graphite, alumina, beryllia, boron-nitride, and zirconia are used with indirect heating, which is often performed through the application of radio-frequency heating. Usually there are distinguished two developed methods: induction heating, highly effective for metals and other good conductors, and dielectric heating for materials with poor electric conductivity. Induction heating is based on application of high-frequency electromagnetic field produced by an inductive coil connected to RF-generator and placed around the crucible with material to be evaporated. The electrical current generated under applied electromagnetic field heats the material. In dielectric heating the heat is generated from dielectric losses that occur when electric dipoles in material reorient themselves in RF electromagnetic field inside capacitor created by two electrodes. Since the refractory metals cannot be evaporated at appreciable rates by the resistive heating due to the high melting point, they can be evaporated by induction heating mentioned earlier, or by electron beam. Both methods are shown illustratively in Fig. 3.6 (c, d).

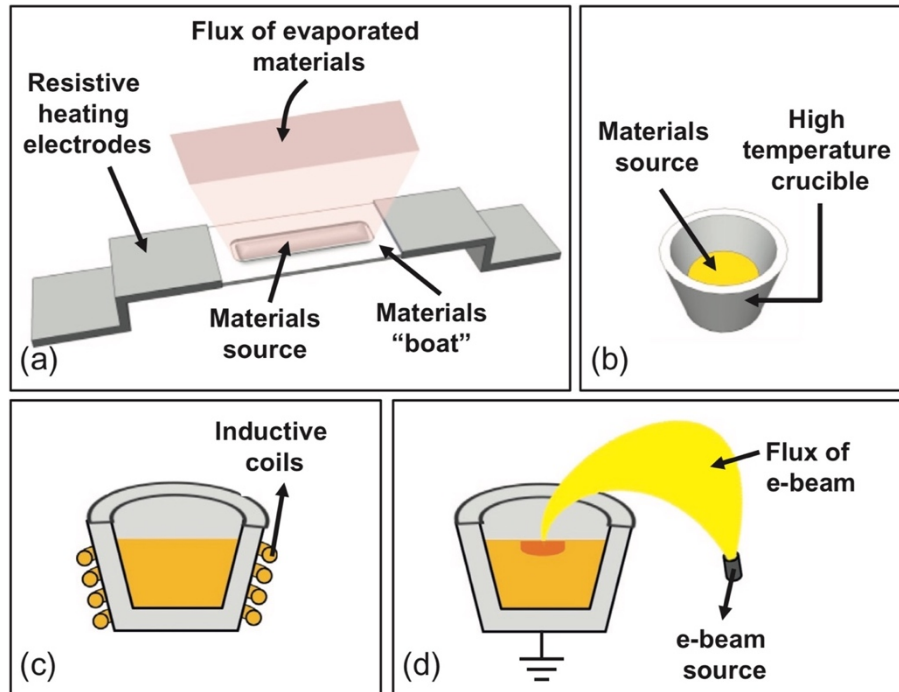

Fig. 3.6 - Schematic illustration of: (a) resistive heating thermal evaporation, (b) crucible containing source materials, (c) inductive heating, and (d) electron beam heating. As taken from [349].

3.3.2. Electron Beam Heating and Flash Evaporation

Electron beam heating also resolves a problem of source material contamination coming from supports, heaters and crucibles during resistive heating and provides no limitation of relatively low input power levels [347]. In electron beam heating deposition process the purity of the evaporated material can be reached because only a small area is heated, and the crucible is maintained at low temperatures.

For the deposition of multi-element material two main approaches can be used: multi-crucible method or single crucible with alloyed source. Two methods can be combined to deposit complex and multi-element structures. Often it may be difficult to achieve desired composition or stoichiometry of deposited films due to the difference in materials vapour pressure and different deposition rates.

Flash evaporation is one of the techniques suitable for the deposition of the film with components which have different vapour pressure. Very rapid vaporization occurs, usually by dropping powders or grains of the source material (mixture) onto a sufficiently hot surface heated by filament or inductive heating. With flash evaporation the easily volatile and less volatile components evaporate completely and condense rapidly onto a relatively cold substrate, reproducing the composition of the source material [350]. This method also prevents harmful reaction between source and crucible and helps to avoid contaminations [351]. Schematically the flash evaporation system for films deposition is shown in Fig. 3.7.

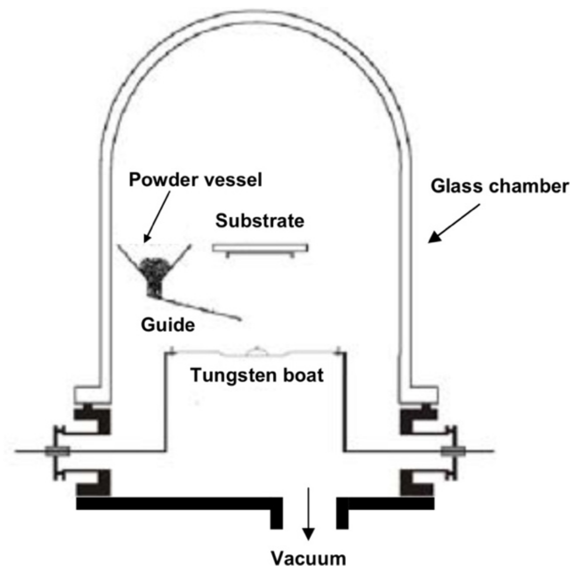

Fig. 3.7 - Schematic diagram of flash evaporation reactor. As taken from [352].

3.3.3. Molecular Beam Epitaxy

Molecular beam epitaxy is an advanced method of thermal evaporation for single-crystal epitaxial films growth providing a high-level control of the chemical composition, doping concentration, uniformity, lattice match, thickness and smoothness of the deposited epitaxial layers. Schematic diagram of a typical molecular beam epitaxy chamber is shown in Fig. 3.8. The method requires an ultra-high vacuum in the deposition chamber (10^{-8}-10^{-9} Pa), where a molecular beam is generated by evaporation the source material usually by resistive or electron beam heating in a deep cylindrical crucible named Knudsen effusion cell and controlled by an automated shutter [351]. Single-crystal substrates are heated to the high temperatures appropriate for chemical reaction, epitaxy and re-evaporation of excess reactants. Ultrapure material sources and ultrahigh vacuum in the deposition chamber ensure high-quality films growth and absence of contaminations. In-situ monitoring techniques, such as reflection high-energy electron diffraction (RHEED) for observation of the morphology and crystallinity of the growing films, electron spectroscopy for chemical analysis (ESCA), Auger spectroscopy and others may be installed in the ultrahigh vacuum deposition chamber. The main disadvantages of molecular beam epitaxy are limited product throughput (very low deposition rates), complex operation and quite expensive equipment.

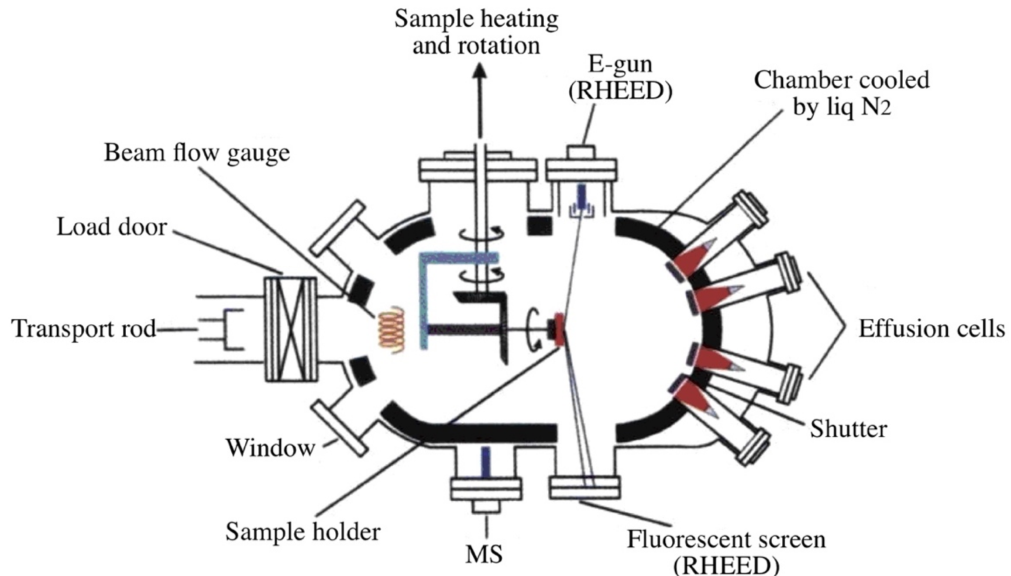

Fig. 3.8 - Scheme of a typical molecular beam epitaxy growth chamber. As taken from [353].

3.3.4. Laser Ablation

Laser ablation or pulsed laser deposition (PLD) technique is based on the interaction of high-powered laser beam with a solid. Typical scheme of a PLD system is shown in Fig. 3.9.

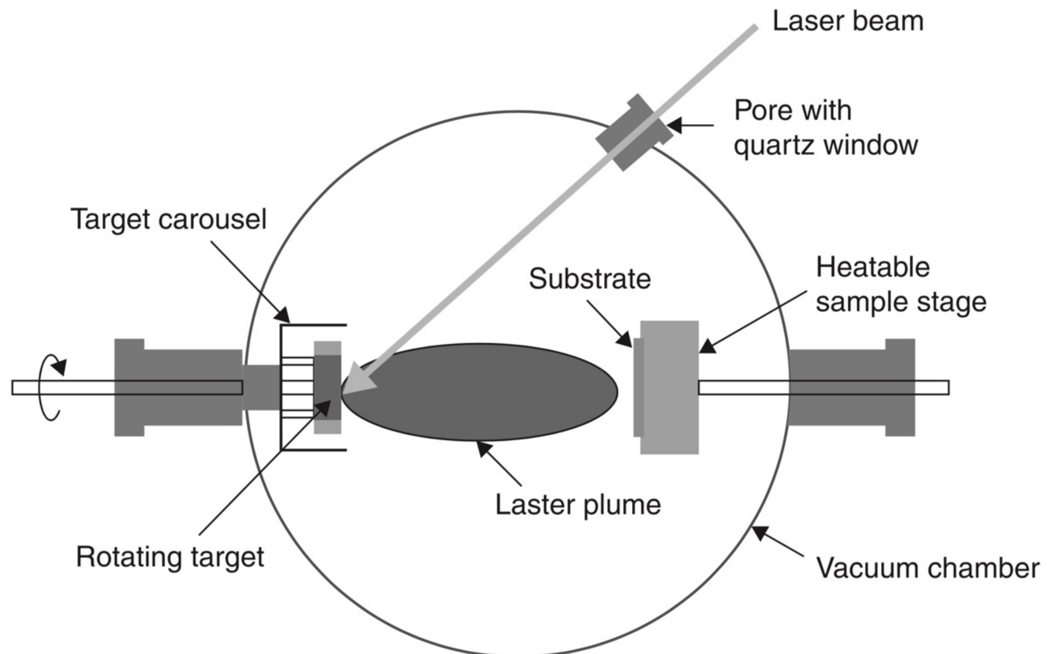

Fig. 3.9 - Schematic view of a PLD system. As taken from [354].

A high-power laser is placed outside the vacuum deposition chamber and focused by external lenses through the quartz window onto the target. The most widely used lasers for PLD are solid state Nd:YAG laser and excimer types [347]. The energy of the absorbed beam converts into thermal, chemical and mechanical energy, causing evaporation of the source material at the surface with possible plasma plume formation at high laser flux. Evaporated material and plasma plume move perpendicularly away from the target and deposit on the substrate. Formed plume

consists of energetic neutral atoms, molecules, ions, electrons, atom clusters, micro-sized particulates, and molten droplets [347]. To avoid the deposition of the micro-sized ejected particles, the substrate may be settled at an off-axis positions [343].

3.3.5. Arc Evaporation

The fabrication of protective coatings by various deposition methods (chemical processes, physical vapour deposition, ion-assisted deposition) allows to solve plenty of problems in industry regarding approaches to improve wear and corrosion resistance, reduce friction, increase fatigue strength of cutting tools and mechanical details. Among this variety of strengthening technologies, a special place is occupied by vacuum-arc deposition often named also as cathodic arc physical vapour deposition (Arc-PVD), which makes it possible to obtain coatings suitable for work under high temperatures and pressures, aggressive environment, high corrosion and intensive wear.

Arc evaporation, or cathodic arc deposition (Arc-PVD), is one of the most widely used physical vapour deposition techniques among evaporation methods for industrial fabrication of protective coatings with high hardness and other mechanical properties. The evolution of industrial cathodic-arc coating started in the 1960s mainly at the National Science Center of the Kharkiv Institute of Physics and Technology (NSC KIPT), Ukraine (at that time, the Ukrainian Soviet Socialist Republic, the Soviet Union), which resulted later in the series of industrial cathodic-arc process equipment called Bulat. In the United States and Japan, the first reports on cathodic-arc were registered in 1960 and since 1979 the Bulat and related plasma sources have been applied in the US vacuum-coating industry allowing the fabrication of high-quality thin films at competitive costs [355].

3.3.5.1. Cathodic Arc Discharge

Cathodic arc deposition method is based on the generation of a highly ionised plasma from the solid (the cathode material) by means of the arc discharge. The arc discharge current is concentrated at the cathode surface, forming isolated bright moving spots of extremely high current density and areal power density (of order 10^{12} A/m^2 and 10^{13} W/m^2 respectively) [356]. The cathodic-arc spot has a very dynamic behaviour and its evolution occurs by four following stages shown in Fig. 3.10: pre-explosion, explosive stage, cooling period and final cooldown. The physics of the cathode process is discussed in great details by A. Anders [357] and in other reviews [355,356].

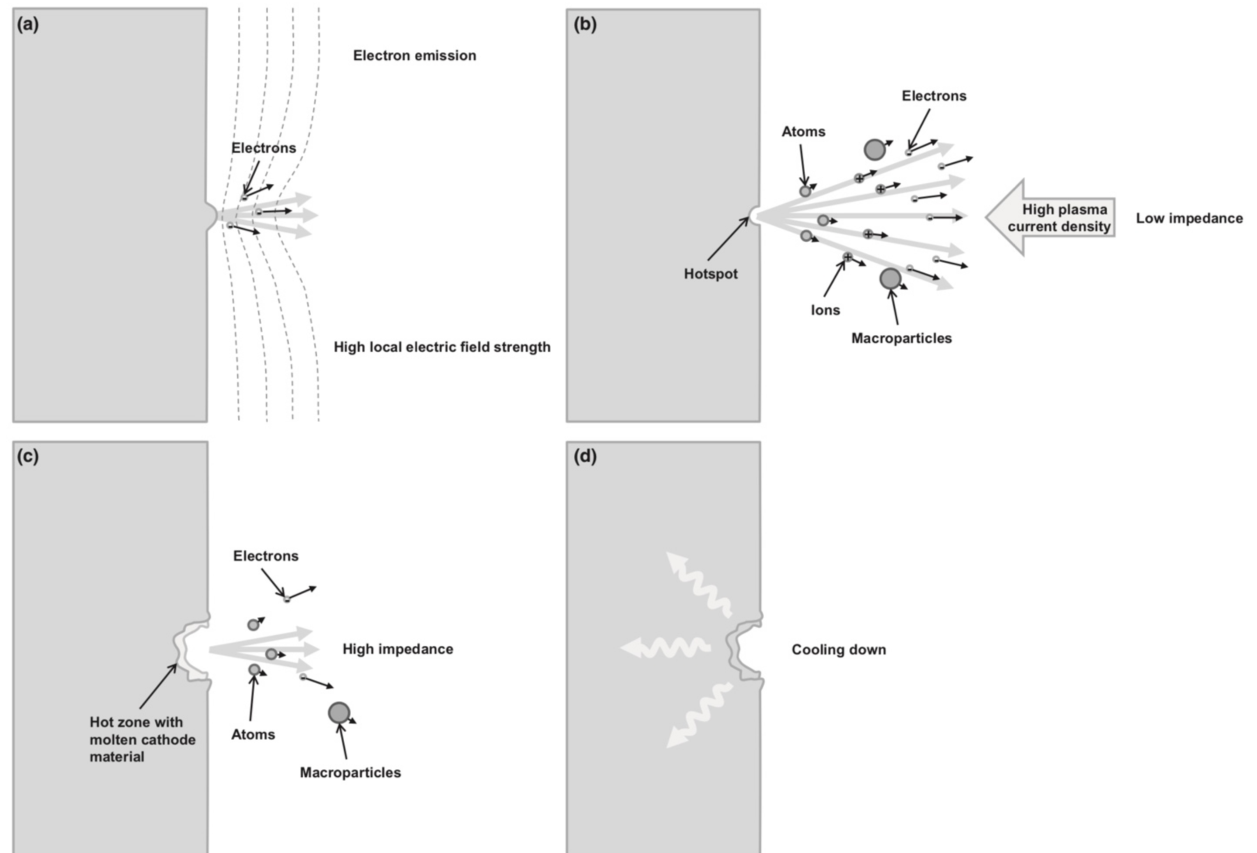

Fig. 3.10 - The evolution of the cathodic-arc process: (a) pre-explosion; (b) explosive stage; (c) cooling with molten cathode material; and (d) final cooling. As taken from [355].

The cathodic arc discharge is characterised by a collective emission of electrons, and the nature of the process lies in the thermo-field emission combined with time-dependent local temperature of the cathode-arc spot. The ignition of the arc at the pre-explosion stage and its burning depend on many aspects, such as electron work function ω, electron field strength, surface geometry and impurities, plasma parameters, ion bombardment, oxide layers on the cathode etc. [355].

The most favorable locations on the cathode surface for the ignition of the arc are those which have lower local work function and enhanced electric field due to the micro- or nanoprotrusions and dielectric contaminations of the surface. When a strong electric field is applied and a high-intensity ion bombardment occurs, the local energy input can lead to the electron emission with thermal runaway and explosive emission stage. Ion bombardment from the plasma and Joule heating by the emission current lead to the local increase of the temperature. The higher temperature then enhances the emission and in turn leads to greater resistive heating and further growth of the temperature. Such loop in a couple with not balanced and usually insufficient cooling leads to the local evaporation of the cathode in an explosive manner called explosive emission of ions and electrons. The process is always associated with the formation of plasma of the emitting material and erosion of a microvolume on the cathode surface [358]. The explosive stage usually has a duration of 10-20 ns with emission of 10^{11}

electrons per 10 ns, while a full cycle takes around 50-70 ns [359]. A large number of atoms are ionised by the bombardment of the ejected electrons [355].

At the postexplosion stage the surface layer of the formed crated is still hot and molten, and the nearby plasma is very dense, therefore, strong field-enhanced thermionic electron emission remains (work function barrier is reduced but not enough for thermo-field emission). Simultaneous evaporation of the liquid cathode material generates neutral vapour of low conductivity, which reduces the flow of current [358].

In the final cool-down stage, the local temperature decreases and the electron emission goes down exponentially. At the same time previously formed plasma has lower density due to expansion, cathode sheath thickness increases and the electric surface field reduces [358]. Hot surface of the cathode may still deliver metal vapour at this stage. At microscopic level the observer can see a sequence of fast cathodic-arc discharges, their ignition, explosion phase and cool-down, which may be interpret as cathodic spot motion.

There are several factors of the cathodic-arc spot decaying: (1) emission area increases due to the thermal conductivity, which leads to the spreading and decrease of the areal power density; (2) in most of the cases, a local resistance of the area increases with higher temperatures, which brings a way for an alternative less resistant spot; (3) neutral metal vapour which is the most resistive phase may cut or decrease the flow of electricity at the second half of the cathode-arc discharge cycle; (4) the competition between a new emission site and the older one with resistive metal vapour accelerates the death of the original site because of less power goes through it.

In the presence of a magnetic field, the arc-discharge and spot move opposite to the direction of the Ampere force [355]. In this way, magnetic fields are used to steer the arc-discharge spot very often.

3.3.5.2. Macroparticle Filtering

The most challenging feature of the cathodic arc deposition is the generation of microparticles. This process is mostly understood as the ejection of droplets from the molten metal poll. This brings defects into the microstructure of the deposited thin films, usually, in the form of flattened droplets if they hit the substrate in the not-solidified phase. Otherwise, the solid particles can bounce off the surface and their probability to stick is lower.

Usually, magnetic filtering may be used to remove microparticles from the cathode-arc plasma flow. There are many types of magnetic filters with different geometry, size and parameters used today. Some of them are shown schematically in Fig. 3.11. The concept is based on the possibility to guide a plasma flow outside the line-of-sight from the cathode surface along the magnetic field lines toward the substrate, while much heavier macroparticles move along almost not affected straight trajectory.

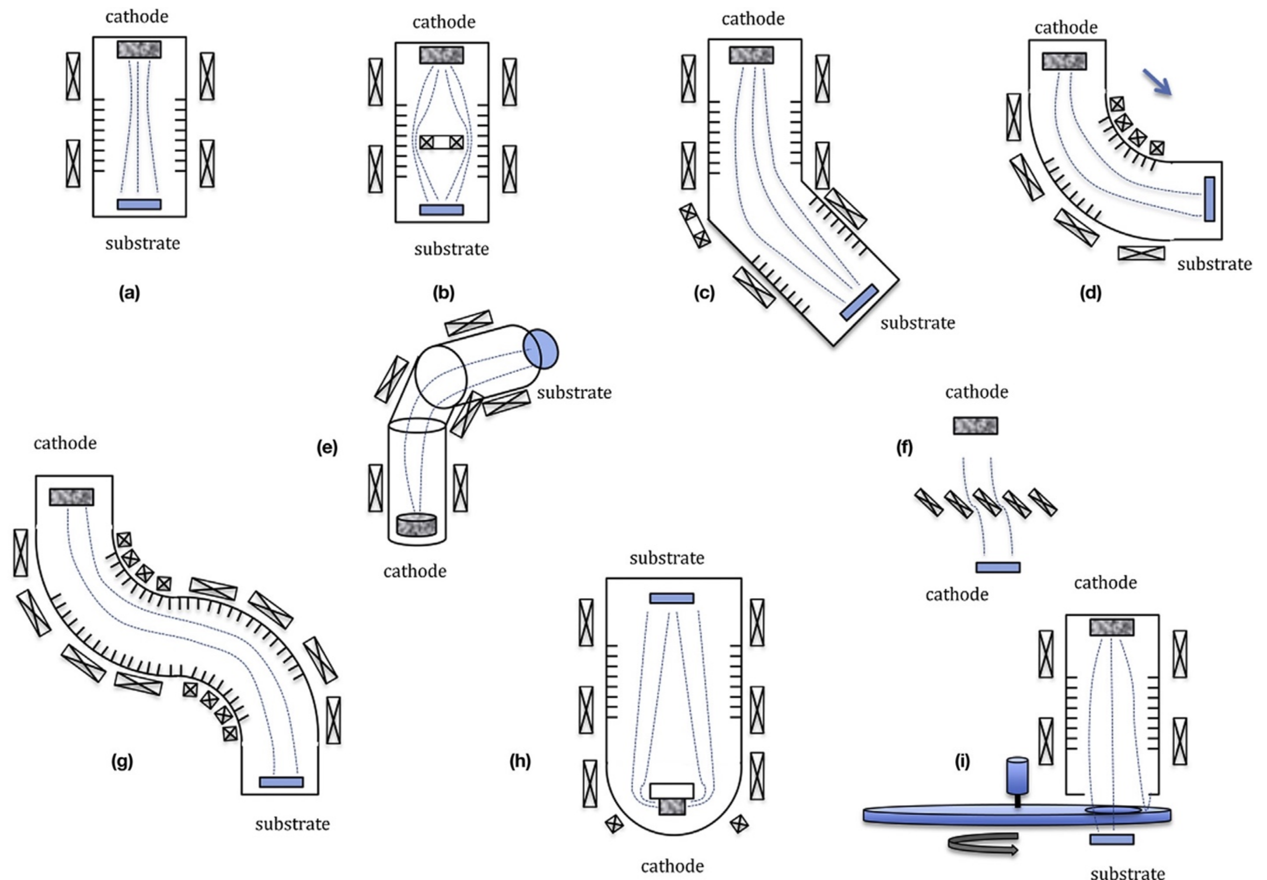

Fig. 3.11 - Different types of filter systems: (a) Rectilinear; (b) rectilinear with a magnetic island; (c) knee; (d) 90° duct; (e) off-plane double bent; (f) Venetian blind; (g) S-filter; (h) dome; and (i) stroboscopic filter. As taken from [355].

3.3.5.3. DC and Pulsed Vacuum Arc Deposition

There are two main technical approaches for vacuum arc deposition process and deposition equipment: continuous (DC) and pulsed modes of operation. Although pulsed and DC arcs operate qualitatively at the same way, their action on the cathode surface has differences and influences the arc spot evolution. Basic setup for both DC and pulsed vacuum arc systems is shown illustratively in Fig. 3.12.

The DC Arc-PVD system is composed of a cooled cathode, annular anode and separate, usually mechanical (spring-loaded electrode), triggering device, which is pushed to contact with the cathode to initiate the arc by caused trigger spark. Often a magnetic field coil is included in the design for cathode spot steering, plasma ionisation and ion energy enhancement.

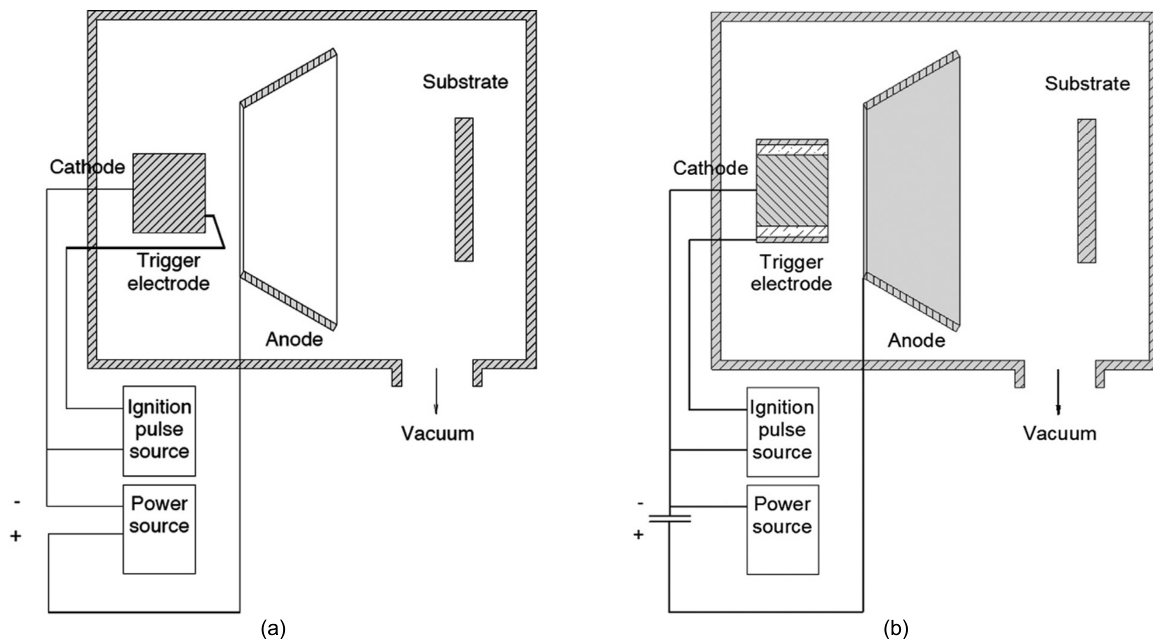

Fig. 3.12 - Basic setup of DC cathodic-arc plasma system (a) and simple pulsed cathodic-arc device (b). As taken from [355].

In the pulsed Arc-PVD device the cathode is connected to a capacitor or a pulse forming network. The need for a frequent and often rapid arc triggering in pulsed mode requires to substitute mechanical trigger typically used for DC arc systems by other concepts. The ignition arc can be obtained when a short high-voltage is applied to the electrode isolated from the cathode. The trigger electrode could be placed at the centre of the cathode, at the outer rim of the cylindrical cathode, or around the cathode in the area between the cathode and anode [355].

Most of the commercially used Arc-PVD systems are used in the DC mode due to their capability of very high deposition rates and large area of coatings fabrication. On the other hand, pulsed systems allow to produce films with better deposition control and enhanced properties. Pulsed Arc-PVD is also associated with relatively small deposition rate, reduced operational power, low heating and less generation of the microparticles.

3.4. Experimental Details on Fabrication of Arc-PVD Multi-Layered CrN/MoN Coatings

CrN/MoN multi-layered coatings were fabricated by vacuum-arc evaporation of chromium and molybdenum cathodes (Arc-PVD) in nitrogen atmosphere using Bulat-6 unit [185,208] designed for deposition of protective and decorative coatings. A principal scheme of the deposition system is shown in Fig. 3.13.

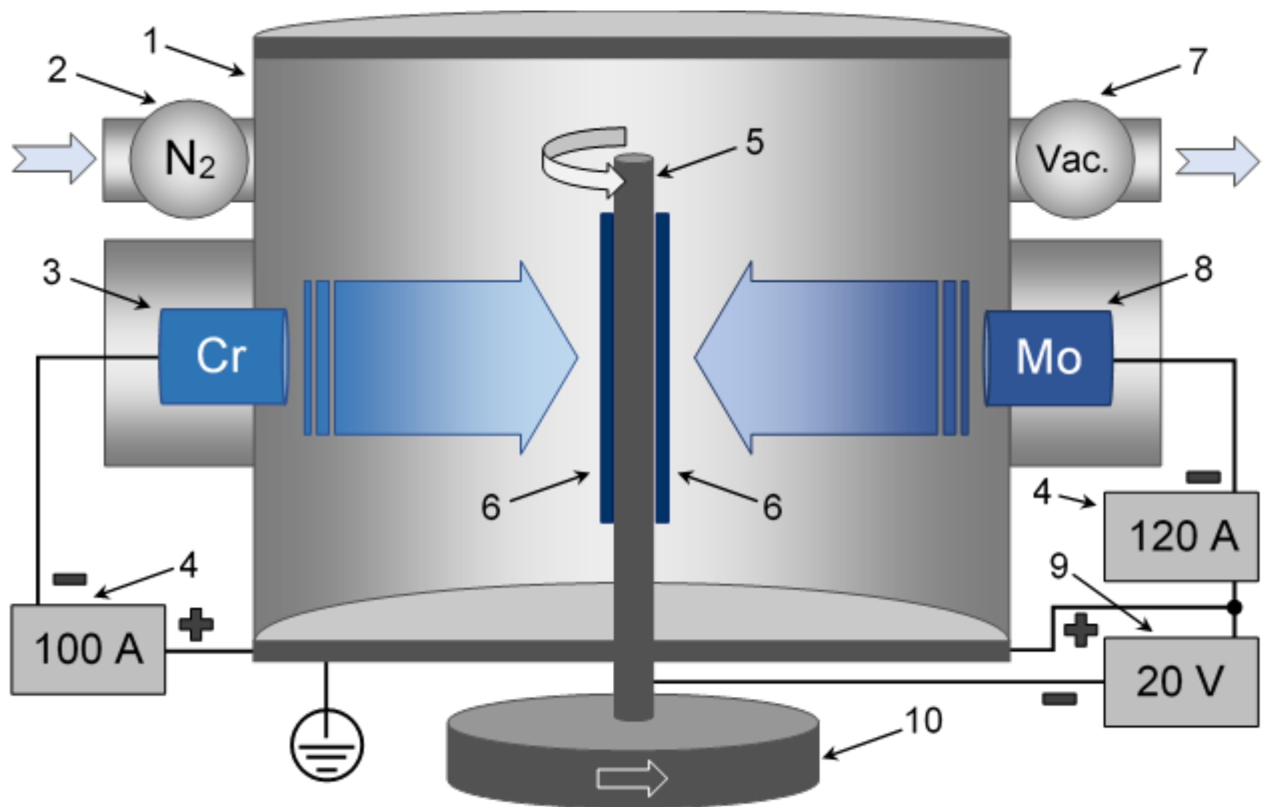

Fig. 3.13 - Principal scheme of vacuum-arc deposition system for multilayer films: 1 - vacuum chamber, 2 - nitrogen supply, 3 - chromium cathode, 4 - arc power supplies, 5 - substrate holder, 6 - substrates, 7 - vacuum pump, 8 - molybdenum cathode, 9 – substrate power supply, 10 - automatic rotation system for substrate holder. Published in [146].

Films were deposited on the polished substrates of stainless steel 12X18H9T with dimensions of 20×20 mm^2 and thickness of 2 mm. Roughness of the surface R_a was up to 0.09 μm. Before the deposition process, the substrate surface was cleaned and activated by metal ion bombardment, by applying the negative potential of -1.3 kV to the substrates for 15 minutes. Cleaning process was performed under continuous rotation of substrate holder and arc current I_{arc} of 120 and 100 A for Cr (chromium X99 rod, purity of 99%) and Mo (pure vacuum melted molybdenum rod, purity 99.99%) cathodes respectively. Then the interlayers of pure metals were deposited during 1 minute and the main process of multilayer CrN/MoN films deposition was performed in Nitrogen atmosphere, up to 1 hour. Although it is not shown in the scheme, the deposition system Bulat-6 is equipped by special filtration system to avoid droplets incorporation in the films, which are usually typical for Arc-PVD processes.

Automatic control system for multilayer coatings deposition have been developed especially for this deposition unit and reported by V. Rudenko et al. [360]. The system provides two modes of multilayer structures fabrication: deposition on flat surfaces and deposition on products having three-dimensional, particularly cylindrical, shapes. A timeline diagram for key-elements of used deposition system is shown in Fig. 3.14 for both modes.

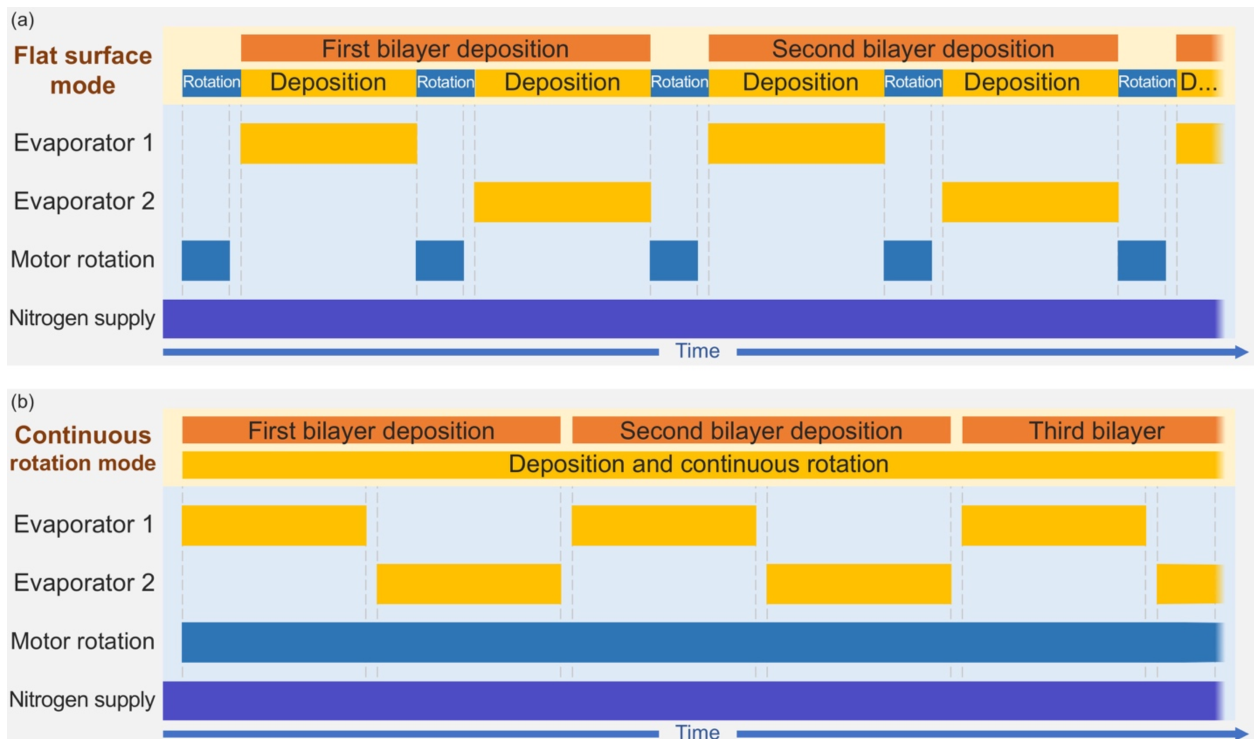

Fig. 3.14 - Timeline diagram for automatic control system used in modified deposition unit "Bulat-6". Two working modes are developed for deposition of multi-layered coatings on flat surfaces (a) and on products having 3D shapes (b). Adapted from [360].

The mode of deposition on flat surfaces, which was used to fabricate coatings studied in this Thesis, assumes a simultaneous work of two evaporators during predetermined time t_E that turn off for the time t_R when the electric motor rotates the sample holder for 180° as shown in Fig. 3.14 (a). The sample holder is a still plate fixed vertically on the rotation system. Samples may be placed on both sides of the plate and constant bias voltage may be applied during the deposition. Time t_E determines the thickness of the individual layer which, multiplied by number of repetitions, gives a total deposition time and coating thickness. A decay after motor work before evaporation starts is required to complete the movement of the rotation system. Timer counting t_E starts when the current of the arc discharge is registered by reed switches.

If it is needed to deposit multilayer coatings on some products having 3D shape, especially cylindric as drills, or other machining tools and inserts, the second mode of the control system may be used when evaporators turn on alternately and the sample holder rotates continuously as seen Fig. 3.14 (b).

Such automatic control system of multilayer coatings deposition provides sharp interfaces between nanolayers, constant normal incidence angle of plasma flow onto the substrates, uniform thickness and properties, and allows to control bilayer thickness with high accuracy and precision. This is hard to achieve with widely used regular method when sample holder rotates continuously between two diametrically placed evaporators, especially on low speeds to achieve individual layer thickness at least of tens nanometers [360].

The constant nitrogen pressure p_N of 0.4, 0.09 and 0.03 Pa was used in the chamber. Three series of samples were deposited with different bias voltages of −20, −150 and −300 V

applied to the substrate. The samples of each series vary in the deposition time of an individual layer: thus, time was kept constant during a single deposition run, but it was halved from one deposition experiment to the next one, keeping the total deposition time constant (1 hour).

Fig. 3.15 demonstrates qualitatively estimated (expected) individual layers thickness in the deposited coating according to the deposition time per layer within the series. The thickness of the coatings changed from 8 to 19 µm. Detailed information about deposition conditions is presented in Table 3.1.

Table 3.1. Deposition parameters of the MoN/CrN coatings. Arc current $I_{arc}(Mo)$ = 120 A, $I_{arc}(Cr)$ = 100 A, total deposition time t_{tot} = 1 h, t_l – one layer deposition time, N_l – number of layers, λ - bilayer thickness. Samples marked with asterisk (*) were deposited in a continuous rotation mode of the substrate holder.

Series	Sample №	p_N, Pa	t_l, s	N_l	U_b, V
1	1.1	0.4	300	12	−20
	1.2		150	25	
	1.3		80	45	
	1.4		40	88	
	1.5		20	180	
	1.6		10	354	
2	2.1	0.4	300	12	−150
	2.2		150	25	
	2.3		80	45	
	2.4		40	88	
	2.5		20	180	
	2.7*	0.09	150	22	
3	3.1	0.4	300	11	−300
	3.2		150	22	
	3.3		80	44	
	3.4		40	88	
	3.5		20	180	
	3.6		10	354	
	3.7*	0.03	150	22	

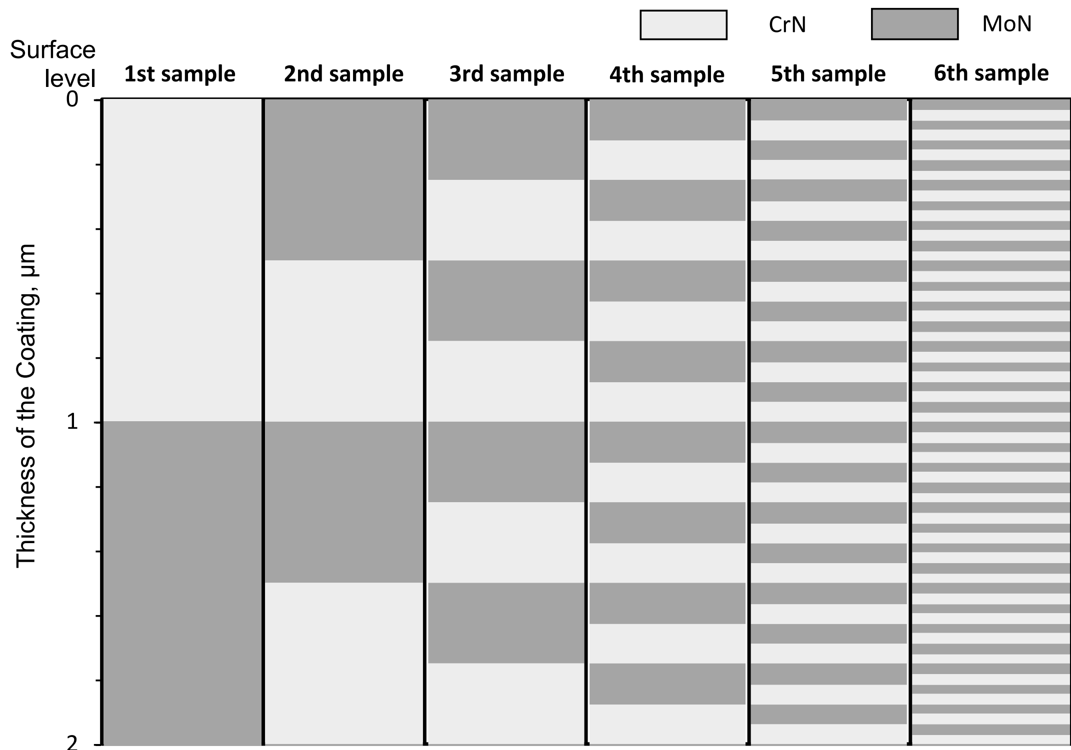

Fig. 3.15 - Illustrative comparison of the individual layer thickness (qualitatively) within the series of coatings according to the deposition time per layer.

Chapter 4.
Micro- and Nanostructural Characterisation

4.1. Multilayer Structures

SEM analysis was used to study the cross-sectional morphology in the films and their multilayer structure. The calculated values of bilayer and total thickness of the deposited films are given in Table 4.1 and they are in accordance with the expected ones. Selected SEM images of the multilayer CrN/MoN coatings with bilayer thickness of 2.26 μm, 0.6 μm and 44 nm are presented in Fig. 4.1. Images of samples 1.1 and 1.3 (Fig. 4.1 (a) and (b)) were taken in secondary electron imaging (SEI) mode, magnification ×5k and ×15k, respectively. Image of sample 1.6 (Fig. 4.1 (c)) was obtained using the backscattered electron detector (BSED) in Z (atomic number) mode, and magnification is ×400k.

Since heavier atoms with higher atomic number Z give brighter shades of grey on SEM images, the MoN layers with greater average Z will result in brighter layers. CrN layers, on the other hand, have a lower average atomic number, thus corresponding to darker layers. The cross-section SEM images confirm the periodic stacking of the MoN/CrN layers and the presence of relatively sharp interfaces, which approves the high quality of Arc-PVD deposited films. Defects due to the substrate surface roughness or droplets in films were easily absorbed and smoothed by a multilayer structure.

The samples demonstrate a well-defined multilayer structure with distinct interfaces and good planarity of the individual layers. It should be noted that the MoN layers (bright in the SEM images) are slightly thinner than the CrN layers (dark areas) due to the different cathode evaporation rate for Cr and Mo, and deposition rates for CrN and MoN layers. Especially it is more evident on the samples with thicker bilayers (see Fig. 4.1 (b)) rather than on thinner ones (with shorter deposition time per layer).

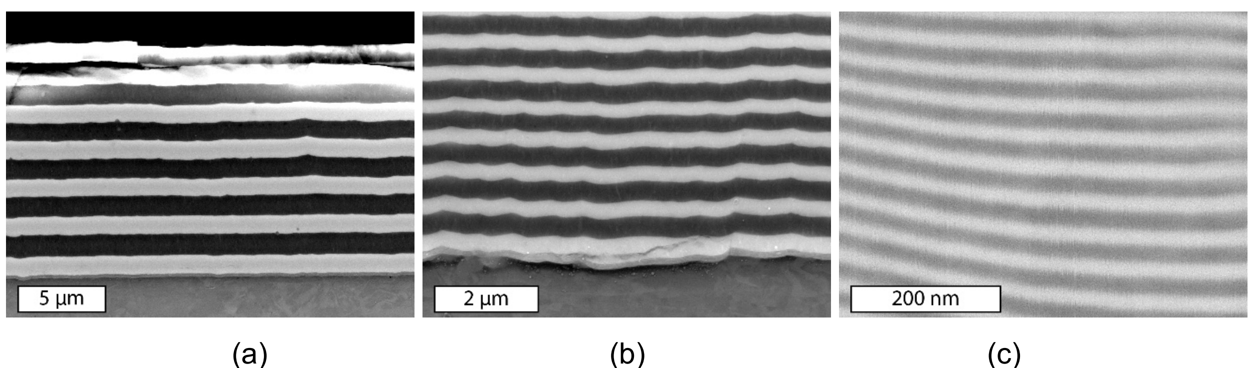

Fig. 4.1 - SEM-images of polished cross-section samples 1.1 (a), 1.3 (b) and 1.6 (c) of multilayer CrN/MoN coatings. Published in [214].

The evolution of deposition rate, calculated by dividing the value of bilayer thickness by the corresponding deposition time (see Table 4.1), is shown in Fig. 4.2.

Table 4.1. Total thickness and thickness of layer period measured by SEM on cross-sections.

Sample	U_b, s	p_N, Pa	Dep. time per layer, s	Bilayer thickness Λ, μm	Total thick., μm
1.1	−20	0.4	300	2.26	13.5
1.2			150	1.18	14.7
1.3			80	0.60	13.6
1.4			40	0.25	11.1
1.5			20	0.12	10.8
1.6			10	0.044	7.8
2.1	−150	0.4	300	2.85	17.1
2.2			150	1.39	17.4
2.3			80	0.69	15.5
2.4			40	0.32	14.1
2.5			20	0.14	12.6
2.7*		0.09	150	0.25	2.8
3.1	−300	0.4	300	3.5	18.9
3.2			150	1.55	17.1
3.3			80	0.74	16.2
3.4			40	0.36	15.8
3.5			20	0.15	13.5
3.6			10	0.075	13.2
3.7*		0.03	150	0.19	2.1

It is seen that for coatings with shorter layer deposition time, the real bilayer thickness starts to be lower than predicted by deposition time control. This can be explained by specific features of the deposition system with an automatic controller of substrate holder rotation and evaporator power supplies. The shorter the deposition time per layer, the more often the substrate holder rotates, and the controller deactivates evaporators. Meanwhile, nitrogen flows to the chamber, and the excess reactive gas causes an increase in pressure and poisoning of the cathodes, resulting in a decrease in the evaporation rates. In turn, it also influences the increase of reactive gas again, even at the beginning of the new layer deposition process.

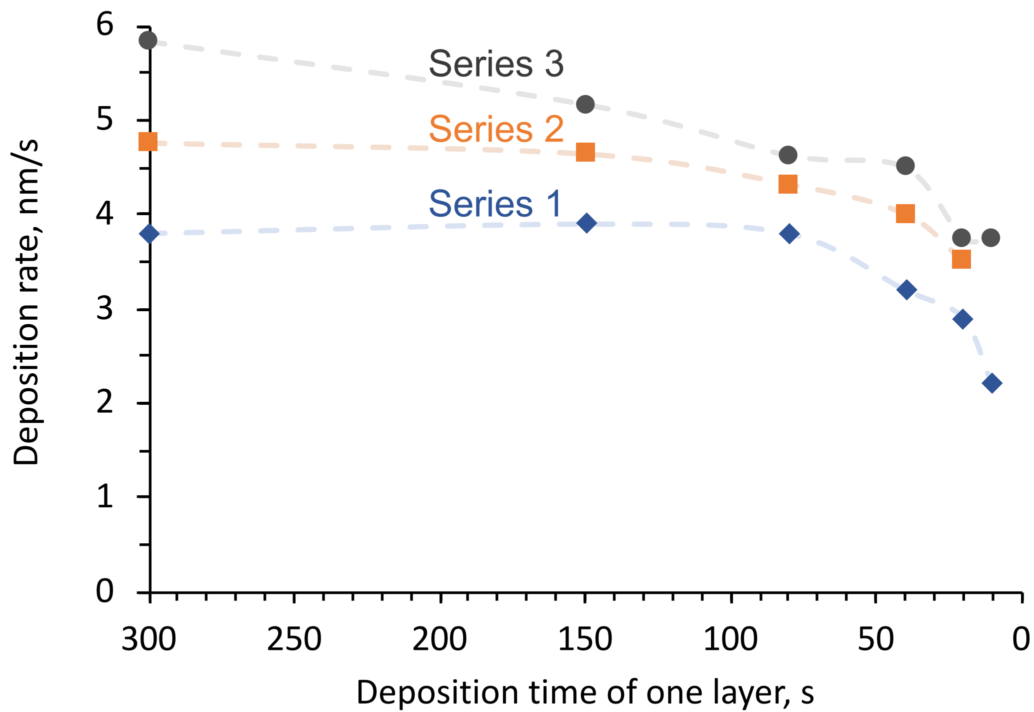

Fig. 4.2 - Dependence of deposition rate on layer deposition time.

Higher deposition rates are observed for the series of coatings fabricated at higher bias voltage (−150 V and −300 V). As highly ionised particles are deposited by the Arc-PVD technique, the bias voltage directly affects the deposition rate. More ionised particles with higher energies are attracted to the substrate at higher bias voltage.

4.2. Elemental Composition

4.2.1. WDS Elemental Analysis

The analysis of elemental composition (see results in Table 4.2) was performed by the WDS technique, which uses characteristic X-rays from the volume of electron beam interaction with studied films. The process of data acquisition and analysis for elemental content and structures of considered films has the features described below.

The elemental composition of coatings was measured by scanning the presence of the four most probable elements, assuming the contribution of chromium, molybdenum, nitrogen and oxygen.

Table 4.2. Elemental concentration in CrN/MoN multilayer films taken by WDS.

Sample	Elements, WDS, top surface			
	Cr, at.%	Mo, at.%	N, at.%	O, at.%
1.1	48.1	0.1	50.1	1.8
1.2	1.1	53.0	41.0	5.0
1.3	1.8	50.3	43.1	4.8
1.4	10.2	41.6	43.5	4.7
1.5	25.5	16.0	56.7	1.8
1.6	27.6	25.1	44.8	2.5

The $K\alpha_1$ line of oxygen, which was used for the analysis ($E_{K\alpha1}(O)$ = 0.525 keV), lies very close to the $L\alpha_1$ line of chromium ($E_{L\alpha1}(Cr)$ = 0.572 keV). Because of this, chromium may contribute to the value of oxygen content in the film's composition. In order to avoid this, the determination of background for oxygen peak acquisition was made by the shoulder on the side opposite to the chromium $L\alpha_1$ line.

Sample 1.1 demonstrates the presence of only Cr and N, which indicates that only the first top surface layer of CrN was exposed to interaction with the electron beam. It means that the thickness of the layers in sample 1.6 is much higher than the penetration depth of the electron beam used. Based on equation (2.1), it is possible to evaluate how deeply the electron beam penetrates the film. The electron beam used in this experiment may reach the depth of up to 0.34 or 0.54 μm for MoN or CrN films, respectively. For coatings with thin enough layers, the average value of penetration depth was used. See the schematic illustration in Fig. 4.3.

As a result, it was identified that in sample 1.1 with Λ = 2.26 μm, only the first layer of CrN was evaluated. The elemental composition was almost 50% both of chromium and nitrogen, ratio Cr/N = 1, which means that stoichiometric CrN film was deposited. The elemental composition of MoN in deposited samples was evaluated on the top layer of sample 1.2: Mo/N = 1.33. Also, assuming the same elemental ratios as for MoN in sample 1.1 and CrN in sample 1.2, it was estimated that the integral elemental composition of sample 1.6 is as follows: Cr - 24.3 at.%, Mo - 26.8 at.%, N - 45.5 at.% and O - 3.4 at.%, which also gives the ratio Mo/Cr = 1.1. When compared with the measured values in Table 4.2 for sample 1.6 (with the thinnest layers, where the electron beam exposed about 22 layers), they are found to be similar, but slight decreasing of Mo fraction and (or) increasing of Cr content (ratio Mo/Cr = 0.9) are observed. Due to the unbalance of interaction volumes of CrN and MoN layers in samples 1.3, 1.4 and 1.5 (see Fig. 4.3), the results of performed WDS elemental analysis for mentioned films could not be considered as completely reliable.

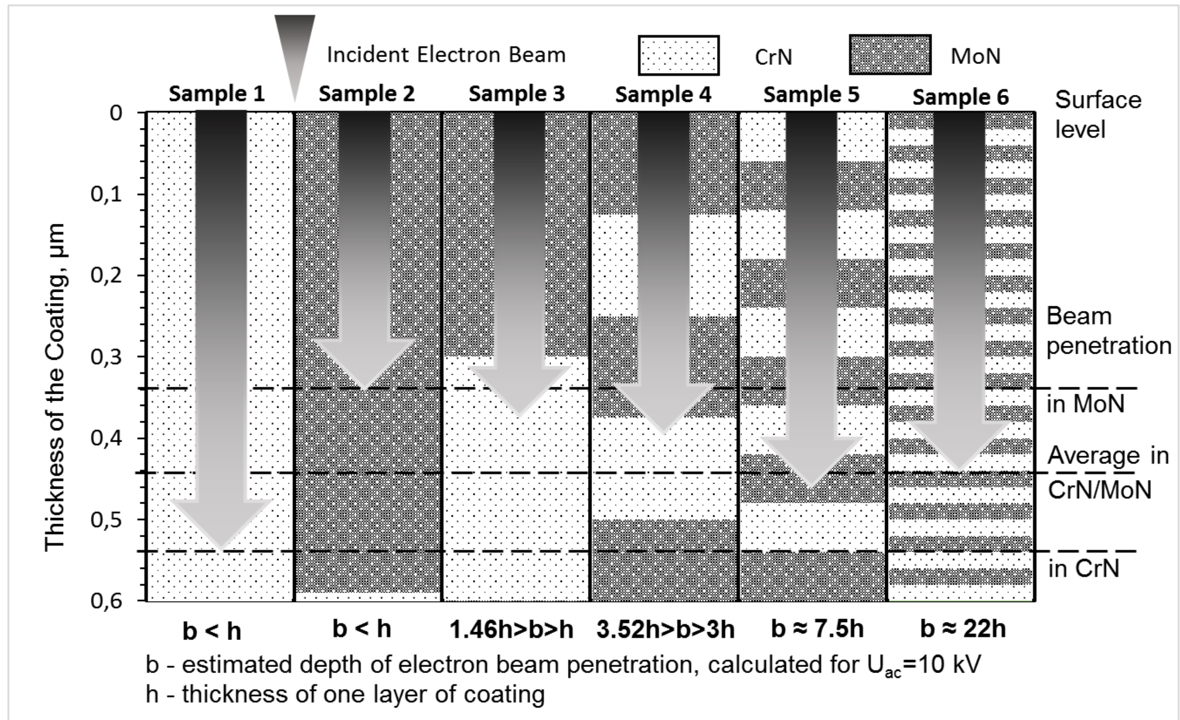

Fig. 4.3 - Estimated penetration depth of electron beam (accelerated voltage U_{ac} = 10 kV) into multilayer CrN/MoN coatings with various bilayer thickness (series 1). Published in [214].

4.2.2. EDS Elemental Analysis

Fig. 4.4 represents the typical EDS-spectrum of CrN/MoN multilayer films deposited at U_b = −150 V (Series 2, sample 2.1). It shows almost the equiatomic elemental composition of the metal components: Mo/Cr atomic ratio varies from 0.90 to 0.93. Similar results were obtained for other series of samples deposited at different bias voltages (U_b = −20, −150 and −300 V). The slight prevalence of chromium atoms may be explained by a small difference in the sputtering yields of Mo and Cr cathodes, as well as in CrN and MoN deposition rates. Unfortunately, even though the EDS technique is appropriate for fast and precise evaluation of metals' concentration, it is not sensitive enough for light elements, such as Nitrogen, and its amount may be underestimated. Therefore, it is preferable to use RBS, SIMS, WDS or other experiments to evaluate the composition of light elements. Nevertheless, the different bias potentials U_b do not significantly affect the atomic concentration of nitrogen, whose atomic ratio in the layers varies from 40 to 60 at.% (for p_N = 0.4 Pa). The relatively higher content of nitrogen was observed in the coatings of Series 2 (U_b = −150 V), probably due to the improvement of the efficiency of the nitride formation. At U_b = −300 V the concentration of nitrogen decreases to relatively low values, which may be explained by selective secondary sputtering and re-deposition effects during the ion bombardment with higher energy [185,230,361]. The dependence of nitrogen ratio on nitrogen pressure in the chamber during deposition is clearer and more evident. When p_N decreases from 0.4 Pa to 0.09 or 0.03 Pa, the atomic concentration of nitrogen drops to 10-20 at.%.

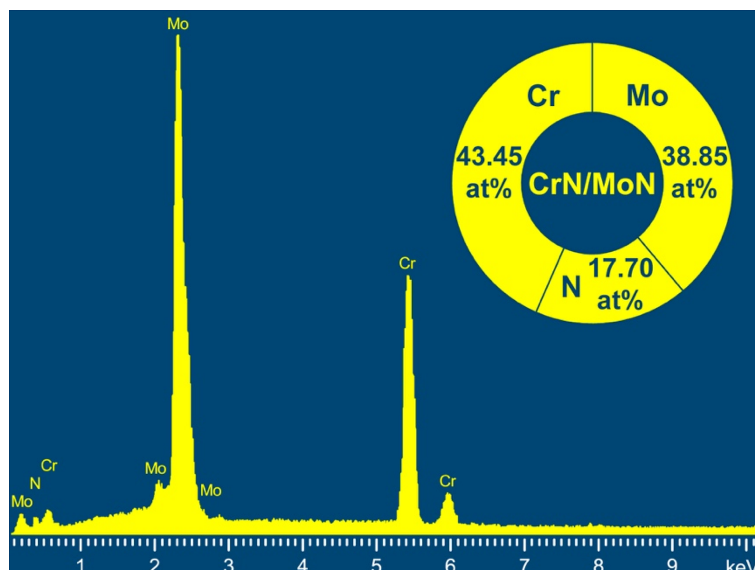

Fig. 4.4 - EDS spectrum and elemental analysis of CrN/MoN multilayer film, sample 2.1. Published in [146].

Fig. 4.5 shows the results of EDS elemental mapping performed on the cross-section of Sample 1.1. Elemental distribution within the CrN and MoN layers is clearly seen. One may notice a higher intensity of the nitrogen signal in CrN layers than for MoN. However, it is suggested to consider these results rather for qualitative study than for quantitative analysis due to the low sensitivity of this technique to light elements. Steel substrate is observed in the figure with elemental mapping for iron.

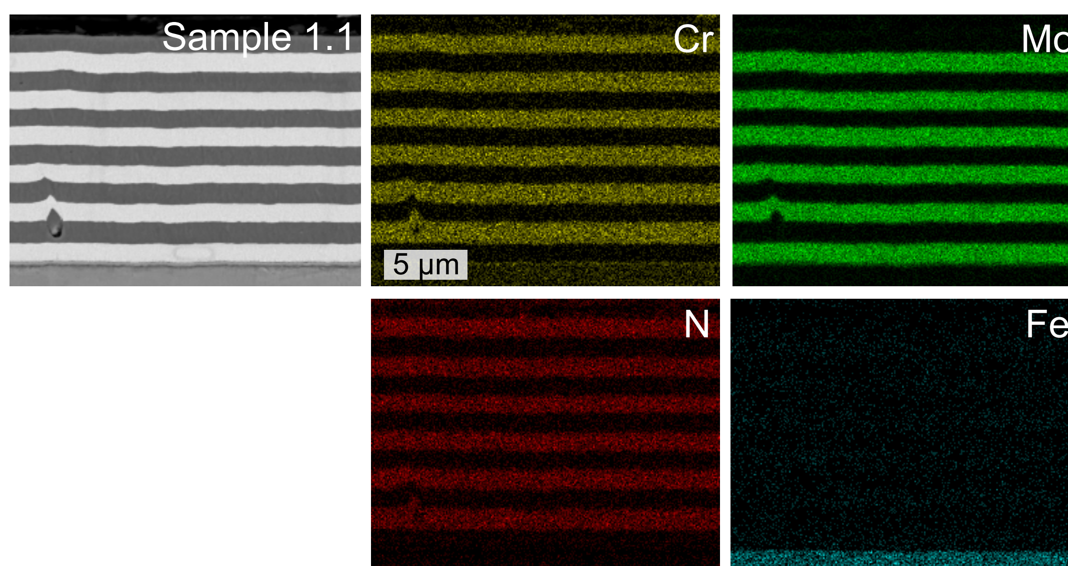

Fig. 4.5 - EDS elemental mapping image for Cr, Mo, N and Fe of Sample 1.1 cross-section.

Fig. 4.6 shows elemental depth profile for Sample 1.1 obtained by EDS line-scan on the cross-sectional specimen. This data and obtained results may be used for the calculation of individual layer thickness. The calculated bilayer thickens of the demonstrated sample is 2.25 µm.

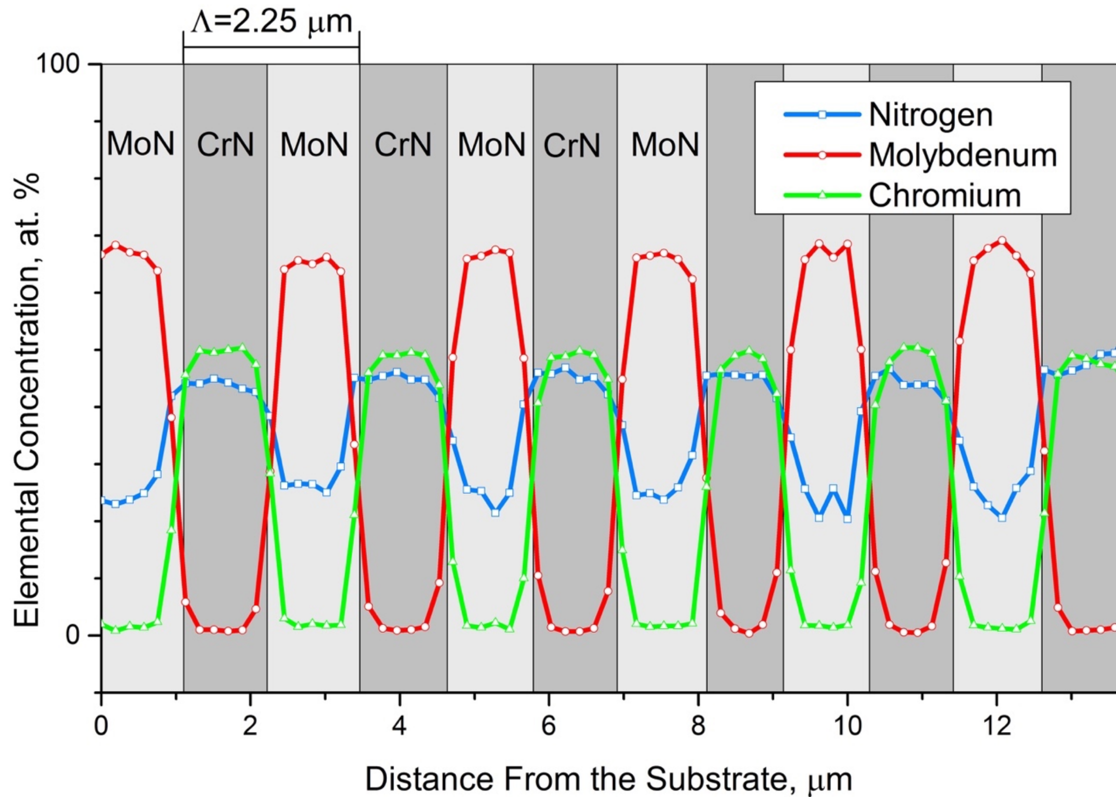

Fig. 4.6 - EDS elemental depth profile for Sample 1.1.

4.2.3. RBS Analysis of Coatings

In order to complement the above-mentioned results, the RBS analysis was used, which is a high-precision non-destructive method and may serve as a reference in plenty of applications. Since the beam has a diameter of about 1 mm, the averaging of layer thickness occurs on a large area. The obtained depth profiles of Cr, Mo and N elements demonstrate a sufficient uniformity of the CrN and MoN layers in the analysed area [188,362]. The RBS depth profiling has been proved as a powerful tool to evaluate the multilayer structure and chemical composition of considered films. However, the RBS technique is not characterised by high accuracy of quantitative identification of light elements, especially when the signal is superimposed with components of such heavy elements as Cr or Mo. In the presented research, the elemental composition depth profiles were simulated in SIMNRA, and the error of nitrogen content by RBS analysis can be 10% or higher.

The results of RBS analysis for CrN/MoN films of Series 3 (U_b = −300 V) with different bilayer thickness are presented in Fig. 4.7. For the first sample (Fig. 4.7 (a)) with the thicker layers, it was possible to obtain the spectrum of only the first MoN top layer (analysed depth is 1.73 µm): Mo ≈ 50 at.% and N ≈ 50 at.%. For the rest of the samples of Series 3 with thinner layers, several periods were clearly observed. Fig. 4.7 (b) shows the spectrum of sample 3.4. The edge of the first peak corresponds to Cr. Thus CrN is the top surface layer of the coating. Then the front of Mo follows, imposed on Cr front, i.e. the front of Mo is shifted by the width of Cr. The peaks on

the RBS spectrum (Fig. 4.7 (c)) correspond to the CrN/MoN period of the multilayer film. The beam of He^+ ions used in the experiment has passed the depth of 5 CrN/MoN bilayers, where the calculated thickness of the CrN layer was 189 nm and 170 nm for MoN, which results in the bilayer thickness of 359 nm. Fig. 4.7 (e) and (f) present the results of RBS analysis for coatings with the thinnest layers (sample 3.6). The spectrum clearly displays the elemental composition of the first three bilayers. The first three peaks correspond to Mo, and the fourth is Cr shifted towards the lower channel numbers by the thickness of Mo. The next Cr and Mo peaks are overlapped due to the small thickness of the individual layers. The thickness of the MoN layers is 37 nm, and the thickness of the CrN layers is 38 nm. Thus, the bilayer thickness (λ) is 75 nm. The results of bilayer thickness evaluation by RBS for all considered CrN/MoN films of Series 3 gave the values identical to the measured by SEM and presented in Table 4.1.

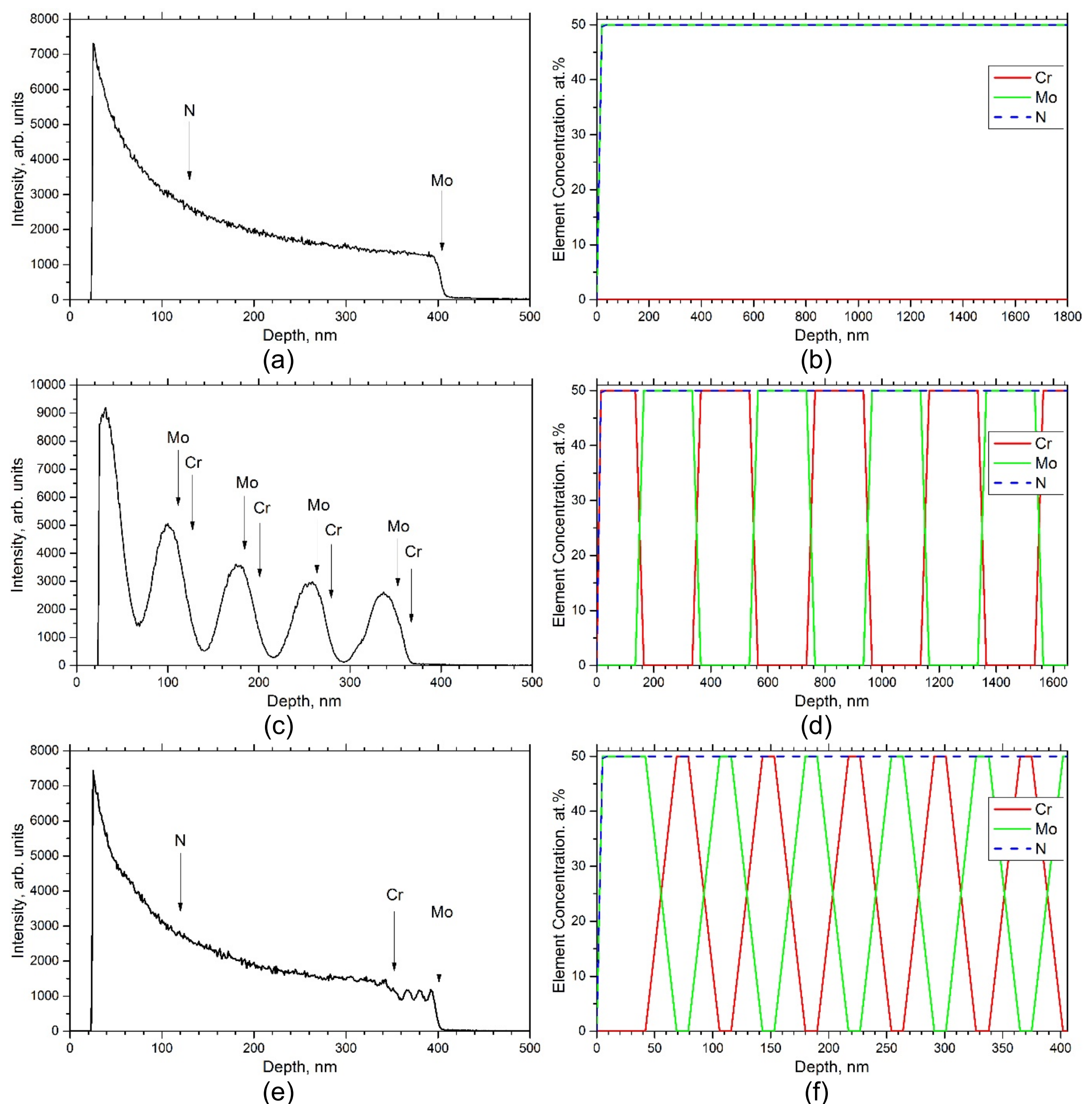

Fig. 4.7 - RBS spectra (left) and depth profiles (right) of elements for samples 3.1 (a, b), 3.4 (c, d) and 3.6 (e, f). Published in [146].

4.2.4. SIMS Analysis

The results of SIMS analysis of elemental composition and multilayer structure of CrN/MoN films for sample 3.6 with the thinnest layers are shown in Fig. 4.8. SIMS is a destructive method of quantitative elemental analysis through the depth of coating. With 5 keV ion beam (Fig. 4.8 (a)) the crater has reached the size of 2×2 mm^2 and almost 1 micron of depth. Due to the reduced ion mixing effect the lower ion beam energy of 1.72 keV (Fig. 4.8 (b)) gives a better resolution but significantly lower sputtering rate: 0.65 nm/min against 6.3 nm/min of the previous acquisition. From SIMS spectra presented in Fig. 4.8 (a) and (b) it is clearly seen the fluctuation of nitrogen content within the layers. The high intensity of the nitrogen peaks coincides with the positions of the chromium peaks maxima. It indicates that the layers of chromium nitride have higher nitrogen content than molybdenum nitride layers and that the formation of multilayer coatings with high mechanical properties is expected [363–365]. These results are in good correlation with the results of X-ray diffraction analysis of phase composition presented below.

Also, the SIMS analysis demonstrates a clear modulation in the composition of the multilayer coatings. Fig. 4.8 (c) shows the multilayer structure of coatings as a plot of normalised Cr and Mo ion current divided by their sum. This relation can describe the concentration of MoN and CrN. The thickness of consecutive bilayers remains constant and is equal to 71 nm, where the thickness of CrN and MoN layers is 36 and 35 nm, respectively. The first 5 periods from the surface of the CrN/MoN films are well defined, while deeper layers are not resolved due to the ion mixing, surface defects and roughness of the coatings.

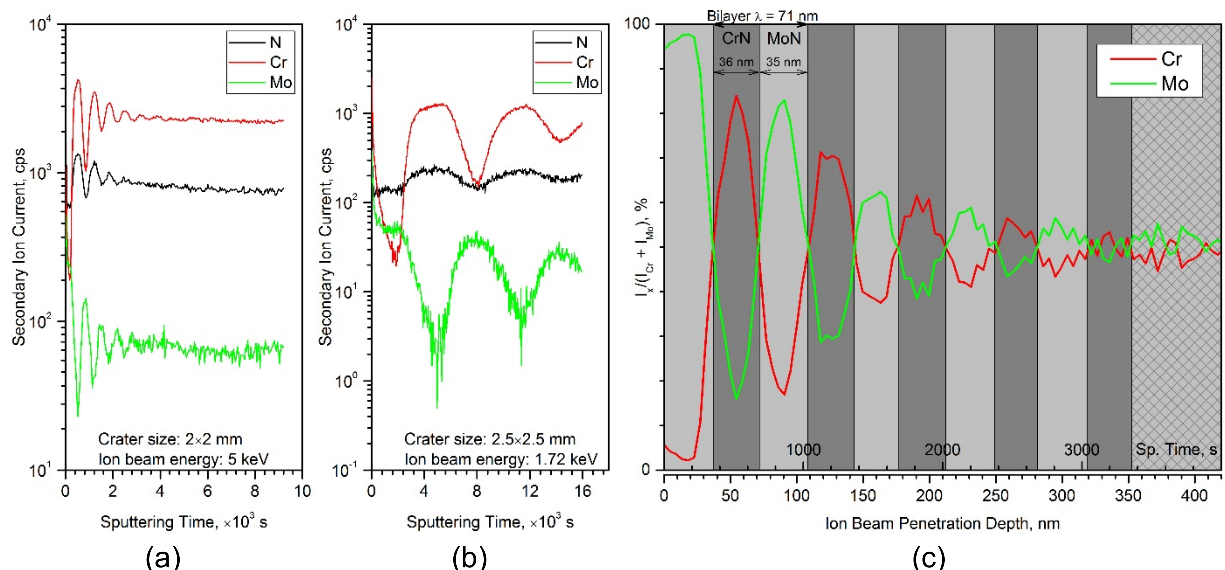

Fig. 4.8 - Results of SIMS analysis of CrN/MoN coatings (sample 3.6). Published in [146].

4.3. Morphology of the Surface

The surface morphology of CrN/MoN coatings with different period thickness is presented in Fig. 4.9. From cross-section study and WDS analysis, it is proved that in Fig. 4.9 (a) the thick top CrN layer of sample 1.1 corresponds to CrN. The morphology is typical for chromium nitrides and it is characterised by high structuring, rocky and rough surface. The surface of sample 1.3 in

Fig. 4.9 (b) has a contribution almost only from the MoN layer, and a more flat surface was observed. Sample 1.6 shown in Fig. 4.9 (c) with the thinner layers includes the combined morphology of CrN and MoN films deposited by Arc-PVD.

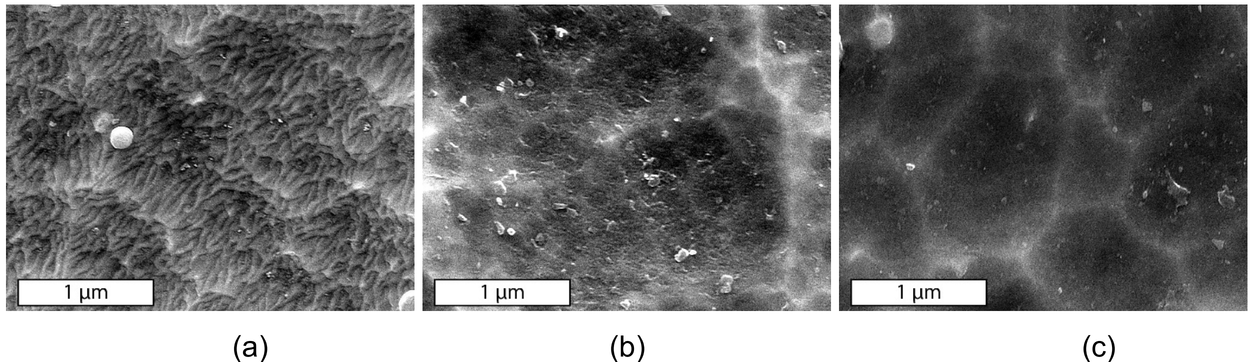

Fig. 4.9 - SEM-images of multilayer CrN/MoN coatings surface for samples 1.1 (a), 1.3 (b) and 1.6 (c). Published in [214].

4.4. Micro- and Nanostructure

4.4.1. X-ray Diffraction Analysis

Fig. 4.10 (a)-(c) show the XRD patterns for the CrN/MoN multilayer coatings deposited with negative U_b of −20, −150 and −300 V. The patterns demonstrate how significant is the influence of bias voltage on the deposited material structure and confirm the polycrystalline nature of the coatings. The identical cubic lattice structure of CrN and Mo_2N with Fm3m space group and similar lattice parameter of 4.163 Å (Mo_2N) and 4.149 Å (CrN) allows forming multilayer CrN/MoN coatings with small internal stresses at the interfaces. On the other hand, it leads to difficulties in distinguishing between CrN and MoN diffraction peaks in XRD patterns. The diffraction patterns of chromium nitride and molybdenum nitride phases are well known. Nevertheless, different deposition conditions may cause the formation of several hexagonal and cubic phases of both nitrides. The comparison of Fig. 4.10 (a), (b) and (c) shows that for bias potential U_b = −20 V the same type of crystal lattice of structural type B1 (fcc of NaCl type) is formed in the coatings, which is typical for CrN and γ-Mo_2N [270]. The predominant [311] orientation of crystallite growth perpendicular to the formed planes was observed from the relative intensification of the corresponding diffraction peaks [366,367].

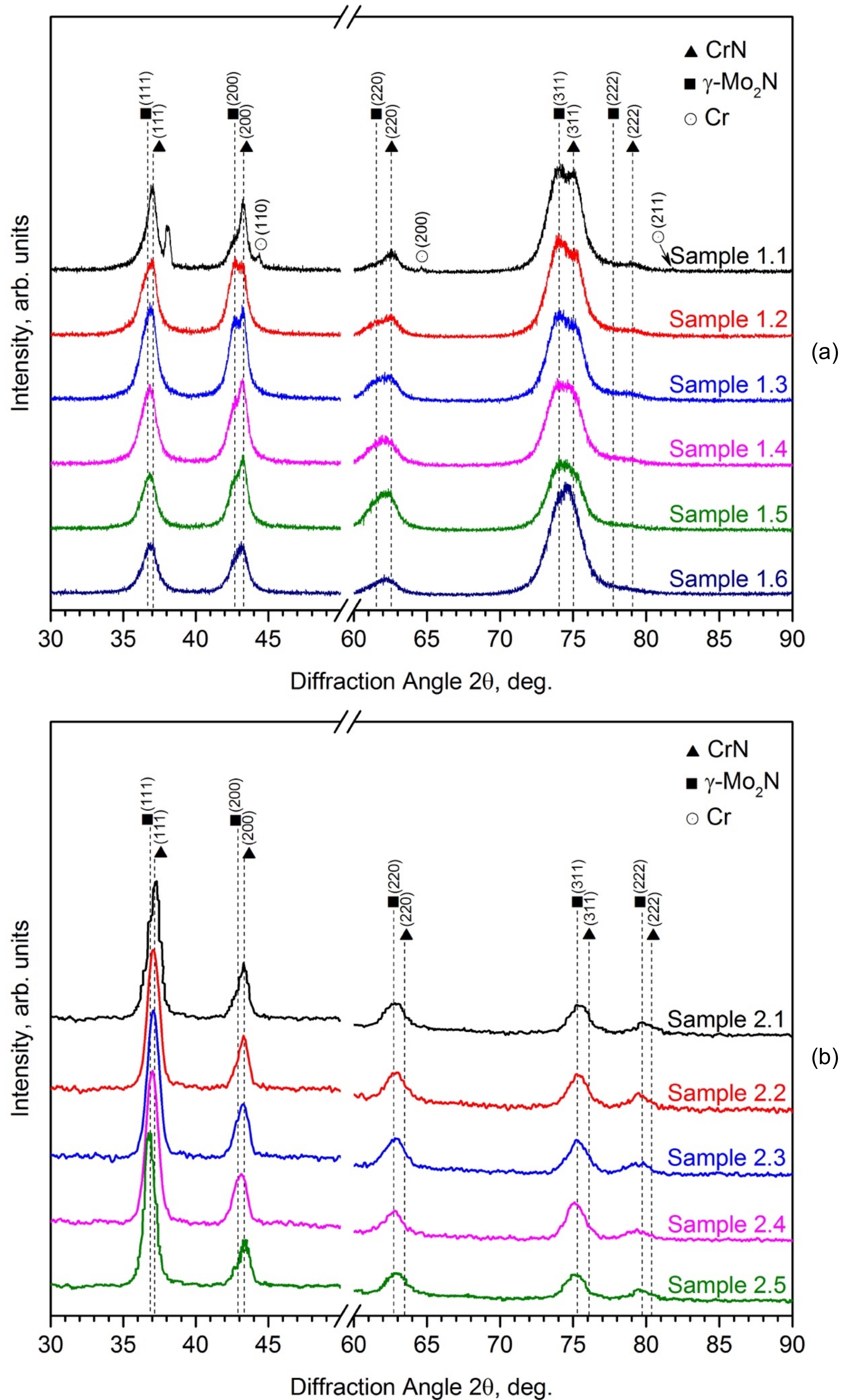

Fig. 4.10 - X-ray diffraction patterns (theta/2theta) of CrN/MoN multi-layered coatings (continued on next page): spectra for samples deposited at a negative bias voltage of −20 V (a), −150 V (b), −300 V (c) and their comparison (d). Published in [146].

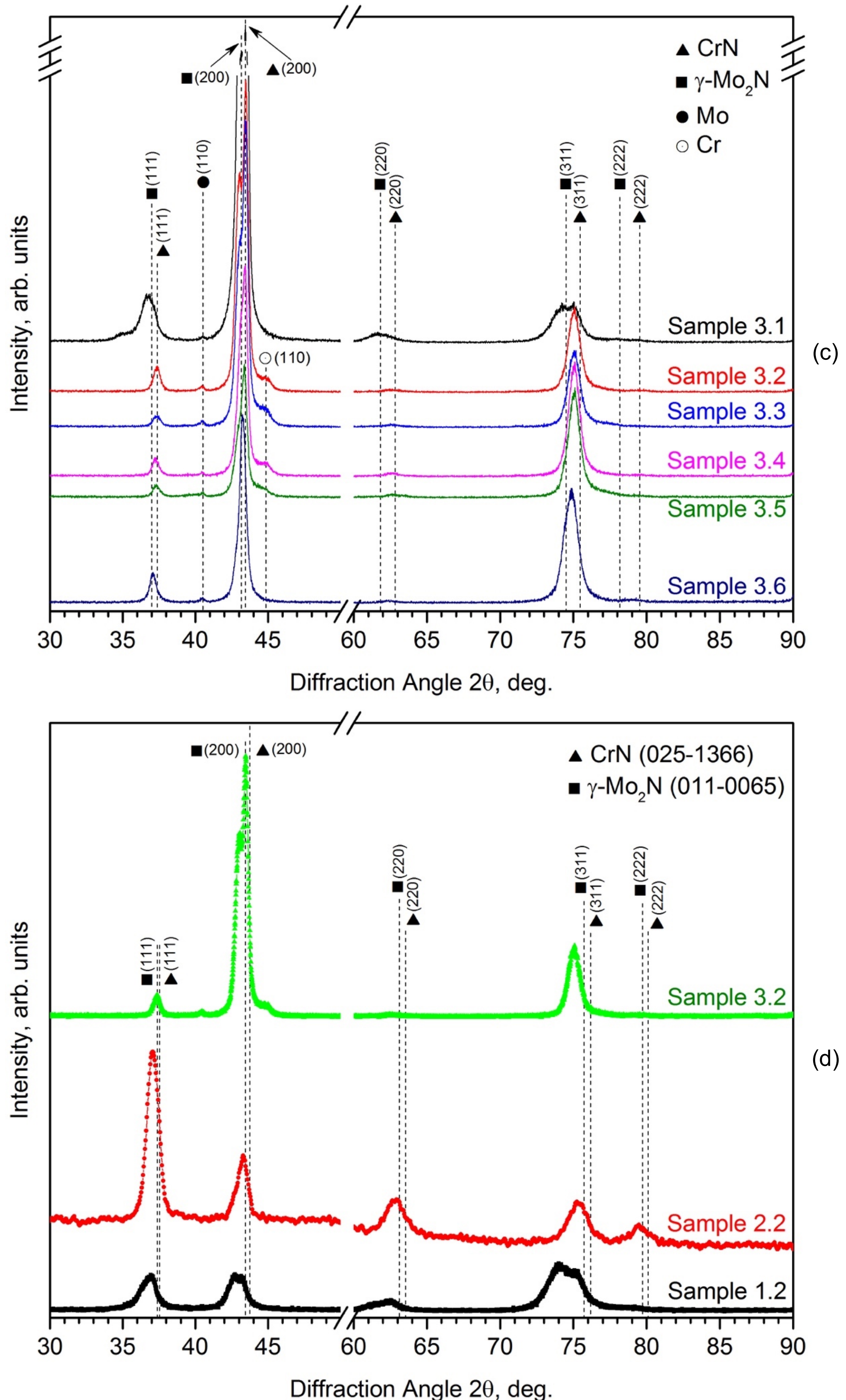

Fig. 4.10 – Continued. X-ray diffraction patterns (theta/2theta) of CrN/MoN multi-layered coatings: spectra for samples deposited at a negative bias voltage of -20 V (a), -150 V (b), -300 V (c) and their comparison (d). Published in [146].

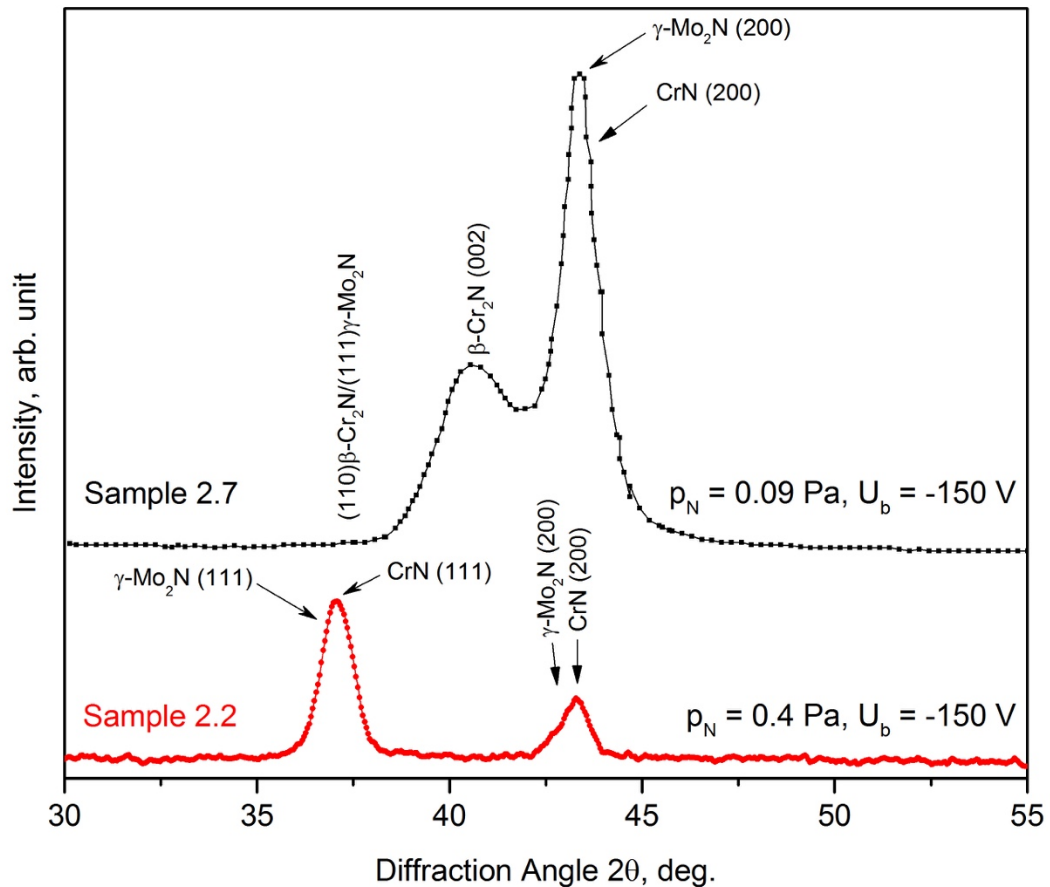

Fig. 4.11 - X-ray diffraction pattern of CrN/MoN multi-layered coatings deposited at different pressures of nitrogen. Published in [146].

The supply of higher negative bias potential $U_b = -150$ V to the substrate forms a different type of texture with [111] direction, whose intensity grows with the increase of bilayer thickness. However, it does not lead to an explicit separation of the diffraction peaks from the corresponding phases of the two nitride layers at high angles, which may indicate the formation of a solid solution on interlayer zones and thin layers. With a subsequent increase of the absolute value of the applied bias potential to $U_b = -300$ V (Fig. 4.10 (c)) the texture changes significantly to [200] direction of crystallite planes in CrN/MoN multilayer films. Thus, the evolution of preferential texture growth from [311] to [111] and then to [200] was observed when the negative bias voltage applied to the substrate decreases from −20 V to −150 V and −300 V respectively (see Fig. 4.10 (d)), which may be related to the interaction of several driving factors such as surface energy, atoms mobility, reactive gas concentration, ion bombardment energy.

In most of the cases, the preferential orientation growth is mainly determined by the least total energy resulting from the competition between strain and surface energy [368]. S.K. Pradhan et. [369], M. Guimaraes et al. [368] and others observed for CrN coatings the formation of (311) texture at low or zero bias, which then changes to (111) or (200) textures. J. Pelleg et al. [370] suggests that if the surface energy is dominant, cubic nitrides grow with the (200) preferential

texture, and if the strain energy is dominant, the texture will be on (111) plane, which corresponds to the lowest surface energy in case of fcc metals. Change from (111) to (311) at low bias may be related to lower energy of ion bombardment and formation of a less dense structure. The presence of structures with coincident values of interplanar distance in zones of interlayer interfaces certifies their interdependent growth [224,366,367,371]. The reduction of nitrogen pressure p_N from 0.4 to 0.09 Pa leads to the formation of β-Cr_2N hexagonal phase and γ-Mo_2N FCC-type phase with identical interplanar spacings for (110)β-Cr_2N/(111)γ-Mo_2N (coincident diffraction peak) and different interplanar spacing for (002)β-Cr_2N and (200)γ-Mo_2N planes (two clearly separated peaks) [270]. This evolution of the texture in CrN/MoN films with decreasing nitrogen pressure is shown in Fig. 4.11. Also, at $p_N = 0.09$ Pa, with an increase of the absolute value of bias potential U_b to −150 V, the preferential growth of crystallites in [002] and [200] directions is observed for the β-Cr_2N and γ-Mo_2N phases, respectively, which leads to the increase of interlayer mismatch.

The analysed XRD spectra demonstrate the shift of the diffraction peaks in the direction of lower angles which indicates the increase of interplanar distances and, hence, lattice constants in the direction normal to the surface. This is a sign of residual stresses presented in the deposited coatings. Although there is no significant evidence from diffraction patterns, relying on chemical composition of the MoN layer, one can assume that an off-stoichiometric MoN_x metastable phase may be formed, since the Mo/N atomic ratio in the layers is close to 1 and the structure of the γ-Mo_2N phase identified by XRD should contain a significant excess of nitrogen. When nitrogen fits into a lattice position, which should be unoccupied in stoichiometric γ-Mo_2N FCC-type phase, the expansion of the lattice occurs. This expansion is in agreement with the results of XRD analysis, where the calculated lattice parameters (a = 4.168 Å for CrN and a =4.205 Å for γ-Mo_2N) are higher than given by references [270].

4.4.2. Low-Angle X-Ray Diffraction Methods

In order to identify the diffraction patterns of individual layers and check more precisely their structure and phase composition, the methods of low-angle X-ray diffraction were used: in-plane XRD and asymmetric scans included GIXRD. Application of such approach where the angle between X-ray incident beam and sample (omega, ω) remains fixed at some value, while only the detector moves during the acquisition, allows performing a depth-sensitive analysis and, thus, evaluation of the defined layers of the multi-layered structure. In this way, the deconvolution of overlapped broad peaks in Fig. 6 may be performed. Fig. 4.12 (a) shows the comparison of GIXRD and in-plane spectra with conventional θ/2θ scan of sample 1.1 and the reference position of the peaks from the database [270].

In addition to the feature of GIXRD analysis which allows controlling X-ray penetration depth by tuning the incident angle, another advantage of in-plane XRD method is the acquisition

of diffraction data from the lattice planes located along the normal to the surface, since the scattering vector **S** lies parallel to the surface, in contrast to the out-of-plane type of scan. In asymmetric θ/2θ scan, including GIXRD, **S** moves continuously with the detector. Therefore, different lattice planes normal to the **S** current position at each point of time will contribute to the resulting diffraction pattern. Fig. 4.12 (b) shows the comparison of in-plane XRD patterns for samples with CrN top layer (sample 1.1) and MoN top layer (sample 1.2). Fig. 4.12 (b) clearly shows the similarity of CrN and MoN diffraction patterns, but successfully distinguishes the positions of diffraction peaks separately for CrN and MoN layers of the deposited multilayer films, which was not possible to achieve from integral spectra shown in Fig. 4.10 (a)-(c). The GIXRD and in-plane XRD data confirm the presence of cubic high-temperature γ-Mo_2N phase and stoichiometric phase of CrN, which corresponds to the performed elemental analysis. Diffraction reflexes inherent to β-Mo_2N or β-Cr_2N phases were not detected, except one peak of (113) β-Cr_2N observed on in-plane XRD patterns of sample 1.1.

In order to check that the beam reaches the only first top layer of the coating, the evaluation of the beam penetration depth was done for low angles including the zone of full reflection (near critical angle) for CrN and MoN (see Fig. 4.13) using Equation (4.1) by [75].

$$h = \frac{\sqrt{2}\lambda}{4\pi}\sqrt{[(\alpha^2 - {\alpha_c}^2)^2 + \beta^2]^{-1/2} - (\alpha^2 - {\alpha_c}^2)}, \qquad (4.1)$$

where h is a penetration depth, Å, λ – X-ray wavelength, Å, α – incident angle, deg., α_c – critical angle, deg., β=λμ/4π – imaginary part of refractive index, $\mu=\mu_m\rho$ – linear absorption coefficient, μ_m – mass absorption coefficient.

Fig. 4.13 demonstrates that for angles used in current analysis the penetration depth of X-ray beam does not exceed 100 nm and for considered samples analysed volume localised in the first top layer of coatings (for sample 1.1 the layer thickness is Λ/2=1.11 μm, for sample 1.2 - Λ/2=0.6 μm).

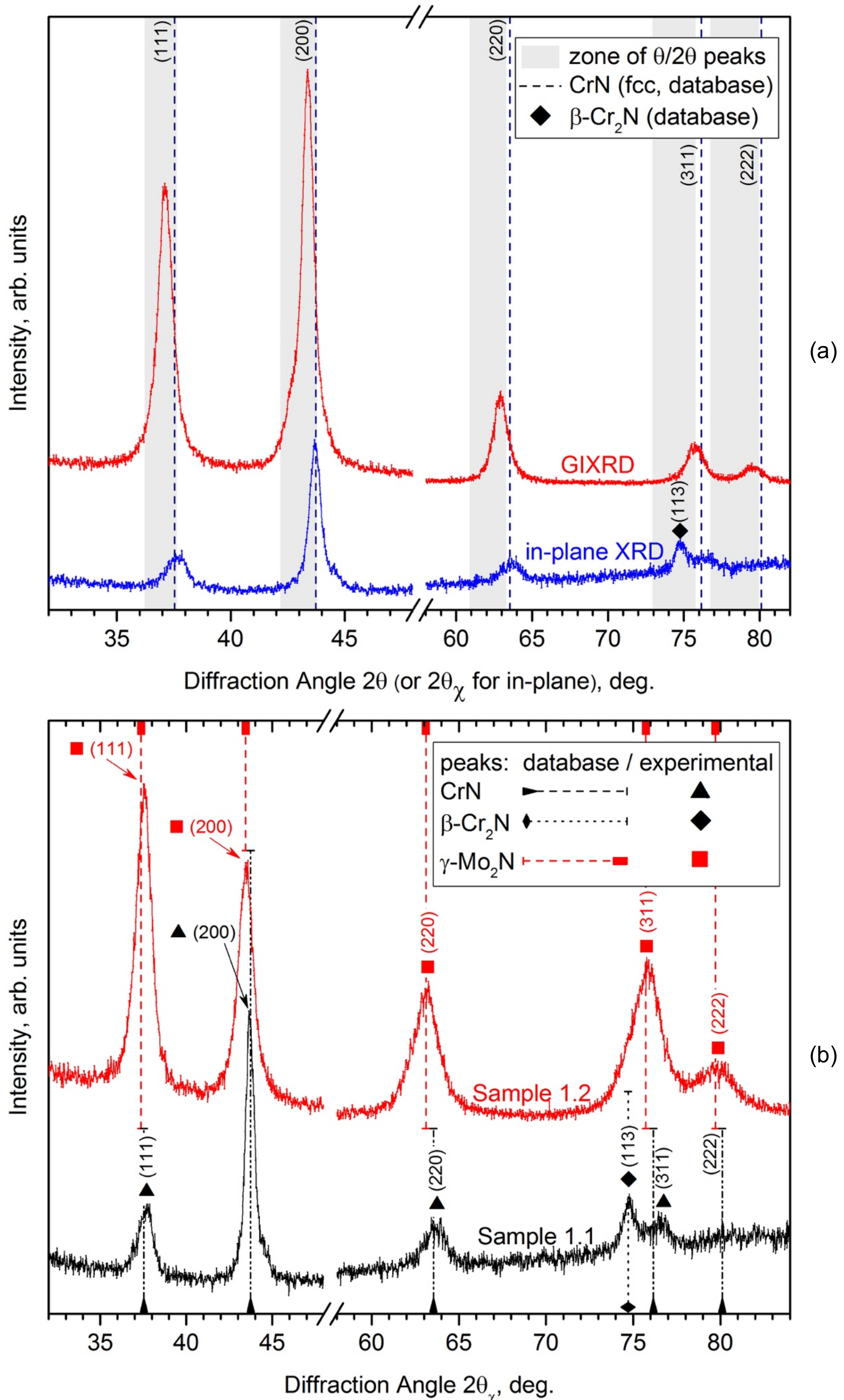

Fig. 4.12 - X-ray diffraction patterns taken in several low-angle modes. (a) GIXRD and in-plane XRD spectra taken for sample 1.1 at incident angle ω = 0.4º. Grey zones show the position of experimental diffraction peaks of θ/2θ scan. (b) In-plane XRD for samples 1.1 (top layer CrN) and 1.2 (top layer MoN) with ω = 0.6º. Published in [146].

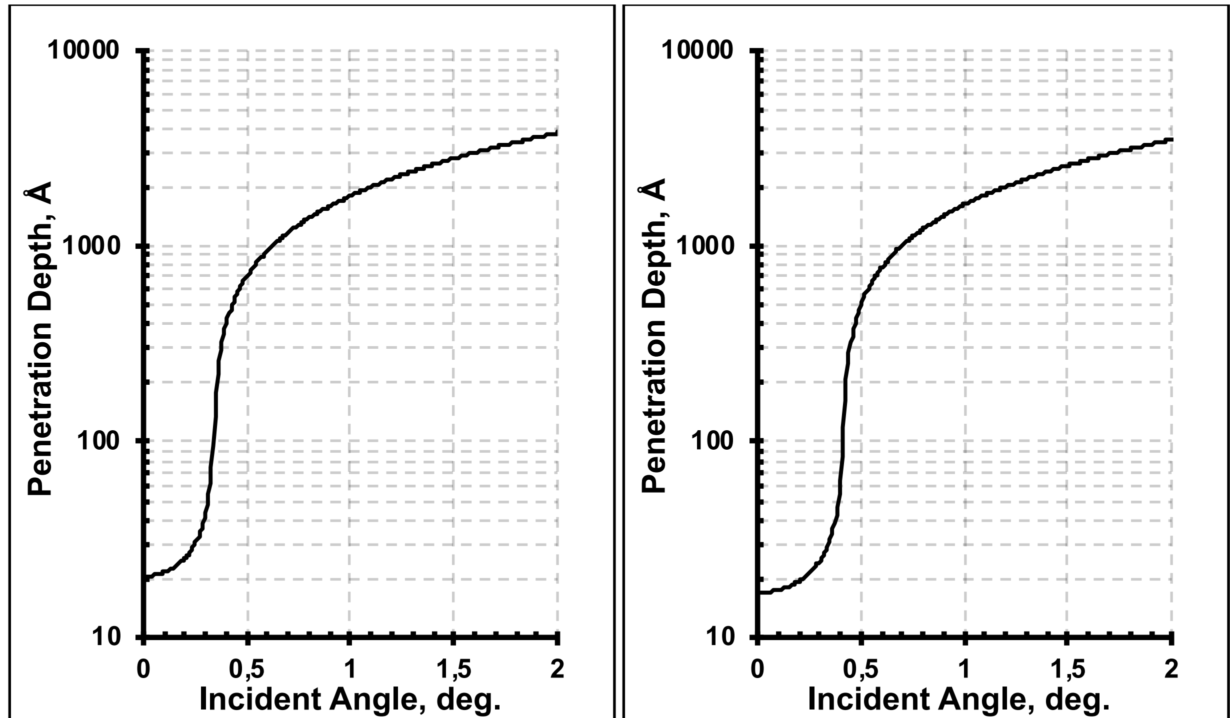

Fig. 4.13 - Dependence of X-ray beam penetration depth on the incident angle in a low range of values for most expected structures of studied multilayer coating: cubic CrN (a) and Mo_2N (b).

4.4.3. Crystallite Size Calculation Using XRD Data

The detailed results of crystallite size calculation for coating of Series 1 are presented in Table 4.3. The average crystallite size was estimated from the XRD data using the Scherrer Equation (2.3). To extract information about separate peaks and to know the full width at half maximum (FWHM), the fittings of the XRD peaks were performed using Crystal Impact's phase identification software “Match!”. Any other factors which can contribute to the width of a diffraction peak besides crystallite size, such as instrumental effects, microstrain, solid solution inhomogeneity etc. have not been taken into account. With the reduction of individual layer thickness in studied CrN/MoN multi-layered films, the peaks get broadened, which may indicate the reduction of crystallite size in presented polycrystalline samples. Crystallite size for coatings of Series 1 decreases from 17.2 nm (for CrN) and 11.5 nm (for γ-Mo_2N) to 8.3 nm and 5.8 nm respectively when the bilayer thickness decreases to 44 nm. For the coatings of Series 2 or 3, deposited at U_b = −150 V or −300 V respectively, the crystallite size estimated from the XRD data using Scherrer Equation (2.3) decreases to 12 nm when the bilayer thickness reaches values of nanometre scale, and the microdeformation of the crystallites is (0.4 ÷ 0.5)%. These values are relatively higher in the coatings of Series 1 deposited at U_b = −20 V: microdeformation was 1.5% for CrN and 2.3% for γ-Mo_2N. It may be explained by the lower mobility of the deposited atoms, which leads to the lower probability of diffusion healing of growth defects [190,372].

Table 4.3 - Crystallite and grain size for multilayer CrN/MoN coatings (Series 1).

Sample number	Crystallite size for selected phase and lattices orientation, nm								Average grain size by EBSD, μm
	CrN				γ-Mo_2N				
	(111)	(200)	(311)	(220)	(111)	(200)	(311)	(220)	
1.1	17.2	14.3	8.9	-	6.4	11.5	8.1	-	0.16
1.2	14.0	13.9	8.7	-	5.6	10.4	8.0	-	0.15
1.3	14.5	13.5	8.4	-	5.6	9.9	8.0	-	0.14
1.4	14.2	12.1	8.2	-	7.4	9.3	7.4	-	0.11
1.5	13.7	9.9	7.7	-	9.4	9.0	7.2	-	-
1.6	9.3	8.3	7.6	-	5.8	8.0	7.0	-	-
1.1 (in-plane)	7.7	14.7	9.7	5.5	-	-	-	-	-
1.2 (in-plane)	-	-	-	-	10.4	9.0	6.5	6.3	-

Values of crystallite size calculated separately for several orientations of diffraction planes for all samples are shown in Fig. 4.14. It confirms the reduce of crystallite size with the decrease of individual layer thickness for all considered cases from 14 to 7 nm.

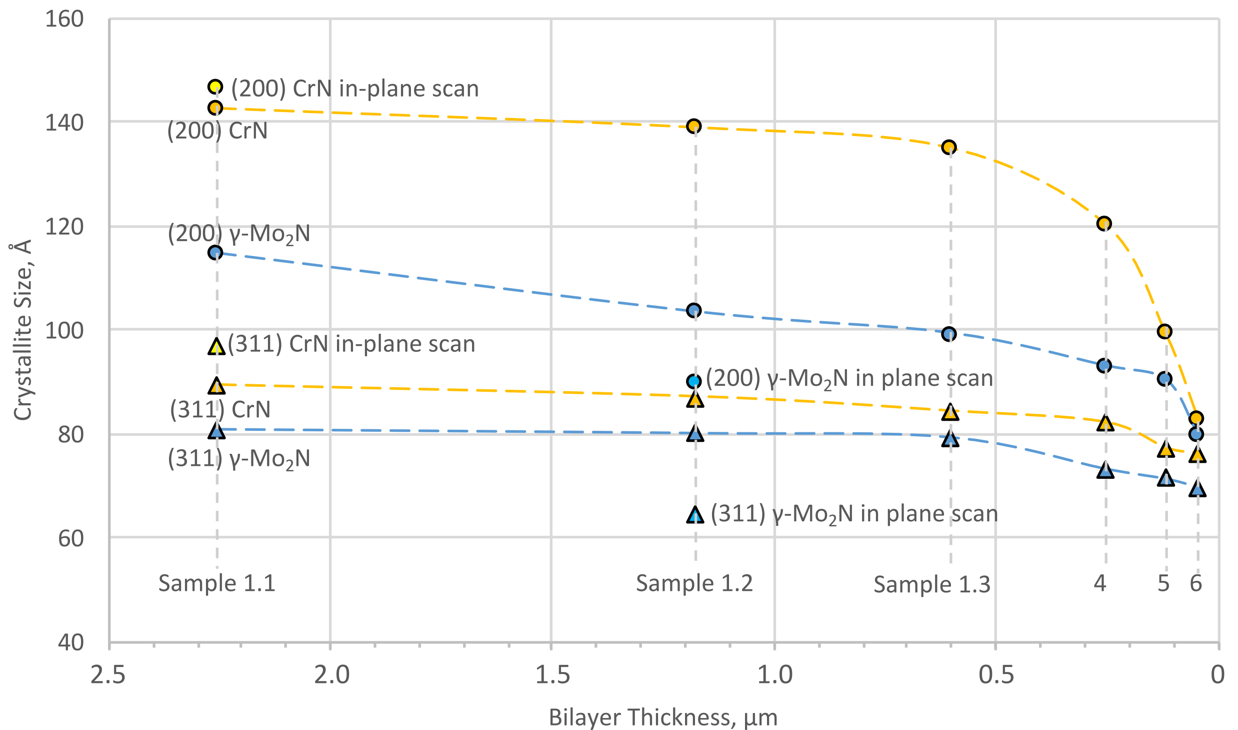

Fig. 4.14 - Crystallites size of CrN/MoN films calculated from XRD data (Series 1).

4.4.4. EBSD Analysis and Grain Size Evaluation

Additional information on the crystal orientation, grain size, and their dependence on the layer thickness was gained from EBSD analysis. Corresponding software allowed studying the structure and evaluating the grain size, as well as to find correlations between these features and layer thickness. As was mentioned in the experimental details (Chapter 2.4.2), the diffraction patterns (Kikuchi patterns) were not observed for MoN layers in all samples, which may be related to the cross-section polishing procedure and damage of the surface of the relatively softer surface of MoN layers (see Fig. 4.15).

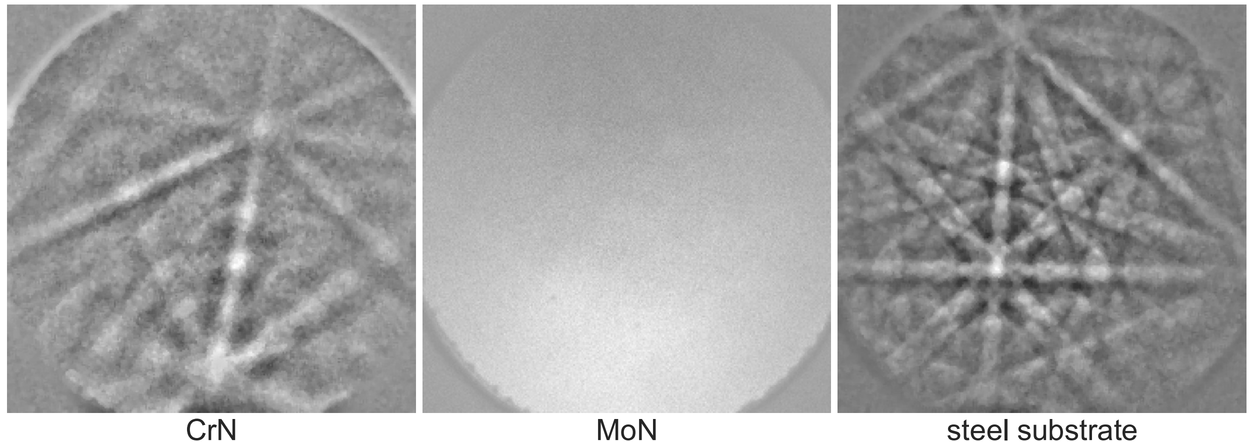

Fig. 4.15 - Kikuchi diffraction patterns obtained on cross-sections of the deposited CrN/MoN coatings.

To show the results of EBSD analysis and to determine the position and shape of grains in the coatings, a unique grains colour map was used (see Fig. 4.16). Colour separation is used to distinguish neighbouring grains. The boundaries between the grains were reconstructed and are shown as polygons. It is clearly seen that the grains have an oblong shape and are oriented in the direction parallel to the film's growth. The columnar structure and high degree of structuring are present in the deposited films, which is typical for Arc-PVD method.

Note that the colours used in Fig. 4.17(a) do not denote any crystal orientation, and grains are simply coloured to distinguish them from neighbouring grains. Fig. 4.17(a) shows an example of a unique grain colour map for part of the CrN layer for sample 1.1. Reconstructed ellipse-shaped grains demonstrate columnar structure and film growth. In order to supplement the information about the films' structure, the inverse pole figure map was used. The inverse pole figure map is a colour-coded map, where the colour gives an indication of the crystal direction aligned with the sample normal. Fig. 4.17(b) demonstrates exactly the same part of the coating as Fig. 4.17(a), but in inverse pole figure mode, and it is seen that some small misorientation is present in grains. Neighbour grains may have similar crystal orientations or completely different ones.

Fig. 4.16 - EBSD results for CrN layer of sample 1.1**:** unique grains colour map with reconstructed boundaries.

Pole figures based on the data of EBSD analysis have shown the prevailing formation of fibre texture in [311] orientation for the samples of Series 1 deposited at $U_b = -20$ V, which is in agreement with the XRD analysis results.

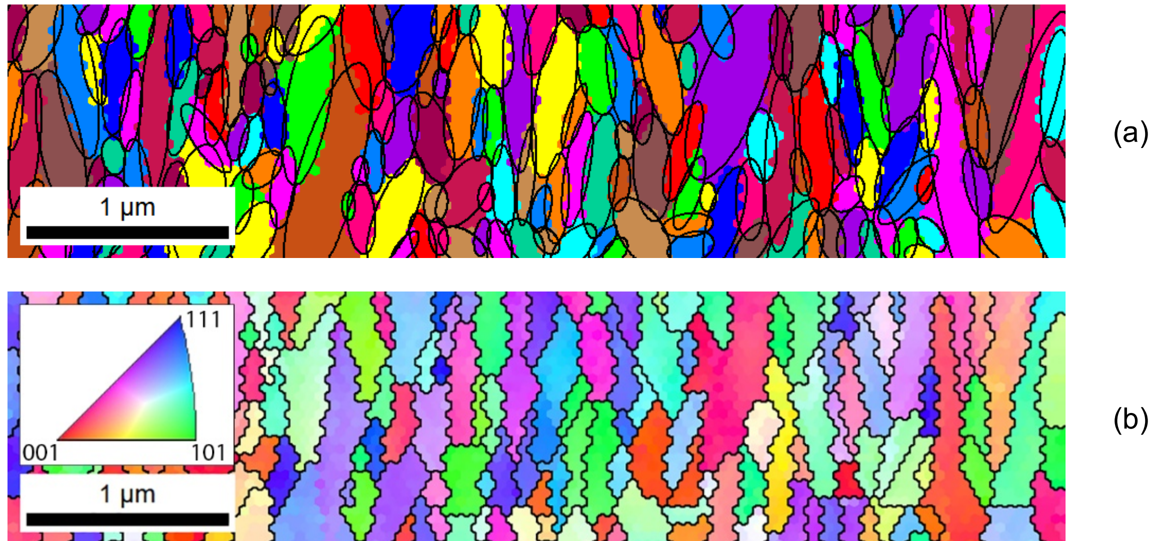

Fig. 4.17 - EBSD mapping for CrN layer of sample 1.1.
Unique grain colour map with shape ellipses boundaries (a), inverse pole figure [311] (b). Published in [214].

The used method also allows the evaluation of grain size. The calculations have clearly shown the persistent decrease of average grain size from 0.16 µm (sample 1.1, λ = 2.26 µm) to 0.11 µm (sample 1.4, λ = 0.25 µm). The further study of the samples with thinner layers using EBSD was not possible due to the resolution limits of the discussed technique.

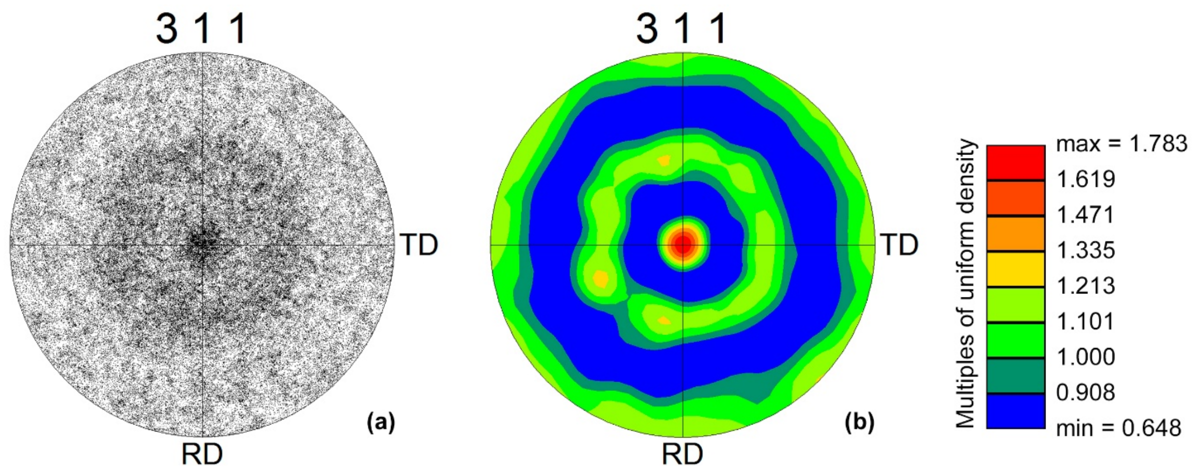

Fig. 4.18 - One of the pole figures and texture calculations for sample 1.1. Published in [214].

The EBSD analysis shows the columnar growth of the deposited multilayer CrN/MoN films, as well as the prevailing texture formation. Fig. 4.18 presents one of the pole figures for sample 1.1 with the highest fibre texture in the orientation (311). These results are also agreed with the XRD patterns analysis, where the high intensity of (311) texture was detected for sample 1.1 (see Fig. 4.10(a)).

Fig. 4.19 demonstrates CrN layers of the same Sample 1 but in different zones of the coating. Columnar growth of the crystals and films within the full profile is observed. It’s seen that the layers closer to the substrate have a larger size of the grains. Grain size reduces with approaching to the surface of the coatings.

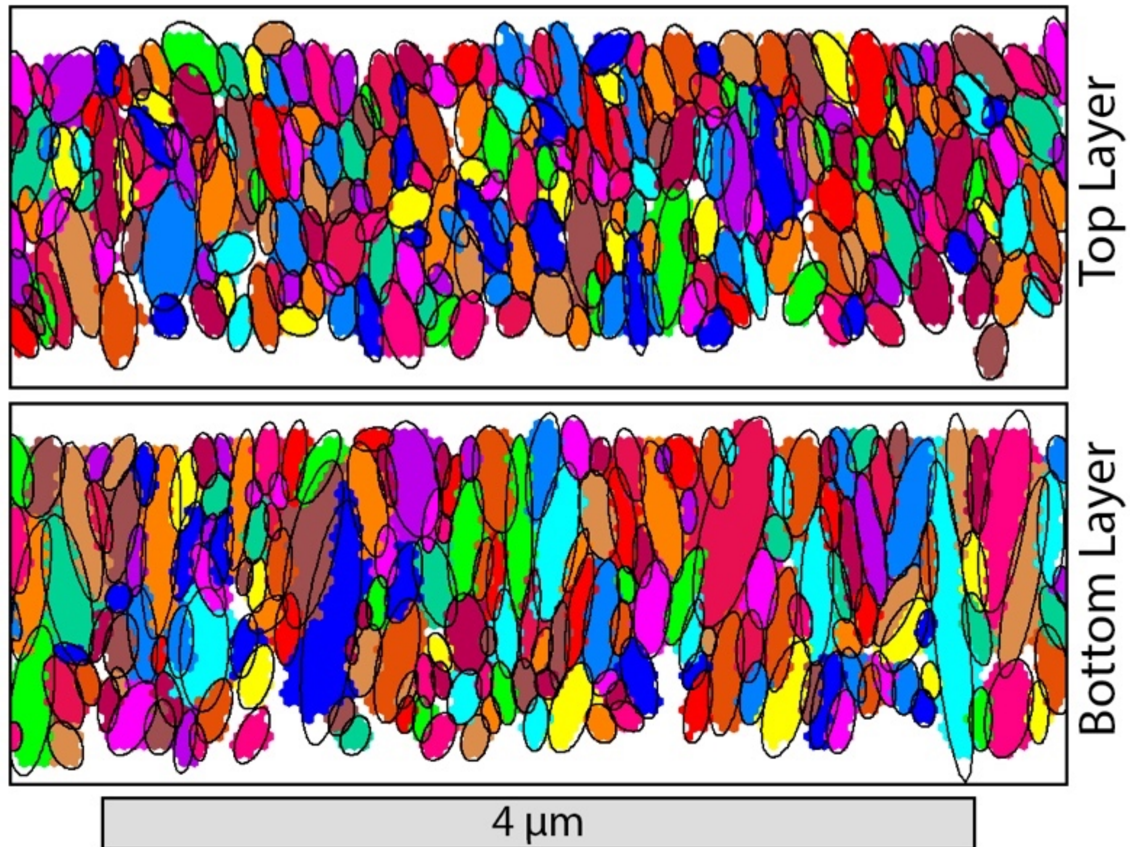

Fig. 4.19 - EBSD unique grain colour map for CrN layers of Sample 1.1 near to the surface and near to the substrate.

The discussed method also allows evaluation of grain size in coatings and to build graphs of their distribution. From Fig. 4.20, it is clear that coatings with smaller layer thickness have smaller grain size. It is seen that sample 1.4 (with the lowest layer thickness of all four analysed) has the lowest fraction of the largest grains, as well as higher values for the smallest grains size. The opposite is observed for sample 1 with the thicker layers. Samples 1.2 and 1.3 demonstrate a gradient transition between the two described states. The detailed information about grain size for studied samples is shown in the last column of Table 4.3. The statistics were taken from the same cross-section area sizes with the height equal to the total thickness of the film and the width of 5.3 µm. It should also be noted that the Y-axis is presented in arbitrary units of fraction, which are not absolute values, to avoid some deviations due to possible small differences in size or range of studied zone of cross-section samples.

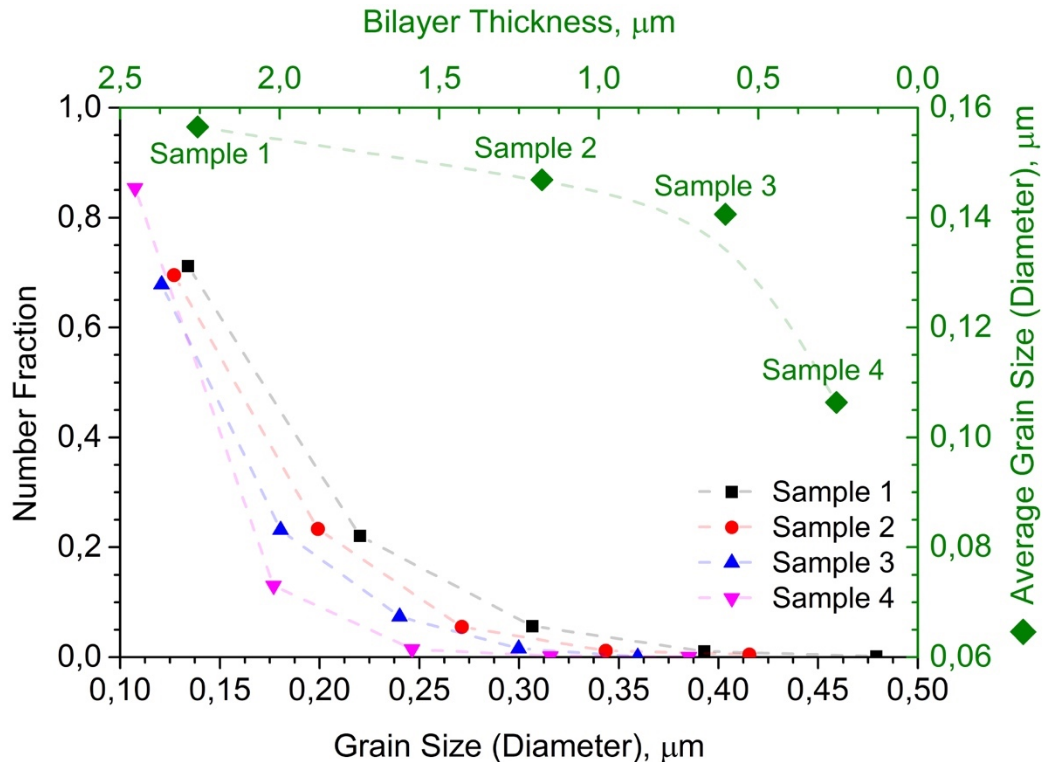

Fig. 4.20 - Grain size distribution and average grain size values in CrN/MoN multilayer coatings with different bilayer thickness (series1). Published in [214].

4.4.5. TEM and SAED Analysis

The results of TEM and SAED analysis for Series 3 (U_b = −300 V) have shown a clear distribution of the layers (Fig. 4.21), with the thickness of the MoN layer about 36 nm, which correlates with the result of RBS analysis (MoN layer thickness is about 37 nm). The SAED method offers a high resolution and has much shorter wavelengths compared to conventional X-rays. On the other hand, the structural factors of electron diffraction are up to 10,000 times higher than for diffraction of X-rays and, thus, provides much higher diffraction beam intensity. Due to the shorter wavelength, the diffraction angles for SAED are only a few degrees, which results in a greatly reduced angular resolution. Because of this, the accuracy of determining the interplanar distances is lower than for XRD (about 1-3%). The higher spatial resolution of SAED makes it possible to probe an area of no more than 2-5 microns in diameter and does not give the whole picture.

The SAED results presented in Fig. 4.21 (b, right) have shown the crystalline structure of the film and the formation of two main characteristic cubic phases CrN and γ-Mo_2N, which coincides with the conclusions of the preliminary XRD analysis. The SAED pattern demonstrates the presence of several crystallite orientations for both cubic structures in polynanocrystalline sample: [111], [200], [220], [222], [311] and others. The relatively high discreteness and thin width of the lines of the diffraction patterns indicate the presence of sufficiently large crystallites and the probable superposition of their crystallographic directions [373]. The very similar cubic structure of CrN and γ-Mo_2N phases in a couple with limited angle resolution by TEM-SAED may not allow defining diffractions separately from CrN and MoN layers of the studied sample, but could help to

estimate average interplanar distances and, thus, lattice parameters as for "solid solution" (Cr,Mo)N. The calculated interplanar distances were 2.40, 2.07, 1.47, 1.25, 1.21, 0.95 and 0.92 Å for (111), (200), (220), (311), (222), (331) and (420) planes respectively, which results in the average lattice parameter in range a = (4.11-4.20) Å.

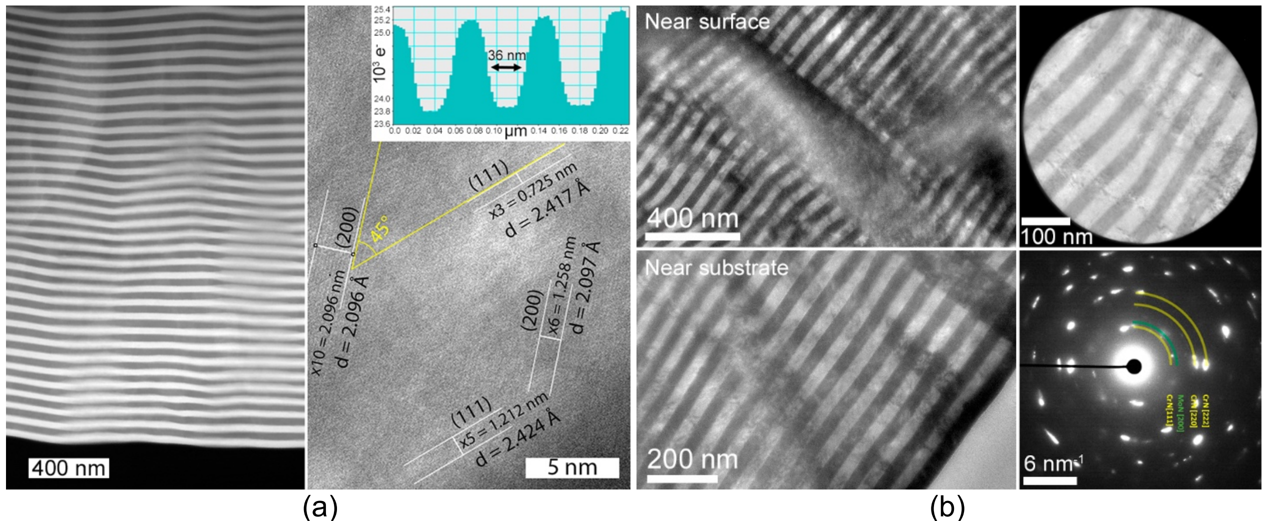

Fig. 4.21 - Results of TEM study for sample 3.6: (a) and (b, left) – TEM and HRTEM images of cross-section sample; (b, right) - SAED pattern and zone of analysis. Published in [146].

The wide range of the lattice parameter values demonstrates the presence of residual stresses in the films. Decreased value of lattice constants a, in comparison to stress-free values from database [270] for CrN (4.149 Å) and γ-Mo_2N (4.163 Å), approves the contribution of compressive stress in the deposited coatings. Higher values of the lattice constants may be due to the lattice extension in the direction normal to the vector of the present compressive stress, and due to the nitrogen incorporation into interstitial sites of MoN_x lattices, which has been discussed already in the XRD section and agrees with results presented there. It should be noted that ultrathin samples for further determination of nanograins size by HRTEM were quite hard to achieve due to the internal stresses of cross-sections which is a sign of the high strain induced by the laminates [202,374].

4.4.6. TEM-EDS Elemental Analysis

Fig. 4.22 represents the results of TEM-EDS analysis performed on sample 3.6. Fig. 4.22 (a) demonstrates almost equal concentration of Cr and Mo elements (41.1 and 42.0 at.% respectively) which confirms the results of previous SEM-EDS and RBS analysis. The concentration of nitrogen was shown on the level up to 16.9 at.%, but low reliability of light elements concentration measurement by EDS technique has been mentioned already. Fig. 4.22 (b) shows depth profile concentration of the considered multilayer sample: layers exhibit good uniformity and stability. In the figure, the depth profile is also combined with the part of the real TEM cross-section image of the same area. The sharp interface between the layers and good contrast are confirmed by TEM technique for the thinnest samples, which was difficult to achieve using SEM.

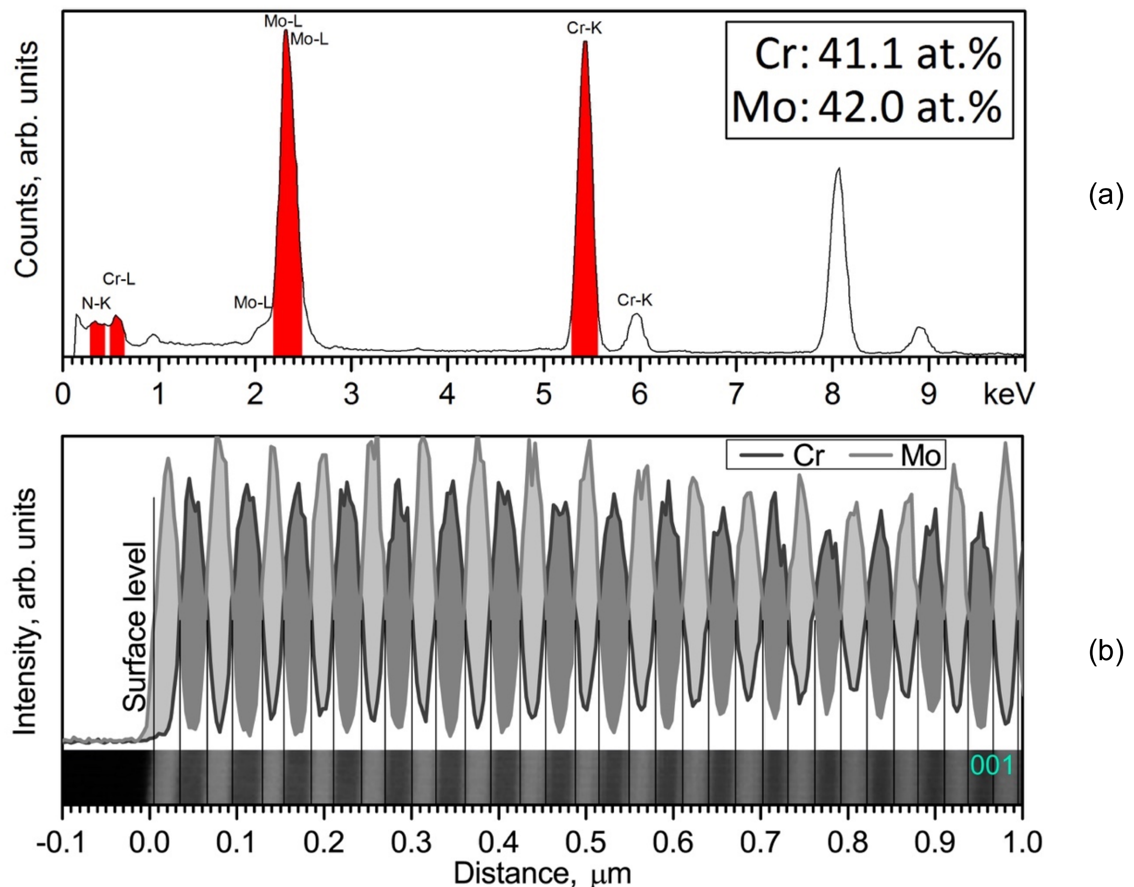

Fig. 4.22 - Results of TEM-EDS analysis for sample 3.6: (a) TEM-EDS spectrum, elemental composition; (b) Cr and Mo elemental depth profile with the corresponding part of TEM cross-section image. Published in [146].

4.5. Evaluation of Residual Stresses

The residual stress in PVD coatings appears mainly due to thermal and internal stresses. The thermal stress is caused by the difference in the temperature between coating and substrate during the cooling process after the deposition and by different thermal expansion coefficients of materials. Its contribution can increase for a system of several layers. The internal stress in PVD coatings occurs during the deposition, and its value depends on the deposition conditions, such as bias potential, chamber pressure and distance to the substrate, as well as on the stoichiometry and layers thickness in the coating [371,372,375,376]. On the other hand, in multilayer systems, the reduction of individual layer thickness leads to the increase of the interlayer interface volume, which releases residual stress. Such effect was recently observed in the coatings with (111) preferential crystallographic orientation.

The residual stress was determined on samples 1.1 and 1.2, giving access to the stress state of the topmost layers, MoN and CrN, respectively. For each sample, several hkl reflections were recorded using asymmetric XRD 2θ scans, and the stress was derived using the $\sin^2\psi$ method. Fig. 4.23 demonstrates examples of XRD patterns used for residual stresses calculations.

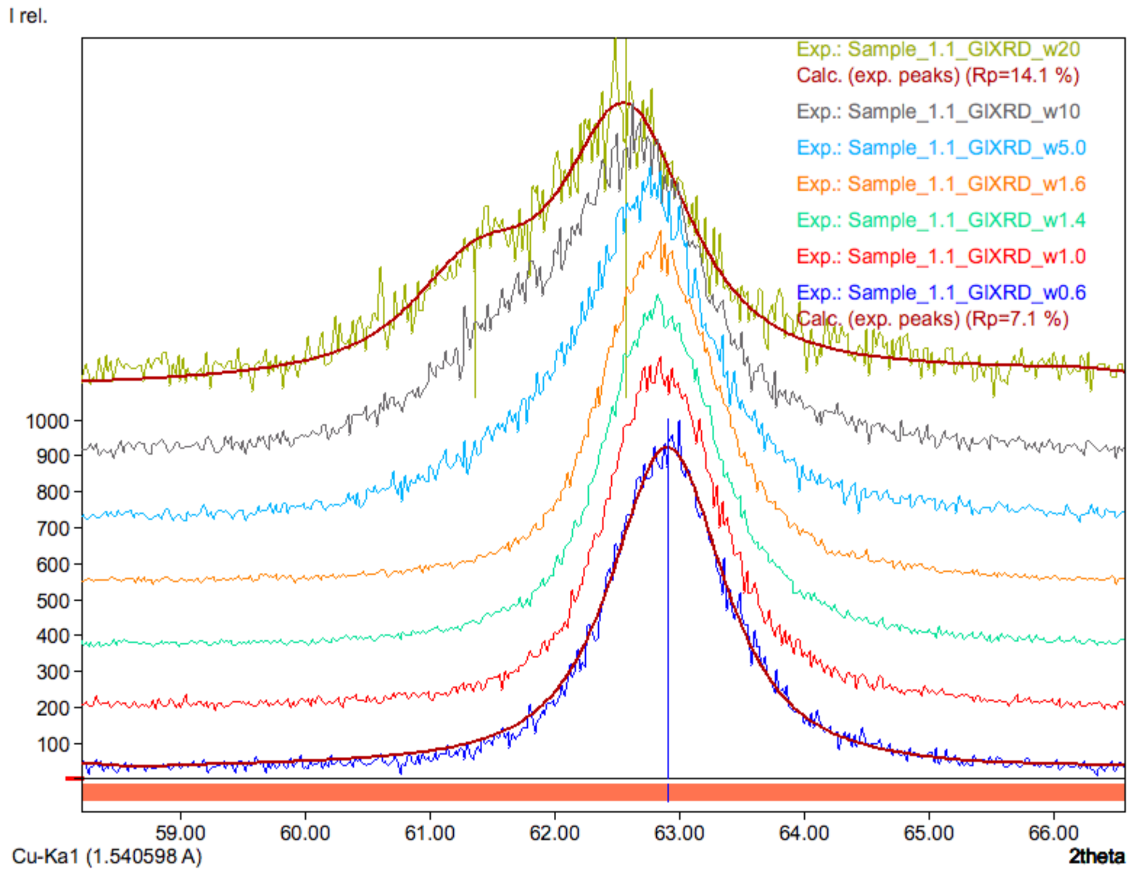

(a)

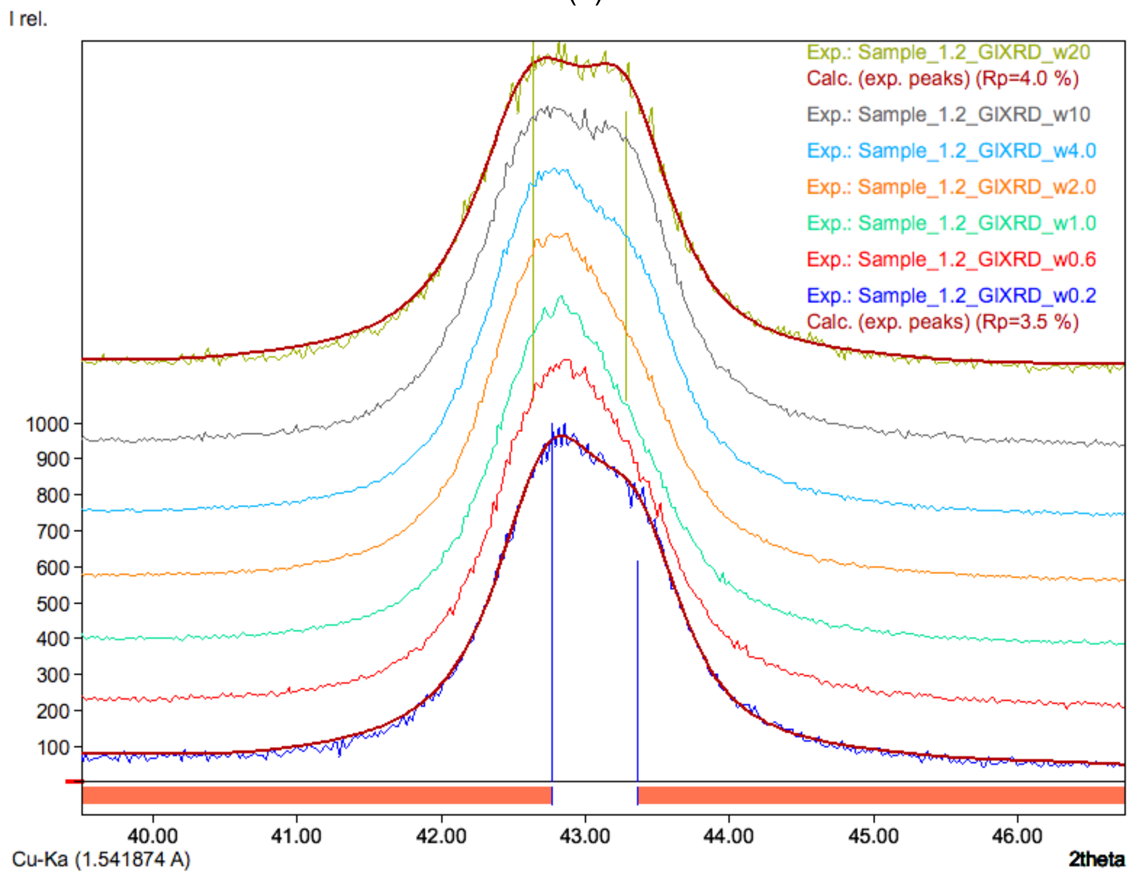

(b)

Fig. 4.23 - Series of XRD patterns at selected incident angles for Sample 1.1 (a) and Sample 1.2 (b).

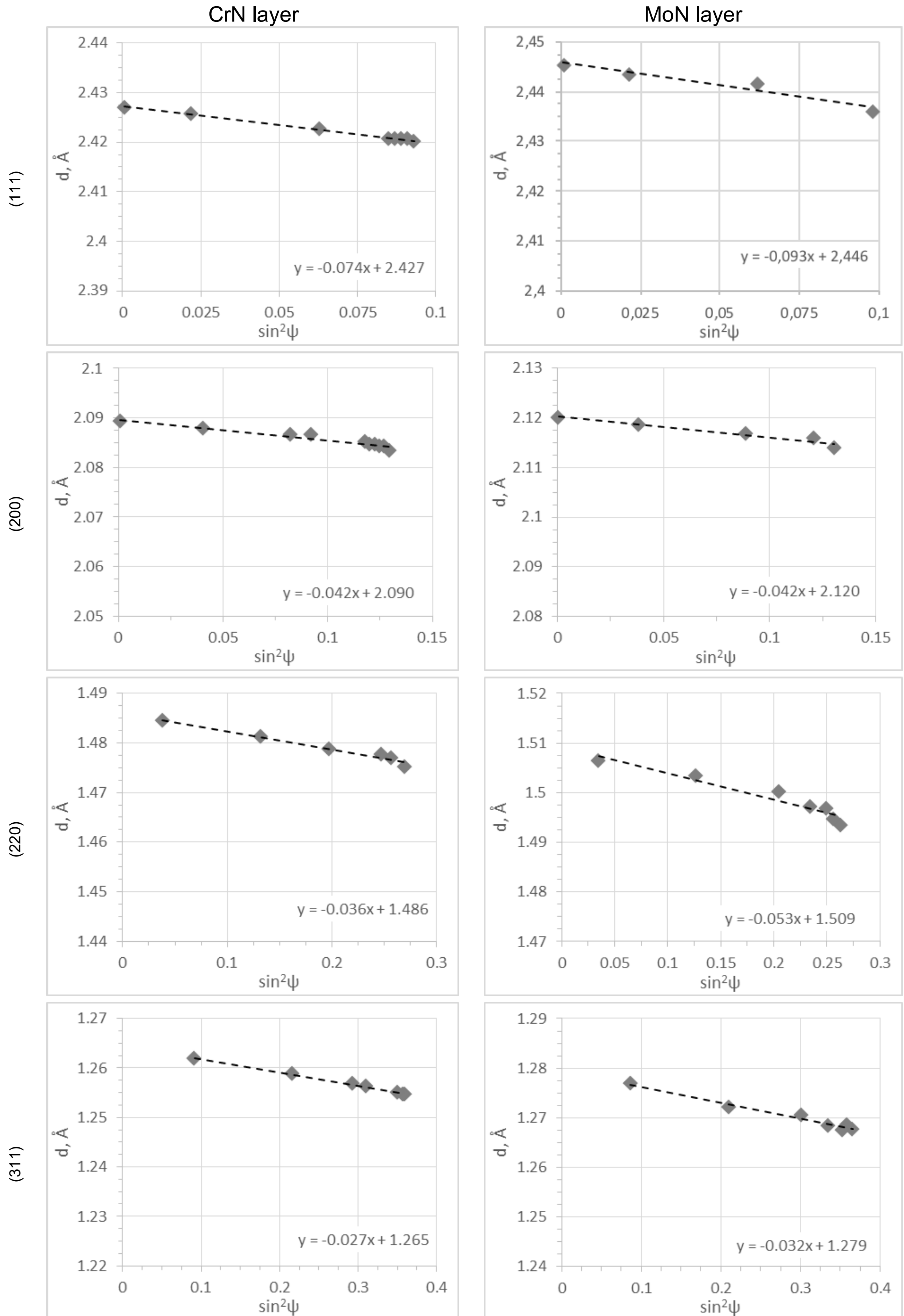

Fig. 4.24 - $\sin^2\psi$ plots recorded for the reflections from (111), (200), (220) and (311) planes of CrN and γ-Mo_2N layers. Partially published in [214].

Using such an XRD analysis approach, it was possible to reach angles between normal to the surface and diffraction vector (normal to the diffraction plane) from 0° up to 40° which improves the accuracy of the calculations. Deconvolution of the overlapped peaks was performed using XRD analysis software Match! as shown for XRD patterns taken at the highest and the lowest incident angles. The shift of the identified peaks positions indicates the presence of the residual stresses in the lattices and films.

Fig. 4.24 shows d-spacing vs $\sin^2\psi$ plots for some of hkl reflections registered from the XRD patterns taken at several fixed positions of the incident angle ω. As seen from the diagrams, both layers are under compressive stress, as manifested from the negative slopes of $\sin^2\psi$ plots.

One may notice the larger inclination of the lines for MoN layers. Detailed results of stress and lattice parameters evaluation are reported in Table 4.4. Out-of-plane lattice constants $a_\perp$ were determined from d-spacing vs $\sin^2\psi$ plots, as well as from XRD θ/2θ patterns, while in-plane lattice constants $a_\parallel$ were deduced from in-plane XRD data.

For both CrN and γ-Mo_2N phases, the in-plane $a_\parallel$ (resp. out-of-plane $a_\perp$) lattice parameters are lower (resp. larger) than reference values from the literature, which is consistent with the existence of biaxial compressive stress. The stress-free lattice parameter, a_0, was calculated from Equation (4.2) [274]:

$$a_0 = a_\perp \left(\frac{1-\nu}{1+\nu}\right) + a_\parallel \left(\frac{2\nu}{1+\nu}\right), \quad (4.2)$$

where ν is the Poisson ratio, taken 0.29 both for CrN and MoN [228,367,377].

Calculated residual stress in samples 1.1 and 1.2 was 5.3 GPa for CrN and 6.9 GPa for γ-Mo_2N. Larger compressive stress was found for the MoN layer compared to CrN one (see Table 4.4), which may be due to higher incorporation of nitrogen atoms in the crystal lattice and correlates with results of elemental composition analysis. For the same reason, an increase of stress-free lattice parameters a_0 in comparison to reference values a_{ref} is observed.

Table 4.4 - Results of residual stresses calculation for multilayer CrN/MoN thin films.

Phase	Residual Stress σ, GPa							Lattice parameters, Å				ε, %
	Plane orientations						Average	$a_\perp$	$a_\parallel$	a_0	a_{ref} [378]	
	111	200	220	311	222	400						
CrN	7.1	4.6	5.7	5.0	6.3	3.1	5.3	4.196	4.134	4.168	4.149	1.5
γ-Mo_2N	8.8	4.6	8.2	5.8	-	-	6.9	4.248	4.153	4.205	4.163	2.3

The stress and strain calculated for the MoN layer have relatively higher values in comparison to CrN; further, calculated lattice parameter a_0 is significantly higher than that of reference γ-Mo_2N, which could also be explained by the presence of the cubic, off-stoichiometric MoN_x metastable phase. This metastable cubic MoN_x phase has a higher lattice constant than γ-Mo_2N, as a result of the filling of unoccupied nitrogen sites [379]. As already reported by Linker

et al. [380] and Perry *et al*. [381], this increase of the lattice parameter (0.419-0.427 nm) happens with increasing nitrogen contents (MoN_x, $0.9 < x < 1.3$). Nitrogen atoms in excess may occupy the 50% vacant octahedral sites of γ-Mo_2N phase, and additionally, they can also occupy interstitial sites, resulting in lattice expansion [382]. This conclusion is also supported by the N content (and oxygen content), which may together justify the presence of that phase [383].

Chapter 5.
Mechanical and Tribological Properties of CrN/MoN Coatings

5.1. Hardness and Elastic Modulus

Microhardness measurements were performed with a diamond Berkovich tip by high-resolution continuously-recording indentation test. Load-unload curves for indentations of Sample 1.1 are shown in Fig. 5.1. Up to 10 acquisitions were made for each sample on different zones of the surface. As seen from the load-unload data, all curves are placed with high precision and almost don't show any deviation, as well as no steps or discontinuities, are present on the loading or unloading parts of the indentation curves in relation to some failures or defects. This is a sign of the high uniformity of the coatings and their high quality in general.

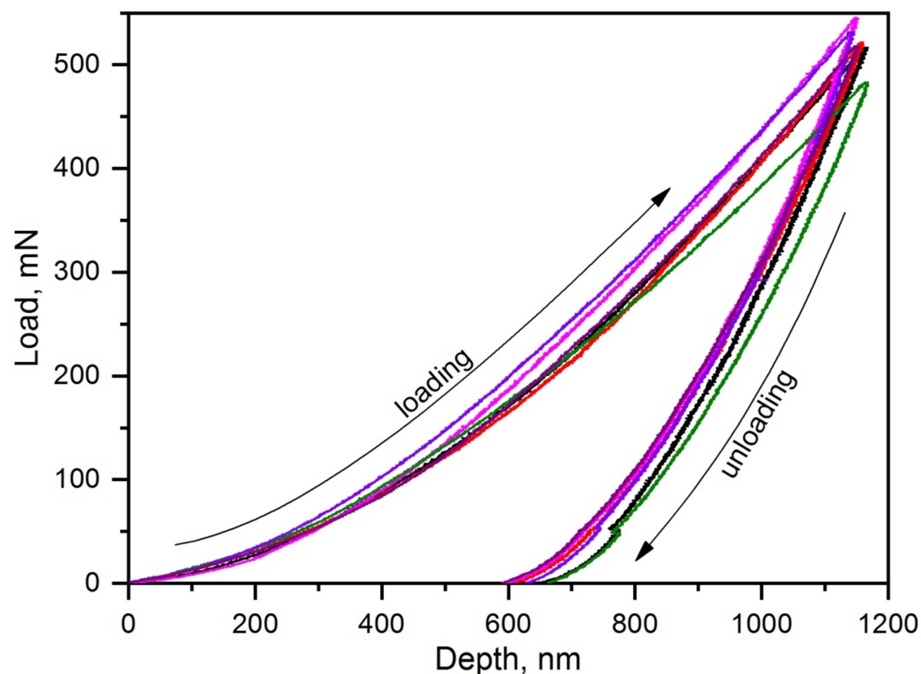

Fig. 5.1 - Load-displacement curves (several acquisitions) of indentation hardness test for Sample 1.1.

As discussed in Chapter 4, and shown in Table 4.1 and Fig. 4.2, due to the decrease of deposition rate from the samples with thicker individual layers to the samples with relatively thinner individual layers, the total thickness of the coatings may vary almost two times between samples (e.g., from Sample 1.1 to Sample 1.6). In this way, the indentation depth limit of 10% of the total thickness of coatings is also different. If the lowest indentation limit is applied for all coatings, the indenter will not reach even the second layer of the coating with thick individual layers, e.g. Sample 1.1 with bilayer period of 2.26 μm (see Fig. 5.2). Therefore, in addition to the indentations with a penetration depth limit of 10% of the total thickness of coatings with thin

individual layers, another set of more deep indentations has been performed, for comparison of the obtained values and to make sure that measurements and results are correct.

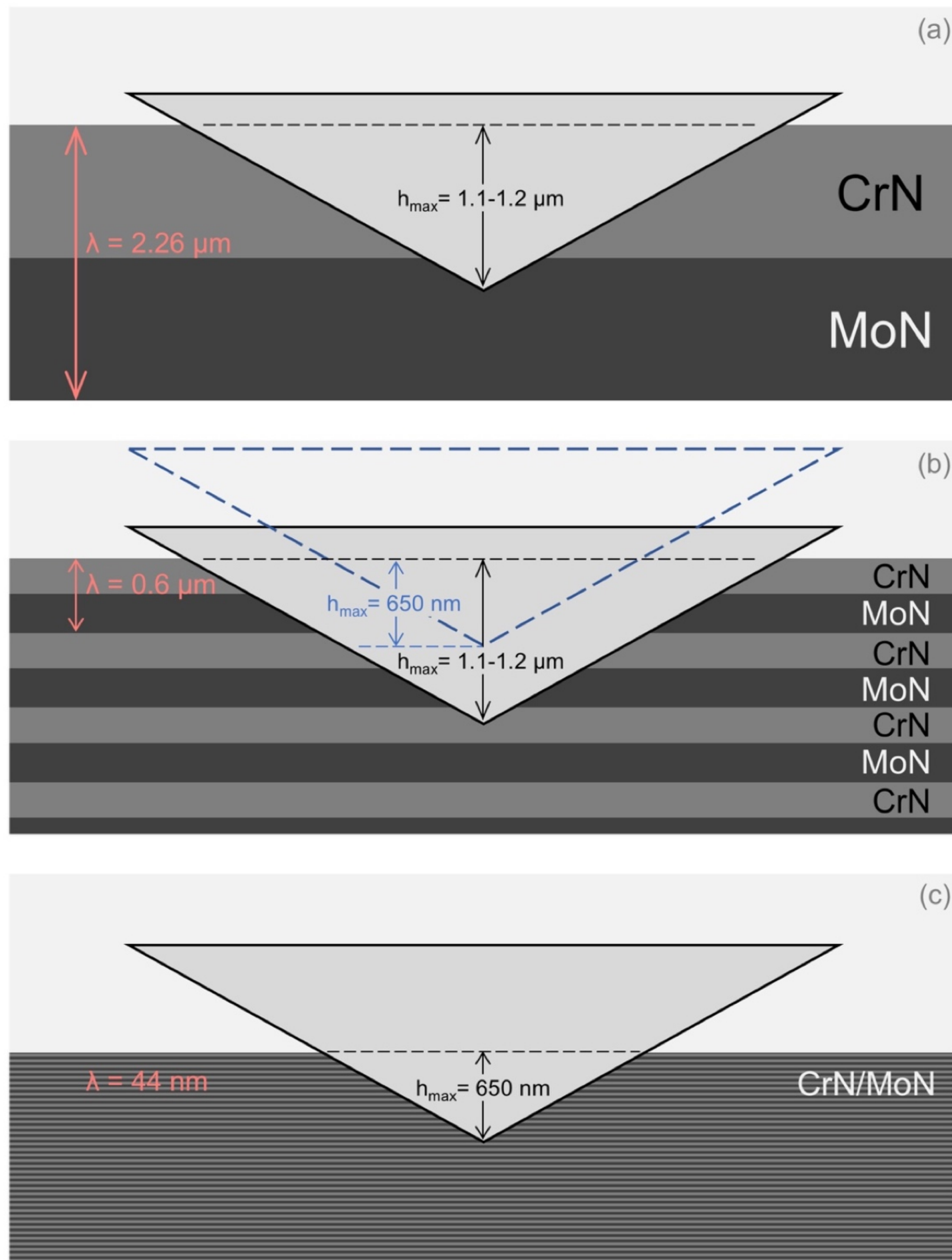

Fig. 5.2 - Schematic cross-section view of the indentation process under the maximum load at the maximum penetration depth, comparison for the multilayer coatings with different bilayer thickness. (a) Sample with bilayer thickness λ = 2.26 μm which is more than the indentation depth, (b) λ = 0.6 μm and indentation depth of 1.2 μm or 650 nm, which is enough to cross a few full bilayers, (c) indentation depth is much more than bilayer thickness λ = 44 nm.

Fig. 5.3 shows an example of two sets of indentations performed under different maximum loads and, thus, with different penetration depths for Sample 1.3. It is seen that curves of both sets demonstrate the same elastoplastic behaviour and calculated values of hardness are also similar. Although it was a very rare issue during microindentation experiments on the studied samples, the black load-unload curve was selected to show an example of pop-in events on the

loading part of the curve. There are two evident discontinuities placed close to each other at about 230-240 mN applied load and correspondent penetration depth of 600 nm. These discontinuities are called pop-ins events and marked in the figure by arrows and dashed circles on the loading part of the load-displacement curve. As such phenomenon was not encountered in the remaining sets of the data and no associated regularities were found, these pop-ins may be attributed to the dislocation nucleation or/and their propagation during loading or due to the micro-cracking [384]. If the depth where such pop-ins happened (about of 600 nm) is compared with the bilayer thickness of the coating of Sample 1.3 (λ = 600 nm), one may assume that the phenomenon occurred at the interlayer interface, which could be a delamination or cracking of the layers, or one of the events mentioned earlier.

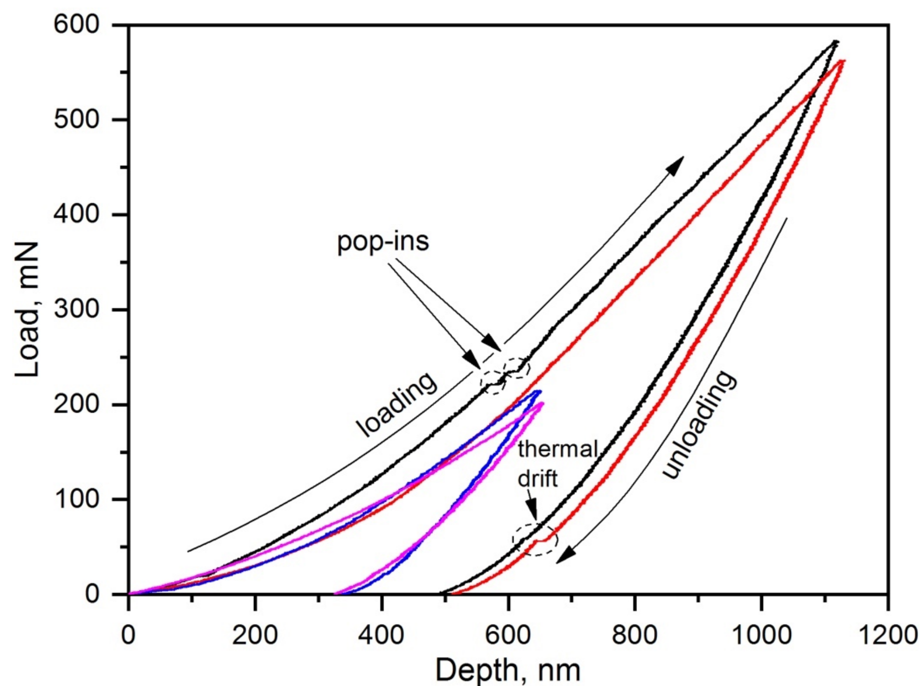

Fig. 5.3 - Load-displacement curves (several acquisitions) of indentation hardness test for Sample 1.3.

Other types of discontinuities may be present on the unloading or reverse part of the load-displacement curve of nano- or microindentation data. In many cases, such events usually called pop-outs may be associated with stress-induced (or pressure-induced, or nanoindentation-induced) phase transformations, which is commonly observed in Si or Si-based structures [385,386]. However, this is not a case for the studied CrN/MoN coatings, and discontinuities observed almost at the end of some load-displacement curves shown in Fig. 5.1, Fig. 5.3 and Fig. 5.4, specially marked with the arrows. These steps of various sizes are a sign of thermal drift, measured during the data acquisition.

If there is a thermal expansion or contraction in the test material or indentation tool during the test, this will result in a positive or negative drift of the measured curves. The drift rate varies in a relatively short time, and a new correction must be calculated for each data acquisition. In most of the thermal drift correction procedures, the measurement of the thermal drift occurs at

the end of the unloading process at 10% of the maximum applied load. At this point, it is possible to assume that for test material at such a low and constant load, the only reason for any displacement is thermal drift. When the indenter reaches 10% of the maximum load during the unloading process, the instrument is stopped at this position for a certain time, and the displacement of the tip is measured. Then the measurements are resumed, and at the end, all the displacements measured during the test should be corrected according to the calculated thermal drift rate.

The time of the thermal drift measurements may be called the dwell period of the thermal drift correction, and for the experiments performed in this study it was 60 s. This period is shown at the reconstructed microindentation timeline in Fig. 5.5 for the acquisition process of data demonstrated for Sample 1.6 in Fig. 5.4. It is also seen that loading and unloading indentation rates were 2 mN/s and 5 mN/s, respectively. Additionally, the delay of 5 s was done at the maximum load to check if there is a risk of creep appearing.

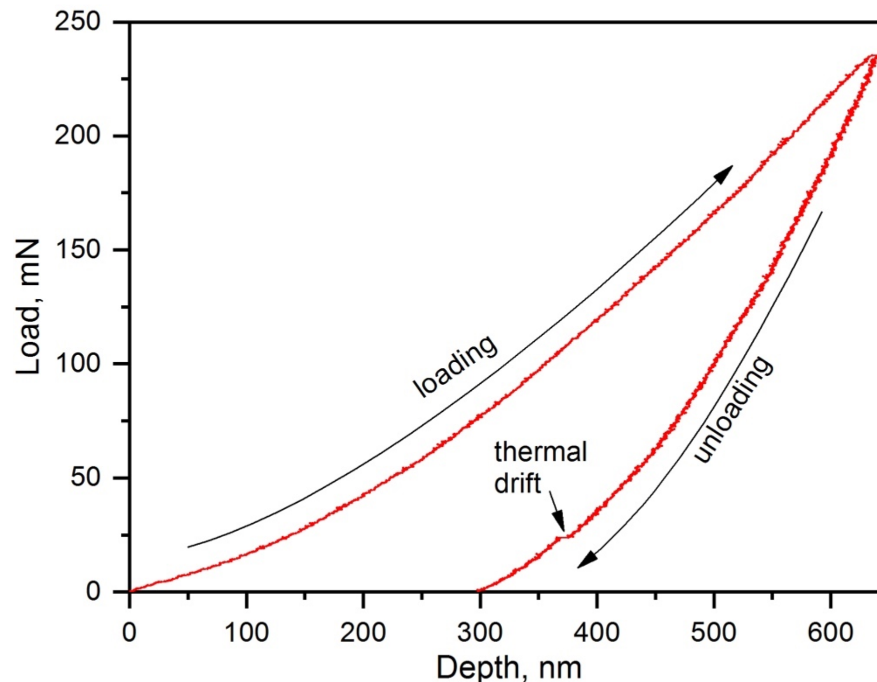

Fig. 5.4 - Load-displacement microindentation curve of hardness test for Sample 1.6

Fig. 5.6 demonstrates the penetration depth of the indenter vs timeline of the microindentation process. Only one out of every ten data points is shown in the figure for better presentation and more clear understanding of processes and acquisition rates. Nonlinear curves of loading and unloading under the linearly growing and decreasing loads are seen. The creep displacement of 5.7 nm at the maximum load of 235 mN during 5 s is clearly shown as well as the thermal drift of 10 nm during 60 s while holding 10% of the maximum load. Corresponding displacement rates were calculated and shown in Fig. 5.6. Although the obtained values are low and don't cause any significant influence at performed conditions on the resulted data, all necessary corrections to the experimental data were applied.

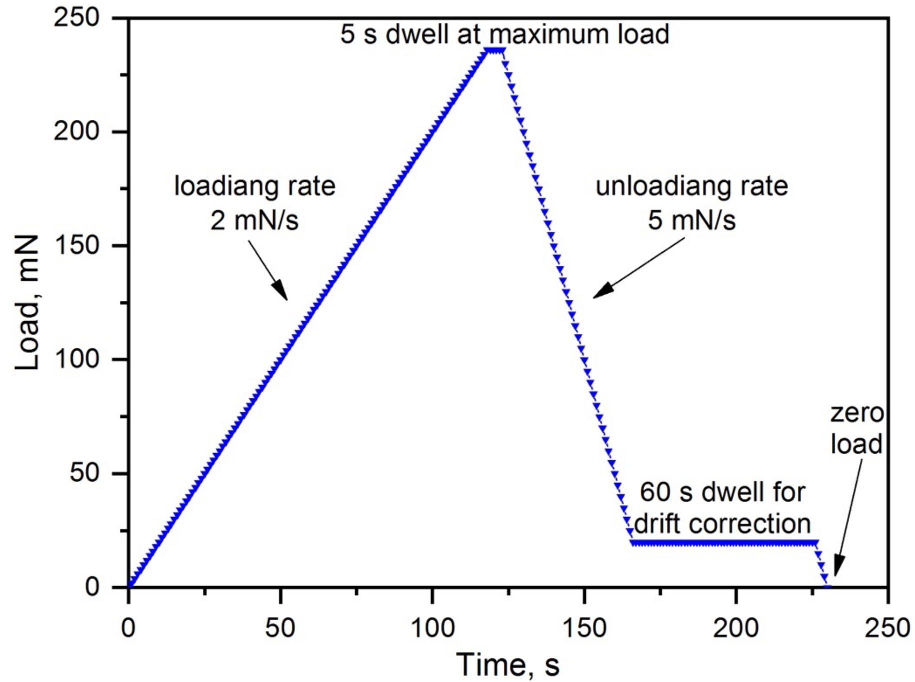

Fig. 5.5 - Timeline of applied load during microindentation of Sample 1.6

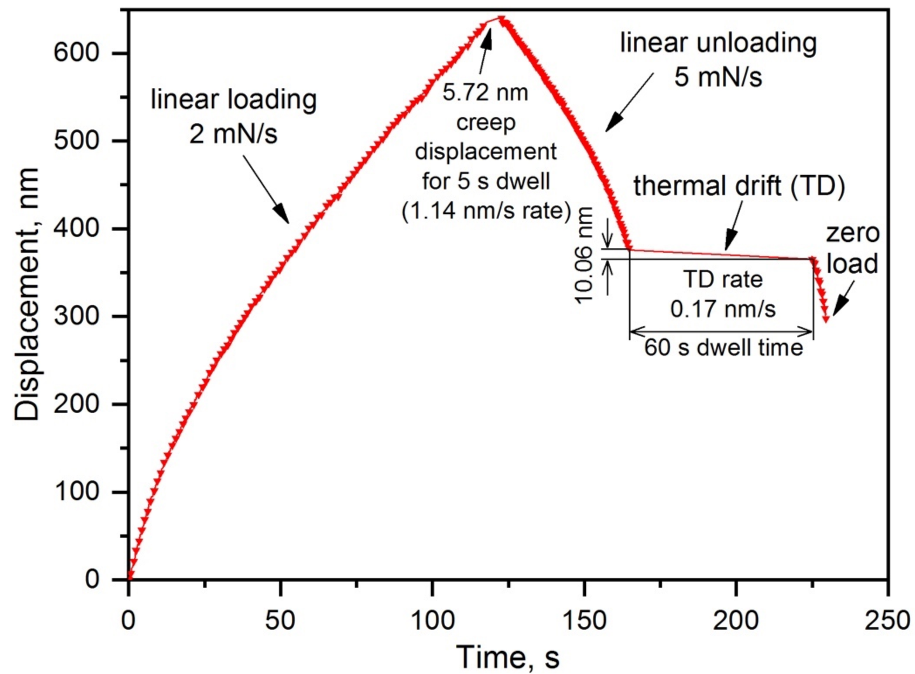

Fig. 5.6 - Displacement timeline during hardness test for Sample 1.6

Fig. 5.7 shows load-displacement curves of microindentations performed on a steel substrate used for the deposition of coatings. As seen from the figure, curves of steel substrate indentation demonstrate much more plastic and less elastic behaviours of the material in comparison to CrN/MoN coated samples. One may compare such load-displacement curves of steel substrate and studied CrN/MoN coatings and notice at the same applied load indenter goes much deeper into the uncoated steel specimen than into the coatings. This indicates the significantly higher hardness of studied multi-layered protective coatings than used steel substrate or potential uncoated tools and goods.

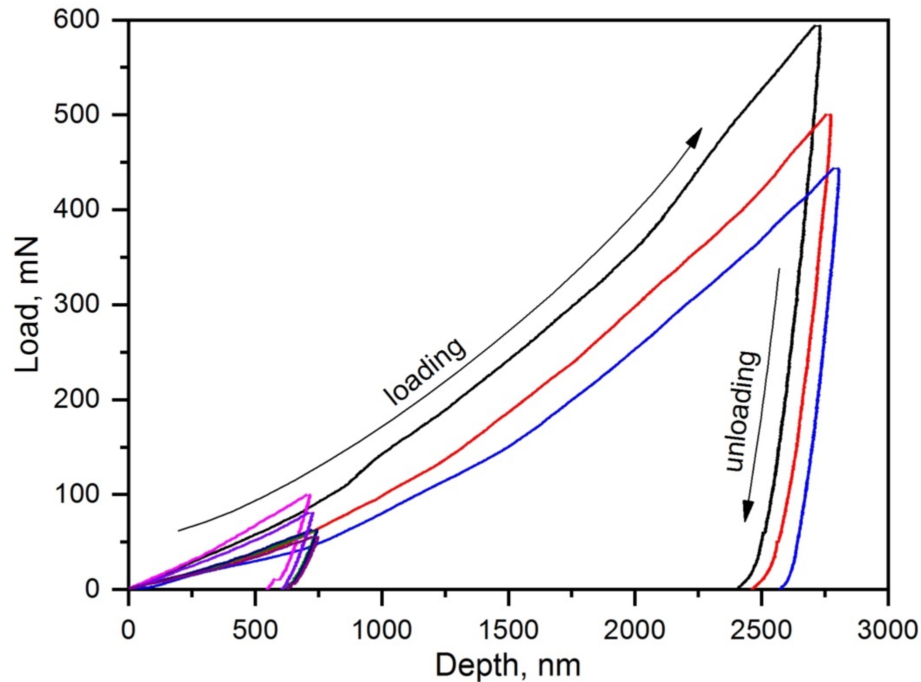

Fig. 5.7 - Load-displacement curves (several acquisitions) of indentation hardness test for uncoated steel substrates.

The results of mechanical properties evaluation are shown in Fig. 5.8. The highest values of measured hardness were demonstrated by the films deposited at the lowest absolute value of the negative bias voltage U_b = −20 V (Series 1). This regime also provides higher nitrogen concentration in the films. For the multilayer samples of Series 1 the hardness growth is observed while the individual layer thickness decreases. Apparently, with the decrease of the individual layer thickness the grain size reduction occurs, and the phenomenon of hardness enhancement may happen due to the Hall-Petch strengthening mechanism [198,387], where the growth of grain boundaries volume obstructs the activity of dislocations movements. An additional barrier for the propagation of dislocations growth and transfer is caused by the increase of interlayer interfaces volume when the number of layers in the films increases with the decrease of the individual layer thickness. This effect also improves protective properties of the multilayer coatings via reduction of cracks propagation towards the substrate by the deflection of cracks on the interlayer interfaces. The results presented in this work are in good agreement with similar results for nanoscale multilayer coatings, where the mechanical properties improve when the bilayer period decreases [34,387–389].

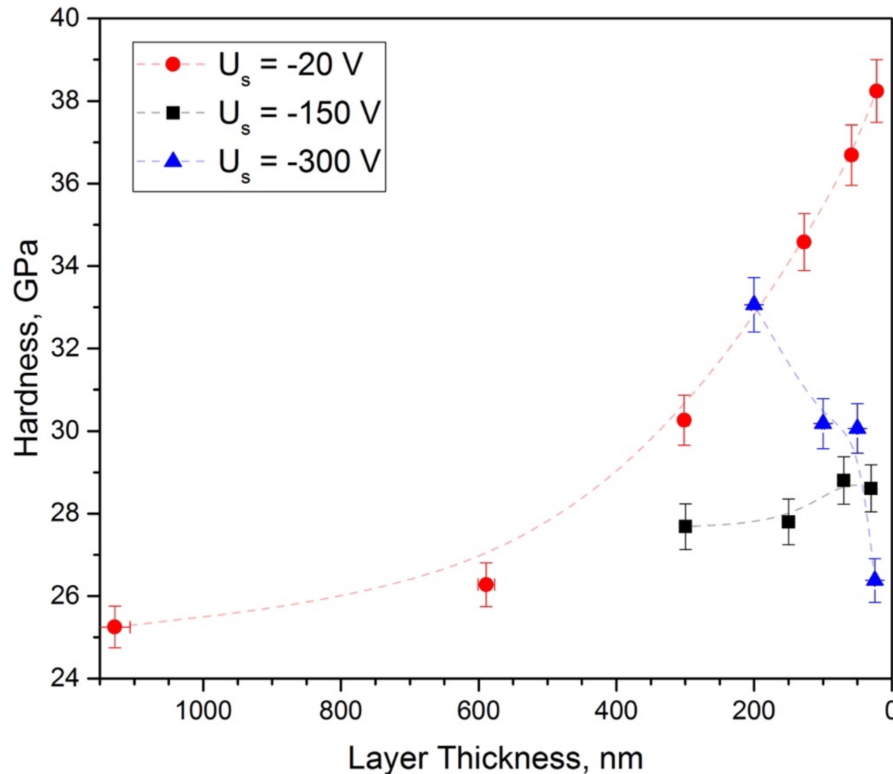

Fig. 5.8 - Results of hardness measurements for three series of CrN/MoN multi-layered coatings. Bias voltage applied to the substrates during deposition was −20, −150 and −300 V. Published in [146].

Mechanical properties, hardness and elasticity modulus vis-a-vis values of bilayer thickness, of samples from Series 1 have been shown separately in Fig. 5.9. It was observed that with the decrease in bilayer thickness, the hardness and Young's Modulus increase. As seen from Fig. 5.8 and Fig. 5.9, the hardness values for the samples of Series 1 are in a range of 25-39 GPa, where the hardness is significantly increased where the individual layer thickness of films is 60 nm or thinner. The lowest values of hardness and Young's Modulus, typical for pure chromium nitrides, correspond to the film with the thicker layers (H = 25 GPa, E = 295 GPa when Λ = 2.26 μm) and the highest – for the films with the thinner layers (H = 38 GPa, E = 357 GPa when Λ = 44 nm). Furthermore, it should be noted that in some coatings (samples 1.4-1.6) the hardness had values above 40 GPa, up to 42.3 GPa, which means they belong to the superhard class.

For the higher absolute value of bias voltage U_b = −150 V such kind of tendency of hardness increase is observed only for the individual layer thickness up to 40-50 nm and then, for thinner layers, the hardness decreases. In correspondence to the XRD structural analysis data, one may assume that the reason for the hardness drop is the loss of barrier properties due to the intensification of the high-energy particles mixing process in a near-interface interlayer zone. In relatively thin layers of coatings (tens of nanometres) it leads to the formation of a large volume of mixed regions with (Cr,Mo)N solid solution state [202,373] and, thereby, to the decrease of hardness values.

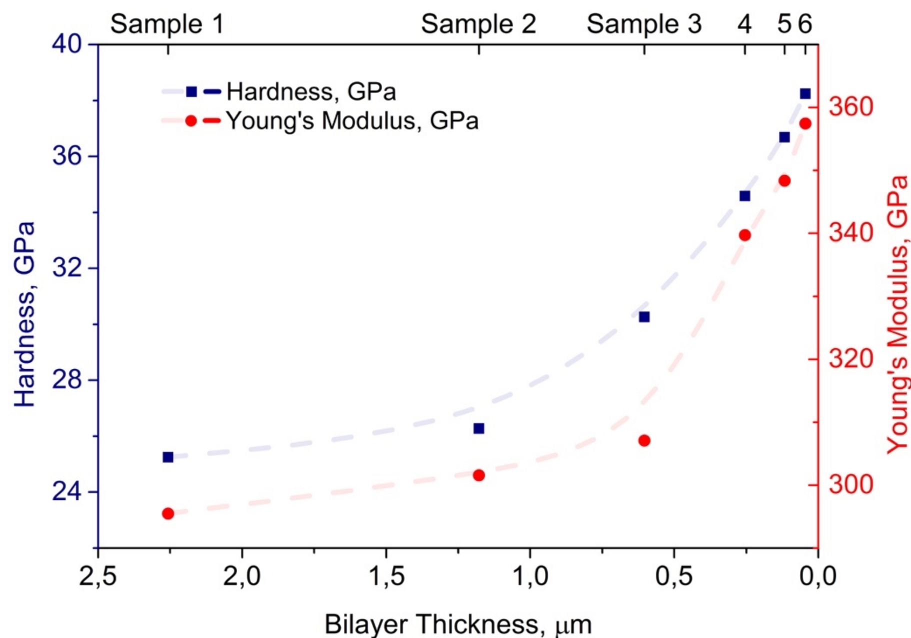

Fig. 5.9 - Results of hardness and Young's modulus measurements vs bilayer thickness for multi-layered CrN/MoN coatings of Series 1. U_s = −20 V. Published in [214].

For U_b = −300 V the above-mentioned relation of hardness drop remains even for thicker layers of the films (see Fig. 5.8 (a), blue line). The highest hardness of coatings is achieved when the CrN phase with cubic lattice and a relatively small region of homogeneity in the composition is present in the layers.

5.2. H/E and H^3/E^2 Ratios

To evaluate the mechanical properties of films and to predict the protective features of coatings, the ratios of hardness to elastic modulus could be used. For the further characterisation of mechanical and, thus, protective properties, the ratio of hardness and Young's modulus is introduced in the form of H/E parameter [38,167,189,361,372,390–393]. The ratio H/E (or H/E*, where $E^* = E/(1 - v^2)$) plays a significant role in the so-called "plasticity index", widely recognised as a reliable parameter of elastic behaviour of surface in contact with external forces. It could characterise protective the properties of coatings in terms of cracking, abrasive wear and serve as a ranking parameter for the toughness of the deposited films.

In Fig. 5.10 the area is divided into two zones along the line H/E = 0.1. As shown, three samples are in the region H/E> 0.1 (high elasticity zone), which characterises them as coatings with increased wear resistance. The growth of the considered mechanical parameters such as hardness, Young's modulus and H/E ratio with the decrease of bilayer thickness of the considered multilayer CrN/MoN coatings of Series 1 is evident. Such a tendency can be associated with a corresponding decrease in the grain size, which leads to an increase of the interphase boundaries and an enhancement of the Hall-Petch effect, preventing the movement of dislocations.

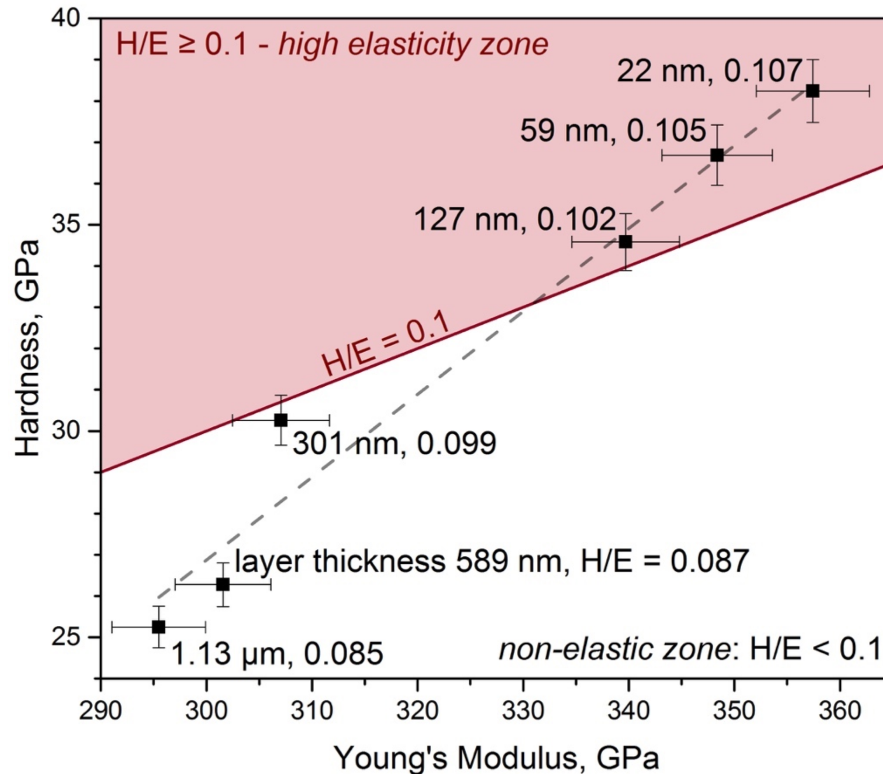

Fig. 5.10 - Hardness vs Young's modulus divided by H/E = 0.1 for Series 1 of CrN/MoN multi-layered coatings. Published in [146].

The ratio H^3/E^2 is another important parameter of mechanical properties characterisation [34,166,394], which allows determination and rank coatings in relation to plastic deformation resistance. The behaviour of ratio H^3/E^2 in terms of films bilayer thickness is described in Fig. 5.11(b, right Y-axis). The observed improvement of the mechanical parameters, such as hardness and following H/E or H^3/E^2 ratios in studied multilayer films, may most likely be related to the decrease of bilayer thickness and subsequently lower values of crystalline/grain sizes. This leads to an increase in interface volume and to the growing role of the boundaries as pinning points in the material. The Hall-Petch strengthening with the decrease of layer thickness leads to the prevention of dislocation movements and will enhance the yield strength of the material and increase the hardness.

When the bilayer thickness decreases, a higher number of layers may be produced within the same total thickness of the coating. It also leads to an increase in the interlayer interfaces number, which blocks the propagation of cracks and dislocations, avoiding the continuity of pinholes and pores [43]. Recent work by Daniel *et al*. [227] on the beneficial impact of interface design on crack deflections has been reported in TiN coatings.

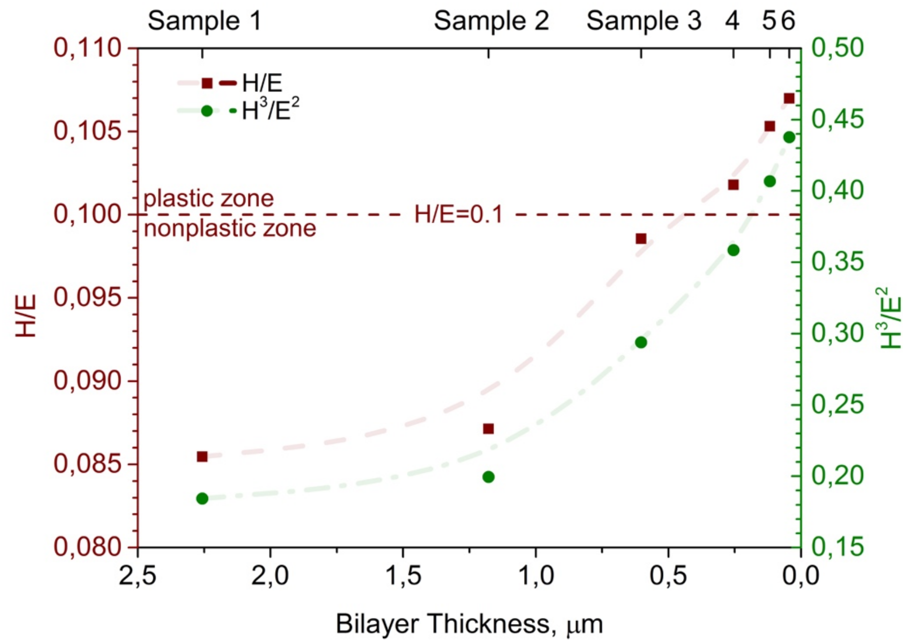

Fig. 5.11 - H/E and H^3/E^2 ratios vs bilayer thickness of multi-layered CrN/MoN coatings of Series 1. Published in [214].

5.3. Wear Resistance and Tribological Properties

The results of tribological tests of all series of coatings with different bilayer thickness, various values of nitrogen pressure and the bias voltage applied to the substrate during the deposition are presented in Table 5.1.

Table 5.1. Tribological properties of CrN/ MoN coatings obtained at Ub = −150 V and different nitrogen pressures.

Sample number	Substrate bias, V	Nitrogen pressure p_N, Pa	Friction coefficient, μ		Wear rate v, $mm^3 \times N^{-1} \times m^{-1}$		R_a, μm
			Initial	During experiment	Counterbody (Al_2O_3)	Coating	
1.4	−20	0.4	0.47	0.535	0.553×10^{-7}	9.8×10^{-7}	0.25
1.6		0.4	0.38	0.435	0.885×10^{-7}	5.92×10^{-7}	0.39
2.4	−150	0.4	0.535	0.579	0.86×10^{-7}	6.36×10^{-7}	0.28
2.7		0.09	0.381	0.586	0.25×10^{-7}	13.45×10^{-7}	0.47
3.4	−300	0.4	0.529	0.68	0.975×10^{-7}	6.85×10^{-7}	0.32
3.7		0.03	0.358	0.34	0.637×10^{-7}	15.34×10^{-7}	0.43
stainless steel 12X18H9T substrate			0.204	0.674	0.269	35.36×10^{-7}	0.088

Fig. 5.12, Fig. 5.13, Fig. 5.14 and Fig. 5.15 show the surface of the counterbody after the interaction with the coating, the wear track, resulting profilograms of the coatings, data recorded during the tribological test and averaged friction coefficients versus corresponding values of the negative bias voltage applied to the substrate during the deposition.

The elemental composition of wear tracks revealed a slight decrease in the nitrogen concentration, while the presence of oxygen and oxides was not observed. In a couple with other results of the tribological test, it demonstrates the adhesive mechanism of wear for all considered

samples regardless of bilayer thickness or bias voltage applied to the substrate. It is characterised by plastic deformation, transfer of material from one surface to another one and by homogeneous wear of coating with symmetrical shape of wear track profile similar to the counterbody shape (Fig. 5.13). In this case, according to the previous works [26,342,395], the amount of transferred material depends on the adhesive bonds strength, which is directly connected with the electronic structure of the Al_2O_3 counterbody and the MoN/CrN coating, and their compatibility to form solid solutions or intermetallic compounds with each other [366,396].

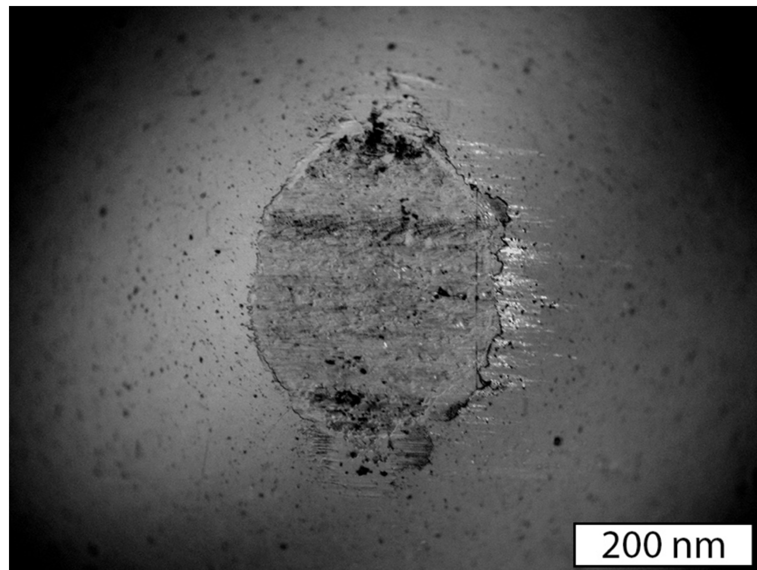

(a)

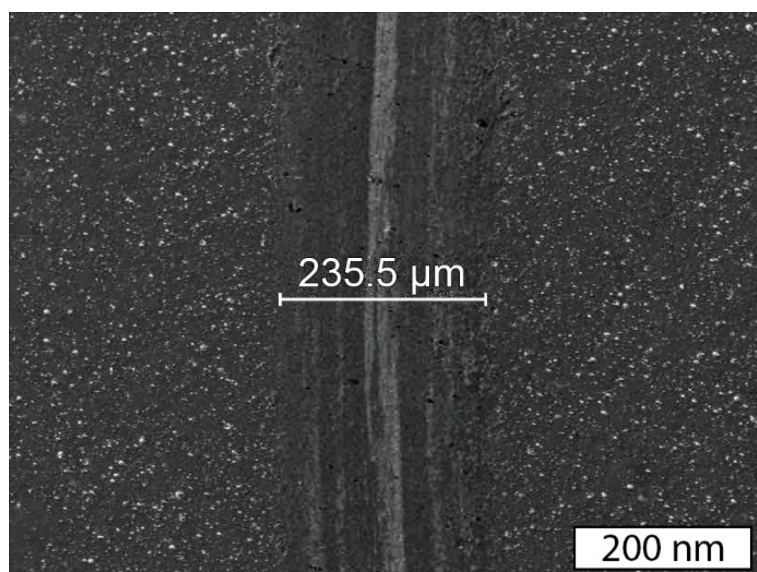

(b)

Fig. 5.12 - Results of tribological tests for Sample 2.4. SEM images of Al_2O_3 counterbody surface after interaction with CrN/MoN multilayer coating (a) and wear track. Published in [146].

However, the change of the friction coefficient occurs (see Fig. 5.14) when the absolute value of negative bias voltage applied to the substrate increases for the samples deposited at the same nitrogen pressure and with similar bilayer thickness (the same number of layers). For samples 1.5, 2.5 and 3.5 the value of friction coefficient increases from 0.337 to 0.585 when the

bias voltage changes from −20 V to −150 V respectively and then slightly decreases to 0.521 when the bias voltage is −300 V. This tendency was observed for the full range of bilayer thickness values for all series of coatings (see Table 5.1). In addition, it should be noted that with the increase of the absolute values of bias voltage the wear rate of the counterbody increases from $0.553{\times}10^{-7}$ $mm^3{\times}N^{-1}{\times}m^{-1}$ to $0.975{\times}10^{-7}$ $mm^3{\times}N^{-1}{\times}m^{-1}$.

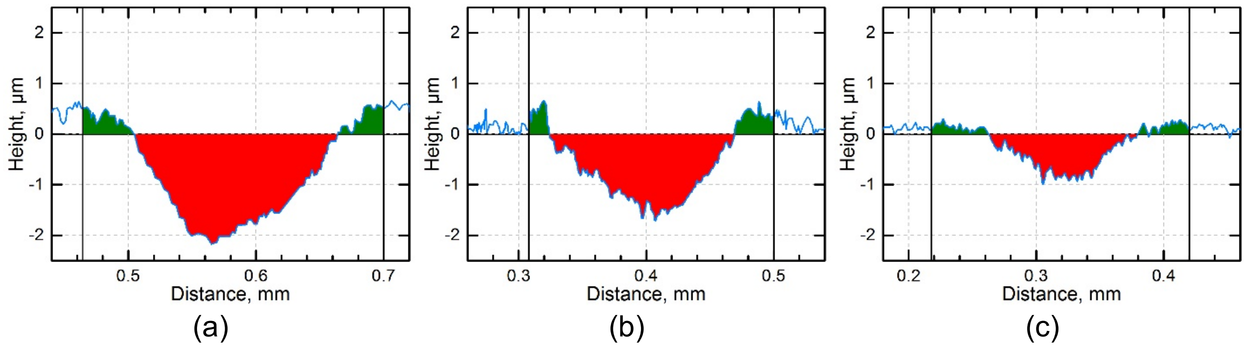

Fig. 5.13 - Results of tribological tests: resulting profilograms of the dynamical test of the coatings for samples 1.3 (a), 1.4 (b) and 1.6 (c) with bilayer thickness 0.6 µm, 0.25 µm and 44 nm respectively. Published in [146].

The results of the tribological tests of the coating deposited at high pressure p_N = 0.4 Pa and bias voltage U_b = −150 V are presented in Fig. 5.15. It is possible to estimate the wear rate in relation to the volume of the wear material. A higher rate of wear indicates that the coating more effectively resists destruction caused by plastic deformation or microcracks during penetration [366,396–398]. As a result, the gradual increase in the friction coefficient (0.62-0.65) respectively to the friction force of 3.65-3.82 N and applied normal load of 6 N is observed. The maximum increase in the coefficient is reached at the end of the path (200 m) with the penetration of the counterbody into the coating. With the increase of the depth, the small transfer of material from the coating to the counterbody is observed. Therefore, the adhesion mechanism of wear occurs.

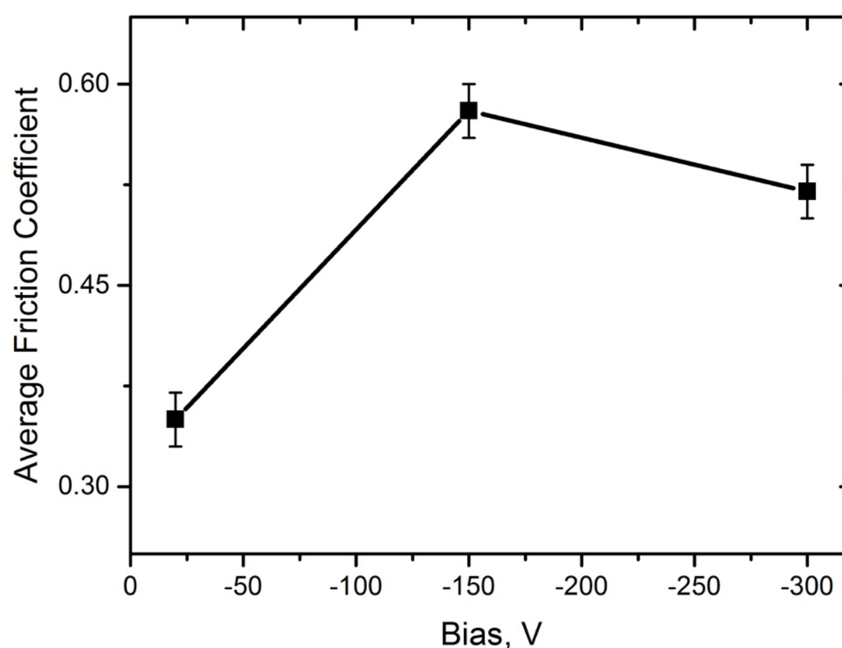

Fig. 5.14 - Results of tribological tests: averaged friction coefficients versus corresponding values of the negative bias voltage applied to the substrate during the deposition. Published in [146].

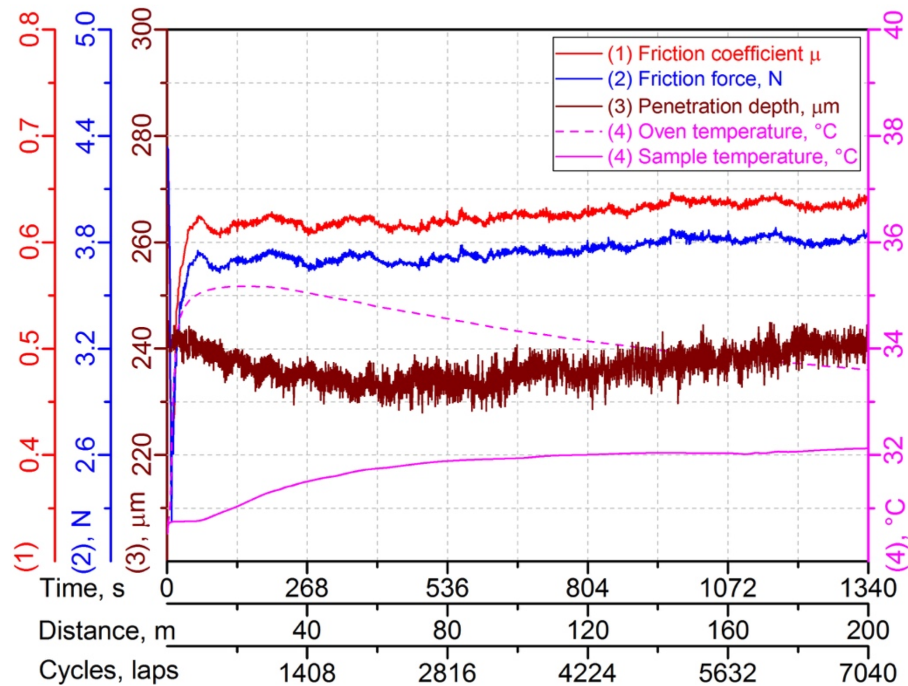

Fig. 5.15 - Results of tribological tests: data recorded during the tribological test with spherical Al_2O_3 counterbody for Sample 2.4. Published in [146].

The decrease of the nitrogen pressure in the chamber from 0.4 to 0.09 or 0.03 Pa leads to the decrease of counterbody wear rate (see Table 5.1) and to the growth of brittleness and wear of the coatings. It may be both due to the coatings' deposition process and due to the formation of different types of crystal lattices in nitride layers: mainly β-Cr_2N, CrN and γ-Mo_2N. At nitrogen pressure p_N = 0.4 Pa only cubic lattices of CrN and γ-Mo_2N phases have been detected, and the double increase of wear resistance was observed.

The reduction of bilayer thickness in the deposited CrN/MoN multilayer films leads to the decrease of wear, which is clearly seen in Fig. 5.13 for samples 1.3, 1.4 and 1.6, where the value of bilayer thickness changes from 0.6 μm to 44 nm.

Thereby, the decrease of the wear rate of the coatings with nanoscale bilayer thickness (tens nanometres) occurs mainly due to the high volume of boundary interfaces (thus, the small size of nanograins) and high number of interlayer interfaces.

The concept of multilayer architecture of the films may provide the enhancement of adhesion and wear resistance due to the prevention of cracks propagation towards the substrate by promoting their deflection. Consequently, multilayer and multicomponent structures improve the mechanical properties of the surface, because interfaces and boundaries block the propagation of dislocations and the deformations locate in near to the surface zone.

Chapter 6.

Final Discussion and Further Perspectives

Multi-layered systems of nanostructured CrN/MoN transition metal nitride coatings deposited by vacuum-arc evaporation of the chromium and molybdenum cathodes in nitrogen atmosphere have been studied in this PhD research. The work was focused on the methods of elemental composition and structural characterisation, mechanical properties and their comparison. The approach to use multilayer architecture with control of individual layer thickness and control of deposition parameters, such as bias voltage or working nitrogen pressure, has been approved as an effective method of transition metals nitride films fabrication for protective application. Produced CrN/MoN coatings demonstrate promising results in comparison to the existed competitors.

6.1. Conclusions: "The Strongest" Layers and Correlation Between Deposition Conditions, Structure and Mechanical Properties

The elemental analysis performed by several methods (RBS, SIMS, EDS, WDS) has shown the good quality of the coatings, and the clear separation of the CrN and MoN layers with sharp interfaces was observed. SEM, SIMS and HRTEM analyses confirm the presence of well-defined multilayer structures and show the compositional and structural assembly of the films. All deposited coatings demonstrate columnar growth with a high degree of structuring.

The increase of the absolute value of negative bias voltage applied to the surface leads to the changes in the preferential crystallographic orientation of two main cubic phases CrN and γ-Mo_2N presented in films from (311) when $U_b = -20$ V to more stable (111) when $U_b = -150$ V and then to (200) at $U_b = -300$ V. When the nitrogen pressure in the chamber decreases to 0.09 Pa the formation of β-Cr_2N phase occurs, which causes the deterioration of tribological properties of the multilayer system.

The decrease of the individual layer thickness of the coatings leads to the decrease of crystallite size (up to 5.8 nm when bilayer thickness is 44 nm), which is clearly seen from the broadening of diffraction peaks on XRD spectra and confirmed by detailed calculations. Thus, the grain size in multilayer coatings can be tuned by the adjustment of the individual layer thickness.

The additional GIXRD and in-plane analyses have confirmed the presence of two main phases γ-Mo_2N and CrN with cubic crystal lattice of NaCl type. The equal interplanar distances in the contacting layers of chromium and molybdenum nitrides indicate the interrelated growth of these two structures, which corresponds to the equiatomic Cr/Mo ratio. The depth profiles from the RBS analysis confirm the homogeneity of the layer.

When most of the deposition conditions are maintained fixed and only the deposition time per sample is changing, the coatings keep similar stable phases and elemental composition (at

least in range of the bilayer thickness considered in the present work), but the structure is changing through the decrease in the grains size in the coatings with lower values of layer thickness. On the one hand, it leads to an increase in the interface volume in CrN/MoN coatings. On the other hand, the number of interlayer interfaces increases due to the decrease in the thickness of individual layers. The mentioned changes lead to the Hall-Petch strengthening of the films, and to the blocking of cracks and dislocations propagation in the multi-layered CrN/MoN coatings.

The measured hardness has reached values of 42.3 GPa. The highest values of hardness up to 42.3 GPa have been registered for the coatings of the series deposited at the lowest absolute value of negative voltage $U_b = -20$ V in the range of individual layer thickness 60-20 nm. The growth of hardness with the decrease of the individual layer thickness to 20 nm occurs mainly due to the Hall-Petch strengthening mechanism.

The tribological tests of coatings have shown a significant effect of the chamber pressure on wear resistance: the coatings deposited at high nitrogen pressure demonstrates better durability and, hence, longer lifetime. Also, it was observed that Series 1 of CrN/MoN coatings deposited at the bias voltage of −20 V demonstrate better tribological properties in comparison to Series 2 and Series 3.

In particular, the best wear performance according to the tribological test has been observed for Sample 1.6 with the thinnest layers. This CrN/MoN coating has the slightly preferential (311) crystallographic orientation of two main cubic phases CrN and γ-Mo_2N, the smallest grain size of 5.8 nm, the highest hardness and H/E = 0.11.

It is an important property of the studied material, which may cause future enhancement of mechanical properties and result in the application of multilayer films as superhard protective coatings appropriate for industrial applications.

6.2. CrN/MoN Hard Coatings as a Solution for Critical Raw Materials Problem in Machining Tools and Other Industrial Applications

The cutting tools distribution in the global market for 2018 by the method and by workpiece material is shown in Fig. 6.1 (a) and (b) respectively. It is seen that milling, turning, and drilling are the most used types of cutting tools. Cemented carbides (a bit more than half of the cutting tools global market) and high-speed steel are still the most used workpiece materials for cutting tools, while ceramic, polycrystalline cubic boron nitride (PCBN), and especially polycrystalline diamond (PCD) have the highest growth rates.

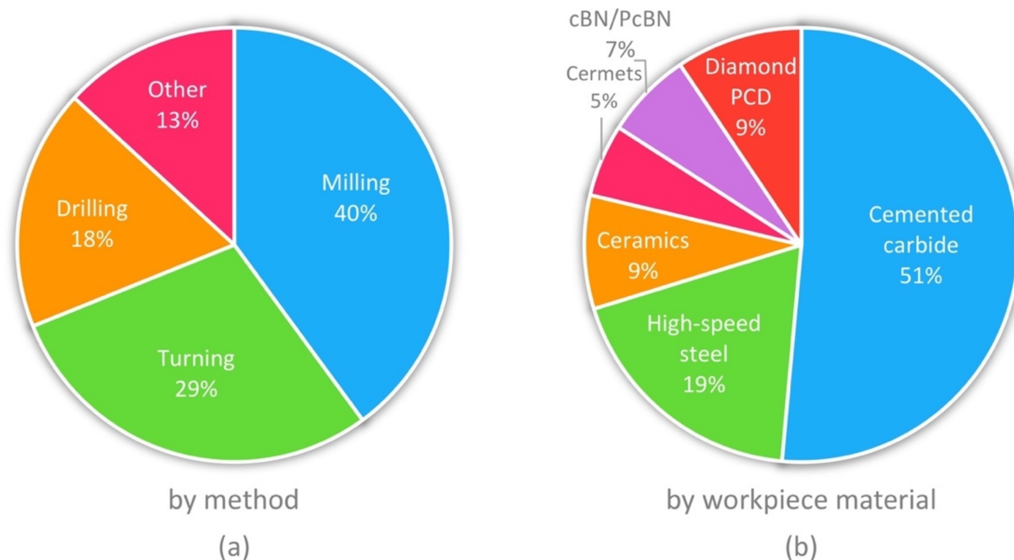

Fig. 6.1 - Cutting tools global market distribution forecast for 2018 by Dedalus Consulting [399]. As taken from [1].

Protective coatings may significantly prolong the lifetime of tools at the same operational speeds or (and) may increase the operational velocities while the lifetime is maintained at the same level and, thus, reduce the consumption of CRM contained in the bulk material. Furthermore, most of the modern coatings are CRM-free.

As seen from the discussion and from Fig. 6.1, there are many coatings that existed to protect cutting tools working under extreme conditions. Firstly, they need to have high hardness and toughness for high wear performance and high quality of machined material. Then they need to be thermally stable and chemically resistant to corrosion and oxidation for a long lifetime in harsh environments and high speeds of machining. Most of the widely used coatings do not contain CRMs, but multi-elemental and high-entropy coatings designed for specific extreme conditions may include them. Transition metals are one of the largest groups of chemical elements in the periodic table and, as one may see in Fig. 6.2, more than a third of them belong to the list of critical raw materials 2011, 2014 and/or 2017. Among them, half of the refractory metals group are marked as CRMs. However, the amount of materials needed for the coating is super-significantly lower than saved CRMs and other materials in tools. Moreover, nano- and microstructural design of protective coatings, such as nanocomposites or multilayers, minimise or completely cut the usage of certain CMRs in coatings. Protective coatings extend the lifetime of cutting tools, improve and simplify their recycling. Therefore, they are a great cost-effective and environmental-friendly solution for the CRMs problem in the cutting tool industry and in a lot of other applications as well.

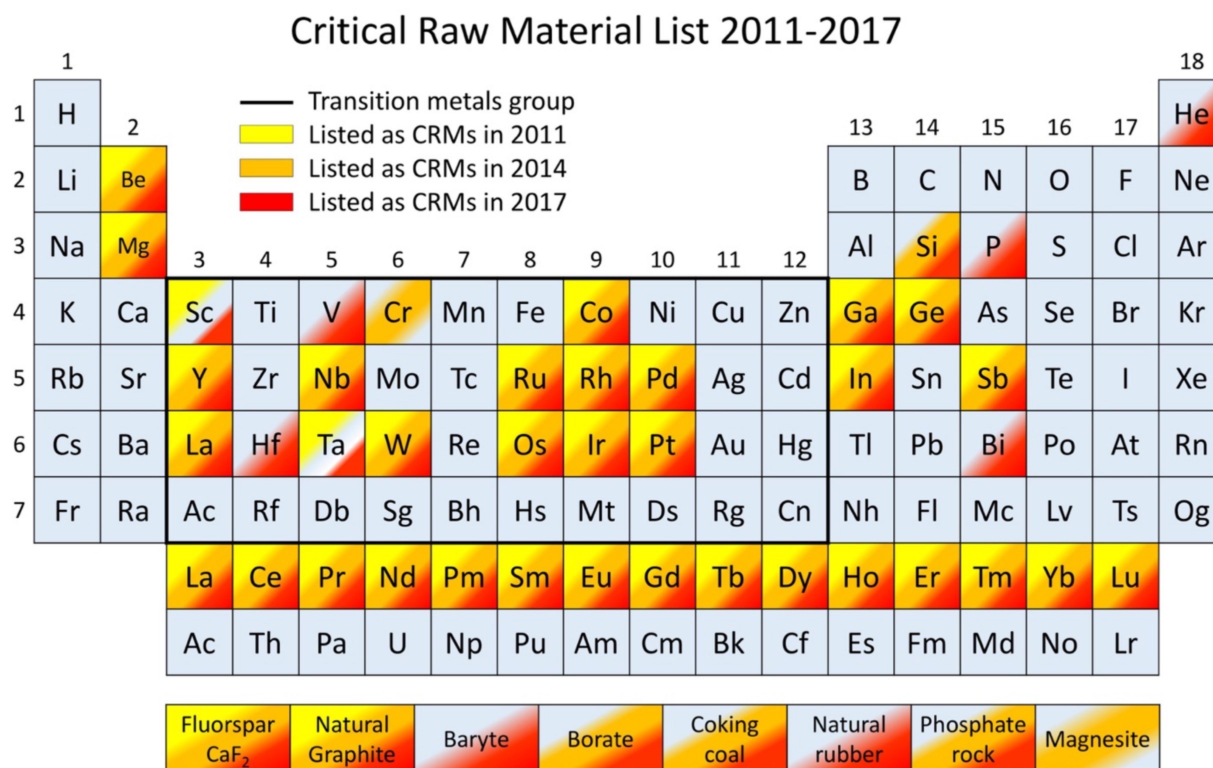

Fig. 6.2 - Critical raw materials list 2011-2017 overlaid on the periodic table of elements. Adapted from the published in [2].

Fig. 6.3 shows the data summarised from available public reports and papers [18–22,213,400–416] about the relation between mechanical properties of coatings and their wear performance as a comparison of the coated and uncoated tools lifetime. The first evaluated parameter of coatings that may characterise protective properties is hardness. It is seen in Fig. 6.3 that in most of the cases it correlates well with a lifetime of coated tools. The higher hardness of the coating, the longer service time it has. Nevertheless, hard materials often may be brittle and vulnerable to wear and failure [417]. The coating should maintain elasticity high enough to withstand the external forces and loads with no brakes. It is possible to evaluate and rank coating by the balance of hardness and elasticity by comparison of H/E ratio, which is quite broadly used nowadays to describe mechanical and protective features of materials. It characterises the resistance of the material to elastic deformation properties of coatings and describes some properties of coatings in terms of cracking or abrasive wear. It is experimentally recognised that H/E ranking can provide extremely close agreement to their ranking in terms of wear and, hence the lifetime of coatings [34,38,390,393,418,419].

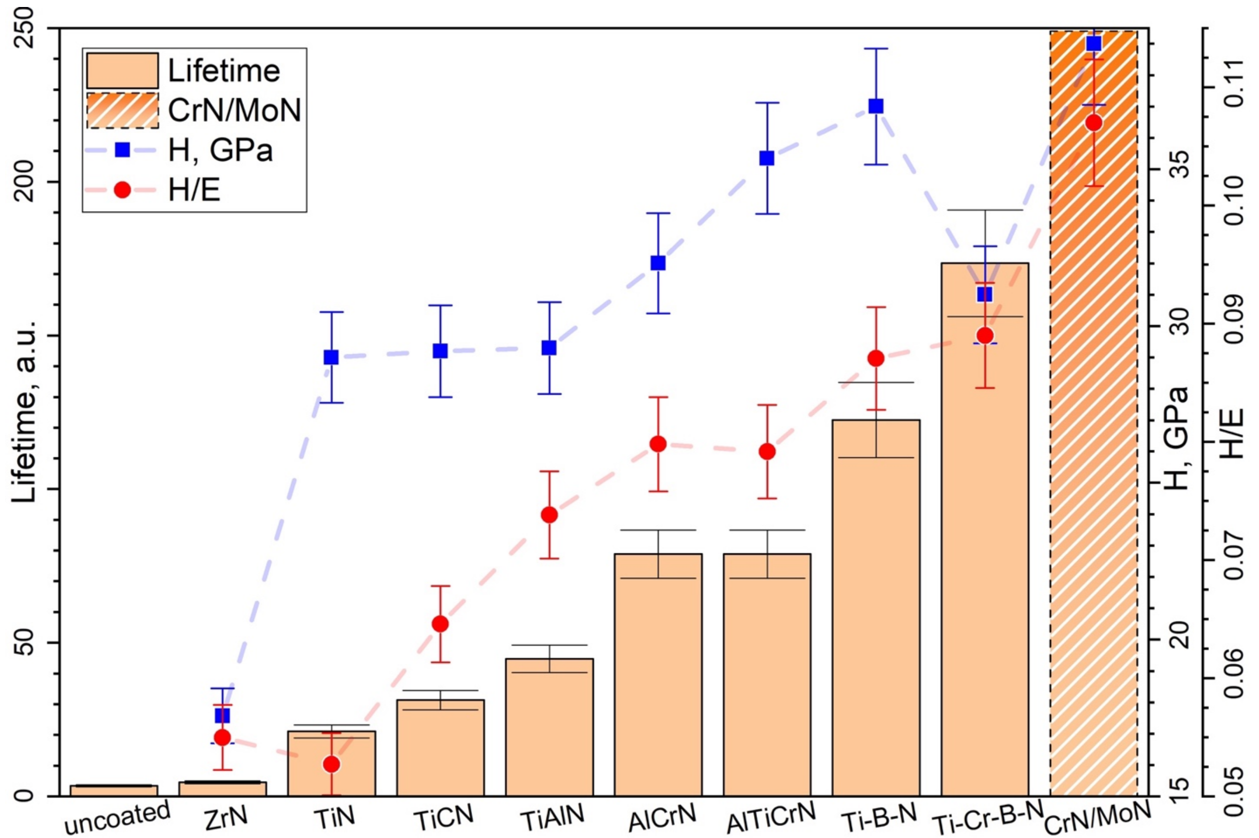

Fig. 6.3 - Lifetime comparison of uncoated steel tool, tools coated with ZrN, TiN, TiCN, TiAlN, AlCrN, AlTiCrN, Ti-B-N, Ti-Cr-B-N-T and CrN/MoN (estimated).

For hard coatings, it is desired to have the H/E ratio equal to or higher than 0.1, which is not a simple task for material science. A couple of hardness value and H/E ratio allow the relative estimation of the wear performance and lifetime of studied CrN/MoN coatings in comparison to others shown in Fig. 6.3. The highest hardness among considered coatings and significantly higher H/E ratio in the zone of the high elasticity give together the reason to assume that the resulting lifetime of tools coated with multilayer CrN/MoN film should be much longer than for the existing coatings presented in Fig. 6.3.

It means that with a long time of tool life, CrN/MoN coatings are the best option to be used as a protective coating and to reduce consumption of critical raw materials.

6.3. Future Work and Perspectives

Since studied CrN/MoN coatings were considered and proposed as protective ones for many industrial applications, it will be important that future research investigates in detail the behaviours of CrN/MoN coatings under extreme conditions of real operations. Thermal stability, oxidation and chemical resistance should be considered to collect new valuable data and expand the range of possible applications.

More detailed experimental study of tribological properties, wear performance and lifetime should be performed, in particular, at high temperatures or on real cutting tools and machine

parts. It would be interesting to benefit from the direct comparison of studied CrN/MoN protective coatings with uncoated samples and samples coated with existing competitive coatings.

Since CrN/MoN coatings for this PhD research were produced only by Arc-PVD method, similar CrN/MoN coatings fabricated by an alternative PVD technique, such as magnetron sputtering, should be studied and compared with Arc-PVD coatings.

Series of CrN/MoN coatings deposited at the substrate bias of −20 V exhibit the best mechanical properties and the increase of hardness when the individual layer thickness decreases. However, the value of individual layer thickness at which the hardness starts to decrease (some peak value) hasn't been reached yet. Thus, additional and useful information should be obtained from the research on CrN/MoN coatings with individual layers thinner than 20 nm and smaller grains of the films. It is expected that even higher values of hardness may be obtained before the hardness becomes to decrease in thinner individual layers with smaller grains of the material (so-called inverse Hall–Petch effect).

Multilayer coatings based on CrN and MoN layers may be considered in combination with introduced high-entropy alloy-based layers for further improvement of mechanical and tribological properties, thermal stability and wear performance under extreme conditions. Machine-learning approach should be applied at this step for the elemental composition screening, optimisation of resulted materials and prediction of physical and mechanical properties.

Future studies could fruitfully explore further functionalisation of CrN/MoN coatings. The possibility of introduction of additional layers or dopants of metallic antimicrobial agents, such as silver, gold and copper, should be considered for the potential production of antimicrobial coatings with enhanced wear resistance for frequently touched surfaces in health care facilities, ATMs, public transport and many others.

List of Publications

Several contributions were made to the scientific community during the PhD study, directly related to the research performed in the present Thesis, including 6 oral communications, 11 posters and the following publications:

1. **Bogdan Postolnyi**, João Pedro Araújo, Alexander Pogrebnjak, Applying of Electron Backscatter Diffraction (EBSD) for Studying Structural and Phase Composition of Multilayer CrN/MoN Coatings Fabricated by Arc-PVD, *Proceedings of the 16th European Microscopy Congress 2016*, Wiley Online Library, 2016, IM06-355, 6951.

2. **B.O. Postolnyi** and J.P. Araujo, Structural analysis of Arc-PVD multilayer metal nitride coatings CrN/MoN using electron backscatter diffraction (EBSD), *2016 International Conference on Nanomaterials: Application & Properties (NAP)*, 2016, 01NTF16-1-4 (IEEE Catalog).

3. **Bogdan Postolnyi**, Oleksandr Bondar, Marek Opielak, Przemysław Rogalski, João Pedro Araújo, Structural analysis of multilayer metal nitride films CrN/MoN using electron backscatter diffraction (EBSD), *Proc. SPIE 10010, Advanced Topics in Optoelectronics, Microelectronics, and Nanotechnologies VIII*, 2016, 100100E.

4. **B.O. Postolnyi**, O.V. Bondar, L. Rebouta, J.P. Araujo, Phase composition and crystallite size study of multilayered transition metal films based on molybdenum and chromium nitrides, in: *2017 IEEE 7th Int. Conf. Nanomater. Appl. Prop., IEEE*, 2017: 02NTF24-1-02NTF24-5.

5. **B.O. Postolnyi**, V.M. Beresnev, G. Abadias, O.V. Bondar, L. Rebouta, J.P. Araujo, A.D. Pogrebnjak, Multilayer design of CrN/MoN protective coatings for enhanced hardness and toughness, *Journal of Alloys and Compounds*, 2017, 725, 1188–1198.

6. A.D. Pogrebnjak, V.M. Beresnev, O.V. Bondar, **B.O. Postolnyi**, K. Zaleski, E. Coy, S. Jurga, M.O. Lisovenko, P. Konarski, L. Rebouta, J.P. Araujo, Superhard CrN/MoN coatings with multilayer architecture, *Materials & Design*, 2018, 153, 47–59.

7. **B.O. Postolnyi**, O.V. Bondar, K. Zaleski, E. Coy, S. Jurga, L. Rebouta, J.P. Araujo, Multilayer Design of CrN/MoN Superhard Protective Coatings and Their Characterisation, in: *A.D. Pogrebnjak, V. Novosad (Eds.), Advances in Thin Films, Nanostructured Materials, and Coatings*, Springer, Singapore, 2019: pp. 17–29.

8. A. Rizzo, S. Goel, M.L. Grilli, R. Iglesias, L. Jaworska, V. Lapkovskis, P. Novak, **B.O. Postolnyi**, D. Valerini, The Critical Raw Materials in Cutting Tools for Machining Applications: A Review, *Materials*, 2020, 13, 1377.

Moreover, additional researches and several collaborations also took places resulting in 15 poster presentations and the following publications:

1. A.D. Pogrebnjak, G. Abadias, O.V. Bondar, **B.O. Postolnyi**, M.O. Lisovenko, O.V. Kyrychenko, A.A. Andreev, V.M. Beresnev, D.A. Kolesnikov, M. Opielak, Structure and Properties of Multilayer Nanostructured Coatings TiN/MoN Depending on Deposition Conditions, *Acta Physica Polonica A*, 2014, 125 (6), 1280-1283.

2. A.D. Pogrebnjak, V.M. Beresnev, O.V. Bondar, G. Abadias, P. Chartier, **B.A. Postol'nyi**, A.A. Andreev, O.V. Sobol', The effect of nanolayer thickness on the structure and properties of multilayer TiN/MoN coatings, *Technical Physics Letters*, 2014, 40 (3), 215-218.

3. A.D. Pogrebnjak, O.V. Bondar, **B.O. Postolnyi**, D. Eyidi, G. Abadias, V.M. Beresnev, O.V. Sobol, Structure and Properties of Arc Evaporated Nanoscale TiN/MoN Multilayered Systems, *5th International Conference Radiation Interaction with Materials: Fundamentals and Applications 2014*. Kaunas: Technologija, 2014. ISSN 2351-583X, p. 21-24.

4. **B.O. Postolnyi**, P. Konarski, F.F. Komarov, O.V. Sobol', O.V. Kyrychenko, D.S. Shevchuk, Study of elemental and structural phase composition of multilayer nanostructured TiN/MoN coatings, their physical and mechanical properties, *Journal of Nano- and Electronic Physics*, 2014, 6 (4), 04016.

5. O.V. Bondar, A.P. Shypylenko, **B.O. Postolnyi**, O.V. Sobol, O. Maksakova, V.M. Beresnev, A.P. Kuzmenko, Y.A. Kravchenko, A.I. Kupchishin, Obtaining of Superhard (Zr-Ti-Cr-Nb)N Coatings and Their Research Using X-Ray Methods, *5th International Conference Radiation Interaction with Materials: Fundamentals And Applications 2014*. Kaunas: Technologija, 2014. ISSN 2351-583X, p. 354-357.

6. O.V. Bondar, **B.O. Postolnyi**, O.V. Sobol, V.M. Beresnev, Properties of Superhard (Zr-Ti-Cr-Nb)N Nanocoatings, *CriMiCo 2014 - 24th International Crimean Conference Microwave and Telecommunication Technology, Conference Proceedings*, 2014, 771-772.

7. **B.O. Postolnyi**, O.V. Bondar, Yu.A. Kravchenko, A.P. Shypylenko, O.V. Sobol, V.M. Beresnev, P. Wegierek, K. Smirnova, Ya. Kravchenko, Structure and Properties of Superhard (Zr-Ti-Cr-Nb)N Coatings, *Proceedings of the International Conference “Nanomaterials: Applications and Properties"*, 2014, 3 (1), 01FNC06(3pp).

8. V.M. Beresnev, O.V. Bondar, **B.O. Postolnyi**, M.O. Lisovenko, G. Abadias, P.C. Chartier, D.A. Kolesnikov, V.N. Borisyuk, B.A. Mukushev, B.R. Zhollybekov, A.A. Andreev, Comparison of tribological characteristics of nanostructured TiN, MoN, and TiN/MoN Arc-PVD coatings, *Journal of Friction and Wear*, 2014, 35 (5), 374-382.

9. Volodymyr Ivashchenko, Stan Veprek, Alexander Pogrebnjak and **Bogdan Postolnyi**, First-principles quantum molecular dynamics study of $Ti_xZr_{1-x}N(111)/SiN_y$ heterostructures and comparison with experimental results, *Science and Technology of Advanced Materials*, 2014, 15, 025007.

10. O.V. Bondar, **B.A. Postol'nyi**, V.M. Beresnev, G. Abadias, P. Chartier, O.V. Sobol, D.A. Kolesnikov, F.F. Komarov, M.O. Lisovenko, A.A. Andreev, Composition, structure and tribotechnical properties of TiN, MoN single-layer and TiN/MoN multilayer coatings, *Journal of Superhard Materials*, 2015, 37 (1), 27-38.

11. A.D. Pogrebnjak, **B.A. Postol'nyi**, Y.A. Kravchenko, A.P. Shipilenko, O.V. Sobol', V.M. Beresnev, A.P. Kuz'menko, Structure and properties of (Zr-Ti-Cr-Nb)N multielement superhard coatings, *Journal of Superhard Materials*, 2015, 37 (2), 101-111.

12. O.V. Bondar, **B.O. Postolnyi**, Yu.A. Kravchenko, A.P. Shypylenko, O.V. Sobol, V.M. Beresnev, A.P. Kuzmenko and P. Zukowski, Fabrication and Research of Superhard (Zr-Ti-Cr-Nb)N Coatings, *Acta Physica Polonica A*, 2015, 128 (5), 867.

13. A.D. Pogrebnjak, O.V. Bondar, G. Abadias, D. Eyidi, V.M. Beresnev, O.V. Sobol, **B.O. Postolnyi** and P. Zukowski, Investigation of Nanoscale TiN/MoN Multilayered Systems, Fabricated Using Arc Evaporation, *Acta Physica Polonica A*, 2015, 128 (5), 836.

14. **B.O. Postolnyi**, G. Abadias, A.D. Pogrebnjak, Joao Pedro Araujo, Luis Rebouta, Marek Opielak, Konrad Kierczyński, Preliminary attempts of multilayer (Ti,Al)N/(Si,Al)N coatings deposition and study, *11-th International Conference ION Implantation and Other Applications of IONS and Elektrons - ION 2016*, 2016, 56.

15. O.V. Bondar, M.O. Lisovenko, K.O. Belovol, **B.O. Postolnyi**, E. Coy, K. Zaleski, P. Zukowski, B.O. Postolnyi, P. Konarski, Structure and elemental composition of multilayered nanocomposite TiN/ZrN coatings before and after annealing in air, in: *2017 IEEE 7th Int. Conf. Nanomater. Appl. Prop., IEEE*, 2017: p. 02NTF04-1-02NTF04-4.

16. A. Pogrebnjak, V. Ivashchenko, O. Bondar, V. Beresnev, O. Sobol, K. Załęski, S. Jurga, E. Coy, P. Konarski, **B. Postolnyi**, Multilayered vacuum-arc nanocomposite TiN/ZrN coatings before and after annealing: Structure, properties, first-principles calculations, *Materials Characterization*, 2017, 134 55–63.

17. O.V. Bondar, A.D. Pogrebnjak, Y. Takeda, **B. Postolnyi**, P. Zukowski, R. Sakenova, V. Beresnev, V. Stolbovoy, Structure and Properties of Combined Multilayer Coatings Based on Alternative Triple Nitride and Binary Metallic Layers, in: *A.D. Pogrebnjak, V. Novosad (Eds.), Advances in Thin Films, Nanostructured Materials, and Coatings*, Springer, Singapore, 2019: pp. 31–40.

18. O.V. Maksakova, R.F. Webster, R.D. Tilley, V.I. Ivashchenko, **B.O. Postolnyi**, O.V. Bondar, Y. Takeda, V.M. Rogoz, R.E. Sakenova, P.V. Zukowski, M. Opielak, V.M. Beresnev, A.D. Pogrebnjak, Nanoscale Architecture of (CrN/ZrN)/(Cr/Zr) Nanocomposite Coatings: Microstructure, Composition, Mechanical Properties and First-principles Calculations, *Journal of Alloys and Compounds*, 2020, 831, 154808.

References

[1] Bobzin K. High-performance coatings for cutting tools. CIRP J Manuf Sci Technol 2017;18:1–9. doi:10.1016/j.cirpj.2016.11.004.

[2] Rizzo A, Goel S, Grilli ML, Iglesias R, Jaworska L, Lapkovskis V, et al. The Critical Raw Materials in Cutting Tools for Machining Applications: A Review. Materials (Basel) 2020;13:1377. doi:10.3390/ma13061377.

[3] European Commission, Deloitte Sustainability, British Geological Survey, Bureau de Recherches Géologiques et Minières, Netherlands Organisation for Applied Scientific Research. European Commission Final Report: Study on the review of the list of critical raw materials. Brussels: 2017. doi:10.2873/876644.

[4] Commission of the European Communities. The raw materials initiative: meeting our critical needs for growth and jobs in Europe. Brussels: 2008.

[5] European Commission. Communication from the Commission to the European Parliament, the Council, the European Economic and Social Committee and the Committee of the Regions: Tackling the Challenges in Commodity Markets and on Raw Materials. Brussels: 2011.

[6] European Commission. Communication from the Commission to the European Parliament, the Council, the European Economic and Social Committee and the Committee of the Regions: On the Review of the List of Critical Raw Materials for the EU and the Implementation of the Raw Materi 2014. https://eur-lex.europa.eu/legal-content/EN/TXT/?uri=CELEX:52014DC0297.

[7] European Commission. Communication from the Commission to the European Parliament, the Council, the European Economic and Social Committee and the Committee of the Regions on the 2017 list of Critical Raw Materials for the EU. Brussels: 2017.

[8] European Commission. Report on Critical Raw Materials and the Circular Economy. 2018.

[9] Pogrebnjak AD, Bagdasaryan AA, Pshyk A, Dyadyura K. Adaptive multicomponent nanocomposite coatings in surface engineering. Physics-Uspekhi 2017;60:586–607. doi:10.3367/UFNe.2016.12.038018.

[10] Bondar OV, Postolnyi BO, Kravchenko YA, Shypylenko AP, Sobol OV, Beresnev VM, et al. Fabrication and Research of Superhard (Zr-Ti-Cr-Nb)N Coatings. Acta Phys Pol A 2015;128:867–71. doi:10.12693/APhysPolA.128.867.

[11] Postolnyi BO, Konarski P, Komarov FF, Sobol' O V., Kyrychenko O V., Shevchuk DS. Study of elemental and structural phase composition of multilayer nanostructured TiN / MoN coatings, their physical and mechanical properties. J Nano- Electron Phys 2014;6:04016.

[12] Pogrebnjak AD, Bondar OV, Abadias G, Eyidi D, Beresnev VM, Sobol OV, et al. Investigation of Nanoscale TiN/MoN Multilayered Systems, Fabricated Using Arc

Evaporation. Acta Phys Pol A 2015;128:836–41. doi:10.12693/APhysPolA.128.836.

[13] Pogrebnyak AD, Kylyshkanov MK, Tyurin YN, Kaverina AS, Yakushchenko I V., Borisenko AA, et al. Properties and structure of oxidized coatings deposited onto Al-Cu and Al-Mg alloys. Tech Phys 2012;57:840–8. doi:10.1134/S1063784212060217.

[14] Pogrebnjak AD, Postol'nyi BA, Kravchenko YA, Shipilenko AP, Sobol' O V., Beresnev VM, et al. Structure and properties of (Zr-Ti-Cr-Nb)N multielement superhard coatings. J Superhard Mater 2015;37:101–11. doi:10.3103/S1063457615020045.

[15] Pogrebnjak AD, Bagdasaryan AA, Beresnev VM, Kupchishin AI, Plotnikov S V., Kravchenko YO. Microstructure and Tribological Properties of Nitride Coatings Based on Zr, Ti, Cr, Nb, And Si Elements. High Temp Mater Process An Int Q High-Technology Plasma Process 2017;21:261–75. doi:10.1615/HighTempMatProc.2018025607.

[16] Pogrebnjak AD, Bondar O V., Abadias G, Ivashchenko V, Sobol O V., Jurga S, et al. Structural and mechanical properties of NbN and Nb-Si-N films: Experiment and molecular dynamics simulations. Ceram Int 2016;42:11743–56. doi:10.1016/j.ceramint.2016.04.095.

[17] Bagdasaryan AA, Pshyk AV, Coy LE, Konarski P, Misnik M, Ivashchenko VI, et al. A new type of (TiZrNbTaHf)N/MoN nanocomposite coating: Microstructure and properties depending on energy of incident ions. Compos Part B Eng 2018;146:132–44. doi:10.1016/j.compositesb.2018.04.015.

[18] Klocke F, Krieg T. Coated Tools for Metal Cutting – Features and Applications. CIRP Ann 1999;48:515–25. doi:10.1016/S0007-8506(07)63231-4.

[19] Vereschaka A, Kataeva E, Sitnikov N, Aksenenko A, Oganyan G, Sotova C. Influence of Thickness of Multilayered Nano-Structured Coatings Ti-TiN-(TiCrAl)N and Zr-ZrN-(ZrCrNbAl)N on Tool Life of Metal Cutting Tools at Various Cutting Speeds. Coatings 2018;8:44. doi:10.3390/coatings8010044.

[20] Levashov EA, Merzhanov AG, Shtanskv DV. Advanced technologies, materials and coatings developed in scientific-educational center of SHS. Galvanotechnik 2009;100:2102–14.

[21] Gu J, Barber G, Tung S, Gu R-J. Tool life and wear mechanism of uncoated and coated milling inserts. Wear 1999;225–229:273–84. doi:10.1016/S0043-1648(99)00074-5.

[22] Vereschaka AA, Grigoriev SN, Sitnikov NN, Oganyan G V., Batako A. Working efficiency of cutting tools with multilayer nano-structured Ti-TiCN-(Ti,Al)CN and Ti-TiCN-(Ti,Al,Cr)CN coatings: Analysis of cutting properties, wear mechanism and diffusion processes. Surf Coatings Technol 2017;332:198–213. doi:10.1016/j.surfcoat.2017.10.027.

[23] Tamerabet Y, Brioua M, Tamerabet M, Khoualdi S. Experimental Investigation on Tool Wear Behavior and Cutting Temperature during Dry Machining of Carbon Steel SAE 1030 Using KC810 and KC910 Coated Inserts. Tribol Ind 2018;40:52–65. doi:10.24874/ti.2018.40.01.04.

[24] Tabor D. The Hardness of Metals. Oxford University Press; 2000.

[25] Kariper IA. Hardness of Thin Films and the Influential Factors. Diam. Carbon Compos. Nanocomposites, InTech; 2016, p. 1–19. doi:10.5772/63302.

[26] Veprek S. Recent search for new superhard materials: Go nano! J Vac Sci Technol A Vacuum, Surfaces, Film 2013;31:050822. doi:10.1116/1.4818590.

[27] Bhaduri A. Hardness. Mech. Prop. Work. Met. Alloy., Singapore: Springer Singapore; 2018, p. 119–71. doi:10.1007/978-981-10-7209-3_3.

[28] Musil J. Hard and superhard nanocomposite coatings. Surf Coatings Technol 2000;125:322–30. doi:10.1016/S0257-8972(99)00586-1.

[29] Veprek S, Veprek-Heijman MGJ. Superhard and Ultrahard Nanostructured Materials and Coatings. Microstruct. Correl. Hard, Superhard, Ultrahard Mater., Cham: Springer International Publishing; 2016, p. 167–210. doi:10.1007/978-3-319-29291-5_6.

[30] Jhi S-H, Ihm J, Louie SG, Cohen ML. Electronic mechanism of hardness enhancement in transition-metal carbonitrides. Nature 1999;399:132–4. doi:10.1038/20148.

[31] Li D, Kaner RB. MATERIALS SCIENCE: Graphene-Based Materials. Science 2008;320:1170–1. doi:10.1126/science.1158180.

[32] Vepřek S. The search for novel, superhard materials. J Vac Sci Technol A Vacuum, Surfaces, Film 1999;17:2401–20. doi:10.1116/1.581977.

[33] Tushinsky LI, Kovensky I, Plokhov A, Sindeyev V, Reshedko P. Mechanical Properties of Coatings, 2002, p. 85–131. doi:10.1007/978-3-662-06276-0_2.

[34] Leyland A, Matthews A. On the significance of the H/E ratio in wear control: a nanocomposite coating approach to optimised tribological behaviour. Wear 2000;246:1–11. doi:10.1016/S0043-1648(00)00488-9.

[35] Musil J, Kunc F, Zeman H, Poláková H. Relationships between hardness, Young's modulus and elastic recovery in hard nanocomposite coatings. Surf Coatings Technol 2002;154:304–13. doi:10.1016/S0257-8972(01)01714-5.

[36] Musil J, Jirout M. Toughness of hard nanostructured ceramic thin films. Surf Coatings Technol 2007;201:5148–52. doi:10.1016/j.surfcoat.2006.07.020.

[37] Leyland A, Matthews A. Design criteria for wear-resistant nanostructured and glassy-metal coatings. Surf Coatings Technol 2004;177–178:317–24. doi:10.1016/j.surfcoat.2003.09.011.

[38] Musil J. Hard nanocomposite coatings: Thermal stability, oxidation resistance and toughness. Surf Coatings Technol 2012;207:50–65. doi:10.1016/j.surfcoat.2012.05.073.

[39] Guo J, Wang H, Meng F, Liu X, Huang F. Tuning the H/E* ratio and E* of AlN coatings by copper addition. Surf Coatings Technol 2013;228:68–75. doi:10.1016/j.surfcoat.2013.04.008.

[40] Liu Z, Li H, Li J, Huang J, Kong J, Xiong D. Tribological Properties Improvement of Mo-

Alloyed HfN Films With a High H/E Ratio at Elevated Temperatures. J Tribol 2021;143. doi:10.1115/1.4047583.

[41] Kim H-K, La J-H, Kim K-S, Lee S-Y. The effects of the H/E ratio of various Cr–N interlayers on the adhesion strength of CrZrN coatings on tungsten carbide substrates. Surf Coatings Technol 2015;284:230–4. doi:10.1016/j.surfcoat.2015.06.077.

[42] Lackner J, Major L, Kot M. Microscale interpretation of tribological phenomena in Ti/TiN soft-hard multilayer coatings on soft austenite steel substrates. Bull Polish Acad Sci Tech Sci 2011;59:343–55. doi:10.2478/v10175-011-0042-x.

[43] Tsui TY, Pharr GM, Oliver WC, Bhatia CS, White RL, Anders S, et al. Nanoindentation and Nanoscratching of Hard Carbon Coatings for Magnetic Disks. MRS Proc 1995;383:447–52. doi:10.1557/PROC-383-447.

[44] Pintaude G. Introduction of the Ratio of the Hardness to the Reduced Elastic Modulus for Abrasion. Tribol. - Fundam. Adv., InTech; 2013. doi:10.5772/55470.

[45] Finkin EF. Examination of Abrasion Resistance Criteria for Some Ductile Metals. J Lubr Technol 1974;96:210–4. doi:10.1115/1.3451924.

[46] Joslin DL, Oliver WC. A new method for analyzing data from continuous depth-sensing microindentation tests. J Mater Res 1990;5:123–6. doi:10.1557/JMR.1990.0123.

[47] Chen X, Du Y, Chung Y-W. Commentary on using H/E and H/E as proxies for fracture toughness of hard coatings. Thin Solid Films 2019;688:137265. doi:10.1016/j.tsf.2019.04.040.

[48] Holleck H. Material selection for hard coatings. J Vac Sci Technol A Vacuum, Surfaces, Film 1986;4:2661–9. doi:10.1116/1.573700.

[49] Mattox DM. Adhesion and Deadhesion. Handb. Phys. Vap. Depos. Process., Elsevier; 2010, p. 439–74. doi:10.1016/B978-0-8155-2037-5.00012-5.

[50] Mellali M, Fauchais P, Grimaud A. Influence of substrate roughness and temperature on the adhesion/cohesion of alumina coatings. Surf Coatings Technol 1996;81:275–86. doi:10.1016/0257-8972(95)02540-5.

[51] Zheng L, Ramalingam S. Stresses in a coated solid due to shear and normal boundary tractions. J Vac Sci Technol A Vacuum, Surfaces, Film 1995;13:2390–8. doi:10.1116/1.579479.

[52] Du J, Tittmann BR, Ju HS. Evaluation of film adhesion to substrates by means of surface acoustic wave dispersion. Thin Solid Films 2010;518:5786–95. doi:10.1016/j.tsf.2010.05.086.

[53] Passeri D, Bettucci A, Rossi M. Acoustics and atomic force microscopy for the mechanical characterization of thin films. Anal Bioanal Chem 2010;396:2769–83. doi:10.1007/s00216-009-3402-8.

[54] Majumdar A, Carrejo JP, Lai J. Thermal imaging using the atomic force microscope. Appl

Phys Lett 1993;62:2501–3. doi:10.1063/1.109335.

[55] Roy M. Protective Hard Coatings for Tribological Applications. Mater. Under Extrem. Cond., Elsevier; 2017, p. 259–92. doi:10.1016/B978-0-12-801300-7.00008-5.

[56] Musil J. Advanced Hard Coatings with Enhanced Toughness and Resistance to Cracking. In: Zhang S, editor. Thin Film. Coatings, CRC Press; 2015, p. 377–463. doi:10.1201/b18729.

[57] Musil J, Jaroš M, Kos Š. Superhard metallic coatings. Mater Lett 2019;247:32–5. doi:10.1016/j.matlet.2019.03.086.

[58] Veprek S, Veprek-Heijman MGJ, Karvankova P, Prochazka J. Different approaches to superhard coatings and nanocomposites. Thin Solid Films 2005;476:1–29. doi:10.1016/j.tsf.2004.10.053.

[59] Pogrebnyak AD, Shpak AP, Azarenkov NA, Beresnev VM. Structures and properties of hard and superhard nanocomposite coatings. Physics-Uspekhi 2009;52:29–54. doi:10.3367/UFNe.0179.200901b.0035.

[60] Lu C, Mai Y-W, Shen Y-G. Recent advances on understanding the origin of superhardness in nanocomposite coatings: A critical review. J Mater Sci 2006;41:937–50. doi:10.1007/s10853-006-6577-9.

[61] Wang YX, Zhang S. Toward hard yet tough ceramic coatings. Surf Coatings Technol 2014;258:1–16. doi:10.1016/j.surfcoat.2014.07.007.

[62] Polini R, Barletta M, Rubino G, Vesco S. Recent Advances in the Deposition of Diamond Coatings on Co-Cemented Tungsten Carbides. Adv Mater Sci Eng 2012;2012:1–14. doi:10.1155/2012/151629.

[63] Kuo C, Wang C, Ko S. Wear behaviour of CVD diamond-coated tools in the drilling of woven CFRP composites. Wear 2018;398–399:1–12. doi:10.1016/j.wear.2017.11.015.

[64] Ramasubramanian K, Arunachalam N, Ramachandra Rao MS. Wear performance of nano-engineered boron doped graded layer CVD diamond coated cutting tool for machining of Al-SiC MMC. Wear 2019;426–427:1536–47. doi:10.1016/j.wear.2018.12.004.

[65] Poulon-Quintin A, Faure C, Teulé-Gay L, Manaud JP. A multilayer innovative solution to improve the adhesion of nanocrystalline diamond coatings. Appl Surf Sci 2015;331:27–34. doi:10.1016/j.apsusc.2015.01.050.

[66] Linnik SA, Gaydaychuk AV, Okhotnikov VV. Improvement to the adhesion of polycrystalline diamond films on WC-Co cemented carbides through ion etching of loosely bound growth centers. Surf Coatings Technol 2018;334:227–32. doi:10.1016/j.surfcoat.2017.11.043.

[67] Ye F, Li Y, Sun X, Yang Q, Kim C-Y, Odeshi AG. CVD diamond coating on WC-Co substrate with Al-based interlayer. Surf Coatings Technol 2016;308:121–7. doi:10.1016/j.surfcoat.2016.06.088.

[68] Wang T, Zhang S, Jiang C, Handschuh-Wang S, Chen G, Zhou X, et al. TiB 2 barrier interlayer approach for HFCVD diamond deposition onto cemented carbide tools. Diam Relat Mater 2018;83:126–33. doi:10.1016/j.diamond.2018.01.020.

[69] Chandran M, Sammler F, Uhlmann E, Akhvlediani R, Hoffman A. Wear performance of diamond coated WC-Co tools with a CrN interlayer. Diam Relat Mater 2017;73:47–55. doi:10.1016/j.diamond.2016.12.001.

[70] Al Mahmud KAH, Kalam MA, Masjuki HH, Mobarak HM, Zulkifli NWM. An updated overview of diamond-like carbon coating in tribology. Crit Rev Solid State Mater Sci 2015;40:90–118. doi:10.1080/10408436.2014.940441.

[71] Fukui H, Okida J, Omori N, Moriguchi H, Tsuda K. Cutting performance of DLC coated tools in dry machining aluminum alloys. Surf Coatings Technol 2004;187:70–6. doi:10.1016/j.surfcoat.2004.01.014.

[72] Erdemir A, Donnet C. Tribology of diamond-like carbon films: recent progress and future prospects. J Phys D Appl Phys 2006;39:R311–27. doi:10.1088/0022-3727/39/18/R01.

[73] Huang L, Yuan J, Li C, Hong D. Microstructure, tribological and cutting performance of Ti-DLC/α-C:H multilayer film on cemented carbide. Surf Coatings Technol 2018;353:163–70. doi:10.1016/j.surfcoat.2018.08.076.

[74] Liu Y, Meletis EI. Evidence of graphitization of diamond-like carbon films during sliding wear. J Mater Sci 1997;32:3491–5. doi:10.1023/A:1018641304944.

[75] Chen JG. Carbide and Nitride Overlayers on Early Transition Metal Surfaces: Preparation, Characterization, and Reactivities. Chem Rev 1996;96:1477–98. doi:10.1021/cr950232u.

[76] Han Y, Dai Y, Shu D, Wang J, Sun B. Electronic and bonding properties of TiB2. J Alloys Compd 2007;438:327–31. doi:10.1016/j.jallcom.2006.08.056.

[77] Rasaki SA, Zhang B, Anbalgam K, Thomas T, Yang M. Synthesis and application of nano-structured metal nitrides and carbides: A review. Prog Solid State Chem 2018;50:1–15. doi:10.1016/j.progsolidstchem.2018.05.001.

[78] Shizhi L, Yulong S, Hongrui P. Ti-Si-N films prepared by plasma-enhanced chemical vapor deposition. Plasma Chem Plasma Process 1992;12:287–97. doi:10.1007/BF01447027.

[79] Vepřek S, Haussmann M, Reiprich S, Shizhi L, Dian J. Novel thermodynamically stable and oxidation resistant superhard coating materials. Surf Coatings Technol 1996;86–87:394–401. doi:10.1016/S0257-8972(96)02988-X.

[80] Mayrhofer PH, Rachbauer R, Holec D, Rovere F, Schneider JM. Protective Transition Metal Nitride Coatings. Compr. Mater. Process., Elsevier; 2014, p. 355–88. doi:10.1016/B978-0-08-096532-1.00423-4.

[81] Kalss W, Reiter A, Derflinger V, Gey C, Endrino JL. Modern coatings in high performance cutting applications. Int J Refract Met Hard Mater 2006;24:399–404. doi:10.1016/j.ijrmhm.2005.11.005.

[82] Fernandes F, Danek M, Polcar T, Cavaleiro A. Tribological and cutting performance of TiAlCrN films with different Cr contents deposited with multilayered structure. Tribol Int 2018;119:345–53. doi:10.1016/j.triboint.2017.11.008.

[83] Danek M, Fernandes F, Cavaleiro A, Polcar T. Influence of Cr additions on the structure and oxidation resistance of multilayered TiAlCrN films. Surf Coatings Technol 2017;313:158–67. doi:10.1016/j.surfcoat.2017.01.053.

[84] Mi P, He J, Qin Y, Chen K. Nanostructure reactive plasma sprayed TiCN coating. Surf Coatings Technol 2017;309:1–5. doi:10.1016/j.surfcoat.2016.11.033.

[85] Sampath Kumar T, Vinoth Jebaraj A, Sivakumar K, Shankar E, Tamiloli N. Characterization of TiCN Coating Synthesized by the Plasma Enhanced Physical Vapour Deposition Process on a Cemented Carbide Tool. Surf Rev Lett 2018;25:1950028. doi:10.1142/S0218625X19500288.

[86] Kong Y, Tian X, Gong C, Chu PK. Enhancement of toughness and wear resistance by CrN/CrCN multilayered coatings for wood processing. Surf Coatings Technol 2018;344:204–13. doi:10.1016/j.surfcoat.2018.03.027.

[87] Myśliński P, Szparaga Ł, Gilewicz A, Mydłowska K, Piątkowska A. Investigations of the thermo-mechanical stability of hybrid layers for tribological applications: Nitrided layer/CrCN coating system. Vacuum 2018;148:276–85. doi:10.1016/j.vacuum.2017.11.037.

[88] Zhang J, Su X, Shan L, Liu Y, Zhang P, Jia Y. Preparation and tribocorrosion performance of CrCN coatings in artificial seawater on different substrates with different bias voltages. Ceram Int 2019;45:9901–11. doi:10.1016/j.ceramint.2019.02.031.

[89] Lorenzo-Martin C, Ajayi O, Erdemir A, Wei R. Tribological performance of quaternary CrSiCN coatings under dry and lubricated conditions. Wear 2017;376–377:1682–90. doi:10.1016/j.wear.2017.01.109.

[90] Lin J, Jang J, Park I-W, Wei R. Structure and properties of CrSiCN coatings deposited by pulsed dc magnetron sputtering for wear and erosion protection. Surf Coatings Technol 2016;287:44–54. doi:10.1016/j.surfcoat.2015.12.068.

[91] Wang Q, Zhou F, Zhu L, Zhang M, Kong J. Mechanical and tribological evaluation of CrSiCN, CrBCN and CrSiBCN coatings. Tribol Int 2019;130:146–54. doi:10.1016/j.triboint.2018.09.025.

[92] Piedrahita WF, Aperador W, Caicedo JC, Prieto P. Evolution of physical properties in hafnium carbonitride thin films. J Alloys Compd 2017;690:485–96. doi:10.1016/j.jallcom.2016.08.109.

[93] Chicco B, Borbidge W., Summerville E. Experimental study of vanadium carbide and carbonitride coatings. Mater Sci Eng A 1999;266:62–72. doi:10.1016/S0921-5093(99)00035-0.

[94] Greer AL. Confusion by design. Nature 1993;366:303–4. doi:10.1038/366303a0.

[95] Yeh J-W, Chen S-K, Lin S-J, Gan J-Y, Chin T-S, Shun T-T, et al. Nanostructured High-Entropy Alloys with Multiple Principal Elements: Novel Alloy Design Concepts and Outcomes. Adv Eng Mater 2004;6:299–303. doi:10.1002/adem.200300567.

[96] Cantor B, Chang ITH, Knight P, Vincent AJB. Microstructural development in equiatomic multicomponent alloys. Mater Sci Eng A 2004;375–377:213–8. doi:10.1016/j.msea.2003.10.257.

[97] Yeh J-W. Recent progress in high-entropy alloys. Ann Chim Sci Des Matériaux 2006;31:633–48. doi:10.3166/acsm.31.633-648.

[98] Miracle DB, Senkov ON. A critical review of high entropy alloys and related concepts. Acta Mater 2017;122:448–511. doi:10.1016/j.actamat.2016.08.081.

[99] Rech J, Battaglia JL, Moisan A. Thermal influence of cutting tool coatings. J Mater Process Technol 2005;159:119–24. doi:10.1016/j.jmatprotec.2004.04.414.

[100] Du F, Lovell MR, Wu TW. Boundary element method analysis of temperature fields in coated cutting tools. Int J Solids Struct 2001;38:4557–70. doi:10.1016/S0020-7683(00)00291-2.

[101] Rech J, Kusiak A, Battaglia J. Tribological and thermal functions of cutting tool coatings. Surf Coatings Technol 2004;186:364–71. doi:10.1016/j.surfcoat.2003.11.027.

[102] Shalaby MA, Veldhuis SC. Wear and Tribological Performance of Different Ceramic Tools in Dry High Speed Machining of Ni-Co-Cr Precipitation Hardenable Aerospace Superalloy. Tribol Trans 2019;62:62–77. doi:10.1080/10402004.2018.1486494.

[103] Song W, Wang Z, Deng J, Zhou K, Wang S, Guo Z. Cutting temperature analysis and experiment of Ti–MoS2/Zr-coated cemented carbide tool. Int J Adv Manuf Technol 2017;93:799–809. doi:10.1007/s00170-017-0509-5.

[104] Gengler JJ, Hu J, Jones JG, Voevodin AA, Steidl P, Vlček J. Thermal conductivity of high-temperature Si–B–C–N thin films. Surf Coatings Technol 2011;206:2030–3. doi:10.1016/j.surfcoat.2011.07.058.

[105] Yip S. The strongest size. Nature 1998;391:532–3. doi:10.1038/35254.

[106] Uhlmann E, Oyanedel Fuentes JA, Gerstenberger R, Frank H. nc-AlTiN/a-Si3N4 and nc-AlCrN/a-Si3N4 nanocomposite coatings as protection layer for PCBN tools in hard machining. Surf Coatings Technol 2013;237:142–8. doi:10.1016/j.surfcoat.2013.09.017.

[107] Ma Q, Li L, Xu Y, Gu J, Wang L, Xu Y. Effect of bias voltage on TiAlSiN nanocomposite coatings deposited by HiPIMS. Appl Surf Sci 2017;392:826–33. doi:10.1016/j.apsusc.2016.09.028.

[108] Settineri L, Faga MG. Laboratory tests for performance evaluation of nanocomposite coatings for cutting tools. Wear 2006;260:326–32. doi:10.1016/j.wear.2005.04.025.

[109] Abadias G, Daniliuk AY, Solodukhin IA, Uglov V V., Zlotsky S V. Thermal Stability of

TiZrAlN and TiZrSiN Films Formed by Reactive Magnetron Sputtering. Inorg Mater Appl Res 2018;9:418–26. doi:10.1134/S2075113318030024.

[110] Musil J, Novák P, Čerstvý R, Soukup Z. Tribological and mechanical properties of nanocrystalline-TiC/a-C nanocomposite thin films. J Vac Sci Technol A Vacuum, Surfaces, Film 2010;28:244–9. doi:10.1116/1.3294717.

[111] El Mel AA, Gautron E, Christien F, Angleraud B, Granier A, Souček P, et al. Titanium carbide/carbon nanocomposite hard coatings: A comparative study between various chemical analysis tools. Surf Coatings Technol 2014;256:41–6. doi:10.1016/j.surfcoat.2013.12.068.

[112] Qiu L, Du Y, Wang S, Li K, Yin L, Wu L, et al. Mechanical properties and oxidation resistance of chemically vapor deposited TiSiN nanocomposite coating with thermodynamically designed compositions. Int J Refract Met Hard Mater 2019;80:30–9. doi:10.1016/j.ijrmhm.2018.12.018.

[113] Schwaller P, Haug F-J, Michler J, Patscheider J. Nanocomposite Hard Coatings: Deposition Issues and Validation of their Mechanical Properties. Adv Eng Mater 2005;7:318–22. doi:10.1002/adem.200500045.

[114] Mahato P, Nyati G, Singh RJ, Mishra SK. Nanocomposite TiSiBC Hard Coatings with High Resistance to Wear, Fracture and Scratching. J Mater Eng Perform 2016;25:3774–82. doi:10.1007/s11665-016-2239-5.

[115] Verma D, Banerjee D, Mishra SK. Effect of Silicon Content on the Microstructure and Mechanical Properties of Ti-Si-B-C Nanocomposite Hard Coatings. Metall Mater Trans A 2019;50:894–904. doi:10.1007/s11661-018-5028-y.

[116] Mahato P, Singh RJ, Mishra SK. Nanocomposite Ti–Si–B–C hard coatings deposited by magnetron sputtering: Oxidation and mechanical behaviour with temperature and duration of oxidation. Surf Coatings Technol 2016;288:230–40. doi:10.1016/j.surfcoat.2016.01.039.

[117] Mahato P, Singh RJ, Pathak LC, Mishra SK. Effect of nitrogen on mechanical, oxidation and structural behaviour of Ti-Si-B-C-N nanocomposite hard coatings deposited by DC sputtering. Surf Interface Anal 2016;48:1080–9. doi:10.1002/sia.6030.

[118] Yi J, Chen S, Chen K, Xu Y, Chen Q, Zhu C, et al. Effects of Ni content on microstructure, mechanical properties and Inconel 718 cutting performance of AlTiN-Ni nanocomposite coatings. Ceram Int 2019;45:474–80. doi:10.1016/j.ceramint.2018.09.192.

[119] Saladukhin IA, Abadias G, Uglov VV, Zlotski SV, Michel A, Janse van Vuuren A. Thermal stability and oxidation resistance of ZrSiN nanocomposite and ZrN/SiNx multilayered coatings: A comparative study. Surf Coatings Technol 2017;332:428–39. doi:10.1016/j.surfcoat.2017.08.076.

[120] Anwar S, Islam A, Bajpai S, Anwar S. Structural and mechanical studies of W2N embedded Si3N4 nanocomposite hard coating prepared by reactive magnetron sputtering. Surf

Coatings Technol 2017;311:268–73. doi:10.1016/j.surfcoat.2016.12.119.

[121] Gleich S, Breitbach B, Peter NJ, Soler R, Bolvardi H, Schneider JM, et al. Thermal stability of nanocomposite Mo_2BC hard coatings deposited by magnetron sputtering. Surf Coatings Technol 2018;349:378–83. doi:10.1016/j.surfcoat.2018.06.006.

[122] Kawasaki M, Nose M, Onishi I, Shiojiri M. Structural Investigation of AlN/SiO_x Nanocomposite Hard Coatings Fabricated by Differential Pumping Cosputtering. Microsc Microanal 2016;22:673–8. doi:10.1017/S1431927616000611.

[123] Veprek S, Zhang RF, Veprek-Heijman MGJ, Sheng SH, Argon AS. Superhard nanocomposites: Origin of hardness enhancement, properties and applications. Surf Coatings Technol 2010;204:1898–906. doi:10.1016/j.surfcoat.2009.09.033.

[124] Veprek S, Veprek-Heijman MGJ. Limits to the preparation of superhard nanocomposites: Impurities, deposition and annealing temperature. Thin Solid Films 2012;522:274–82. doi:10.1016/j.tsf.2012.08.048.

[125] Kumar CS, Patel SK. Application of surface modification techniques during hard turning: Present work and future prospects. Int J Refract Met Hard Mater 2018;76:112–27. doi:10.1016/j.ijrmhm.2018.06.003.

[126] Ziebert C, Stüber M, Leiste H, Ulrich S, Holleck H. Nanoscale PVD Multilayer Coatings. Encycl. Mater. Sci. Technol., Elsevier; 2011, p. 1–8. doi:10.1016/B978-0-08-043152-9.02267-3.

[127] Inspektor A, Salvador PA. Architecture of PVD coatings for metalcutting applications: A review. Surf Coatings Technol 2014;257:138–53. doi:10.1016/j.surfcoat.2014.08.068.

[128] Pogrebnjak A, Smyrnova K, Bondar O. Nanocomposite Multilayer Binary Nitride Coatings Based on Transition and Refractory Metals: Structure and Properties. Coatings 2019;9:155. doi:10.3390/coatings9030155.

[129] Khadem M, Penkov O V., Yang H-K, Kim D-E. Tribology of multilayer coatings for wear reduction: A review. Friction 2017;5:248–62. doi:10.1007/s40544-017-0181-7.

[130] Wang J, Yazdi MAP, Lomello F, Billard A, Kovács A, Schuster F, et al. Influence of microstructures on mechanical properties and tribology behaviors of $TiN/Ti_XAl_{1-X}N$ multilayer coatings. Surf Coatings Technol 2017;320:441–6. doi:10.1016/j.surfcoat.2016.11.101.

[131] Andersen KN, Bienk EJ, Schweitz KO, Reitz H, Chevallier J, Kringhøj P, et al. Deposition, microstructure and mechanical and tribological properties of magnetron sputtered TiN/TiAlN multilayers. Surf Coatings Technol 2000;123:219–26. doi:10.1016/S0257-8972(99)00473-9.

[132] Contreras E, Bejarano G, Gómez M. Synthesis and microstructural characterization of nanoscale multilayer TiAlN/TaN coatings deposited by DC magnetron sputtering. Int J Adv Manuf Technol 2019;101:663–73. doi:10.1007/s00170-018-2972-z.

[133] Zha X, Jiang F, Xu X. Investigating the high frequency fatigue failure mechanisms of mono and multilayer PVD coatings by the cyclic impact tests. Surf Coatings Technol 2018;344:689–701. doi:10.1016/j.surfcoat.2018.03.101.

[134] Pshyk A.V., Kravchenko Y, Coy E, Kempiński M, Iatsunskyi I, Załęski K, et al. Microstructure, phase composition and mechanical properties of novel nanocomposite (TiAlSiY)N and nano-scale (TiAlSiY)N/MoN multifunctional heterostructures. Surf Coatings Technol 2018;350:376–90. doi:10.1016/j.surfcoat.2018.07.010.

[135] Illana A, Almandoz E, Fuentes GG, Pérez FJ, Mato S. Comparative study of CrAlSiN monolayer and CrN/AlSiN superlattice multilayer coatings: Behavior at high temperature in steam atmosphere. J Alloys Compd 2019;778:652–61. doi:10.1016/j.jallcom.2018.11.199.

[136] Chang Y-Y, Chiu W-T, Hung J-P. Mechanical properties and high temperature oxidation of CrAlSiN/TiVN hard coatings synthesized by cathodic arc evaporation. Surf Coatings Technol 2016;303:18–24. doi:10.1016/j.surfcoat.2016.02.047.

[137] Seidl WM, Bartosik M, Kolozsvári S, Bolvardi H, Mayrhofer PH. Mechanical properties and oxidation resistance of Al-Cr-N/Ti-Al-Ta-N multilayer coatings. Surf Coatings Technol 2018;347:427–33. doi:10.1016/j.surfcoat.2018.05.025.

[138] Chang Y-Y, Weng S-Y, Chen C-H, Fu F-X. High temperature oxidation and cutting performance of AlCrN, TiVN and multilayered AlCrN/TiVN hard coatings. Surf Coatings Technol 2017;332:494–503. doi:10.1016/j.surfcoat.2017.06.080.

[139] Chang Y-Y, Chang H, Jhao L-J, Chuang C-C. Tribological and mechanical properties of multilayered TiVN/TiSiN coatings synthesized by cathodic arc evaporation. Surf Coatings Technol 2018;350:1071–9. doi:10.1016/j.surfcoat.2018.02.040.

[140] Braic M, Balaceanu M, Parau AC, Dinu M, Vladescu A. Investigation of multilayered TiSiC/NiC protective coatings. Vacuum 2015;120:60–6. doi:10.1016/j.vacuum.2015.06.019.

[141] Buchinger J, Koutná N, Chen Z, Zhang Z, Mayrhofer PH, Holec D, et al. Toughness enhancement in TiN/WN superlattice thin films. Acta Mater 2019;172:18–29. doi:10.1016/j.actamat.2019.04.028.

[142] Pogrebnjak A, Ivashchenko V, Bondar O, Beresnev V, Sobol O, Załęski K, et al. Multilayered vacuum-arc nanocomposite TiN/ZrN coatings before and after annealing: Structure, properties, first-principles calculations. Mater Charact 2017;134:55–63. doi:10.1016/j.matchar.2017.10.016.

[143] Major L, Major R, Kot M, Lackner JM, Major B. Ex situ and in situ nanoscale wear mechanisms characterization of Zr/Zr_xN tribological coatings. Wear 2018;404–405:82–91. doi:10.1016/j.wear.2018.03.011.

[144] Pogrebnjak AD, Kravchenko YO, Bondar O V., Zhollybekov B, Kupchishin AI. Structural Features and Tribological Properties of Multilayer Coatings Based on Refractory Metals.

Prot Met Phys Chem Surfaces 2018;54:240–58. doi:10.1134/S2070205118020107.

[145] Postolnyi BO, Bondar O V., Zaleski K, Coy E, Jurga S, Rebouta L, et al. Multilayer Design of CrN/MoN Superhard Protective Coatings and Their Characterisation. In: Pogrebnjak AD, Novosad V, editors. Adv. Thin Film. Nanostructured Mater. Coatings, Singapore: Springer; 2019, p. 17–29. doi:10.1007/978-981-13-6133-3_2.

[146] Pogrebnjak AD, Beresnev VM, Bondar OV, Postolnyi BO, Zaleski K, Coy E, et al. Superhard CrN/MoN coatings with multilayer architecture. Mater Des 2018;153:47–59. doi:10.1016/j.matdes.2018.05.001.

[147] Beake BD, Fox-Rabinovich GS. Progress in high temperature nanomechanical testing of coatings for optimising their performance in high speed machining. Surf Coatings Technol 2014;255:102–11. doi:10.1016/j.surfcoat.2014.02.062.

[148] Chowdhury S, Beake B, Yamamoto K, Bose B, Aguirre M, Fox-Rabinovich G, et al. Improvement of Wear Performance of Nano-Multilayer PVD Coatings under Dry Hard End Milling Conditions Based on Their Architectural Development. Coatings 2018;8:59. doi:10.3390/coatings8020059.

[149] Bagdasaryan AA, Pshyk AV, Coy LE, Kempiński M, Pogrebnjak AD, Beresnev VM, et al. Structural and mechanical characterization of (TiZrNbHfTa)N/WN multilayered nitride coatings. Mater Lett 2018;229:364–7. doi:10.1016/j.matlet.2018.07.048.

[150] Lin Y, Zia AW, Zhou Z, Shum PW, Li KY. Development of diamond-like carbon (DLC) coatings with alternate soft and hard multilayer architecture for enhancing wear performance at high contact stress. Surf Coatings Technol 2017;320:7–12. doi:10.1016/j.surfcoat.2017.03.007.

[151] Yang K, Liao B, Zhu H, Zhu W, He H, Liu Y, et al. Influence of the Cr interlayer on the microstructure of sputtered TiN coatings deposited on zirconium alloy. Mater Res Express 2018;6:026420. doi:10.1088/2053-1591/aaf041.

[152] Abadias G, Chason E, Keckes J, Sebastiani M, Thompson GB, Barthel E, et al. Review Article: Stress in thin films and coatings: Current status, challenges, and prospects. J Vac Sci Technol A Vacuum, Surfaces, Film 2018;36:020801. doi:10.1116/1.5011790.

[153] Luo Q, Jones AH. High-precision determination of residual stress of polycrystalline coatings using optimised XRD-sin2ψ technique. Surf Coatings Technol 2010;205:1403–8. doi:10.1016/j.surfcoat.2010.07.108.

[154] Bouzakis K-D, Michailidis N, Skordaris G, Bouzakis E, Biermann D, M'Saoubi R. Cutting with coated tools: Coating technologies, characterization methods and performance optimization. CIRP Ann 2012;61:703–23. doi:10.1016/j.cirp.2012.05.006.

[155] Chen Y, Wang J, Chen M. Enhancing the machining performance by cutting tool surface modifications: a focused review. Mach Sci Technol 2019:1–33. doi:10.1080/10910344.2019.1575412.

[156] Oliaei SNB, Karpat Y, Davim JP, Perveen A. Micro tool design and fabrication: A review. J Manuf Process 2018;36:496–519. doi:10.1016/j.jmapro.2018.10.038.

[157] Swan S, Bin Abdullah MS, Kim D, Nguyen D, Kwon P. Tool Wear of Advanced Coated Tools in Drilling of CFRP. J Manuf Sci Eng 2018;140:111018. doi:10.1115/1.4040916.

[158] Volosova M, Grigoriev S, Metel A, Shein A. The Role of Thin-Film Vacuum-Plasma Coatings and Their Influence on the Efficiency of Ceramic Cutting Inserts. Coatings 2018;8:287. doi:10.3390/coatings8080287.

[159] Mitterer C. PVD and CVD Hard Coatings. Compr. Hard Mater., Elsevier; 2014, p. 449–67. doi:10.1016/B978-0-08-096527-7.00035-0.

[160] Rokni MR, Nutt SR, Widener CA, Champagne VK, Hrabe RH. Review of Relationship Between Particle Deformation, Coating Microstructure, and Properties in High-Pressure Cold Spray. J Therm Spray Technol 2017;26:1308–55. doi:10.1007/s11666-017-0575-0.

[161] Pogrebnjak AD, Bagdasaryan AA, Yakushchenko I V, Beresnev VM. The structure and properties of high-entropy alloys and nitride coatings based on them. Russ Chem Rev 2014;83:1027–61. doi:10.1070/RCR4407.

[162] Mayrhofer PH, Mitterer C, Hultman L, Clemens H. Microstructural design of hard coatings. Prog Mater Sci 2006;51:1032–114. doi:10.1016/j.pmatsci.2006.02.002.

[163] Cavaleiro A, De Hosson JTM, editors. Nanostructured Coatings. New York, NY: Springer New York; 2006. doi:10.1007/978-0-387-48756-4.

[164] Wo PC, Zhao XL, Munroe PR, Zhou ZF, Li KY, Habibi D, et al. Extremely hard, damage-tolerant ceramic coatings with functionally graded, periodically varying architecture. Acta Mater 2013;61:193–204. doi:10.1016/j.actamat.2012.09.049.

[165] Pogrebnjak AD, Rogoz VM, Bondar O V., Erdybaeva NK, Plotnikov S V. Structure and physicomechanical properties of NbN-based protective nanocomposite coatings: A review. Prot Met Phys Chem Surfaces 2016;52:802–13. doi:10.1134/S2070205116050191.

[166] Ivashchenko V, Veprek S, Pogrebnjak A, Postolnyi B. First-principles quantum molecular dynamics study of $Ti_xZr_{1-x}N(111)/SiN_y$ heterostructures and comparison with experimental results. Sci Technol Adv Mater 2014;15:025007. doi:10.1088/1468-6996/15/2/025007.

[167] Polcar T, Cavaleiro A. High-temperature tribological properties of CrAlN, CrAlSiN and AlCrSiN coatings. Surf Coatings Technol 2011;206:1244–51. doi:10.1016/j.surfcoat.2011.08.037.

[168] Samani MK, Ding XZ, Khosravian N, Amin-Ahmadi B, Yi Y, Chen G, et al. Thermal conductivity of titanium nitride/titanium aluminum nitride multilayer coatings deposited by lateral rotating cathode arc. Thin Solid Films 2015;578:133–8. doi:10.1016/j.tsf.2015.02.032.

[169] Ma F, Li J, Zeng Z, Gao Y. Structural, mechanical and tribocorrosion behaviour in artificial seawater of CrN/AlN nano-multilayer coatings on F690 steel substrates. Appl Surf Sci

2018;428:404–14. doi:10.1016/j.apsusc.2017.09.166.

[170] Vaz F, Ferreira J, Ribeiro E, Rebouta L, Lanceros-Méndez S, Mendes JA, et al. Influence of nitrogen content on the structural, mechanical and electrical properties of TiN thin films. Surf Coatings Technol 2005;191:317–23. doi:10.1016/j.surfcoat.2004.01.033.

[171] Mayrhofer PH, Kunc F, Musil J, Mitterer C. A comparative study on reactive and non-reactive unbalanced magnetron sputter deposition of TiN coatings. Thin Solid Films 2002;415:151–9. doi:10.1016/S0040-6090(02)00511-4.

[172] Subramanian B, Muraleedharan CV, Ananthakumar R, Jayachandran M. A comparative study of titanium nitride (TiN), titanium oxy nitride (TiON) and titanium aluminum nitride (TiAlN), as surface coatings for bio implants. Surf Coatings Technol 2011;205:5014–20. doi:10.1016/j.surfcoat.2011.05.004.

[173] Chim YC, Ding XZ, Zeng XT, Zhang S. Oxidation resistance of TiN, CrN, TiAlN and CrAlN coatings deposited by lateral rotating cathode arc. Thin Solid Films 2009;517:4845–9. doi:10.1016/j.tsf.2009.03.038.

[174] Musil J, Jaroš M, Kos Š, Čerstvý R, Haviar S. Hard TiN 2 dinitride films prepared by magnetron sputtering. J Vac Sci Technol A 2018;36:040602. doi:10.1116/1.5038555.

[175] Xie ZH, Hoffman M, Munroe P, Singh R, Bendavid A, Martin PJ. Microstructural response of TiN monolithic and multilayer coatings during microscratch testing. J Mater Res 2007;22:2312–8. doi:10.1557/jmr.2007.0292.

[176] Yousaf MI, Pelenovich VO, Yang B, Liu CS, Fu DJ. Effect of bilayer period on structural and mechanical properties of nanocomposite TiAlN/MoN multilayer films synthesized by cathodic arc ion-plating. Surf Coatings Technol 2015;282:94–102. doi:10.1016/j.surfcoat.2015.10.018.

[177] Rocha LA, Ariza E, Ferreira J, Vaz F, Ribeiro E, Rebouta L, et al. Structural and corrosion behaviour of stoichiometric and substoichiometric TiN thin films. Surf Coatings Technol 2004;180–181:158–63. doi:10.1016/j.surfcoat.2003.10.059.

[178] Abadias G, Djemia P, Belliard L. Alloying effects on the structure and elastic properties of hard coatings based on ternary transition metal (M=Ti, Zr or Ta) nitrides. Surf Coatings Technol 2014;257:129–37. doi:10.1016/j.surfcoat.2014.08.022.

[179] Wang F, Holec D, Odén M, Mücklich F, Abrikosov IA, Tasnádi F. Systematic ab initio investigation of the elastic modulus in quaternary transition metal nitride alloys and their coherent multilayers. Acta Mater 2017;127:124–32. doi:10.1016/j.actamat.2017.01.017.

[180] Ghafoor N, Petrov I, Klenov DO, Freitag B, Jensen J, Greene JE, et al. Self-organized anisotropic $(Zr_{1-x}Si_x)N_y$ nanocomposites grown by reactive sputter deposition. Acta Mater 2015;82:179–89. doi:10.1016/j.actamat.2014.09.029.

[181] Yalamanchili K, Schramm IC, Jiménez-Piqué E, Rogström L, Mücklich F, Odén M, et al. Tuning hardness and fracture resistance of $ZrN/Zr_{0.63}Al_{0.37}N$ nanoscale multilayers by

stress-induced transformation toughening. Acta Mater 2015;89:22–31. doi:10.1016/j.actamat.2015.01.066.

[182] Abadias G, Uglov VV, Saladukhin IA, Zlotski SV, Tolmachova G, Dub SN, et al. Growth, structural and mechanical properties of magnetron-sputtered ZrN/SiN_x nanolaminated coatings. Surf Coatings Technol 2016;308:158–67. doi:10.1016/j.surfcoat.2016.06.099.

[183] Stueber M, Holleck H, Leiste H, Seemann K, Ulrich S, Ziebert C. Concepts for the design of advanced nanoscale PVD multilayer protective thin films. J Alloys Compd 2009;483:321–33. doi:10.1016/j.jallcom.2008.08.133.

[184] Xue P, Yang L, Diao D. Nanocrystalline/amorphous biphase enhanced mechanical properties in multilayer carbon films. Surf Coatings Technol 2018;334:1–6. doi:10.1016/j.surfcoat.2017.10.061.

[185] Pogrebnjak AD, Eyidi D, Abadias G, Bondar OV, Beresnev VM, Sobol OV. Structure and properties of arc evaporated nanoscale TiN/MoN multilayered systems. Int J Refract Met Hard Mater 2015;48:222–8. doi:10.1016/j.ijrmhm.2014.07.043.

[186] Koshy RA, Graham ME, Marks LD. Synthesis and characterization of CrN/Mo_2N multilayers and phases of Molybdenum nitride. Surf Coatings Technol 2007;202:1123–8. doi:10.1016/j.surfcoat.2007.07.090.

[187] Koshy RA, Graham ME, Marks LD. Temperature activated self-lubrication in CrN/Mo_2N nanolayer coatings. Surf Coatings Technol 2010;204:1359–65. doi:10.1016/j.surfcoat.2009.09.026.

[188] Han B, Wang Z, Devi N, Kondamareddy KK, Wang Z, Li N, et al. RBS Depth Profiling Analysis of (Ti, Al)N/MoN and CrN/MoN Multilayers. Nanoscale Res Lett 2017;12:161. doi:10.1186/s11671-017-1921-3.

[189] Kuleshov AK, Uglov V V., Chayevski V V., Anishchik VM. Properties of coatings based on Cr, Ti, and Mo nitrides with embedded metals deposited on cutting tools. J Frict Wear 2011;32:192–8. doi:10.3103/S106836661103007X.

[190] Nordin M, Larsson M, Hogmark S. Mechanical and tribological properties of multilayered PVD TiN/CrN, TiN/MoN, TiN/NbN and TiN/TaN coatings on cemented carbide. Surf Coatings Technol 1998;106:234–41. doi:10.1016/S0257-8972(98)00544-1.

[191] Abadias G, Dub S, Shmegera R. Nanoindentation hardness and structure of ion beam sputtered TiN, W and TiN/W multilayer hard coatings. Surf Coatings Technol 2006;200:6538–43. doi:10.1016/j.surfcoat.2005.11.053.

[192] Koehler JS. Attempt to Design a Strong Solid. Phys Rev B 1970;2:547–51. doi:10.1103/PhysRevB.2.547.

[193] Lehoczky SL. Retardation of Dislocation Generation and Motion in Thin-Layered Metal Laminates. Phys Rev Lett 1978;41:1814–8. doi:10.1103/PhysRevLett.41.1814.

[194] Barshilia H, Deepthi B, Rajam K. Transition Metal Nitride–Based Nanolayered Multilayer

Coatings and Nanocomposite Coatings as Novel Superhard. Nanostructured Thin Film. Coatings Mech. Prop., CRC Press; Taylor & Francis Group; 2010, p. 427–80. doi:10.1201/b11763-11.

[195] Li N, Liu X-Y. Review: mechanical behavior of metal/ceramic interfaces in nanolayered composites—experiments and modeling. J Mater Sci 2018;53:5562–83. doi:10.1007/s10853-017-1767-1.

[196] Liu Y, Bufford D, Wang H, Sun C, Zhang X. Mechanical properties of highly textured Cu/Ni multilayers. Acta Mater 2011;59:1924–33. doi:10.1016/j.actamat.2010.11.057.

[197] Misra A, Hirth JP, Kung H. Single-dislocation-based strengthening mechanisms in nanoscale metallic multilayers. Philos Mag A 2002;82:2935–51. doi:10.1080/01418610208239626.

[198] Matizamhuka W. Structure-Properties Relationships. Microstruct. Correl. Hard, Superhard, Ultrahard Mater., Cham: Springer International Publishing; 2016, p. 75–103. doi:10.1007/978-3-319-29291-5_3.

[199] Pogrebnjak AD, Ivashchenko VI, Skrynskyy PL, Bondar OV, Konarski P, Załęski K, et al. Experimental and theoretical studies of the physicochemical and mechanical properties of multi-layered TiN/SiC films: Temperature effects on the nanocomposite structure. Compos Part B Eng 2018;142:85–94. doi:10.1016/j.compositesb.2018.01.004.

[200] Bobzin K, Brögelmann T, Kruppe NC, Arghavani M, Mayer J, Weirich TE. Plastic deformation behavior of nanostructured CrN/AlN multilayer coatings deposited by hybrid dcMS/HPPMS. Surf Coatings Technol 2017;332:253–61. doi:10.1016/j.surfcoat.2017.06.092.

[201] Jian J, Lee JH, Liu Y, Khatkhatay F, Yu K, Su Q, et al. Plastic deformation in nanocrystalline TiN at ultra-low stress: An in situ nanoindentation study. Mater Sci Eng A 2016;650:445–53. doi:10.1016/j.msea.2015.10.002.

[202] Chen W, Lin Y, Zheng J, Zhang S, Liu S, Kwon SC. Preparation and characterization of CrAlN/TiAlSiN nano-multilayers by cathodic vacuum arc. Surf Coatings Technol 2015;265:205–11. doi:10.1016/j.surfcoat.2015.01.023.

[203] Wang H, Zeng H, Li Q, Shen J. Superlattice supertoughness of TiN/ M N (M = V, Nb, Ta, Mo, and W): First-principles study. Thin Solid Films 2016;607:59–66. doi:10.1016/j.tsf.2016.03.061.

[204] Badiger P V., Desai V, Ramesh MR. Development and Characterization of Ti/TiC/TiN Coatings by Cathodic Arc Evaporation Technique. Trans Indian Inst Met 2017;70:2459–64. doi:10.1007/s12666-017-1107-9.

[205] Caicedo JC, Amaya C, Yate L, Nos O, Gomez ME, Prieto P. Hard coating performance enhancement by using $[Ti/TiN]_n$, $[Zr/ZrN]_n$ and $[TiN/ZrN]_n$ multilayer system. Mater Sci Eng B 2010;171:56–61. doi:10.1016/j.mseb.2010.03.069.

[206] Bondar O V., Postol'nyi BA, Beresnev VM, Abadias G, Chartier P, Sobol O V., et al. Composition, structure and tribotechnical properties of TiN, MoN single-layer and TiN/MoN multilayer coatings. J Superhard Mater 2015;37:27–38. doi:10.3103/S1063457615010050.

[207] Pogrebnjak AD, Beresnev VM, Bondar O V., Abadias G, Chartier P, Postol'nyi BA, et al. The effect of nanolayer thickness on the structure and properties of multilayer TiN/MoN coatings. Tech Phys Lett 2014;40:215–8. doi:10.1134/S1063785014030092.

[208] Beresnev VM, Bondar O V., Postolnyi BO, Lisovenko MO, Abadias G, Chartier P, et al. Comparison of tribological characteristics of nanostructured TiN, MoN, and TiN/MoN Arc-PVD coatings. J Frict Wear 2014;35:374–82. doi:10.3103/S1068366614050031.

[209] Pogrebnjak AD, Abadias G, Bondar OV, Postolnyi BO, Lisovenko MO, Kyrychenko OV, et al. Structure and Properties of Multilayer Nanostructured Coatings TiN/MoN Depending on Deposition Conditions. Acta Phys Pol A 2014;125:1280–3. doi:10.12693/APhysPolA.125.1280.

[210] Navinšek B, Panjan P, Milošev I. Industrial applications of CrN (PVD) coatings, deposited at high and low temperatures. Surf Coatings Technol 1997;97:182–91. doi:10.1016/S0257-8972(97)00393-9.

[211] Pogrebnjak AD, Ivasishin OM, Beresnev VM. Arc-Evaporated Nanoscale Multilayer Nitride-Based Coatings for Protection Against Wear, Corrosion, and Oxidation. Usp Fiz Met 2016;17:1–28. doi:10.15407/ufm.17.01.001.

[212] Gilewicz A, Warcholinski B. Deposition and characterisation of Mo_2N/CrN multilayer coatings prepared by cathodic arc evaporation. Surf Coatings Technol 2015;279:126–33. doi:10.1016/j.surfcoat.2015.08.042.

[213] Jauberteau I, Bessaudou A, Mayet R, Cornette J, Jauberteau J, Carles P, et al. Molybdenum Nitride Films: Crystal Structures, Synthesis, Mechanical, Electrical and Some Other Properties. Coatings 2015;5:656–87. doi:10.3390/coatings5040656.

[214] Postolnyi BO, Beresnev VM, Abadias G, Bondar OV, Rebouta L, Araujo JP, et al. Multilayer design of CrN/MoN protective coatings for enhanced hardness and toughness. J Alloys Compd 2017;725:1188–98. doi:10.1016/j.jallcom.2017.07.010.

[215] Polcar T, Martinez R, Vítů T, Kopecký L, Rodriguez R, Cavaleiro A. High temperature tribology of CrN and multilayered Cr/CrN coatings. Surf Coatings Technol 2009;203:3254–9. doi:10.1016/j.surfcoat.2009.04.005.

[216] Nouveau C, Djouadi M., Decès-Petit C, Beer P, Lambertin M. Influence of CrxNy coatings deposited by magnetron sputtering on tool service life in wood processing. Surf Coatings Technol 2001;142–144:94–101. doi:10.1016/S0257-8972(01)01092-1.

[217] Milošev I, Strehblow H-H, Navinšek B. Comparison of TiN, ZrN and CrN hard nitride coatings: Electrochemical and thermal oxidation. Thin Solid Films 1997;303:246–54. doi:10.1016/S0040-6090(97)00069-2.

[218] Wang Y, Chen Y, Zhao D, Lu X, Liu W, Qi F, et al. Deformation mechanism of CrN/nitriding coated steel in wear and nano-scratch experiments under heavy loading conditions. Appl Surf Sci 2018;447:100–6. doi:10.1016/j.apsusc.2018.03.213.

[219] Gilewicz A, Warcholinski B. Tribological properties of CrCN/CrN multilayer coatings. Tribol Int 2014;80:34–40. doi:10.1016/j.triboint.2014.06.012.

[220] Ou YX, Lin J, Tong S, Sproul WD, Lei MK. Structure, adhesion and corrosion behavior of CrN/TiN superlattice coatings deposited by the combined deep oscillation magnetron sputtering and pulsed dc magnetron sputtering. Surf Coatings Technol 2016;293:21–7. doi:10.1016/j.surfcoat.2015.10.009.

[221] Yang ZX, Kuang XY, Wang ZH, Zhong MM, Huang XF. The mechanical properties of MoN under high pressure and effect of metallic bonding on its hardness. Solid State Sci 2014;28:20–5. doi:10.1016/j.solidstatesciences.2013.12.002.

[222] Hazar H. Characterization of MoN coatings for pistons in a diesel engine. Mater Des 2010;31:624–7. doi:10.1016/j.matdes.2009.06.006.

[223] Anitha VP, Major S, Chandrashekharam D, Bhatnagar M. Deposition of molybdenum nitride thin films by r.f. reactive magnetron sputtering. Surf Coatings Technol 1996;79:50–4. doi:10.1016/0257-8972(95)02425-5.

[224] Yashar PC, Sproul WD. Nanometer scale multilayered hard coatings. Vacuum 1999;55:179–90. doi:10.1016/S0042-207X(99)00148-7.

[225] Yao SH, Su YL. The tribological potential of CrN and Cr(C,N) deposited by multi-arc PVD process. Wear 1997;212:85–94. doi:10.1016/S0043-1648(97)00128-2.

[226] Medvedeva A, Bergström J, Gunnarsson S, Andersson J. High-temperature properties and microstructural stability of hot-work tool steels. Mater Sci Eng A 2009;523:39–46. doi:10.1016/j.msea.2009.06.010.

[227] Daniel R, Meindlhumer M, Baumegger W, Zalesak J, Sartory B, Burghammer M, et al. Grain boundary design of thin films: Using tilted brittle interfaces for multiple crack deflection toughening. Acta Mater 2017;122:130–7. doi:10.1016/j.actamat.2016.09.027.

[228] Bouaouina B, Besnard A, Abaidia SE, Haid F. Residual stress, mechanical and microstructure properties of multilayer Mo_2N/CrN coating produced by R.F Magnetron discharge. Appl Surf Sci 2017;395:117–21. doi:10.1016/j.apsusc.2016.04.024.

[229] Grankin SS, Beresnev VM, Sobol OV, Stolbovoy VA, Novikov VY, Lytovchenko SV, et al. Structure, Substructure, Hardness and Adhesion Strength of Multiperiod Composite Coatings MoN/CrN. J Nano- Electron Phys 2015;7:04050-1-04050–5.

[230] Beresnev VM, Klimenko SA, Sobol' O V., Grankin SS, Stolbovoi VA, Turbin P V., et al. Effect of the deposition parameters on the phase–structure state, hardness, and tribological characteristics of Mo_2N/CrN vacuum–arc multilayer coatings. J Superhard Mater 2016;38:114–22. doi:10.3103/S1063457616020052.

[231] Postolnyi B, Bondar O, Opielak M, Rogalski P, Araújo JP. Structural analysis of multilayer metal nitride films CrN/MoN using electron backscatter diffraction (EBSD). In: Vladescu M, Tamas R, Cristea I, editors. Proc. SPIE - Int. Soc. Opt. Eng., vol. 10010, 2016, p. 100100E. doi:10.1117/12.2243279.

[232] Postolnyi BO, Araujo JP. Structural analysis of Arc-PVD multilayer metal nitride coatings CrN/MoN using electron backscatter diffraction (EBSD). 2016 Int. Conf. Nanomater. Appl. Prop., IEEE; 2016, p. 01NTF16-1-01NTF16-4. doi:10.1109/NAP.2016.7757249.

[233] Postolnyi B, Araújo JP, Pogrebnjak A. Applying of Electron Backscatter Diffraction (EBSD) for Studying Structural and Phase Composition of Multilayer CrN/MoN Coatings Fabricated by Arc-PVD. Eur. Microsc. Congr. 2016 Proc., Weinheim, Germany: Wiley-VCH Verlag GmbH & Co. KGaA; 2016, p. 673–4. doi:10.1002/9783527808465.EMC2016.6951.

[234] Luo L. Electron Microscopy, Materials & Mechanisms Lab 2018. https://www.luolangli.com/microscopy (accessed November 4, 2019).

[235] Inkson BJ. Scanning electron microscopy (SEM) and transmission electron microscopy (TEM) for materials characterization. Mater. Charact. Using Nondestruct. Eval. Methods, Elsevier; 2016, p. 17–43. doi:10.1016/B978-0-08-100040-3.00002-X.

[236] Ilitchev A. How Do You Make an Electron Beam? – Electron Source Fundamentals 2019. https://www.thermofisher.com/blog/microscopy/how-do-you-make-an-electron-beam-electron-source-fundamentals/ (accessed November 13, 2019).

[237] Central Microscopy Research Facility. Scanning Electron Microscopy n.d. https://cmrf.research.uiowa.edu/scanning-electron-microscopy (accessed November 13, 2019).

[238] Han W, Jiao H, Fox D. Scanning Electron Microscopy, 2018, p. 35–68. doi:10.1007/978-981-13-0454-5_2.

[239] MyScope Microscopy Training: Scanning Electron Microscopy. Intro n.d. https://myscope.training/#/SEMlevel_2_3 (accessed November 14, 2019).

[240] Ul-Hamid A. Contrast Formation in the SEM. A Beginners' Guid. to Scanning Electron Microsc., Cham: Springer International Publishing; 2018, p. 77–128. doi:10.1007/978-3-319-98482-7_3.

[241] Bell DC, Erdman N. Introduction to the Theory and Advantages of Low Voltage Electron Microscopy. Low Volt. Electron Microsc., Chichester, UK: John Wiley & Sons, Ltd; 2012, p. 1–30. doi:10.1002/9781118498514.ch1.

[242] Ul-Hamid A. Components of the SEM. A Beginners' Guid. to Scanning Electron Microsc., Cham: Springer International Publishing; 2018, p. 15–76. doi:10.1007/978-3-319-98482-7_2.

[243] Scharf D. Detectors: Secondary Electron Detectors, Image Quality & Contrast 2004. http://www.scharfphoto.com/articles/detectors (accessed November 15, 2019).

[244] Miles J. Detection of Chiral Organic Compounds with Femtosecond Lasers. Queen's University, 2016. doi:10.13140/RG.2.2.33544.67842.

[245] Goldstein JI, Newbury DE, Echlin P, Joy DC, Lyman CE, Lifshin E, et al. Specimen Preparation of Hard Materials: Metals, Ceramics, Rocks, Minerals, Microelectronic and Packaged Devices, Particles, and Fibers. Scanning Electron Microsc. X-ray Microanal., Boston, MA: Springer US; 2003, p. 537–64. doi:10.1007/978-1-4615-0215-9_11.

[246] Fitzgerald R, Keil K, Heinrich KFJ. Solid-State Energy-Dispersion Spectrometer for Electron-Microprobe X-ray Analysis. Science 1968;159:528–30. doi:10.1126/science.159.3814.528.

[247] Ul-Hamid A. Microchemical Analysis in the SEM. A Beginners' Guid. to Scanning Electron Microsc., Cham: Springer International Publishing; 2018, p. 265–307. doi:10.1007/978-3-319-98482-7_7.

[248] Goldstein JI, Newbury DE, Echlin P, Joy DC, Lyman CE, Lifshin E, et al. X-Ray Spectral Measurement: EDS and WDS. Scanning Electron Microsc. X-ray Microanal., Boston, MA: Springer US; 2003, p. 297–353. doi:10.1007/978-1-4615-0215-9_7.

[249] Liao Y. Silicon Drift EDS Detectors (SDDs) - Practical Electron Microscopy and Database 2018. https://www.globalsino.com/EM/page2532.html (accessed November 28, 2019).

[250] Lutz G. Silicon drift and pixel devices for X-ray imaging and spectroscopy. J Synchrotron Radiat 2006;13:99–109. doi:10.1107/S0909049506002214.

[251] Curceanu C, Amirkhani A, Baniahmad A, Bazzi M, Bellotti G, Berucci C, et al. X-ray Detectors for Kaonic Atoms Research at DAΦNE. Condens Matter 2019;4:42. doi:10.3390/condmat4020042.

[252] Raja PM V., Barron AR. An Introduction to Energy Dispersive X-ray Spectroscopy - Chemistry LibreTexts 2019. https://chem.libretexts.org/Bookshelves/Analytical_Chemistry/Book%3A_Physical_Methods_in_Chemistry_and_Nano_Science_(Barron)/01%3A_Elemental_Analysis/1.12%3A_An_Introduction_to_Energy_Dispersive_X-ray_Spectroscopy (accessed November 21, 2019).

[253] Thermo Fisher Scientific Inc. Principles and Applications of Parallel Beam Wavelength Dispersive X-ray Spectroscopy. White Pap 52608 2014.

[254] Oxford Instruments NanoAnalysis. An Introduction to Energy-Dispersive and Wavelength-Dispersive X-Ray Microanalysis. Microsc Anal X-Ray Suppl 2006;4:S5–8.

[255] Australian Bureau of Statistics. Statistical Language - Quantitative and Qualitative Data 2013. https://www.abs.gov.au/websitedbs/a3121120.nsf/home/statistical+language+-+quantitative+and+qualitative+data (accessed December 6, 2019).

[256] Goldstein JI, Newbury DE, Echlin P, Joy DC, Lyman CE, Lifshin E, et al. Scanning Electron Microscopy and X-ray Microanalysis. Boston, MA: Springer US; 2003. doi:10.1007/978-1-

4615-0215-9.

[257] Nguyen VN, Nguyen QM, Huong Thao DT, Huang SC. An Investigation of Dissimilar Welding Aluminum Alloys to Stainless Steel by the Tungsten Inert Gas (TIG) Welding Process. Mater Sci Forum 2017;904:19–23. doi:10.4028/www.scientific.net/MSF.904.19.

[258] Goldstein JI, Newbury DE, Echlin P, Joy DC, Lyman CE, Lifshin E, et al. Qualitative X-Ray Analysis. Scanning Electron Microsc. X-ray Microanal., Boston, MA: Springer US; 2003, p. 355–90. doi:10.1007/978-1-4615-0215-9_8.

[259] Goldstein JI, Newbury DE, Echlin P, Joy DC, Lyman CE, Lifshin E, et al. Special Topics in Electron Beam X-Ray Microanalysis. Scanning Electron Microsc. X-ray Microanal., Boston, MA: Springer US; 2003, p. 453–536. doi:10.1007/978-1-4615-0215-9_10.

[260] Mikuśkiewicz M, Stopyra M, Moskal G. Synthesis and Thermal Properties of Cerium-Dysprosium Oxide. Arch Metall Mater 2016;61:965–9. doi:10.1515/amm-2016-0164.

[261] Xiao J, Prud'homme N, Li N, Ji V. Influence of humidity on high temperature oxidation of Inconel 600 alloy: Oxide layers and residual stress study. Appl Surf Sci 2013;284:446–52. doi:10.1016/j.apsusc.2013.07.117.

[262] Potts PJ. Electron probe microanalysis. A Handb. Silic. Rock Anal., Boston, MA: Springer US; 1987, p. 326–82. doi:10.1007/978-1-4615-3270-5_10.

[263] Nobel Media AB. Wilhelm Conrad Röntgen – Facts. NobelPrize.org. 2019.

[264] Rigaku Corporation. Presentation and Training for Rigaku SmartLab diffractometer. 2015.

[265] Cockcroft JK. Generation of X-rays. Course Mater Master - Sch Crystallogr Birkbeck Coll Univ London 2006. http://pd.chem.ucl.ac.uk/pdnn/inst1/xrays.htm (accessed August 19, 2019).

[266] Dinnebier RE, Billinge SJL. Chapter 1. Principles of Powder Diffraction. Powder Diffr., Cambridge: Royal Society of Chemistry; 2008, p. 1–19. doi:10.1039/9781847558237-00001.

[267] Jiang L, Verman B, Kim B, Platonov Y, Al-Mosheky Z, Smith R, et al. Application of Multilayer Optics to X-ray Diffraction Systems. Rigaku J 2001;18:13–22.

[268] Takeshi O. Principles and applications of multilayer mirror optics for X-ray diffraction measurements. Rigaku J 2017;33:15–9.

[269] Rigaku Corporation. Help Manual to the SmartLab Guidance v.2.1.0.0 - Sample Alignment Part. 2014.

[270] ICDD Powder Diffraction Files: No. 00-006-0694 for Cr (bcc), No. 00-042-1120 for Mo (bcc), No. 00-011-0065 for CrN (fcc), No. 00-035-0803 for β-Cr_2N, No. 00-025-1366 for γ-Mo_2N (fcc) and No. 00-025-1368 for β-Mo_2N. 2004.

[271] Scherrer P. Bestimmung der Größe und der inneren Struktur von Kolloidteilchen mittels Röntgenstrahlen. Nachrichten von Der Gesellschaft Der Wissenschaften Zu Göttingen, Math Klasse 1918;1918:98–100.

[272] Deveci M, Stresstech. Measurement Methods of Residual Stresses. Stress Bull 2003.

[273] Fitzpatrick ME, Fry AT, Holdway P, Kandil FA, Shackleton J, Suominen L. Determination of Residual Stresses by X-ray Diffraction – Issue 2. Teddington, UK: National Physical Laboratory; 2005.

[274] Gall D, Shin C-S, Spila T, Odén M, Senna MJH, Greene JE, et al. Growth of single-crystal CrN on MgO(001): Effects of low-energy ion-irradiation on surface morphological evolution and physical properties. J Appl Phys 2002;91:3589–97. doi:10.1063/1.1446239.

[275] Wroński S, Wierzbanowski K, Baczmański A, Lodini A, Braham C, Seiler W. X-ray grazing incidence technique—corrections in residual stress measurement—a review. Powder Diffr 2009;24:S11–5. doi:10.1154/1.3139054.

[276] Schwartz AJ, Kumar M, Adams BL, Field DP, editors. Electron Backscatter Diffraction in Materials Science. Boston, MA: Springer US; 2009. doi:10.1007/978-0-387-88136-2.

[277] Maitland T, Sitzman S. Backscattering Detector and EBSD in Nanomaterials Characterization. Scanning Microsc. Nanotechnol., New York, NY: Springer New York; 2006, p. 41–75. doi:10.1007/978-0-387-39620-0_2.

[278] Tkadletz M, Schalk N, Daniel R, Keckes J, Czettl C, Mitterer C. Advanced characterization methods for wear resistant hard coatings: A review on recent progress. Surf Coatings Technol 2016;285:31–46. doi:10.1016/j.surfcoat.2015.11.016.

[279] Steinmetz DR, Zaefferer S. Towards ultrahigh resolution EBSD by low accelerating voltage. Mater Sci Technol 2010;26:640–5. doi:10.1179/026708309X12506933873828.

[280] Humphreys F. Characterisation of fine-scale microstructures by electron backscatter diffraction (EBSD). Scr Mater 2004;51:771–6. doi:10.1016/j.scriptamat.2004.05.016.

[281] Goldstein JI, Newbury DE, Michael JR, Ritchie NWM, Scott JHJ, Joy DC. Backscattered Electrons. Scanning Electron Microsc. X-Ray Microanal., New York, NY: Springer New York; 2018, p. 15–28. doi:10.1007/978-1-4939-6676-9_2.

[282] Oxford Instruments. EBSD.com. Index Diffr Patterns from All Cryst Syst 2019. http://www.ebsd.com/ebsd-applications/ebsd-gallery/indexed-diffraction-patterns-from-all-crystal-systems (accessed October 30, 2019).

[283] Zaefferer S. On the formation mechanisms, spatial resolution and intensity of backscatter Kikuchi patterns. Ultramicroscopy 2007;107:254–66. doi:10.1016/j.ultramic.2006.08.007.

[284] Yoda R. Electron Backscatter Diffraction. Compend. Surf. Interface Anal., Singapore: Springer Singapore; 2018, p. 127–32. doi:10.1007/978-981-10-6156-1_22.

[285] EDAX, AMETEK Inc. DigiView EBSD Camera by EDAX 2017. https://www.edax.com/products/ebsd/digiview-ebsd-camera (accessed October 30, 2019).

[286] Wallace S, EDAX, AMETEK Inc. Understanding and Optimizing EBSD Camera Settings (Presentation) 2016:42. https://rsc.aux.eng.ufl.edu/_files/documents/964.pdf (accessed November 1, 2019).

[287] Williams DB, Carter CB. Electron Sources. Transm. Electron Microsc., Boston, MA: Springer US; 2009, p. 73–89. doi:10.1007/978-0-387-76501-3_5.

[288] Williams DB, Carter CB. The Instrument. Transm. Electron Microsc., Boston, MA: Springer US; 2009, p. 141–71. doi:10.1007/978-0-387-76501-3_9.

[289] Yang Y, Wang K, Liang H-W, Liu G-Q, Feng M, Xu L, et al. A new generation of alloyed/multimetal chalcogenide nanowires by chemical transformation. Sci Adv 2015;1:e1500714. doi:10.1126/sciadv.1500714.

[290] Kisielowski C, Freitag B, Bischoff M, van Lin H, Lazar S, Knippels G, et al. Detection of Single Atoms and Buried Defects in Three Dimensions by Aberration-Corrected Electron Microscope with 0.5-Å Information Limit. Microsc Microanal 2008;14:469–77. doi:10.1017/S1431927608080902.

[291] Sawada H, Tanishiro Y, Ohashi N, Tomita T, Hosokawa F, Kaneyama T, et al. STEM imaging of 47-pm-separated atomic columns by a spherical aberration-corrected electron microscope with a 300-kV cold field emission gun. J Electron Microsc (Tokyo) 2009;58:357–61. doi:10.1093/jmicro/dfp030.

[292] Williams DB, Carter CB. High-Resolution TEM. Transm. Electron Microsc., Boston, MA: Springer US; 2009, p. 483–509. doi:10.1007/978-0-387-76501-3_28.

[293] Brabazon D, Raffer A. Advanced Characterization Techniques for Nanostructures. Emerg. Nanotechnologies Manuf., Elsevier; 2010, p. 59–91. doi:10.1016/B978-0-8155-1583-8.00003-X.

[294] Mattox DM. Substrate (“Real”) Surfaces and Surface Modification. Handb. Phys. Vap. Depos. Process., Elsevier; 2010, p. 25–72. doi:10.1016/B978-0-8155-2037-5.00002-2.

[295] Encyclopædia Britannica. Surface Analysis: Secondary ion mass spectroscopy and ion scattering spectroscopy n.d.

[296] Heidelberg University. Heidelberg Ion Probe - SIMS Basics 2017. https://www.geow.uni-heidelberg.de/HIP/instrumentation_en.html (accessed December 12, 2019).

[297] Semitracks Inc. Failure Analysis Materials Characterization - Secondary Ion Mass Spectrometry 2019. https://www.semitracks.com/reference-material/failure-and-yield-analysis/failure-analysis-materials-characterization/secondary-ion-mass-spectrometry.php (accessed December 12, 2019).

[298] Kim Y-P, Shon HK, Shin SK, Lee TG. Probing nanoparticles and nanoparticle-conjugated biomolecules using time-of-flight secondary ion mass spectrometry. Mass Spectrom Rev 2015;34:237–47. doi:10.1002/mas.21437.

[299] Naito M. Direct imaging type SIMS instrument. 4912326, 1990.

[300] Banica FG. Surface Analysis: Secondary Ion Mass Spectrometry (SIMS)-A short overview 2009. http://folk.ntnu.no/floban/KJ 3055/Surface/SIMS.htm (accessed December 14, 2019).

[301] Yalçın ŞH. Advanced Analytical Chemistry Course: Secondary Ion Mass Spectrometry (SIMS) 2017. http://web.iyte.edu.tr/~serifeyalcin/lectures/chem502/L7.pdf (accessed December 14, 2019).

[302] Craven J, School of GeoSciences of the University of Edinburgh. Secondary Ion Mass Spectrometry 2019. https://www.ed.ac.uk/files/atoms/files/sims4.pdf (accessed December 14, 2019).

[303] Plasma Physics Research Centre IAU. Secondary Ion Mass Spectrometry Instrumentation Tutorial n.d. http://pprco.tripod.com/SIMS/Instrumentation.htm (accessed December 15, 2019).

[304] Shimadzu Corp. Introduction to mass analyzers 2019. https://www.shimadzu.com/an/lcms/support/fundamental/mass_analyzers.html (accessed December 15, 2019).

[305] (U.S.) GS, Snavely PD, Hobbs SW, Shanks WC, Criss RE, Hays WH, et al. New Frontiers in Stable Isotopic Research: Laser Probes, Ion Probes, and Small-sample Analysis. U.S. Government Printing Office; 1989.

[306] Vickerman JC. Molecular Surface Mass Spectrometry by SIMS. Surf. Anal. Princ. Tech., Chichester, UK: John Wiley & Sons, Ltd; n.d., p. 113–205. doi:10.1002/9780470721582.ch4.

[307] Khan O. Mass Analyzers (Mass Spectrometry) - Chemistry LibreTexts 2019. https://chem.libretexts.org/Bookshelves/Analytical_Chemistry/Supplemental_Modules_(Analytical_Chemistry)/Instrumental_Analysis/Mass_Spectrometry/Mass_Spectrometers_(Instrumentation)/Mass_Analyzers_(Mass_Spectrometry) (accessed December 16, 2019).

[308] Gates P, School of Chemistry of the University of Bristol. Mass Spectrometry Facility - Quadrupole 2014. http://www.chm.bris.ac.uk/ms/quadrupole.xhtml (accessed December 16, 2019).

[309] Palmetshofer L. Rutherford Backscattering Spectroscopy (RBS). Surf. Thin Film Anal., Weinheim, Germany: Wiley-VCH Verlag GmbH & Co. KGaA; 2011, p. 191–202. doi:10.1002/9783527636921.ch11.

[310] Alford TL, Feldman LC, Mayer JW. Atomic Collisions and Backscattering Spectrometry. Fundam. Nanoscale Film Anal., Boston, MA: Springer US; n.d., p. 12–33. doi:10.1007/978-0-387-29261-8_2.

[311] Goncharova L. RBS Tutorial Files. Rutherford Backscattering Spectrom Tutirial 2013. http://www.physics.uwo.ca/~lgonchar/research/links/June3_2013/RBS_June3_2013_slides.pdf (accessed December 19, 2019).

[312] Döbeli M. Material Analysis - Rutherford Backscattering Spectrometry (RBS) 2001. https://www.phys.ethz.ch/content/dam/ethz/special-interest/phys/particle-physics/ion-beam-physics-dam/documents/MaterialsAnalysis.pdf (accessed December 19, 2019).

[313] Alford TL, Feldman LC, Mayer JW. Energy Loss of Light Ions and Backscattering Depth Profiles. Fundam. Nanoscale Film Anal., Boston, MA: Springer US; n.d., p. 34–58. doi:10.1007/978-0-387-29261-8_3.

[314] Eurofins Scientific. RBS Tutorial: Instrumentation - EAG Laboratories 2019. https://www.eag.com/resources/tutorials/rbs-tutorial-instrumentation/ (accessed December 22, 2019).

[315] Cameca. NanoSIMS 50 User's Guide: Primary column. n.d.

[316] Hinterberger F. Electrostatic accelerators. In: Brandt D, editor. CAS - Cern Accel. Sch. KVI Spec. CAS Course Small Accel., Zeegse: 2006, p. 95–112. doi:10.5170/CERN-2006-012.95.

[317] Christine S, Encyclopædia Britannica. Particle Accelerator 2018. https://www.britannica.com/technology/particle-accelerator (accessed December 29, 2019).

[318] Kim DK. Nanoindentation - Lecture 1 - Basic Pronciples 2007:10. https://www.slideshare.net/viet4777/nano-indentation-lecture1?from_action=save.

[319] Sundararajan G, Roy M. Hardness Testing. Encycl. Mater. Sci. Technol., Elsevier; 2001, p. 3728–36. doi:10.1016/B0-08-043152-6/00665-3.

[320] Matsuda K, Kaneta M. Analysis of the Vickers hardness of electroplated coatings. Philos Mag A 1996;74:1171–84. doi:10.1080/01418619608239717.

[321] Saha R, Nix WD. Effects of the substrate on the determination of thin film mechanical properties by nanoindentation. Acta Mater 2002;50:23–38. doi:10.1016/S1359-6454(01)00328-7.

[322] Puchi-Cabrera ES, Staia MH, Iost A. Modeling the composite hardness of multilayer coated systems. Thin Solid Films 2015;578:53–62. doi:10.1016/j.tsf.2015.01.070.

[323] Fernandes JV, Trindade AC, Menezes LF, Cavaleiro A. A model for coated surface hardness. Surf Coatings Technol 2000;131:457–61. doi:10.1016/S0257-8972(00)00839-2.

[324] Korsunsky AM, McGurk MR, Bull SJ, Page TF. On the hardness of coated systems. Surf Coatings Technol 1998;99:171–83. doi:10.1016/S0257-8972(97)00522-7.

[325] ISO 14577-1: Metallic materials — Instrumented indentation test for hardness and materials parameters. Geneva: 2015.

[326] Broitman E. Indentation Hardness Measurements at Macro-, Micro-, and Nanoscale: A Critical Overview. Tribol Lett 2017;65:23. doi:10.1007/s11249-016-0805-5.

[327] Knoop F, Peters CG, Emerson WB. A sensitive pyramidal-diamond tool for indentation measurements. J Res Natl Bur Stand (1934) 1939;23:39. doi:10.6028/jres.023.022.

[328] National Bureau of Standards. Specifications for Knoop Indenters, Letter Circular LC819, Washington, D.C. USA: 1946.

[329] Fischer-Cripps AC. Nanoindentation. New York, NY: Springer New York; 2011. doi:10.1007/978-1-4419-9872-9.

[330] Oliver WC, Pharr GM. An improved technique for determining hardness and elastic modulus using load and displacement sensing indentation experiments. J Mater Res 1992;7:1564–83. doi:10.1557/JMR.1992.1564.

[331] Oliver WC, Pharr GM. Measurement of hardness and elastic modulus by instrumented indentation: Advances in understanding and refinements to methodology. J Mater Res 2004;19:3–20. doi:10.1557/jmr.2004.19.1.3.

[332] Pharr GM, Oliver WC, Brotzen FR. On the generality of the relationship among contact stiffness, contact area, and elastic modulus during indentation. J Mater Res 1992;7:613–7. doi:10.1557/JMR.1992.0613.

[333] Fischer-Cripps AC. Depth-Sensing Indentation Testing. Introd. to Contact Mech., Springer, Boston, MA; 2007, p. 189–99. doi:10.1007/978-0-387-68188-7_11.

[334] Ètvrtlík R, Stranyánek M, Boháè P, Jastrabík L. NanoTest^{TM} NT600 - A Device for Analyses of Mechanical Properties of Materials. Mater Struct 2006;13:90–3.

[335] Beake B, Goodes S, Jones S, Parkinson R, Pickford N, Smith J. NanoTest On-line Help File Version 1.0 and NanoTest Manual Version 3.0. Unit 3, The Byre, Wrexham Technology Park, Wrexham, LL13 7YP, United Kingdom: 2004.

[336] Verma D, Qu T, Tomar V. Scale Dependence of the Mechanical Properties and Microstructure of Crustaceans Thin Films as Biomimetic Materials. JOM 2015;67:858–66. doi:10.1007/s11837-015-1337-4.

[337] Xu L, Kong L, Zhao H, Wang S, Liu S, Qian L. Mechanical Behavior of Undoped n-Type GaAs under the Indentation of Berkovich and Flat-Tip Indenters. Materials (Basel) 2019;12:1192. doi:10.3390/ma12071192.

[338] ASTM International. ASTM G40-17, Standard Terminology Relating to Wear and Erosion. West Conshohocken: 2017. doi:10.1520/G0040-17.

[339] Hutchings I, Gee M, Santner E. Friction and Wear. Springer Handb. Mater. Meas. Methods, Berlin, Heidelberg: Springer Berlin Heidelberg; 2006, p. 685–710. doi:10.1007/978-3-540-30300-8_13.

[340] Seyfert C. Tribometers, Rotational, for Sliding Wear and Friction. Encycl. Lubr. Lubr., Berlin, Heidelberg: Springer Berlin Heidelberg; 2014, p. 2138–55. doi:10.1007/978-3-642-22647-2_144.

[341] Hashemi SM, Parvin N, Valefi Z. Effect of microstructure and mechanical properties on wear behavior of plasma-sprayed Cr_2O_3-YSZ-SiC coatings. Ceram Int 2019;45:5284–96. doi:10.1016/j.ceramint.2018.11.226.

[342] Gulbiński W, Suszko T. Thin films of Mo_2N/Ag nanocomposite—the structure, mechanical and tribological properties. Surf Coatings Technol 2006;201:1469–76. doi:10.1016/j.surfcoat.2006.02.017.

[343] Adachi H, Wasa K. Thin Films and Nanomaterials. Handb. Sputtering Technol., Elsevier;

2012, p. 3–39. doi:10.1016/B978-1-4377-3483-6.00001-2.

[344] Gobbi AL, Nascente PAP. D.C. Sputtering. Encycl. Tribol., Boston, MA: Springer US; 2013, p. 699–706. doi:10.1007/978-0-387-92897-5_1029.

[345] Waite MM, Shah SI, Glocker DA. Sputtering Sources. SVC Bull 2010;Spring:42–50.

[346] Bundesmann C, Neumann H. Tutorial: The systematics of ion beam sputtering for deposition of thin films with tailored properties. J Appl Phys 2018;124:231102. doi:10.1063/1.5054046.

[347] Ohring M. Thin-Film Evaporation Processes. Mater. Sci. Thin Film., Elsevier; 2002, p. 95–144. doi:10.1016/B978-012524975-1/50006-9.

[348] Mak CL. Department of Applied Physics, The Hong Kong Polytechnic University. Classif Depos Technol n.d.:29. http://ap.polyu.edu.hk/apaclmak/MSC-TFT2.pdf (accessed December 10, 2019).

[349] Adeyeye AO, Shimon G. Growth and Characterization of Magnetic Thin Film and Nanostructures, 2015, p. 1–41. doi:10.1016/B978-0-444-62634-9.00001-1.

[350] Frey H. Vacuum Evaporation. Handb. Thin-Film Technol., Berlin, Heidelberg: Springer Berlin Heidelberg; 2015, p. 13–71. doi:10.1007/978-3-642-05430-3_3.

[351] Lévy F. Film Growth and Epitaxy: Methods. Ref. Modul. Mater. Sci. Mater. Eng., Elsevier; 2016. doi:10.1016/B978-0-12-803581-8.01012-2.

[352] Kurosaki J-I, Tanaka S, Miyazaki K, Tsukamoto H. The Development of the Micro-Generator on the Substrate Based Thin Film. ASME 2008 First Int. Conf. Micro/Nanoscale Heat Transf. Parts A B, ASMEDC; 2008, p. 1083–8. doi:10.1115/MNHT2008-52198.

[353] Barron AR. Molecular Beam Epitaxy. Chem. Electron. Mater., OpenStax CNX; 2009.

[354] Shang SM, Zeng W. Conductive nanofibres and nanocoatings for smart textiles. Multidiscip. Know-How Smart-Textiles Dev., Elsevier; 2013, p. 92–128. doi:10.1533/9780857093530.1.92.

[355] Koskinen J. Cathodic-Arc and Thermal-Evaporation Deposition. Compr. Mater. Process., Elsevier; 2014, p. 3–55. doi:10.1016/B978-0-08-096532-1.00409-X.

[356] Sanders DM, Anders A. Review of cathodic arc deposition technology at the start of the new millennium. Surf Coatings Technol 2000;133–134:78–90. doi:10.1016/S0257-8972(00)00879-3.

[357] Anders A. Cathodic Arcs. vol. 50. New York, NY: Springer New York; 2010. doi:10.1007/978-0-387-79108-1.

[358] Anders A. Unfiltered and Filtered Cathodic Arc Deposition. Handb. Depos. Technol. Film. Coatings, Elsevier; 2010, p. 466–531. doi:10.1016/B978-0-8155-2031-3.00010-7.

[359] M. B. Bochkarev. Ecton processes of low current vacuum arc imaged with streak technique. XXIst Int. Symp. Discharges Electr. Insul. Vacuum, 2004. Proceedings. ISDEIV., vol. 1, IEEE; n.d., p. 241–4. doi:10.1109/DEIV.2004.1418650.

[360] Rudenko VP, Stolbovoy VA, Serdyuk IV, Kartmazov KG. Control system for superhard multi-layered Arc-PVD coatings deposition (Original in Russian: Система управления нанесением сверхтвердых нанослойных вакуумно-дуговых покрытий. Восточно-Европейский журнал передовых технологий.). Eastern-European J Enterp Technol 2010;6:66–9.

[361] Shen L, Wang N. Effect of Nitrogen Pressure on the Structure of Cr-N, Ta-N, Mo-N, and W-N Nanocrystals Synthesized by Arc Discharge. J Nanomater 2011;2011:1–5. doi:10.1155/2011/781935.

[362] Xu XM, Wang J, An J, Zhao Y, Zhang QY. Effect of modulation structure on the growth behavior and mechanical properties of TiN/ZrN multilayers. Surf Coatings Technol 2007;201:5582–6. doi:10.1016/j.surfcoat.2006.07.132.

[363] Rogström L, Johnson LJS, Johansson MP, Ahlgren M, Hultman L, Odén M. Thermal stability and mechanical properties of arc evaporated ZrN/ZrAlN multilayers. Thin Solid Films 2010;519:694–9. doi:10.1016/j.tsf.2010.08.119.

[364] R Development Core Team R. Computational Many-Particle Physics. vol. 739. Berlin, Heidelberg: Springer Berlin Heidelberg; 2008. doi:10.1007/978-3-540-74686-7.

[365] Han B, Pelenovich VO, Yousaf MI, Yan SJ, Wang W, Zhou SY, et al. Properties of CrN/Mo_2N nano-multilayer films synthesized by multi-cathodic arc ion plating system. Thin Solid Films 2016;619:160–5. doi:10.1016/j.tsf.2016.10.074.

[366] Wang Q, Zhou F, Yan J. Evaluating mechanical properties and crack resistance of CrN, CrTiN, CrAlN and CrTiAlN coatings by nanoindentation and scratch tests. Surf Coatings Technol 2016;285:203–13. doi:10.1016/j.surfcoat.2015.11.040.

[367] Sarioglu C, Demirler U, Kazmanli MK, Urgen M. Measurement of residual stresses by X-ray diffraction techniques in MoN and Mo_2N coatings deposited by arc PVD on high-speed steel substrate. Surf Coatings Technol 2005;190:238–43. doi:10.1016/j.surfcoat.2004.08.184.

[368] Guimaraes MCR, de Castilho BCNM, Nossa T de S, Avila PRT, Cucatti S, Alvarez F, et al. On the effect of substrate oscillation on CrN coatings deposited by HiPIMS and dcMS. Surf Coatings Technol 2018;340:112–20. doi:10.1016/j.surfcoat.2018.02.028.

[369] Pradhan SK, Nouveau C, Vasin A, Djouadi M-A. Deposition of CrN coatings by PVD methods for mechanical application. Surf Coatings Technol 2005;200:141–5. doi:10.1016/j.surfcoat.2005.02.038.

[370] Pelleg J, Zevin LZ, Lungo S, Croitoru N. Reactive-sputter-deposited TiN films on glass substrates. Thin Solid Films 1991;197:117–28. doi:10.1016/0040-6090(91)90225-M.

[371] Högberg H, Hultman L, Emmerlich J, Joelsson T, Eklund P, Molina-Aldareguia JM, et al. Growth and characterization of MAX-phase thin films. Surf Coatings Technol 2005;193:6–10. doi:10.1016/j.surfcoat.2004.08.174.

[372] Monshi A, Foroughi MR, Monshi MR. Modified Scherrer Equation to Estimate More Accurately Nano-Crystallite Size Using XRD. World J Nano Sci Eng 2012;02:154–60. doi:10.4236/wjnse.2012.23020.

[373] Pemmasani SP, Valleti K, Gundakaram RC, Rajulapati K V., Mantripragada R, Koppoju S, et al. Effect of microstructure and phase constitution on mechanical properties of $Ti_{1-x}Al_xN$ coatings. Appl Surf Sci 2014;313:936–46. doi:10.1016/j.apsusc.2014.06.112.

[374] Tavares CJ, Rebouta L, Almeida B, Bessa e Sousa J. Structural characterization of multilayered sputtered TiN/ZrN coatings. Surf Coatings Technol 1998;100–101:65–71. doi:10.1016/S0257-8972(97)00589-6.

[375] Söderberg H, Odén M, Molina-Aldareguia JM, Hultman L. Nanostructure formation during deposition of TiN/SiN_x nanomultilayer films by reactive dual magnetron sputtering. J Appl Phys 2005;97:114327. doi:10.1063/1.1935135.

[376] Yang Q, Zhao LR, McKellar R, Patnaik PC. Microstructure and mechanical properties of multi-constituent superlattice coatings. Vacuum 2006;81:101–5. doi:10.1016/j.vacuum.2006.03.002.

[377] Wiklund U, Bromark M, Larsson M, Hedenqvist P, Hogmark S. Cracking resistance of thin hard coatings estimated by four-point bending. Surf Coatings Technol 1997;91:57–63. doi:10.1016/S0257-8972(96)03123-4.

[378] Powder Diffraction Files: card 065-2899 for fcc-CrN, card 025-1366 for fcc-γ-Mo2N. n.d.

[379] Klimashin FF, Koutná N, Euchner H, Holec D, Mayrhofer PH. The impact of nitrogen content and vacancies on structure and mechanical properties of Mo–N thin films. J Appl Phys 2016;120:185301. doi:10.1063/1.4966664.

[380] Linker G, Smithey R, Meyer O. Superconductivity in MoN films with NaCl structure. J Phys F Met Phys 1984;14:L115–9. doi:10.1088/0305-4608/14/7/005.

[381] Perry AJ, Baouchi AW, Petersen JH, Pozder SD. Crystal structure of molybdenum nitride films made by reactive cathodic arc evaporation. Surf Coatings Technol 1992;54–55:261–5. doi:10.1016/S0257-8972(09)90060-3.

[382] Lowther JE. Lattice model for the properties of non-stoichiometric cubic and hexagonal molybdenum nitride. J Alloys Compd 2004;364:13–6. doi:10.1016/S0925-8388(03)00537-1.

[383] Barbosa J, Cunha L, Rebouta L, Moura C, Vaz F, Carvalho S, et al. Properties of MoN_xO_y thin films as a function of the N/O ratio. Thin Solid Films 2006;494:201–6. doi:10.1016/j.tsf.2005.07.192.

[384] Jian S-R, Chen G-J, Lin T-C. Berkovich Nanoindentation on AlN Thin Films. Nanoscale Res Lett 2010;5:935–40. doi:10.1007/s11671-010-9582-5.

[385] Harea EE, Aifantis KE. Understanding the evolution of the pop-out effect in Si-based structures for photovoltaics. Surf Eng Appl Electrochem 2014;50:497–503. doi:10.3103/S1068375514060040.

[386] Jiapeng S, Cheng L, Han J, Ma A, Fang L. Nanoindentation Induced Deformation and Pop-in Events in a Silicon Crystal: Molecular Dynamics Simulation and Experiment. Sci Rep 2017;7:10282. doi:10.1038/s41598-017-11130-2.

[387] Gleiter H. Nanocrystalline materials. Prog Mater Sci 1989;33:223–315. doi:10.1016/0079-6425(89)90001-7.

[388] Ivashchenko VI, Porada OK, Ivashchenko LA, Timofeeva II, Dub SM, Skrinskii PL. Mechanical and tribological properties of TiN and SiCN nanocomposite coatings deposited using methyltrichlorosilane. Powder Metall Met Ceram 2008;47:95–101. doi:10.1007/s11106-008-0013-4.

[389] Pogrebnjak AD, Beresnev VM. Hard Nanocomposite Coatings, Their Structure and Properties. In: Farzad E, editor. Nanocomposites - New Trends Dev., InTech; 2012, p. 123–60. doi:10.5772/50567.

[390] Caicedo JC, Zambrano G, Aperador W, Escobar-Alarcon L, Camps E. Mechanical and electrochemical characterization of vanadium nitride (VN) thin films. Appl Surf Sci 2011;258:312–20. doi:10.1016/j.apsusc.2011.08.057.

[391] Zhu M, Xuan F, Chen J. Influence of microstructure and microdefects on long-term fatigue behavior of a Cr–Mo–V steel. Mater Sci Eng A 2012;546:90–6. doi:10.1016/j.msea.2012.03.030.

[392] Ivashchenko VI, Veprek S, Turchi PEA, Shevchenko VI. First-principles study of TiN/SiC/TiN interfaces in superhard nanocomposites. Phys Rev B 2012;86:014110. doi:10.1103/PhysRevB.86.014110.

[393] Musil J. Flexible hard nanocomposite coatings. RSC Adv 2015;5:60482–95. doi:10.1039/C5RA09586G.

[394] Marulanda DM, Olaya JJ, Piratoba U, Mariño A, Camps E. The effect of bilayer period and degree of unbalancing on magnetron sputtered Cr/CrN nano-multilayer wear and corrosion. Thin Solid Films 2011;519:1886–93. doi:10.1016/j.tsf.2010.10.010.

[395] Hogmark S, Jacobson S, Larsson M. Design and evaluation of tribological coatings. Wear 2000;246:20–33. doi:10.1016/S0043-1648(00)00505-6.

[396] Öztürk A, Ezirmik KV, Kazmanlı K, Ürgen M, Eryılmaz OL, Erdemir A. Comparative tribological behaviors of TiN, CrN and MoNCu nanocomposite coatings. Tribol Int 2008;41:49–59. doi:10.1016/j.triboint.2007.04.008.

[397] Seibert F, Döbeli M, Fopp-Spori DM, Glaentz K, Rudigier H, Schwarzer N, et al. Comparison of arc evaporated Mo-based coatings versus Cr_1N_1 and ta–C coatings by reciprocating wear test. Wear 2013;298–299:14–22. doi:10.1016/j.wear.2012.11.085.

[398] Ávila RF, Mancosu RD, Machado AR, Vecchio SD, da Silva RB, Vieira JM. Comparative analysis of wear on PVD TiN and $(Ti_{1-x}Al_x)N$ coatings in machining process. Wear 2013;302:1192–200. doi:10.1016/j.wear.2013.01.112.

[399] Dedalus Consulting, New York 2014.

[400] Hafedh D, Kaouthar K, Larbi Ahmed BC. Nanoindentation of Thin Films Prepared by Physical Vapor Deposition. Int J Chem Mol Nucl Mater Metall Eng 2015;9:368–71.

[401] Kulkarni AP, Joshi GG, Sargade VG. Performance of PVD AlTiCrN coating during machining of austenitic stainless steel. Surf Eng 2013;29:402–7. doi:10.1179/1743294413Y.0000000130.

[402] Kulkarni AP, Sargade VG. Characterization and Performance of AlTiN, AlTiCrN, TiN/TiAlN PVD Coated Carbide Tools While Turning SS 304. Mater Manuf Process 2015;30:748–55. doi:10.1080/10426914.2014.984217.

[403] Zhou H, Zheng J, Gui B, Geng D, Wang Q. AlTiCrN coatings deposited by hybrid HIPIMS/DC magnetron co-sputtering. Vacuum 2017;136:129–36. doi:10.1016/j.vacuum.2016.11.021.

[404] Chuan SP, Ghani JA, Tomadi SH, Hassan CHC. Analysis of Ti-base Hard Coating Performance in Machining Process: A Review. J Appl Sci 2012;12:1882–90. doi:10.3923/jas.2012.1882.1890.

[405] Strnad G, Chetan P. Novel Coatings for High Performance Cutting and Dry Machining. In: Moldovan L, editor. 6th Int. Conf. Interdiscip. Eng. Interdiscip. Dev. New Technol., Petru Maior" University Publishing House; 2012, p. 75–80.

[406] Stone DS, Yoder KB, Sproul WD. Hardness and elastic modulus of TiN based on continuous indentation technique and new correlation. J Vac Sci Technol A Vacuum, Surfaces, Film 1991;9:2543–7. doi:10.1116/1.577270.

[407] Shtansky DV, Kiryukhantsev-Korneev PV, Sheveyko AN, Kutyrev AE, Levashov EA. Hard tribological Ti–Cr–B–N coatings with enhanced thermal stability, corrosion- and oxidation resistance. Surf Coatings Technol 2007;202:861–5. doi:10.1016/j.surfcoat.2007.05.064.

[408] Rebholz C, Ziegele H, Leyland A, Matthews A. Structure, mechanical and tribological properties of Ti–B–N and Ti–Al–B–N multiphase thin films produced by electron-beam evaporation. J Vac Sci Technol A Vacuum, Surfaces, Film 1998;16:2851–7. doi:10.1116/1.581431.

[409] Mo JL, Zhu MH, Leyland A, Matthews A. Impact wear and abrasion resistance of CrN, AlCrN and AlTiN PVD coatings. Surf Coatings Technol 2013;215:170–7. doi:10.1016/j.surfcoat.2012.08.077.

[410] Holleck H, Schier V. Multilayer PVD coatings for wear protection. Surf Coatings Technol 1995. doi:10.1016/0257-8972(95)02555-3.

[411] Lind L, Peetsalu P, Sergejev F. Wear of different PVD coatings at industrial fine-blanking field tests. Mater Sci 2015;21. doi:10.5755/j01.ms.21.3.7249.

[412] Beake BD, Ning L, Gey C, Veldhuis SC, Komarov A, Weaver A, et al. Wear performance of different PVD coatings during hard wet end milling of H13 tool steel. Surf Coatings

Technol 2015;279:118–25. doi:10.1016/j.surfcoat.2015.08.038.

[413] Payán-Díaz S, De La Cruz W, Talamantes-Soto R, Hurtado-Macías A, Hirata GA. Effect of volume fraction on mechanical properties of Zr/ZrN multilayer systems. Ceram Int 2016;42:18806–12. doi:10.1016/j.ceramint.2016.09.025.

[414] Auger MA, Araiza JJ, Falcony C, Sánchez O, Albella JM. Hardness and tribology measurements on ZrN coatings deposited by reactive sputtering technique. Vacuum 2007;81:1462–5. doi:10.1016/j.vacuum.2007.04.009.

[415] Thulasi Raman KH, Kiran MSRN, Ramamurty U, Mohan Rao G. Structural and mechanical properties of room temperature sputter deposited CrN coatings. Mater Res Bull 2012;47:4463–6. doi:10.1016/j.materresbull.2012.09.051.

[416] Reiter AE, Derflinger VH, Hanselmann B, Bachmann T, Sartory B. Investigation of the properties of Al1−xCrxN coatings prepared by cathodic arc evaporation. Surf Coatings Technol 2005;200:2114–22. doi:10.1016/j.surfcoat.2005.01.043.

[417] Zabinski J, Voevodin A. Ceramic and Other Hard Coatings. In: Vižintin J, Kalin M, Dohda K, Jahanmir S, editors. Tribol. Mech. Syst., Three Park Avenue New York, NY 10016-5990: ASME; 2004, p. 157–81. doi:10.1115/1.802094.ch9.

[418] Yang TS, Yao SH, Chang YY, Deng JH. Contact Behavior of Composite CrTiSiN Coated Dies in Compressing of Mg Alloy Sheets under High Pressure. Materials (Basel) 2018;11:88. doi:10.3390/ma11010088.

[419] Matthews A, Leyland A. Materials Related Aspects of Nanostructured Tribological Coatings. SVC Bull 2009;Spring:40–5.